Local flow conditions in the Bergen valley based on observations and numerical simulations

Master Thesis in Meteorology

Aslaug Skålevik Valved

October 2012

UNIVERSITY OF BERGEN
GEOPHYSICAL INSTITUTE

The picture on the front page was taken during field work at the site of the Ulriksbakken Automatic Weather Station in December 2011. Mount Løvstakken is standing tall above the clouds on the opposite side of the Bergen valley.

Acknowledgements

I would like to express my gratitude for all help given by my supervisor, Joachim Reuder, throughout this study. His ideas, advices, guidance and particularly all the long hours of work at the end of this project, are highly appreciated. In addition, I would like to thank for the opportunity to work with a subject that is of great interest for me, and for making this a reality. I am also grateful for all the help given by my co-supervisor, Marius Opsanger Jonassen. All technical support from him with WRF and Matlab has been of enormous help. Without his effort, this thesis would not have been as comprehensive as it is now. I would also like to thank for his guidance along the way, his proof-reading at the end, and for including me in his article.

Another important contributor to this thesis is Anak Bhandari. I highly appreciate all his work and help with the weather stations and rawdata. It is due to him that this study now has long time series with observations. I am also very glad for being included in the field work, which has been a great experience that I would not have missed out on.

I would also like to acknowledge Ole Edvard Grov and Jan Asle Olseth for providing me with the Florida and Ulriken data, Tim Hewson at the UK Met Office for providing me with the synoptic charts and Haraldur Olafsson for his ideas for this thesis, and for encouraging me to present my work at the EGU conference in Vienna 2012. I would also like to thank Idar Barstad, Stefan Sobolowski and Michel d. S. Mesquita at the Bjerknes Centre for making it possible for me to present my work at the EGU conference, and for everything they have thought me.

WRF and NCL have been a challenge, and I would like to thank my WRF and NCL buddy, Marina Lara Dütsch, for her company, help and support. I would also like to give a special thank to Andrea Eugster, Marie Eide and Lauritz Skålevik Valved for taking their time to proof-read my thesis.

My study time has been an unforgettable time, and I would like to thank former and current students at GFI for this time and help along the way.

Last but not least, I would like to give a special and warm appreciation to my friends, family and Per Åge for being there for me through all these years, and for helping me with the field work, independent of the weather conditions.

Abstract

The complex topography and variability in surface roughness in the Bergen valley affects the flow conditions in a multitude of ways. The steep mountains give shelter during strong synoptic flow, but the orography of Bergen can also lead to problems, such as accumulation of pollutants. A network of seven automatic weather stations has been installed to represent the horizontal and vertical variety of meteorological conditions in the Bergen valley. More than 17 months of data from 2010-2012 have been evaluated to give a general overview of the flow conditions. Case studies covering the local effect of strong synoptic wind and thermally induced circulation have also been investigated. Numerical simulations using the Weather Research and Forecasting Model (WRF) have been compared with the observations for the two case studies covering the thermally induced flow, namely the land-sea breeze circulation and an inversion. The quality of the WRF model has also been tested, which showed that the model's accuracy was good when simulating the sea breeze, but less accurate during inversions.

The dense network and long time series have resulted in some new and interesting results. The results show that a typical vertical extension of the sea breeze exceeds the height of Løvstakken, and at the Ulriken side of the valley, anabatic flow is enhanced by the sea breeze. There are also strong local differences in the directional distribution of the flow, as the station downstream of Isdalen reveals a completely different wind distribution than at Florida, located only 1.7 km apart. The results also show that the wind speed at the lower elevated stations exceeds the wind speed at Ulriken for particular wind directions at Ulriken. This is linked to the direction of the large-scale flow and the local topography. Typical wind directions and wind speeds for inversions to develop are found, revealing that southerly and easterly directions are the most common ones. Observations of fronts passing a location confirm well established theory on the subject.

The numerical simulations have led to new results for the sea breeze in the Bergen valley, for example the existence of a stronger sea breeze on a larger scale outside the coast of Bergen. Numerical simulations also show the reason for the strong inversion during southeasterly flow in November 2011, as warm air was transported toward the valley during high atmospheric stability.

This study has resulted in a broader understanding of the flow conditions in the Bergen valley, but it has also resulted in more questions to be answered in the future.

Contents

Chapter 1

Introduction

The city of Bergen lies protected in a valley surrounded by steep mountain slopes that range between 300 to 600 m on both sides, and open areas in the SE and in the NW, where the open area continues into Byfjorden. The complex topography and variability in surface roughness affect the wind in a multitude of ways, causing a high local variability. In general, the Bergen valley lies rather protected from strong winds. Jonassen et al. (2012b) studied *the Bergen shelter* in detail, and found that the Løvstakken and the Fløyen massifs both protect the Bergen valley area from strong winds related to southwesterly windstorms. On the other hand, the stagnation of the air due to the orography in the Bergen valley can also cause problems with respect to air quality. Especially during wintertime in Bergen, inversions often lead to accumulation of pollutants, a well known problem for the people living in Bergen. During summertime, thermally induced wind systems, as the land-sea breeze and mountain-valley winds, are important for the ventilation of the Bergen valley. These wind systems prevent the accumulation of emissions by cars and ships in otherwise weak synoptic wind conditions.

A characterization of the different flow conditions in the Bergen valley is the main aim for this study. For this purpose, a dense network of observational stations has been set up. These observations are then combined with numerical simulations to better understand the relevant processes and flow conditions. Case studies are used to investigate typical flow conditions for the Bergen valley, but also to investigate the capability of state-of-the-art models to represent these conditions in complex terrain for different synoptic situations.

Flow conditions in the Bergen area have been investigated in several earlier studies. Berge and Hassel (1984) categorized different types of inversions in the Bergen area, along with local drainage flows, and Dyngeseth (1998) brought their work further using observations they collected, along with numerical simulations. Utaaker (1995) did a more climatic study for temperature inversions and flow conditions for different parts of the Bergen area. The land-sea breeze circulation has been discussed from a climatic

point of view by Utaaker (1995) and later by Jonassen et al. (2012a), while Dyngeseth (1998) did a more detailed study of one particular land-sea breeze case, based on observations from 1997 and numerical simulations. The simulations performed by Dyngeseth (1998) were done with the non-hydrostatic mesoscale model, MEMO, a high resolution model which does not take synoptic flow into account.

In more recent years, Barstad and Grønås (2005) studied the effect of different synoptic conditions on the southwest coast of Norway, as the flow impinged on the mountain range, Langfjella, using numerical simulations. Jonassen et al. (2012a) took it a step further, and connected the synoptic flow to the local impact on the southwest coast of Norway, including Bergen and the surrounding area, based on observations and numerical simulations. Jonassen et al. (2012b) further investigated the so-called Bergen orographic wind shelter during the impact of southwesterly windstorms in the Bergen valley. Their research was based on observations and numerical simulations. Their research also focused on getting detailed landuse and topography datasets to get as realistic results as possible with high resolution simulations, using the Weather Research and Forecasting Model (WRF).

The development of numerical models over the last years has made it possible to perform simulations with high resolutions on regional scales with great accuracy. Such simulations are used in this study to fill in information which is not possible to get from the observations. The results in two of the case studies are therefore supplemented by numerical simulations using the WRF model, with the detailed landuse and topography datasets from Jonassen et al. (2012b). The accuracy of the model on these particular situations has also been tested by comparing simulated time series with the observations.

The theory which this study is based on is described in chapter 2, followed by a description of the WRF model and its setup in chapter 3. The location of the area of interest, and site descriptions for the observational stations are given in chapter 4. The instrumentation and a description of the field work and data handling, along with the challenges that have occurred, are described in chapter 5. The first results in this study are presented in chapter 6, where the general flow conditions in the Bergen valley are investigated, based on the observations for the whole period of collected data (23 November 2010 to 01 July 2012). In the following chapters, shorter time periods for specific synoptic situations and local effects are investigated. The local effect of strong synoptic wind is investigated in chapter 7, where two severe southwesterly storms that hit the west coast of Norway in November and December 2011 are studied. Jonassen et al. (2012a) also focused on southwesterly storms to investigate the Bergen shelter, using the observations collected in this study, along with numerical simula-

tions. Because of this, the results in this study are based on the observations and not numerical simulations. For further details about southwesterly storms hitting Bergen, see Jonassen et al. (2012a), which is also attached at the end of this thesis. The two following chapters focus on situations with low or no synoptic wind, where the flow conditions are thermally induced. These two case studies include both observations and numerical simulations. The first of these two case studies focuses on the land-sea breeze circulation which dominates during summer, and is presented in chapter 8. The last case study focuses on an inversion case, which is typical during winter in the Bergen valley, and is presented in chapter 9. Finally, a summary of the most important conclusions and an outlook are given in chapter 10.

Chapter 2

Theory

2.1 Introduction

The structure of the Bergen valley is quite complex. It contains steep topography connected to the sea. Due to this complex structure, a large variety of effects have to be considered to understand the local flow characteristics. First of all, the large scale synoptic situation will affect the local weather. Strong winds such as low pressure systems or fronts passing can lead to blocking, speed-up and channeling of the wind, in addition to changing characteristics of the surface weather. During weak synoptic winds and high pressure systems, thermal induced circulations can be present. The topography and shape of the valley can cause mountain and valley wind circulation, or valley inversion, and the fjord can cause land-sea breeze circulation. The city of Bergen itself may also affect the local weather, especially in the temperature and wind field. However, the features described in the following are ideal and single event cases. In reality, several of these can coexist and work together or against each other.

2.2 The local effect of passing fronts

When an extratropical cyclone is about to develop, like the one illustrated in figure 2.1, an observer at the surface will first experience a warm front. As the warm front approaches, the isobars will tighten and the wind will get stronger and turn clockwise. The temperature will rise, and the pressure will drop (Wallace and Hobbs, 2006). The highest wind speeds however, are usually observed in the warm sector, the sector between the warm and the cold front, relatively close to the center of the system. The wind speed and the speed of the system are mainly in the same direction in this area. As the cold front passes, the wind will veer clockwise and become gusty and the temperature will drop. The isobars tend to have a sharp bend, and may suddenly change direction along the cold front. The pressure drops as the front approaches, but will rise again after the front has passed, due to the higher density of the cold air (Wallace and Hobbs, 2006). After the cold front has passed, the wind weakens. The conditions

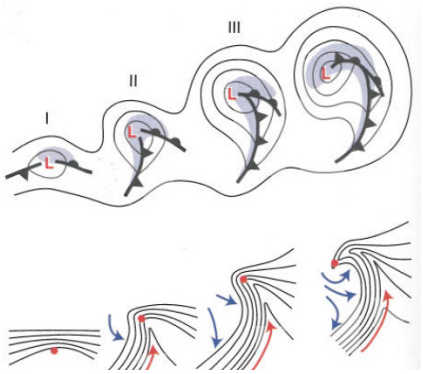

Figure 2.1: *The four stages of the Norwegian polar front cyclone model from the Bergen School of Meteorology. A warm and a cold front develops into an occluded front and an extratropical cyclone. Top: Idealized frontal structure and isobars. The shaded areas show regions of precipitation. Bottom: The black lines are isotherms, and the colored arrows indicate the airflow relative to the center of the cyclone (red dot). Red arrows denotes the warm sector, and flow in the cold air mass are denoted by blue arrows (Wallace and Hobbs, 2006).*

around the occluded front depend on the conditions ahead of the front. However, an occluded front is generally warmer than the cold front, and the wind will continue to veer clockwise.

It can in some cases be difficult to locate fronts using temperature gradients. Factors such as time of the day, cloud amount, altitude of the station, distance to water, and the heat island effect (section 2.7) can affect the temperatures. The moisture gradient can therefore be a more reliable indicator of a front in some cases. The reason for this is that the moisture gradient has less diurnal variability than the temperature gradient, especially during spring and summer. On the other hand, topographic features and land-sea geometry can cause a rise in the moisture field that is not caused by a passing front (Wallace and Hobbs, 2006).

2.3 Orographically modified winds

Topography can modify the wind field, depending on the steepness, height, shape and extension. According to Oke (1987), typical wind patterns can be explained depending on the size of the topography, when assuming neutrally stratified flow normal to the long axis of the obstacle. Figure 2.2(a) shows typical patterns over moderate topography. There will be a speed up over a small hill or an island, while there will be a slowdown right before and after it. There can also be a speed up around it. When there is an elevation or lowering in the terrain, there will be a speed up at the edge of the elevation, and a slowdown at the bottom. If the topography narrows, for example

at the beginning of a valley, there can be a speed up. Figure 2.2(b) illustrates flow over steep topography. When a flow approaches a steep ridge, the pressure builds up in front of the ridge, and flow that deflects downward, creates eddies. The wind in this area is weak and turbulent. However, most of the flow goes upward and speeds up over the ridge. A flow separation then occurs, and a new area with weak and turbulent wind is formed. This area is sheltered from the mean wind, but can experience strong short-term gusts. Lee waves can form aloft if the air is stably stratified. If air flow across a steep valley, the wind will be mostly undisturbed, but a lee eddy can be formed in the bottom of the valley, giving varied, but light wind in this area. If the flow goes across a wide valley, a combination of the two cases previously described may occur. When the flow moves toward a steep cliff, there will be a strong speed up over the edge, and eddies may form in front and after the cliff. If the flow goes down a cliff, strong eddies will form under the cliff. Further, if the flow move toward a steep hill or an island, a strong speed up will occur both in front of the hill/island and along the sides. The wind separates at the top and the sides, creating lee eddies. The wind close to the surface on the lee side may be in the opposite direction as the main flow. The speed in this area is reduced, but very turbulent. This turbulent wake area can extend for a long distance. In a sharp constriction scenario, the flow will speed up where the topography narrows, but also create areas with turbulent air, both in front and after the constriction.

A nondimensional parameter, the *Froude number*, is widely used in the characterization of flow over mountains. The Froude number is defined as U/Nh, where U is the upstream wind, N is the Brunt Väisälä-frequency (a measure of stability), and h is the mountain height (Wallace and Hobbs, 2006; Ólafsson and Bougeault, 1996). For small values of Fr, the flow is blocked and forced around the mountain, while for large values of Fr, the wind tends to go over the barrier (Wallace and Hobbs, 2006). A low number corresponds to high stability and/or a high mountain, and a low number corresponds to low stability and/or a low mountain.

Another orographic feature, is forced channeling of the wind, which is described by Whiteman and Doran (1993) as geostrophic wind over the valley that is channeled by the sidewalls, so that the wind inside the valley is aligned with the valley axis. Sudden shifts in wind direction may occur inside the valley if the geostrophic wind shifts direction, as e.g. during the passage of a front.

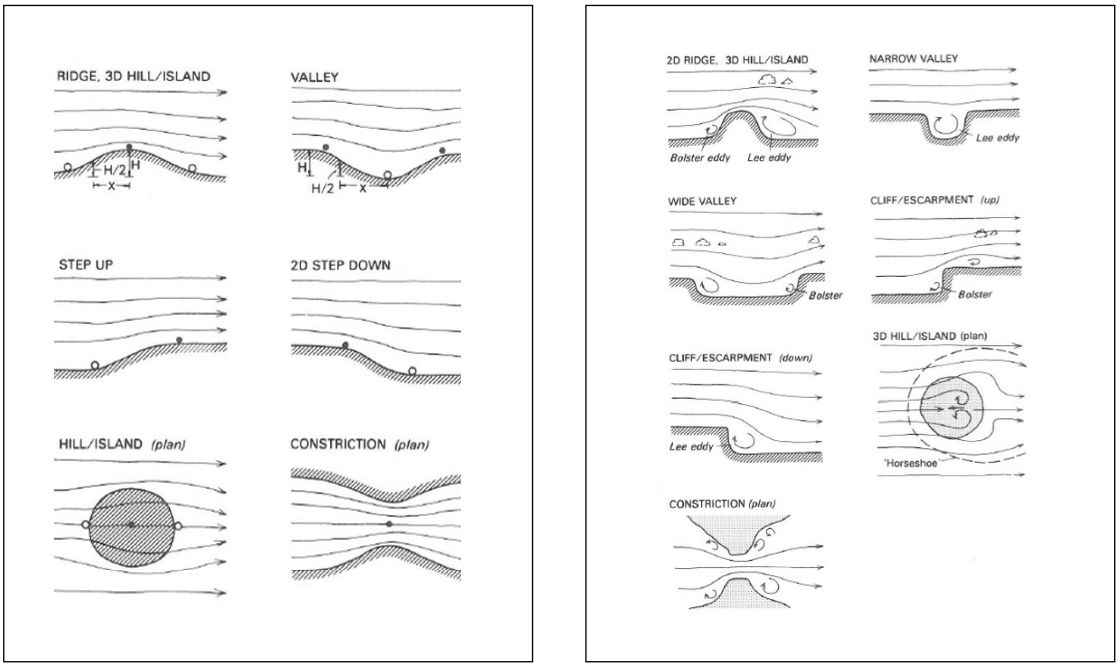

(a) (b)

Figure 2.2: *Typical pattern of airflow over (a) moderate topography and (b) steep topography. In (a), black points illustrates the location of maximum wind speed, and white points the location of minimum wind speed. From Oke (1987).*

2.4 Mountain and valley wind circulation

Three-dimensional diurnal circulations may form in or right above a valley and its ridges (Stull, 1988). These enclosed circulations are the mountain and valley winds, which are driven by thermal forcing. The mountain and valley winds are generated by pressure gradients caused by temperature differences that form along the valley axis as the air above the slope of the valley either heats or cools. The circulation system is independent of the large-scale wind and is developed locally within the valley (Whiteman and Doran, 1993). However, the existence of the circulation system depends on the right conditions. It is best developed in anticyclonic weather with clear sky and weak large scale winds (preferably below 2-3 m/s (Zardi and Whiteman, 2012)) during summer, allowing maximum incoming solar radiation during the day, and maximum outgoing longwave radiation from the ground during the night (Zardi and Whiteman, 2012). According to Rampanelli et al. (2004), the valley has to widen into what can be considered a plain in one of the ends, as it is the difference in hydrostatic pressure between the valley and the plain that provides the basic force that drives the circulation system. The plain can also be an open area such as a lake, ocean, or a larger valley (Stull, 1988).

Figure 2.3 from Oke (1987) shows the diurnal circulation for an idealized N - S oriented

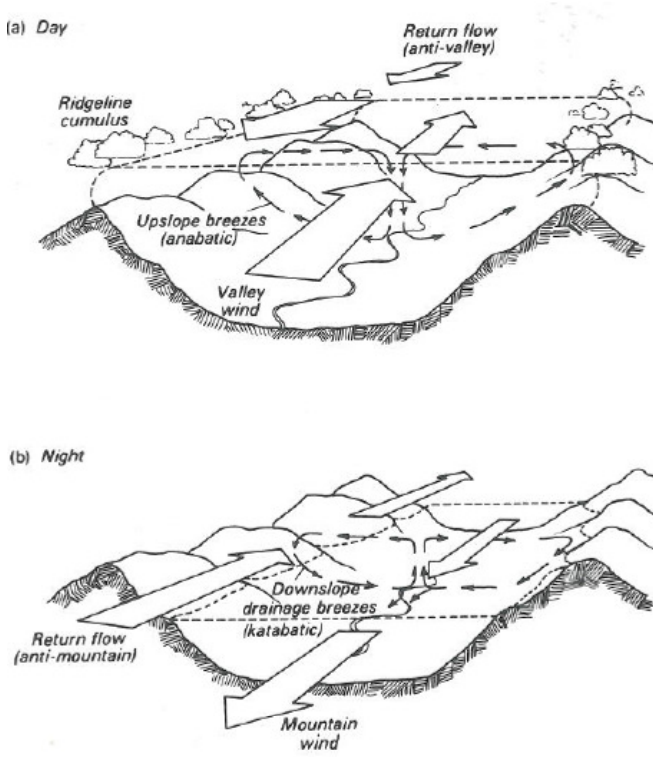

Figure 2.3: *(a) Valley wind system during daytime, and (b) mountain wind system during nighttime. From Oke (1987).*

valley that widens into a plain. The sun starts to heat during the morning, and the air above the slopes heats to higher temperatures than the air in the center of the valley. A shallow and unstable upslope flow of typically 2-4 m/s then starts to develop, called *anabatic flow*, that may form anabatic clouds along the valley ridges. The peak of maximum wind speed is around 20-40 m above the surface (Oke, 1987), due to a decrease in wind speed close to the ground caused by friction (Zardi and Whiteman, 2012). A flow across the valley develops and sinks in the middle of the valley because of conservation of continuity. This circulation transports sensible heat and heats up the entire atmosphere of the valley. The atmosphere in the valley is then warmer than the atmosphere further down the valley or over the plain, and it is this pressure difference that causes the *valley wind*, in the plain to valley direction. This flow will fill the entire valley, and is at its strongest close to the ground since the pressure difference is at its highest there. The valley wind speeds in the center of the valley are typically between 3 and 10 m/s (Zardi and Whiteman, 2012), or between 5 and 6 m/s 10 m above the ground (Utaaker, 1991). To maintain continuity, a counter flow is developed above the ridges, called the *anti-valley wind* (Oke, 1987).

During nighttime, the surface starts to cool due to heat loss by longwave radiation, and the cold, shallow air layer slides down the slopes due to gravity. This flow, called *katabatic flow*, reaches around 2-3 m/s, but can exceed this if the layer thickens or if the

slope is steeper. This flow may be blocked by obstacles, before it continues downward, so the flow is not a continuous flow (other possible reasons for this discontinuity are discussed in Zardi and Whiteman (2012)). The air transported downward converges and rises in the center of the valley, but is also combined into the so-called *mountain wind*, from the valley toward the plain. Due to friction close to the ground, the mountain wind has a jet-like shape in the vertical with its maxima tens to houndreds of meters above the ground in the middle of the valley. The mountain wind can therefore be referred to as *the down valley jet*. This is often enhanced where the valley widens or forms into a plain (Zardi and Whiteman, 2012). Again, a counter flow develops, called the *anti-mountain wind* (Oke, 1987). Katabatic flows are also common over snow and ice covered surfaces, such as glaciers (Oke, 1987; Zardi and Whiteman, 2012).

The conditions described above are ideal and simplified. In reality, ambient or large scale winds may alter or destroy weak circulations due to topography and temperature differences (Stull, 1988), such as the mountain and valley wind systems, but also the land-sea breeze circultation, and the valley inversion (section 2.5 and 2.6).

2.5 Land-sea breeze circulation

Another temperature driven diurnal circulation system is the land-sea breeze circulation, where the driving mechanism is the temperature difference between the sea and landmass. The diurnal change in surface temperature in water is very small compared to the land surface (Oke, 1987). The surface heats and cools quickly over land, but slowly over water. There are different reasons for this: The transmission of shortwave radiation penetrates deep into the water compared to the landmass, and due to mixing and convection, the heat in the water is transferred to a larger area. The water also converts a lot of its energy into latent heat instead of sensible heat through evaporation. In addition, the water has a large heat capacity. These temperature differences cause corresponding pressure differences over land and sea, which causes sea breeze during daytime, and land breeze during the night (Oke, 1987; Utaaker, 1991).

Figure 2.4 illustrates the land-sea breeze circulation. In the morning, the air over land heats more rapidly than over the sea, causing the air column over land to expand more rapidly, resulting in higher pressure aloft over land than at the same level over the sea. The pressure difference causes a flow from land toward the sea aloft (called the return flow). This will lead to a higher pressure over the water surface that results in a flow from the sea toward land at the surface, called the *sea breeze*. The return flow aloft then brings the warm air back toward the sea again, where it sinks. At night the land surface cools more rapidly than the sea surface, making an inverse circulation with the *land breeze* from the land toward the sea, and a return flow aloft (Oke, 1987).

The sea breeze and land breeze are different in strength. The sea breeze starts as a weak breeze in the morning, and strengthens throughout the day as the temperature difference between land and sea gets larger, and a steady breeze is formed. The earth's rotation causes the breeze to rotate and become almost parallel to the coastline. In fjords and valleys, the sea breeze continues aligned along the fjord or valley, making the cold air from the sea to wedge under the warmer land air, creating the *sea breeze front*. The sea breeze front is often associated with cumulus clouds forming over land and travels toward the sea where they dissipate (Oke, 1987; Utaaker, 1991). The sea breeze front travels faster than the propagation speed of the sea breeze, and has usually speeds of 5-7 m/s (Stull, 1988), while the sea breeze propagation speed is commonly around 2-5 m/s (Oke, 1987), and the return flow around 1-2 m/s. The depth of the sea breeze is commonly 100-500 m, but can vary between 500 and 2000 m when including the return circulation (Stull, 1988). The sea breeze can extend inland as far as 30 km (Oke, 1987). For comparison, the land breeze is usually 1-2 m/s, and has less vertical and horizontal extension. The sea and land breeze circulations are most likely to develop during anticyclonic weather in the summer (Oke, 1987). At some locations, such as the Bergen valley, the mountanins are close to the sea, and the sea and land breeze can interact with the valley and mountain wind. The flows can counteract and more or less cancel each other out, or they can enhance each other (Stull, 1988).

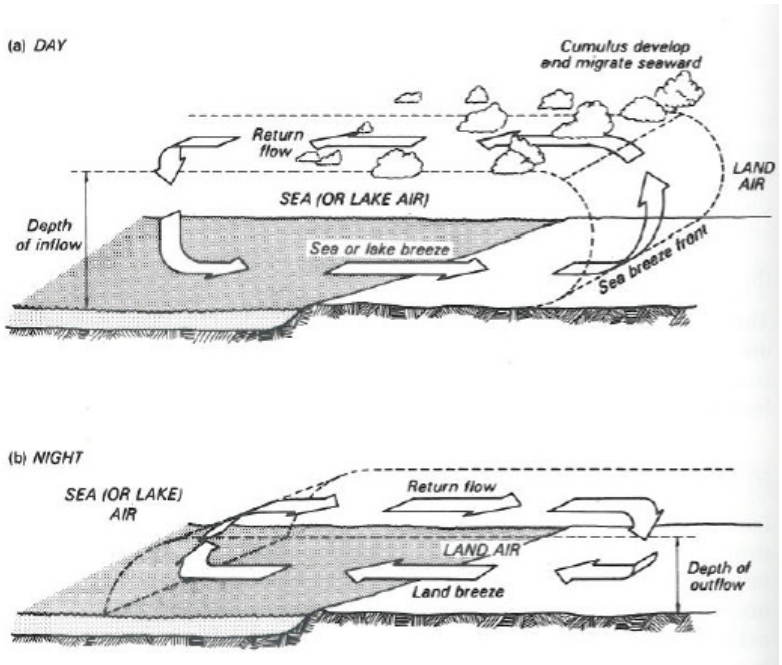

Figure 2.4: *(a) Sea breeze circulation system during daytime, and (b) land breeze circulation system during nighttime. From Oke (1987).*

2.6 Valley inversion

Another thermally induced phenomena that can develop in a valley, is the *valley inversion* (Fig. 2.5). The valley inversion can develop during clear and calm nights or during cold winter days. As for the katabatic winds (Ch. 2.4), the radiation loss at the surface cools the air above the valley slopes, making the air denser than the ambient air. A slow, sinking flow of about 1 m/s fills the bottom of the valley with cold air (Oke, 1987). Since the cold air gathers in the bottom of the valley, the temperature increases with height, and a valley inversion is developed (Fig 2.5a). The continuous radiation loss throughout the night at both the bottom of the valley and the slopes, increases the thickness of the inversion layer. The stable stratification of the layer makes the top of the inversion to act as a lid for pollutants and other air molecules. The valley inversion is very efficient in decoupling from the conditions in the atmosphere above. Above the top of the inversion, the temperature normally decreases adiabatically (Oke, 1987). When solar heating begins, a shallow mixed layer is created at the bottom and sides of the valley, confining the stable core (Fig. 2.5b). As the heating continues, a warm adiabatic flow propagates up the slopes of the valley, removing masses of cold air and lowering the inversion top (Fig. 2.5c), until the inversion breaks down into a mixed layer (Fig. 2.5d). During cold, stable winter days, the inversion can build up over several days, and not break down until the temperature or the wind increases.

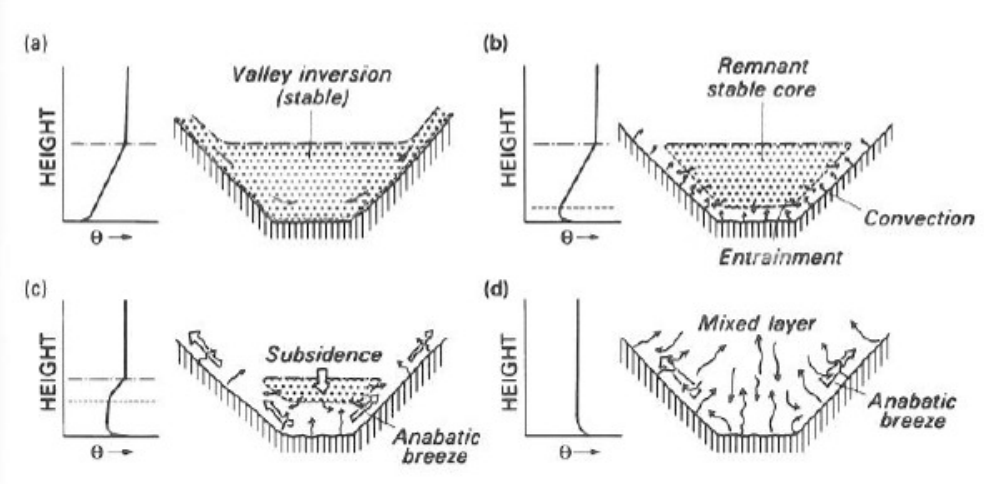

Figure 2.5: *The cycle of the valley inversion including potential temperature profiles and the cross section of the valley. (a) Valley inversion at night, (b) surface warming after sunrise, (c) lowering of the inversion top and start of an anabatic breeze, (d) breakdown of the inversion 3-5 hours afer sunrise. From Oke (1987).*

2.7 Heat island effect

Cities are anthropogenic sources of heat and pollution. In addition, the city is covered by buildings, asphalt and concrete, which are dry and watertight surfaces that have large heat capacities. Much of the incoming solar radiation is stored within these surfaces due to their low albedo. More heat is therefore stored within a city than in its surroundings. The isotherms over a city look like the topography contours of an island, resulting in the term *heat island* (Stull, 1988). The largest heat island effect is seen at a clear night with weak winds (Utaaker, 1991). While the surrounding countryside of the city cools rather quickly during a clear night, the city cools down much slower due to its large heat capacity. After sunrise, the city warms slower than the countryside (Oke, 1987), and the city may even be colder than its surroundings during the day (Utaaker, 1991).

Wind speeds within the city are usually weaker compared to the wind at the corresponding height at the countryside due to friction. Still, there are a few exceptions. Fast moving air aloft can be deflected downward by a tall building, causing strong winds along the streets in the same direction as the flow. The horizontal temperature gradient between the city and the countryside can also cause a low-level breeze from the countryside to the city during calm, clear nights. A closed circulation similar to the sea breeze circulation can then be formed over the city (Oke, 1987). However, this circulation is much weaker than the sea breeze circulation, and may not even be noticeable under ideal conditions (Utaaker, 1991), in particular for rather small cities as Bergen.

Chapter 3

The Weather Research and Forecasting Model

Numerical simulations in addition to observations are used in this study when investigating the flow regimes in the Bergen valley. A numerical weather prediction (NWP) and atmospheric simulation system, The Weather Research and Forecasting Model (WRF) is used for this purpose (Skamarock et al., 2008). The WRF model has been developed in collaboration between several companies and scientists[1], and the aim was to enhance the understanding of mesoscale weather and to improve the transfer between research and operational forecasting. The detailed information on the WRF model in the following sections is mainly based on the work of Skamarock et al. (2008).

3.1 The components of the WRF model

Figure 3.1 shows the data flow and program components of the WRF model system (for the ARW solver). The WRF pre-processing system (WPS) is a set of programs that prepares terrestrial and meteorological data and transform the data for input to the Advanced Research WRF (ARW) solver. There are two dynamical solvers available for WRF, the ARW solver, and a non-hydrostatic mesoscale model (NMM). The ARW solver is used in this study.

The first step in the WPS is to define a physical grid and to interpolate terrestrial static fields to the model domain. This is done in **geogrid**. **Ungrib** decodes large-

[1]The Mesoscale and Microscale Meteorology (MMM) Division at the National Center for Atmosphercia Reasearch (NCAR), the National Centers for Environmental Prediction (NCEP) and Earth System Reaserch Laboratory (ESRL) at the National Oceanic and Atmospheric Administration (NOAA), the Departement of Defence's Air Force Weather Agency (AFWA) and Naval Research Laboratory (NRL), the Center for Analysis and Prediction of Storms (CAPS) at the University of Oklahoma, and the Federal Aviation Administration (FAA), with the participation of university scientists.

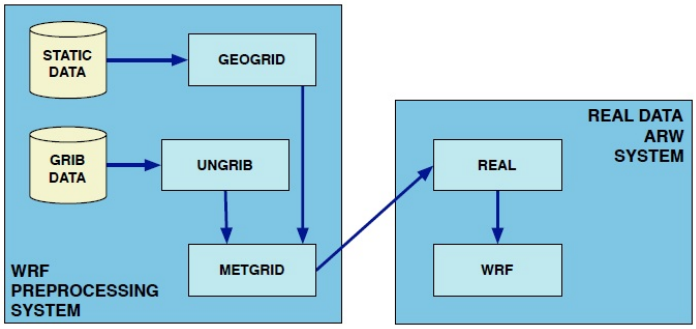

Figure 3.1: *The components of the WRF model (for the ARW system). From Skamarock et al. (2008).*

scale atmospheric analysis or forecast data and creates temporary files, which **metgrid** uses to horizontally interpolate meteorological data onto the model domain. Metgrid creates files containing a three-dimensional snapshot of the horizontal atmosphere, that the ARW pre-processor program (real) uses to create initial and boundary conditions to the WRF model. After the real-data processor is done, the WRF model can run, and the output files can be post processed to be graphically visualized. In this study, NCAR Command Language (NCL)[2] and Matlab are used for post processing.

The details of the steps described above will be explained in the following sections.

3.2 Governing equations

The ARW solver uses the Euler equations on the compressible and nonhydrostatic flux form. The vertical coordinate in the equations is a terrain-following mass coordinate, η (Laprise, 1992) (Fig. 3.4), defined as

$$\eta = (p_h - p_{ht})/\mu \text{ where } \mu = p_{hs} - p_{ht} \tag{3.1}$$

where p_h is the hydrostatic component of the pressure, while p_{hs} and p_{ht} are values following the surface and the top, respectively. μ represents the mass per unit area at the point (x,y) in the model domain. The flux form variables can then be written as

$$\mathbf{V} = \mu\mathbf{v} = (U, V, W), \quad \Omega = \mu\dot{\eta}, \quad \Theta = \mu\theta. \tag{3.2}$$

$\mathbf{v}$ = (u,v,w) are covariant velocities in the two horizontal and vertical directions, $\omega = \dot{\eta}$ is the contravariant vertical velocity and θ is the potential temperature. Also present in the governing equations are the non-conserved variables $\phi = gz$ (geopotential), p (pressure), and $\alpha = 1/\rho$ (inverse density). Using the definitions described above, the

[2]The NCAR Command Language (Version 6.0.0) [Software]. (2012). Boulder, Colorado: UCAR/NCAR/CISL/VETS. http://dx.doi.org/10.5065/D6WD3XH5

Euler equations can be written as

$$\partial_t U + (\nabla \cdot \mathbf{V}u) - \partial_x(p\phi_\eta) + \partial_\eta(p\phi_x) = F_U \tag{3.3}$$

$$\partial_t V + (\nabla \cdot \mathbf{V}v) - \partial_y(p\phi_\eta) + \partial_\eta(p\phi_y) = F_V \tag{3.4}$$

$$\partial_t W + (\nabla \cdot \mathbf{V}w) - g(\partial_\eta p - \mu) = F_W \tag{3.5}$$

$$\partial_t \Theta + (\nabla \cdot \mathbf{V}\theta) = F_\Theta \tag{3.6}$$

$$\partial_t \mu + (\nabla \cdot \mathbf{V}) = 0 \tag{3.7}$$

$$\partial_t \phi + \mu^{-1}[(\mathbf{V} \cdot \nabla\phi) - gW] = 0 \tag{3.8}$$

In addition, the diagnostic equation for the inverse density is

$$\partial_\eta \phi = -\alpha\mu, \tag{3.9}$$

and the equation of state is

$$p = p_0(R_d\theta/p_0\alpha)^\gamma, \tag{3.10}$$

where p_0 is a reference pressure, R_d is the gas constant for dry air and $\gamma = c_p/c_v = 1.4$ is the ratio of the heat capacity for dry air. The right hand side in equation 3.3 - 3.8 includes model physics, turbulent mixing, spherical projections, and earth's rotation.

The differential operators in equation 3.3 - 3.8 are defined as and the equation of state

$$\nabla \cdot \mathbf{V}a = \partial_x(Ua) + \partial_y(Va) + \partial_\eta(\Omega a), \tag{3.11}$$

and

$$\mathbf{V} \cdot \nabla a = U\partial_x a + V\partial_y a + \Omega\partial_\eta a, \tag{3.12}$$

where a is a general constant.

The final form of the equations are shown in Skamarock et al. (2008) where the effect of moisture in the atmosphere, map projections, and Coriolis and curvature terms are included. Perturbation variables are also included to reduce truncation and rounding errors.

3.3 Stability and time discretization

The ARW solver uses a time-split integration scheme to handle different wavelengths and frequencies of the waves in the atmosphere. The frequency modes are split into high- and low frequency modes. The low frequency modes are integrated using a third-order Runge-Kutta (RK3) time integration scheme. The time-split RK3 integration technique is explained in detail in Wicker and Skamarock (2002). To maintain numerical stability, the high frequency modes are integrated over a smaller time step than the more stable low frequency modes. Both time steps are limited by the Courant number $u\Delta t/\Delta x$. For the ARW, it is common to choose a time step (in seconds) which is six times the horizontal grid distance (in kilometers) with the aforementioned limitations in mind.

3.4 Space discretization

In the ARW solver, the spatial discretization uses a so called C grid staggering for the variables, meaning that the velocities points (u,v and w points) are located one-half grid length apart from the thermodynamic variables (mass points). This is shown in figure 3.4, where the mass points are located at θ. The column mass μ, the geopotential ϕ (defined at the w points), and moisture variables q_m (defined at the mass points) are not shown in the figure. Pressure p and inverse density, α, are computed at the mass points.

The vertical grid length $\Delta\eta$ is not a fixed constant. η decreases monotonically with height, from 1 at the surface, to 0 at the top (see figure 3.4). The horizontal grid length in the model, Δx and Δy, are held constant.

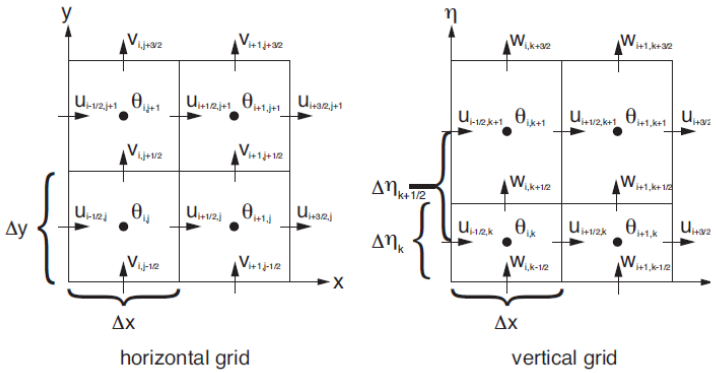

Figure 3.2: *The ARW horizontal and vertical grid. From Skamarock et al. (2008).*

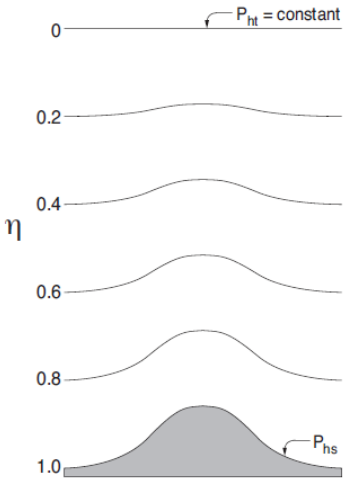

Figure 3.3: *The ARW vertical coordinate, η. At the higher levels, η follows the pressure, and at lower levels, η follows the terrain. From Skamarock et al. (2008).*

3.5 Initial and boundary conditions

There are two types of initial conditions the ARW solver can be run with. For idealized situations, the initial conditions can be user-defined. For real-data cases, as in this study, interpolated data from an external analysis or forecast can be used. The physical grid is defined in WPS, as described in section 3.1. This includes projection type, location on the globe, number of grid points, nest locations, and grid distances. Following the steps described in section 3.1, 3-dimensional fields of the atmosphere are created, containing temperature, relative humidity, and horizontal velocity components. The surface is also included, with 2-dimensional static terrestrial fields of terrain elevation, vegetation/land-use type, land/water mask, latitude and longitude and other static fields. 2-dimensional fields depending on time are also included, such as pressure, sea surface temperature, skin temperature and different soil and ice parameters. The ARW then vertically interpolates from the top and down toward the surface.

The lateral boundary conditions for the coarse grid consists of two zones, namely the specified and the relaxation zone, shown in figure 3.4(a). The specified zone in the coarse grid is determined by interpolation from the external analysis or forecast, and are supplied by WPS. The specified zone constrain the lateral boundaries on all sides of the coarse domain, and contains horizontal velocity fields, potential temperature, humidity and perturbation fields. In the relaxation zone, the model is nudged or relaxed toward the large-scale forecast. The outer rows and columns of the finer domains use time-dependent lateral boundary conditions from the parent domain.

When there are grids with finer resolution than the coarse domain (see figure 3.4(b)), the ARW uses horizontal nesting. Nesting can be either 1-way or 2-way, and refers

to how the coarse and finer domains interact. For both options, the boundary conditions are interpolated from the coarse grid to the fine grid, and this is also how the information exchange is in 1-way nesting. There are two options for the 1-way nesting. The simulations can either be run as separate simulations, or they can run at the same time. In 2-way nesting, the fine grid solution replaces values in the coarse grid that lies inside the fine grid, so the interaction goes both ways.

The nest lateral boundary conditions act similarly as for the specified boundary condition, except the relaxation zone is not active.

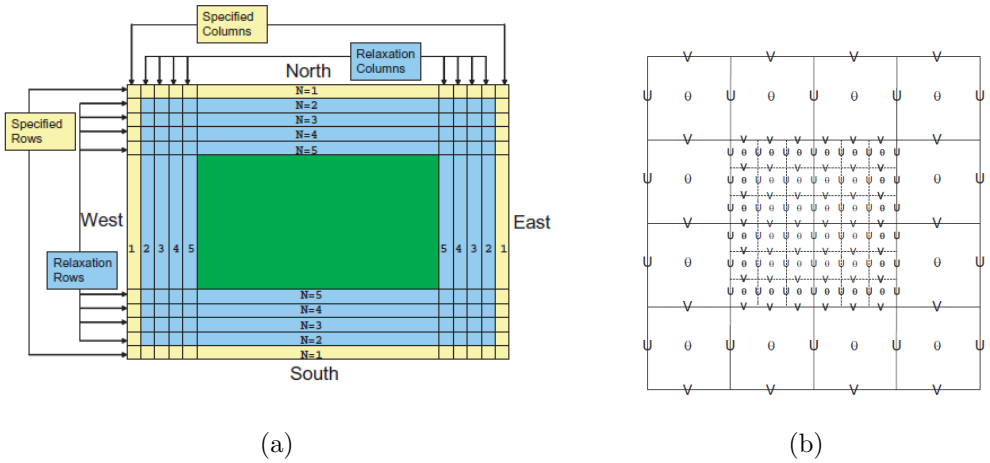

(a) (b)

Figure 3.4: *(a) Location of specified and relaxation zones. (b) C grid staggering for a parent domain and fine domain. Solid lines: coarse grid cell boundaries. Dashed lines: fine grid cell boundaries. From Skamarock et al. (2008).*

3.6 Model setup

In this study, a sea breeze and an inversion case have been simulated. The simulated time period for the sea breeze case is 23.08.2011 00:00 UTC - 25.08.2011 00:00 UTC, and 10.11.2011 18:00 UTC - 12.11.2011 06:00 UTC for the inversion case. The purpose of these simulations is to compare the model results against the observations, and to investigate the three-dimensional wind fields for these cases in the Bergen valley. The quality of the model results are also evaluated.

Version 3.3.1 of the WRF model has been used. In the simulations, three 1-way nested polar stereographic domains are used. The horizontal resolutions of the domains are 4.5 km, 1.5 km and 500 m (Fig. 3.5). The outermost domain is centered at 60.8°N and 5.5°E, with 160 x 160 grid points. This domain covers the southern part of Norway, and expands 720 $\times$ 270 km^2. The second domain has 103 x 103 grid points, and covers most of Hordaland. The third domain has 85 x 85 grid points and covers the

city of Bergen, and some of the area around the city. The expansion of this domain is 42.4 × 42.5 km^2. All three domains have 62 vertical levels with increased density toward the ground. The top of the model is defined at 50 hPa. The three domains are shown in figure 3.5. The innermost domain is used in further evaluations in this study.

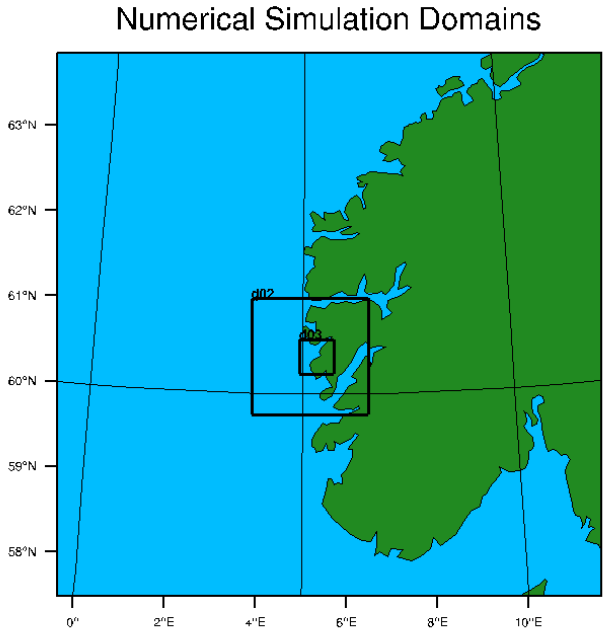

Figure 3.5: *Location and size of the three model domains. The horizontal resolution of the three domains are 4.5 km, 1.5 km and 500 m.*

The initial conditions in the simulations are taken from the 6 hourly analysis data from European Centre of Medium range Weather Forecasting (ECMWF) with 0.125° horizontal resolution.

Different sets of model physics are available in WRF. The ones described in table 3.1[3] have been selected for the presented simulations, and details about the different schemes are listed in chapter 8 in Skamarock et al. (2008).

Furthermore, a more detailed landuse and topography dataset has been used, respectively the GlobCorine and ASTER (Advanced Spaceborne Thermal Emission and Reflection Radiometer) dataset. Figures of the topography for the three domains can be seen in appendix A, along with the landuse for the innermost domain. A detailed analysis of the landuse and topography datasets and their impacts on WRF simulations is given by Jonassen et al. (2012b).

[3] *http* : *//www.mmm.ucar.edu/wrf/users/docs/user_guide/users_guide_chap5.html*, *Accessed* : 12.07.2012

http : *//wrfportal.org/namelist_input_options.html*, *Accessed* : 12.07.2012

Table 3.1: *The model physics schemes used in the simulations.*

Category	Scheme
Microphysics	WRF Single-Moment 3-class (WSM3) (Hong et al., 2004; Dudhia, 1989)
Radiation (LW)	RRTM (Mlawer et al., 1997)
Radiation (SW)	Duhida (Dudhia, 1989)
Surface layer	Eta similarity. Used in Eta model (Janjic, 1996, 2002)
Land surface	Noah Land surface Model (Chen and Dudhia, 2001)
Planetary boundary layer	Mellor-Yamada-Janic (Eta) (Janjic, 1990, 1996, 2002)

In addition to the three-dimensional WRF output files, time series for each of the seven AWS (Ch.4) are created in the model. These TS-files have very short time steps (seconds between each time step), making it possible to compare interpolated 10 minutes model values to the 10 minutes observations.

Chapter 4

Location and site description

The area of interest in this study is the Bergen valley, located at the southwest coast of Norway. It surrounds the city centre of Bergen with steep mountains that range up to 300 to 600 m. There are especially two mountains that dominate the topography of the Bergen valley. These are Ulriken and Løvstakken. They confine the NW - SE oriented Bergen valley respectively on the E and W side. There is an open area toward the fjord, Byfjorden, NW in the Bergen valley, and an open area toward SE. Figure 4.1 shows an overview of the location of the Bergen valley (a) and a detailed map of the area of interest (b) along with the sites of the automatic weather stations (AWSs) used in this study. Figures 4.2 (a) and (b) visualize the Bergen valley with some of the stations marked in red.

The stations used in this study have been selected to represent the whole range of relevant altitudes in the Bergen valley area. Two of the stations, Florida and Ulriken, are run in a collaboration between Aanderaa data instruments (AADI) and the Geophysical Institute, University of Bergen (GFI). The other stations have been deployed temporarily for this study. An overview of the locations of the AWSs is given in table 4.1.

S1 is located at the highest mountain in the Bergen valley, Ulriken, at 605 m a.s.l. and 4 m a.g.l. There is a large mast approximately 50 m NW of the AWS that can lead to disturbances in the measurements. It is quite open toward all other directions. The sector between W, SW and S is open toward the mountainside, while the sector between N, E and SE is a mountainous landscape. Since Ulriken is the highest mountain in the area, the mountanious landscape seems somewhat flat but rugged in this sector. The highest peak of Mount Ulriken is located E of the AWS.

S2 is situated on the western flank of Mount Ulriken at the tip of a small hill at 408 m a.s.l. and 2.1 m a.g.l. The sector between NW, W and S is completely open, and wind coming from these directions will not meet any obstacles (Fig. 4.4 (b) and

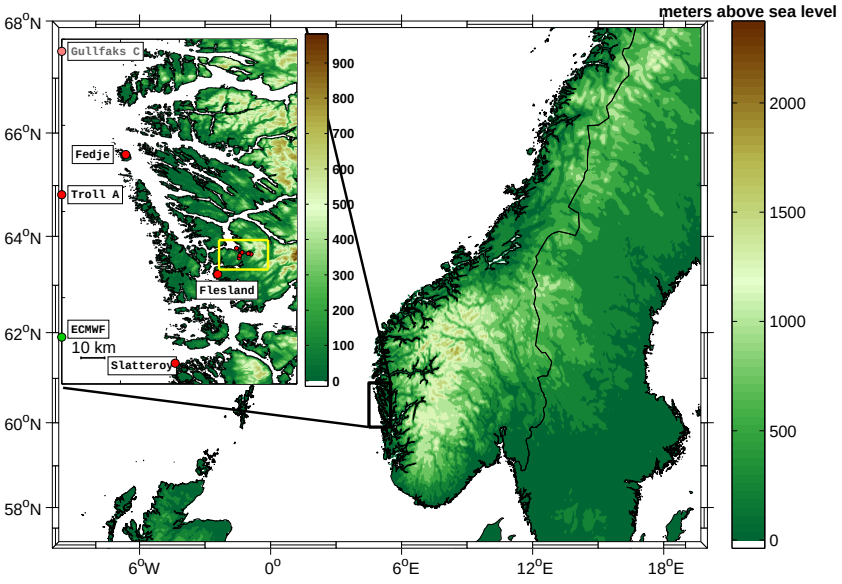

(a)

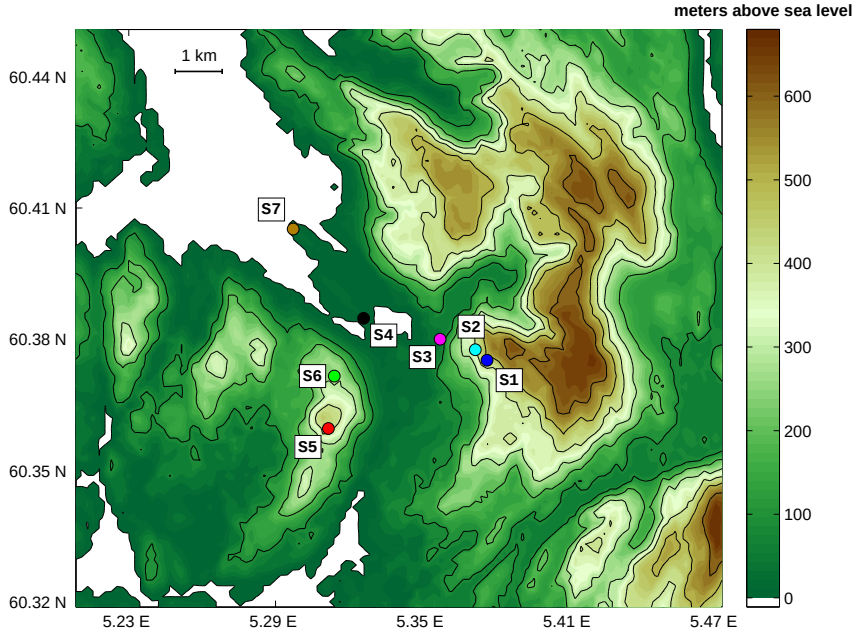

(b)

Figure 4.1: *(a) Location of the Bergen valley at the southwest coast of Norway. The yellow box in the small picture shows the location of the Bergen valley, which is shown magnified in (b). The red markers inside the yellow box indicate the location of S1 - S7 (Tab. 4.1). The red markers outside the yellow box show the location of other observations used in an earlier study by Jonassen et al. (2012a).*

(a)

(b)

Figure 4.2: *Pictures of the Bergen valley taken from Mount Ulriken. The stations that can be seen from this site are marked in red. Picture (a) shows the open area toward the Byfjorden in the NW. Mount Løvstakken is situated to left in the picture. Picture (b) shows the opening of the Bergen valley toward SE. Mount Løvstakken is right in the picture.*

(a)

(b)

(c)

Figure 4.3: *Pictures showing the site of S1. (a) There is a large mast approximately 50 m NW of the AWS. (b) S1 toward E-SE. (c) The open sector between W, SW and S. Mount Løvstakken is in the middle of the picture and is located W of Mount Ulriken.*

Table 4.1: *Sites and description of the automatic weather stations used to collect data for this study.*

Station number	Station name	Altitude [m a.s.l.]	Altitude [m a.g.l.]	Lat. °N	Lon. °E	Description
S1	Ulriken	605	4	60.377	5.379	Top of Mount Ulriken. 4 m mast.
S2	Ulriksbakken	408	2.1	60.379	5.373	Mountainside of Ulriken. 2 m mast.
S3	Haukeland	64	10	60.380	5.362	Roof of Haukeland Elementary School. 2 m mast.
S4	Florida	48	30	60.384	5.332	Roof of the Geophysical Institute. 4 m mast.
S5	Løvstakken	472	2.1	60.360	5.321	Top of Mount Løvstakken. 2 m mast.
S6	Strandafjellet	303	2	60.372	5.323	Small mountain connected to Løvstakken. 2 m mast.
S7	Nordnes	48	30	60.400	5.304	Roof of the Institute of Marine Research. 2 m mast.

(a)

(b)

(c)

Figure 4.4: *Pictures showing the site of S2. The pictures are taken toward Mount Ulriken (a), SE (b), and NW (c).*

(c)). The mountainside of Ulriken is located E of S2, and the area close to the AWS toward N, E and SE is dominated by trees (Fig. 4.4(a)).

S3 is sited at the base of Mount Ulriken at the roof of Haukeland Elementary School at 64 m a.s.l. and approximately 15 m a.g.l. (Fig. 4.5). There are many tall buildings in the surrounding area, and especially the wind measurements will be affected by this. In addition, S3 was mounted at the same site as an already existing Davis weather station that is part of a school project in the Bergen area. The instruments of the Davis weather station may also affect the measurements, especially wind and precipitation. The siting was limited by infrastructural constraints. The site of S3 can give a good picture on how the meteorological parameters are in an urban area.

S4 is situated at the Geophysical Institute at the University of Bergen, located at Florida, which is in the middle of the Bergen valley. The AWS is placed on the observational tower of the building, at 48 m a.s.l. and around 30 m a.g.l. (Fig. 4.6(a)). The surroundings of S4 are dominated by streets and buildings (Fig. 4.6 (b) and (c)). S4 is located directly SE of S7.

S5 is placed on the top of Mount Løvstakken, at 472 m a.s.l. and 2.1 m a.g.l. Mount Løvstakken is located on the opposite side of the Bergen valley compared to Mount Ulriken (Fig. 4.7(b)), and is a free standing mountain with slopes on all sides, so the AWS has no shelter from either side. The wind that hits S5 will be undisturbed

(a) (b)

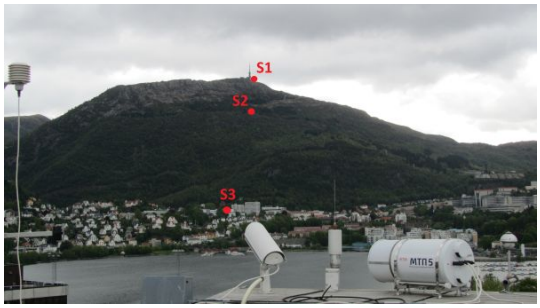

(c)

Figure 4.5: *Pictures showing the site of S3. (a) S3 is located at the roof of Haukeland Elementary School. (b) S3 with Mount Ulriken in the background. (c) Picture showing the overview of the location of S1, S2 and S3, taken from the site of S4. The stations are marked in red.*

(a) (b)

(c)

Figure 4.6: *Pictures showing the site of S4. (a) The Geophysical Institute. The AWS is located at the top of the tower. (b) Picture taken from the site of S4 toward NE along the Bergen valley. (c) Picture taken from the site of S4 toward SE along the Bergen valley.*

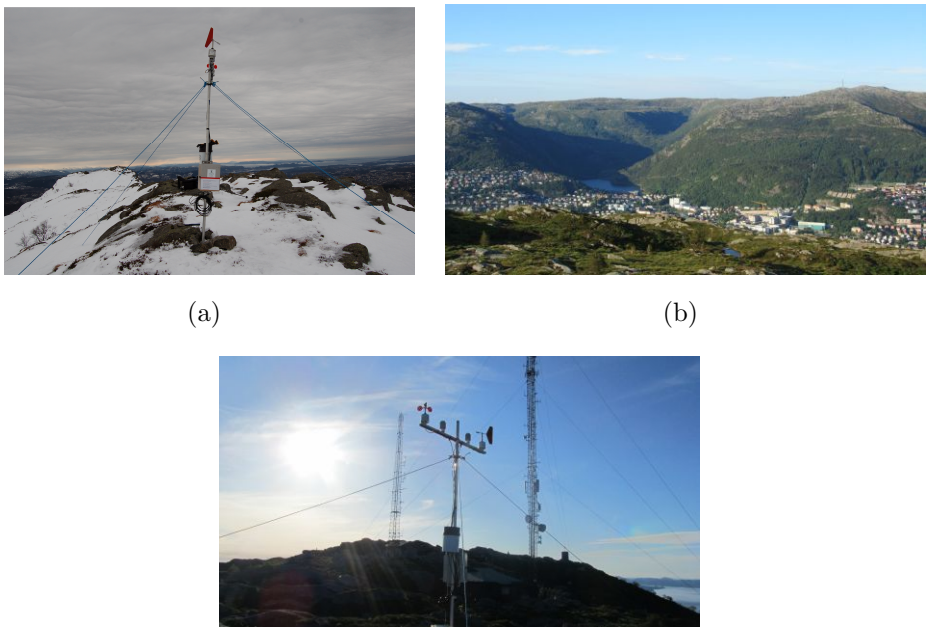

(a) (b)

(c)

Figure 4.7: *Pictures showing the site of S5 at the top of Mount Løvstakken. (a) S5 toward S. (b) Picture taken toward the Bergen valley. The water in the picture is called Svartediket located in the valley, Isdalen. Mount Ulriken is right in the picture. (c) There are two large masts NW of AWS. The closest one is approximately 50 m away from the AWS.*

(Fig. 4.7(a)), except for some possible disturbance from two large masts approximately 50-100 m NW of the AWS (Fig. 4.7(c)).

S6 is situated on a small mountain called Strandafjellet, at 303 m a.s.l. and 2 m a.g.l. Strandafjellet is connected by a ridge to Løvstakken, where Strandafjellet is located NW of Løvstakken. The sector between N, W and SW is open. Figure 4.8(b) shows S6 in the northward direction. The wind coming from E will most likely be affected by Mount Ulriken (Fig. 4.8(a)), and wind coming from S and SE will most likely be affected by Mount Løvstakken (Fig. 4.8(c)). There are a few small trees in the vicinity of S6.

S7 is located N of S6, on the roof of the high-rise building of the Institute of Marine Research at 48 m a.s.l. and approximately 40 m a.g.l. (Fig. 4.9(a)). This building is located at the tip of Nordnes, close to Byfjorden. The sector between N and W is completely open toward Byfjorden, and wind coming from these directions will be undisturbed. S4 and S7 follow a straight NW-SE alignment, the same direction as the Bergen valley.

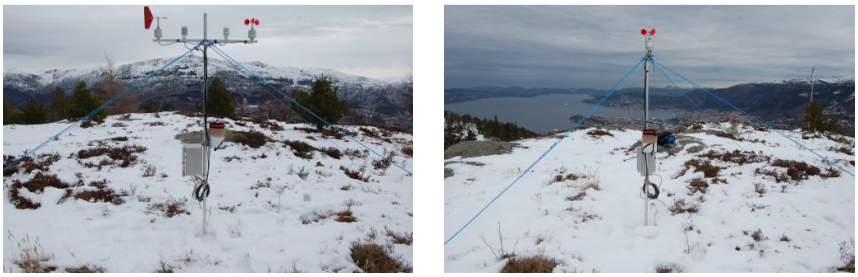

(a) (b)

(c)

Figure 4.8: *Pictures showing the site of S6. S6 is placed on the top of the small mountain, Strandafjellet, which is connected to Løvstakken. (a) S6 toward Mount Ulriken and the Bergen valley, (b) S6 seen in the northward direction toward the site of S7. (c) Picture of Mount Løvstakken and Strandafjellet, taken from Mount Ulriken. The stations are marked in red.*

(a) (b) (c)

Figure 4.9: *Pictures showing the site of S7. (a) S7 at the roof of the Institute of Marine Research. (b) Picture of S7 taken directly toward SE and the location of S4. Mount Ulriken is left in the picture and Mount Løvstakken is right in the picture. Strandafjellet is located in front of Mount Løvstakken in this picture. (c) Picture taken at the roof of the Institute of Marine Research toward NW and Byfjorden.*

Due to logistical reasons, permissions and safe locations when planning and installing the AWSs, the AWSs ended up with different types of locations and heights above the ground. The AWSs that are situated at the roof of a bulding (S3, S4 and S7) can have flow distortions by the building in the measurements. This must be taken into account when the observations from these stations are compared with observations from the AWSs that are located closer to the ground (S1, S2, S5 and S6). In addition to the flow distortion, the difference in height above the ground must be taken into account when comparing the different stations. Some of the stations are placed 2 m a.g.l while others are 30 and 40 m a.g.l. However, the largest difference in height is the height above sea level. The stations are located between 48 m a.s.l. and 605 m a.s.l. This will affect the values of the observed parameters. Other differences in the surroundings also have to be taken into account. There can be a speed up due to topography in some of the stations, while blocking from obstacles in other stations may be present. For these reasons, the information in figure 4.1(b) and table 4.1 are important to keep in mind in the following chapters.

Chapter 5

Instrumentation and data

5.1 Instrumentation

The five automatic weather stations (AWSs) that were deployed temporarily for this study (Ch. 4) have approximately 2 m masts and sensors from Aanderaa Data Instruments AS (AADI) (2000). The sensors measure wind direction, average wind speed, wind gust (maximum wind speed over a 2-second period), temperature and relative humidity. All sensors are scanned approximately every 4 seconds by a Sensor Scanning Unit 3010 (Aanderaa Data Instruments AS (AADI), 2001). The readings are averaged and stored every 10 minutes on-site on a Data Storage Unit (DSU) 2990 (Aanderaa Data Instruments AS (AADI), 2010). The whole system runs on batteries, which have to be changed regularly along with the data storage unit. In addition, HOBO RG2-M rain gauges (Onset Computer Corporation, 2001) mounted at the 2 m masts measure precipitation. The HOBO rain gauge runs on its own batteries, and stores the data on-site using its own data logger. The two already existing AWSs at Mount Ulriken (S1) and Florida (S4) are also from AADI. These AWSs have 4 m masts. The AWS at Mount Ulriken has sensors for wind direction, wind speed, temperature and relative humidity, while the AWS at Florida in addition also measures pressure. The data are transmitted directly to a computer at GFI by radio communication for these two sites.

5.2 Data

5.2.1 Time period

The five AWSs that were put up specifically in connection to this study were installed during fall and winter 2010. The installation date for each of the AWSs can be seen in table 5.1. All deployed AWSs are still running and collecting data. However, to get the same amount of data for all the stations, the time period for evaluation in this study has been selected as *23 Nov 2010 00:00 UTC to 01 Jul 2012 00:00 UTC*. Missing data

Figure 5.1: *AWS at Mount Løvstakken. From the left: Sensor for wind direction, temperature, relative humidity and wind speed. Gust is measured by the same sensor as wind speed. The data logger, the DSU and the batteries are inside the box. HOBO rain gauge is mounted above the box at 110 cm above ground (black and white cylinder). The four ropes are attached to poles of either wood or steel in the ground. An early stage of icing at the sensors can be seen in the picture.*

and data of particularly bad quality (for details see chapter 5.4) within the time period of the study are set to *not a number* (NaN). The number of days with missing data out of the overall number of 618 days for each station in the time period 23 Nov 2010 to 01 Jul 2012 are given in table 5.1. One day with a complete set of observations contains 144 measurements per parameter. In table 5.1, a day is defined as "missing data" when it has less than 24 accepted data points of wind speed observations. However, all the data are evaluated even if a day is defined as "missing data". The percentage of total amount of 10 minutes available data for wind speed is also given in table 5.1.

Table 5.1: *Amount of data available for AWS S1-S7. The table shows the installation date for each of the stations, and the number of days with missing data out of 618 days for the time period 23 Nov 2010 00:00 UTC - 1 Jul 2012 00:00 UTC, and the percentage of total amount of 10 minutes avaiable data for wind speed.*

Station	Station deployed	Days with missing data	Data availablility
Ulriken (S1)	14.10.2010 00:00 UTC	12	94.8 %
Ulriksbakken (S2)	15.11.2010 10:40 UTC	25	95.3 %
Haukeland (S3)	28.10.2012 11:00 UTC	38	92.9 %
Florida (S4)	14.10.2010 00:00 UTC	0	99.7 %
Løvstakken (S5)	09.11.2010 14:00 UTC	70	85.7 %
Strandafjellet (S6)	23.11.2010 10:00 UTC	92	84.4 %
Nordnes (S7)	14.10.2010 09:10 UTC	72	87.3 %

5.2.2 Field work

This study has required fieldwork throughout the whole period from early October 2010 and up to the end of the study. The first step in the process was to plan the desired distribution and altitude of the weather stations. The next step was to investigate possible sites and get necessary permissions. After that, the five AWSs were installed. The need for control at these AWSs, to see if everything worked properly and fix problems that occurred, was high in the beginning. The data scanning unit (DSU) that saves the raw data has capacity to save data for up to 75 days. Even so, each of the five stations was controlled approximately once a month until the summer 2011, due to unstable batteries. If problems occurred, more trips/hikes to the stations were needed. After the summer 2011, when the batteries seemed to last for around 4 months, the five AWSs were controlled around once per two months to change the DSU. The AWSs were in addition controlled out of schedule throughout the whole period after extreme weather events and in especially cold weather to avoid too much icing on the sensors. However, with hindsight, the AWSs should have been controlled more often to avoid long periods with problems (see chapter 5.3.2). A logbook containing controls of the AWSs, dates of special weather events and problems with the AWSs has been written during this whole study.

On the longer term, and with respect to state-of-the-art in measurement technique, the old stations should be replaced by new ones, allowing for online status control at least once a day.

5.3 Quality control

5.3.1 Calibration

To test and monitor the sensors accuracy, additional measurements have been done on-site with a psychrometer (Fischer, 2005) and a barometer (Vaisala, 2001). The dry air temperature, T_d, and the wet bulb temperature, T_w, have been measured with the psychrometer. The barometer was used to measure the pressure. Based on these measurements, the temperature and relative humidity sensor on the different AWSs can be tested. The measurements were done once at each AWS (S1-S7) during the deployment period. The results are presented in table 5.3.1. T_d, T_w and the pressure are used to calculate the dew point temperature, T_{dew}. T_d, T_{dew} and the pressure are then used to calculate the relative humidity, RH_{calc}. T_d measured by the psychrometer and the calculated RH_{calc} are further compared to the observations, $T_{d,obs}$ and RH_{obs} done by the specific AWS at the same time.

Table 5.2: *T_d measured by the psychrometer and RH_{calc} calculated from the psychrometer and brometer measurements are compared to the corresponding measurements done by the AWSs, $T_{d,obs}$ and RH_{obs}.*

Stations	S1	S2	S3	S4	S5	S6	S7
Date	15.05.12	26.06.12	21.11.11	26.06.12	28.06.12	10.11.11	14.04.12
Time [UTC]	11:20	16:50	09:40	11:20	18:40	13:40	08:50
Pressure [hPa]	971.85	967.17	1010.80	1009.45	953.14	990.78	993.57
T_d [°C]	3.0	8.9	10.0	12.0	13.7	8.7	7.1
T_w [°C]	2.4	7.8	6.0	9.8	8.7	6.1	5.3
RH_{calc} [%]	90	86	54	75	51	68	76
$T_{d,obs}$ [°C]	2.6	8.8	9.9	11.4	13.1	8.7	5.2
RH_{obs} [%]	100	82	58	70	39	71	78

For S2, S3, S4, S6 and S7, RH_{calc} and RH_{obs} agree within ± 2.5% in relative humidity. This is approximately within the accuracy of the sensors and therefore within acceptable limits. At S1, the difference is 10 %. A small error in temperature reading, can result in large errors when calculating RH_{calc}. At S5, the difference reaches 12 %, indicating a more serious problem. The explanation can either be a human error while reading the temperatures, or a real offset in the humidity sensor. However, this is not a significant problem for this partiular study, since the moisture is not a main focus.

The measured T_d from the psychrometer and $T_{d,obs}$ from the AWSs have acceptable deviations of maximal 0.6 °C for all stations, except for S7. Here, the deviation is reading almost 2 °C, indicating either a human error when reading the temperatures from the psychrometer, or that the temperature sensor at the AWS needs calibration. The latter has been the case for several sensors during this study (see section 5.4).

Figure 5.2: *Barometer to the left and psychrometer to the right.*

5.3.2 Challenges

A number of challenges have occurred during the field work of collecting data. Some of the challenges are due to external influence caused by either weather conditions or people. These types of challenges will be described in this section. Other types of challenges that have appeared during the study, such as problems with the sensors, batteries, the sensor scanning unit, the data scanning unit or radio connection will be described in section 5.4, as well as the handling of them.

Challenges due to outer influences are:

- The cup anemometer at Mount Ulriken blew off due to high wind speeds on 13 Feb 2011. A new cup anemometer was installed on 16 Feb 2011. This was replaced again on 6 Mar 2012.
- One of the wooden poles that stabilized the weather mast at Strandafjellet broke somewhere between 18 Feb 2011 and 17 Mar 2011. The weather mast tilted approximately 12 degrees toward SE. The AWS was repaired on 17 Mar 2011. This inclination has not been taken into accounted in the data evaluation. Future users of the data are advised to use the wind measurements within this time period with caution. See figure 5.3.

(a) (b)

Figure 5.3: *Tilted weather mast due to a broken pole at Strandafjellet Feb/Mar 2011 (a) before and (b) after repair on 17 Mar 2011.*

- The weather mast at Løvstakken tilted approximately 5 degrees toward W from around Feb 2011 and up to 18 Apr 2011. The reason for the long period was because of a frozen ground, so it was not possible to correct the weather mast before the ice melted.
- The sensorarms at the AWSs have not always been facing directly N-S. The sensorarm at Ulriksbakken pointed approximately 7 degrees toward NW somewhere after 25 Mar 2011 and up to 15 Apr 2011. The AWS at Strandafjellet pointed

approximately 20 degrees toward E somewhere after 17 Mar 2011 and up to 18 Apr 2011, and the sensorarm at Løvstakken pointed approximately 20 degrees toward W somewhere after 12 Apr 2012 and up to 19 Jun 2012, and somewhere after 28 Jun 2012 and up to 28 Jul 2012. These deviations have not been taken into account in this research, and future users of the data are advised to use wind direction measurements within this time period with caution.

- The AWS at Haukeland Elementary School was vandalized and tore down during Easter 2011. The last measurement was taken on 18 Apr 2011 at 17:20 UTC. The AWS was reinstalled on 11 May 2011. See figure 5.4.

Figure 5.4: *Vandalism of the AWS at Haukeland Elementary School during Easter 2011.*

- The screw connected to the wind vane at the AWS at Løvstakken (S5) loosened somewhere after 28 May 2011 and was fastened again on 16 Jul 2011. The wind vane was tilted horizontally to the side and pushed to the end of the sensor (while it should be vertically placed in the middle of the sensor). The wind direction measurements within this time period are therefore uncertain. A screw at the wind vane at the AWS at Strandafjellet (S6) was also loose somewhere after 4 Feb 2011 and up to 18 Feb 2011. The tilting of the wind vanes at S5 and S6 have not been taken into account in this study.

- A TV antenna was installed on the AWS at Haukeland Elementary School by the school 22 Aug 2011. This can lead to disturbances in wind speed coming from W.

- The cup anemometer at Mount Løvstakken started to make a creaking sound somewhere between 12 Apr 2012 and 27 May 2012. The cup anemometer was replaced on 19 Jun 2012. Some of the wind speed and gust data have been set to NaN, and the remaining wind speed and gust data within this time period should be used with caution.

- The inside of the instrumentation box at Haukeland Elementary School got covered by a wasps' nest somewhere after 8 Jun 2012. The DSU containing the last data used in this study was also covered by the nest (see figure 5.5). This data were unharmed, but the batteries may run out before the problem is solved, so this can lead to a period without data for this station.

(a) (b)

Figure 5.5: *Wasps' nest inside the instrumentation box at the AWS at Haukeland Elementary School June 2012 (a). The last data used in this study were on this particular DSU (b).*

- The batteries have been unstable at several occasions, and stopped working much earlier than expected, giving long periods without data. Cold weather is one of the reasons why the batteries did not last as long as expected in some cases.

- The lid of the HOBO rain gauge has been covered in snow and ice on a regular basis during the winter months. At some occasions, the lid has blown off due to high wind speeds.

- Problems with icing on the sensors have occurred many times. Icing was observed at the wind cup anemometer at Ulriksbakken on 18 Dec 2011. The last control before this was on 8 Nov 2011, meaning that the wind speed registered at Ulriksbakken during the storm Berit (24-26 Nov 2011) may be too low. Icing can in some cases lead to no wind speed at all. This has been a problem to several of the AWSs, especially during the winter months. Other sensors have also been affected by icing, and can in some cases be hard to detect. However, icing can in many cases be seen in the data as unrealistic values. Such values have manually been set to NaN where this has been evident (see section 5.4).

- Another problem that has occurred in the dataset, is spikes in wind speed and wind gust. When the wind speed in some cases get very high, the wind speed sensor has a speed up, and a spike appears in the data set. Such values have manually been set to NaN (see section 5.4).

- High wind speeds have also caused problems with the poles and the ropes holding the AWSs in position in many occasions. This has led to a slightly tilted weather mast in some cases. The extreme cases are described above.

Many of the challenges described above have not been corrected in the dataset. Future users of the data are therefore advised to use data for the dates mentioned in this section with caution. Especially the wind measurements are sensitive for either a vertically or a horizontally tilted weather mast. When the weather mast is tilted horizontally, the wind direction measurements are incorrect, and the corresponding wind speeds measured are coming from a different direction than shown in the data. Further, the cup anemometers that measure wind speed are quite sensitive to a vertical tilt of the weather mast. The cup anemometer measures the horizontal components of the wind, and with a tilt, the measured wind speed will have a vertical component, which will most likely lead to a lower registered wind speed than the actual one. However, the issues with the data that *are* handled in this study are described in detail in the next section.

5.4 Data handling

A number of problems have first been evident after the data have been collected. These problems have occurred due to sensor dysfunction, calibration issues, problems with the power connection, radio connection, the sensor scanning unit or the data scanning unit. These issues have caused problems that needed to be solved before the data could be used in this study. Some of the issues mentioned in section 5.3.2 also needed to be addressed. The data handling from the collected raw data and up to the time series that are used in this study are thus described in this section.

As mentioned in section 5.1, the data scanning unit (DSU) saves the raw data on site at the AWSs. The DSU then has to be brought back to the GFI, where the raw data in 10-bits binary code have to be calibrated using calibration constants for each sensor. The computed time series can then be read into Matlab.

Different problems with the dataset arose. The AWS at the five stations (S2, S3, S5, S6 and S7) could not register the time 00:00:00 UTC, so the time column was empty even though the other values were present in the data. Every file that had this problem had to be corrected. The time 23:50:00 was found by a for-loop, and then

the time 00:00:00 was automatically put in. After this had been done, all the new files were read in and put together in one time series per station.

The next problem that had to be solved was to fix the sampling interval, which is 10 minutes in this study. However, the sampling interval was not always 10 minutes, but in some cases 8 minutes, 11 minutes etc., and in some cases different in seconds as well. In addition, the sampling interval was not consistent, so even if the sampling interval started with 10 minutes, it could suddenly shift to 9 minutes, then back to 10 minutes and so on. Also, the AWSs should be activated on whole 10 minutes after changing batteries or the DSU. Due to a slight difference between the GPS time and the time of the sensor scanning unit, or wrong timing on-site, this was not always done. For these reasons, the time series had uneven time intervals and different sampling times. The seconds had to be rounded off to whole minutes, and the minutes were then rounded off to whole 10 minutes, making a consistent time interval on whole 10 minutes.

The sampling interval was as mentioned 10 minutes. Due to connection or registration problems, some of the 10 minutes values were missing, leaving a gap of 20 minutes or more between two measurements. This problem was evident for all the AWSs, including the station at Florida and Ulriken. It also happened that the batteries wore out before expected, leaving a large gap of missing data (for example at Strandafjellet between 22 Apr 2012 and 19 Jun 2012). A Matlab program was therefore used to fill in NaN where the time interval was more than 10 minutes.

Finally, data of bad quality were removed and set to NaN. However, not all known periods with bad data were handled. Both the data that were removed and data that are adviced to be used with caution are described in the following.

Some of the data with bad quality are automatically registered for the station at Florida and Ulriken. This is marked in an own column in the dataset. All the data that were marked as bad or untrustworthy for Florida and Ulriken were set to NaN. However, not all of the data with bad quality were marked. To investigate the problems, monthly plots for all the stations were made. Some values of particularly bad quality were directly removed. For all the stations this included relative humidity under 5%. In addition, some of the parameters at the different stations were unrealistic and set to NaN. These were wind speeds over 50 m/s at Ulriken, gust over 40 m/s at Haukeland, pressure below 800 hPa at Florida and wind speed over 35 m/s at Løvstakken.

Long periods with data of bad quality have been registered on several occasions. At Løvstakken, a lot of bad data were registered between 24 Mar 2011 11:50 UTC and

25 Apr 2011 00:00 UTC. Wind speed, wind gust, wind direction and relative humidity were set to NaN within this time period, giving the spring data at Løvstakken a month less with data. The temperature data at Løvstakken from 01 Feb 2012 to 01 Jul 2012 also showed wrong values, and were set to NaN (see section 5.3.1). At Nordnes, the wind speed and gust data showed unrealistic values for May and June 2012, indicating a malfunctioning cup anemometer. The wind speed and gust data were set to NaN for this time period.

As described in section 5.3.2, problems with icing and spikes due to high wind speeds, or a dysfunction in the sensor over a short time became quite evident, especially during the winter months. By looking at the monthly plots, an approximate time for each spike/icing were found. The same incidents were then found in the time series, and manually set to NaN if the value seemed unrealistic in comparison with the data surrounding the incidents. There were especially many spikes in wind speed and wind direction, but also some in relative humidity and temperature. Spikes in the Florida data were also removed. Icing was especially evident in the wind direction, wind speed and wind gust data, but also in the temperature data in some occasions.

After removing bad data, a common time period for all the stations were chosen to be further used in the study (Ch. 5.2.1).

Although some of the bad data have been removed, there are still data of varying quality left in the dataset. This includes the dates described in section 5.3.2, but also other issues that have come up during the field work and data handling. In particular the relative humidity (RH) data are of rather low quality and should be used with caution throughout the whole time period of the study. The RH data from Haukeland from around June 2011 and up to 29 August 2011 are especially bad. A new RH sensor was installed here on 29 Aug 2011. The RH sensor at Ulriken was replaced on 2 Sep 2011, and the RH sensor at Løvstakken was replaced on 14 Oct 2011. Another issue that arose was a problem with the temperature sensor at Ulriken. The temperature values showed approximately 2 °C above actual temperature during January 2012. This deviation has not been taken into account in this study. It is uncertain for how long the temperature sensor measured incorrectly, but it is recommended to use temperature data for the whole Jan 2012 and up to 8 Feb 2012 with caution.

Chapter 6

General flow conditions

Before looking at specific case studies in the Bergen valley, the general flow conditions of the area are investigated. For this purpose, wind speed and wind direction data between 23 Nov 2010 and 1 Jul 2012 for the seven AWSs are analyzed. First, wind roses for the whole period and the four seasons are presented, where December, January and February constitute the winter months, March, April and May the spring months, June, July and August the summer months, and September, October and November the fall months. After that, the effects of topography and wind direction on the observed wind speeds in the Bergen area are analyzed by wind speed ratios. Based on this, some general features of the flow conditions in the Bergen valley can be revealed.

6.1 Results

The wind roses

Figures 6.1 - 6.7 show the frequency and distribution of wind speed and wind direction for the seven AWSs during the whole period and the four seasons. The circles denoting the frequency of occurrence in percent correspond to 5, 10 and 15 % for all stations except for Florida (Fig. 6.4), where the scale has been expanded to 5, 15 and 25 % due to the very strong channeling of the wind for this station. For four of the stations, a very strong SSE-NNW distribution is evident. Two of those stations, Florida and Nordnes, are located close to sea level, while the two other stations, Ulriksbakken and Strandafjellet, are higher elevated. The SSE-NNW distribution follows the same direction as the Bergen valley. The wind at the Haukeland station, located between Ulriksbakken and Florida, shows a completely different distribution. This implies a strong local influence. Regarding wind speeds, the Ulriken station has the highest wind speeds, and is the only station where the wind speed exceeds 20 m/s. The stations in the bottom of the Bergen valley (Haukeland, Florida and Nordnes) have much lower wind speeds, and do not exceed more than 15 m/s during the measurement period. For most of the time, the wind speeds at these stations are even below 10 m/s.

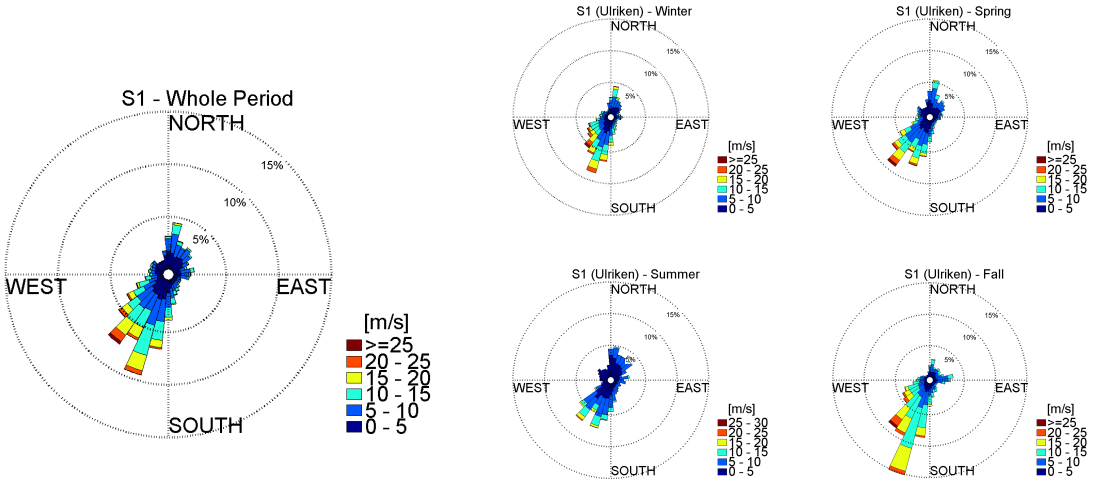

(a) Whole period - S1 (b) Seasons - S1

Figure 6.1: *Wind roses for Ulriken (S1) for (a) the whole period, and (b) the four seasons.*

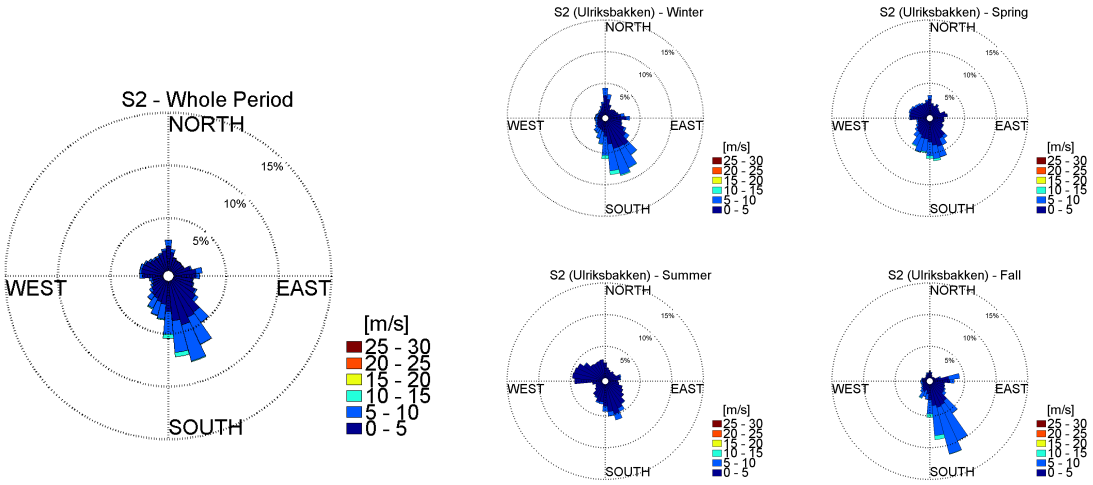

(a) Whole period - S2 (b) Seasons - S2

Figure 6.2: *Wind roses for Ulriksbakken (S2) for (a) the whole period, and (b) the four seasons.*

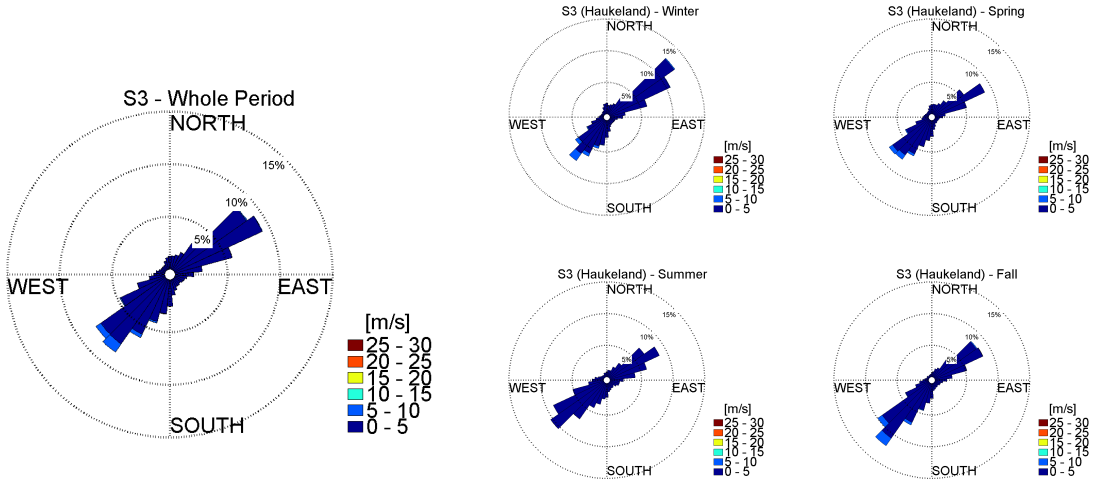

(a) Whole period - S3 (b) Seasons - S3

Figure 6.3: *Wind roses for Haukeland (S3) for (a) the whole period, and (b) the four seasons.*

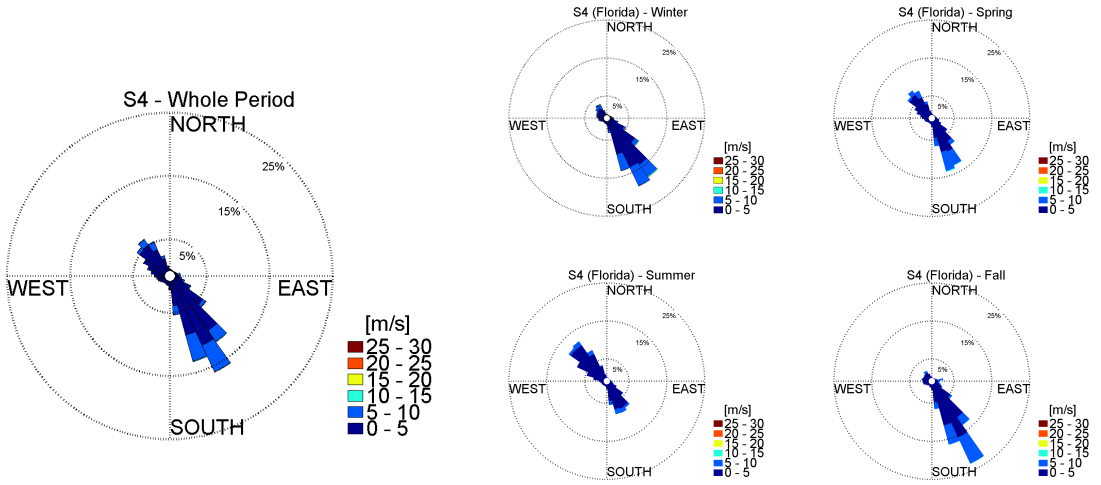

(a) Whole period - S4 (b) Seasons - S4

Figure 6.4: *Wind roses for Florida (S4) for (a) the whole period, and (b) the four seasons.*

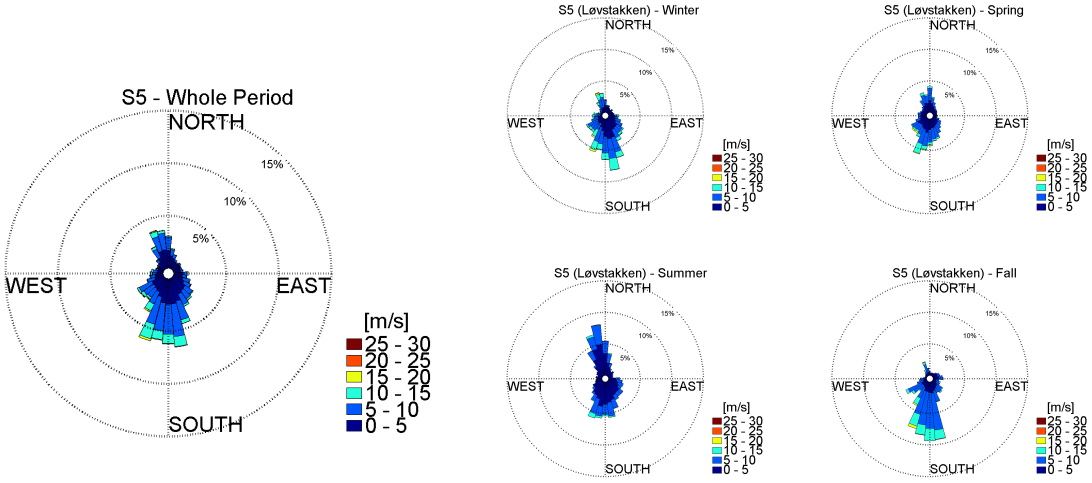

(a) Whole period - S5 (b) Seasons - S5

Figure 6.5: *Wind roses for Løvstakken (S5) for (a) the whole period, and (b) the four seasons.*

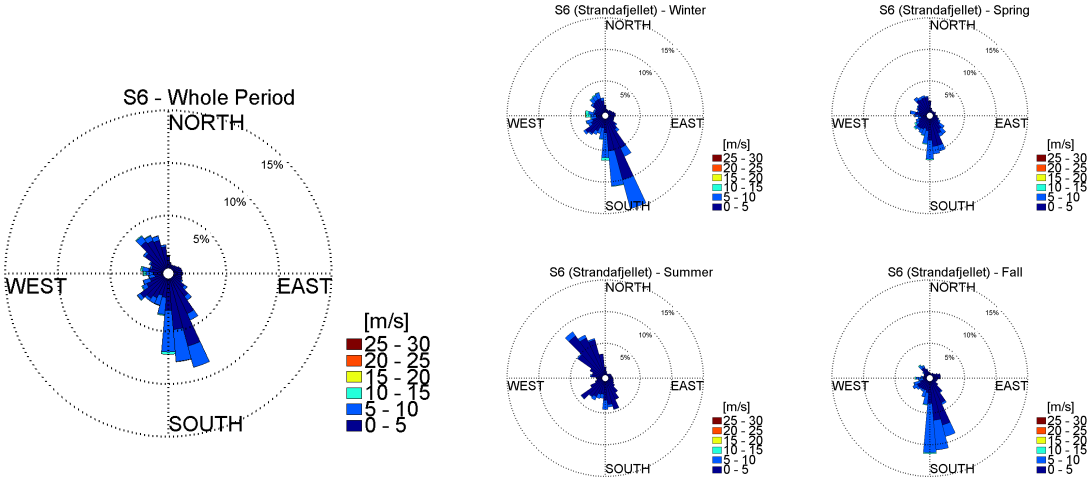

(a) Whole period - S6 (b) Seasons - S6

Figure 6.6: *Wind roses for Strandafjellet (S6) for (a) the whole period, and (b) the four seasons.*

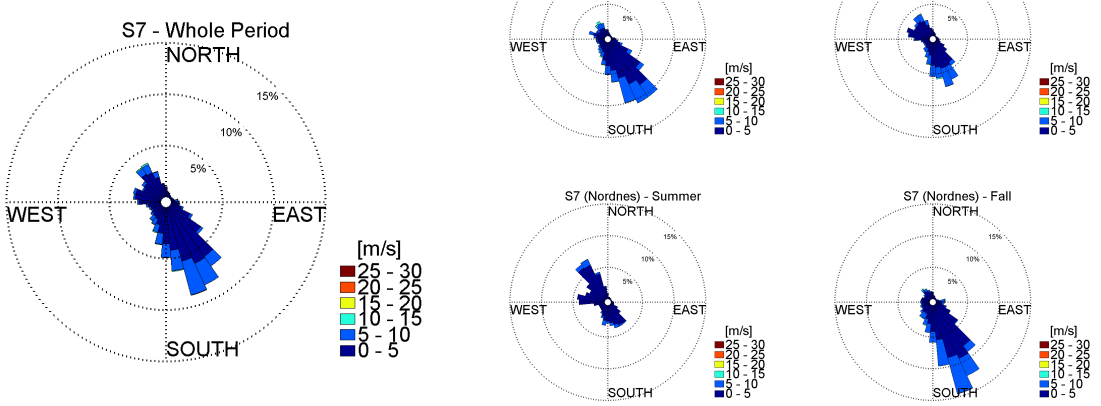

(a) Whole period - S7

(b) Seasons - S7

Figure 6.7: *Wind roses for Nordnes (S7) for (a) the whole period, and (b) the four seasons.*

At Ulriken (S1), the station expected to be the best representation of the large-scale synoptic situation, the main wind direction for the flow is from SW. This is also the sector where the highest wind speeds occur (Fig. 6.1). The wind is strongest during the fall, while the wind speed is lowest during summer. There is relatively little seasonal variation in the wind direction distribution at Ulriken. Winds from the sector N to NE are most frequent in the summer months. The corresponding wind speeds are typically low. There is almost no wind from NW and SE. Assuming Ulriken is the most representative station for the large-scale wind, SW is the common large-scale wind direction above the Bergen area.

At Ulriksbakken (S2), the main wind direction is from S-SE (Fig. 6.2). The highest wind speeds are again during fall and winter, and the lowest during summer. The wind is in general much weaker than at Ulriken. The directional distribution at Ulriksbakken is broader than for Ulriken, and with distinct seasonal variation. During summer, wind from W-NW is quite pronounced in addition to the main wind direction from S-SE. Some of the wind comes from E during fall and winter, and some from N during winter and spring. However, the main wind direction during winter and fall is SSE, and around S during spring. Some of the wind during spring comes from W-NW, but with lower frequency than during summer. In the overall period, there is almost no wind coming from NE, just a small portion of weak wind during summer and spring.

The wind at Haukeland (S3) has a completely different distribution compared to the other sites (Fig. 6.3). The wind follows a very narrow SW-NE oriented wind direction

distribution for all seasons. However, there is a distinct change in the frequency of occurrence of winds from SE and NW. During the winter months, the largest portion of the wind comes from NE. Some of the wind comes from SW, which is also where the strongest wind of 5-10 m/s comes from. During spring, the wind is almost evenly distributed between NE and SW. The highest wind speeds of 5-10 m/s still come from SW. During the summer months, the main wind direction is SW, but there is also a noticeable portion of wind from NE. The wind speed does not exceed 5 m/s during the summer months. The main wind direction during fall is from SW. The wind speed reaches 5-10 m/s during these months. There is still a noticeable portion of wind coming from NE with wind speeds between 0-5 m/s.

The wind at Florida (S4) also follows a very distinct distribution in the NW - SE direction, with almost no wind coming from other directions (Fig. 6.4). The seasonal variability in the directional distribution is higher than at Haukeland. The maximum wind speed barely reaches 15 m/s, but most commonly, the wind speed does not exceed 10 m/s. The wind is mainly coming from SE, but also some from NW. During winter and fall, the wind comes nearly exclusively from SE. During the spring months, the wind is more evenly distributed between NW and SE, but the largest portion still comes from SE. During the summer months, the predominant wind direction is NW.

At Løvstakken (S5), most of the wind comes from the sector SE-SW (Fig. 6.5). There is also a secondary peak in wind coming from NNW. The directional distribution is relatively broad. However, wind from NE is almost absent. The seasonal variability is quite high. The winter months have a very similar distribution as the whole period described above, only with a larger frequency of wind coming from SE. The highest wind speeds, reaching 15-20 m/s, come from SW and NW. During spring, the main wind direction is SW. Some of the wind also comes from SE and the northerly directions. During the summer months, the main wind direction is from NW, but some of the wind comes from the sector between SE-SW. During fall, almost all of the winds occur in the sector SE-SW, where most of the wind comes from SSE, while the highest wind speeds come from SW, reaching 15-20 m/s.

The wind at Strandafjellet (S6) follows a similar pattern as the wind at Løvstakken, but with much less wind coming from SSW, and with generally lower wind speeds (Fig. 6.6). The main wind direction is from SSE, where the highest wind speeds, reaching 10-15 m/s, come from S. There is also a peak in wind from NW, as for Løvstakken. Some wind comes from SW, while wind from NE is absent. The seasonal variability is still quite high. The dominant wind direction during the winter months is SSE, where the wind speed from S reaches 10-15 m/s. A small portion of the wind comes from the sector between SW-NW. The main wind direction during spring is from SSE. A small

portion of the wind comes from the sector between SW-NW. The wind speed does not exceed 5-10 m/s during these months. During summer, the wind mainly comes from NW, same as at Løvstakken, but with a slightly more westerly component. Some of the wind also comes from the sector between SE-SW. During fall, SSE directions dominate.

As for Haukeland and Florida, the wind at Nordnes (S7) also has a very distinct flow distribution, with wind almost exclusively coming from SE, with a weak secondary peak from NW (Fig. 6.7). The wind speeds are generally low. There is a very distinct seasonal variability in the wind directions. During winter and fall, the wind almost only comes from SE, while northeasterly directions dominate during the summer months. During spring, the wind directions are more evenly distributed between SE and NW, however the southeasterly direction is slightly more common. During the winter months, the wind speed barely reaches 10-15 m/s from NW, otherwise, the wind speed does not exceed 10 m/s.

The wind speed ratios

The relationship between the large-scale wind and the local wind in the Bergen valley is investigated. The wind at Ulriken is assumed to be the best representative for the large-sclae wind. To study the behavior of the wind at the individual stations compared to the wind at Ulriken, wind speed ratios are investigated. The wind speed ratio (WSR) used in this study is defined as the wind speed at one of the stations S2-S7 divided by the wind speed at Ulriken (S1). The wind speed ratio, presented in figures 6.8 and 6.9, is plotted against the wind direction at Ulriken. If the WSR is higher than 1, it means that the wind speed at the chosen station is higher than at Ulriken. The different subplots correspond to certain wind speed intervals for the Ulriken wind measurements used to calculate the WSR. The color code of the data points refers to the temperature difference, ΔT, between Florida and Ulriken. The WSR for two of the stations, Florida (Fig. 6.8) and Strandafjellet (Fig. 6.9) is presented in this chapter. The WSRs for all the stations can be found in figures B.2-B.7 in the appendix. For dry- to wet-adiabatic conditions in a well mixed atmosphere, the values of ΔT should vary between 6 and 3 °C (green and black color in the figures). Values smaller than this indicate the presence of an inversion between the levels of Florida and Ulriken. The more negative ΔT is, the stronger the inversion. The blue color in the figures indicates a weak inversion, whereas red color indicates a strong inversion.

The wind speed intervals are generally separated into different sectors. When the wind speed at Ulriken exceeds 15 m/s, there is almost no wind from NNW. Wind speeds between 15 and 20 m/s at Ulriken are from the sector between 0 and 290°, while wind speeds over 20 m/s mainly occur from SW (also shown in figure 6.1), with only a few cases of wind from NNE.

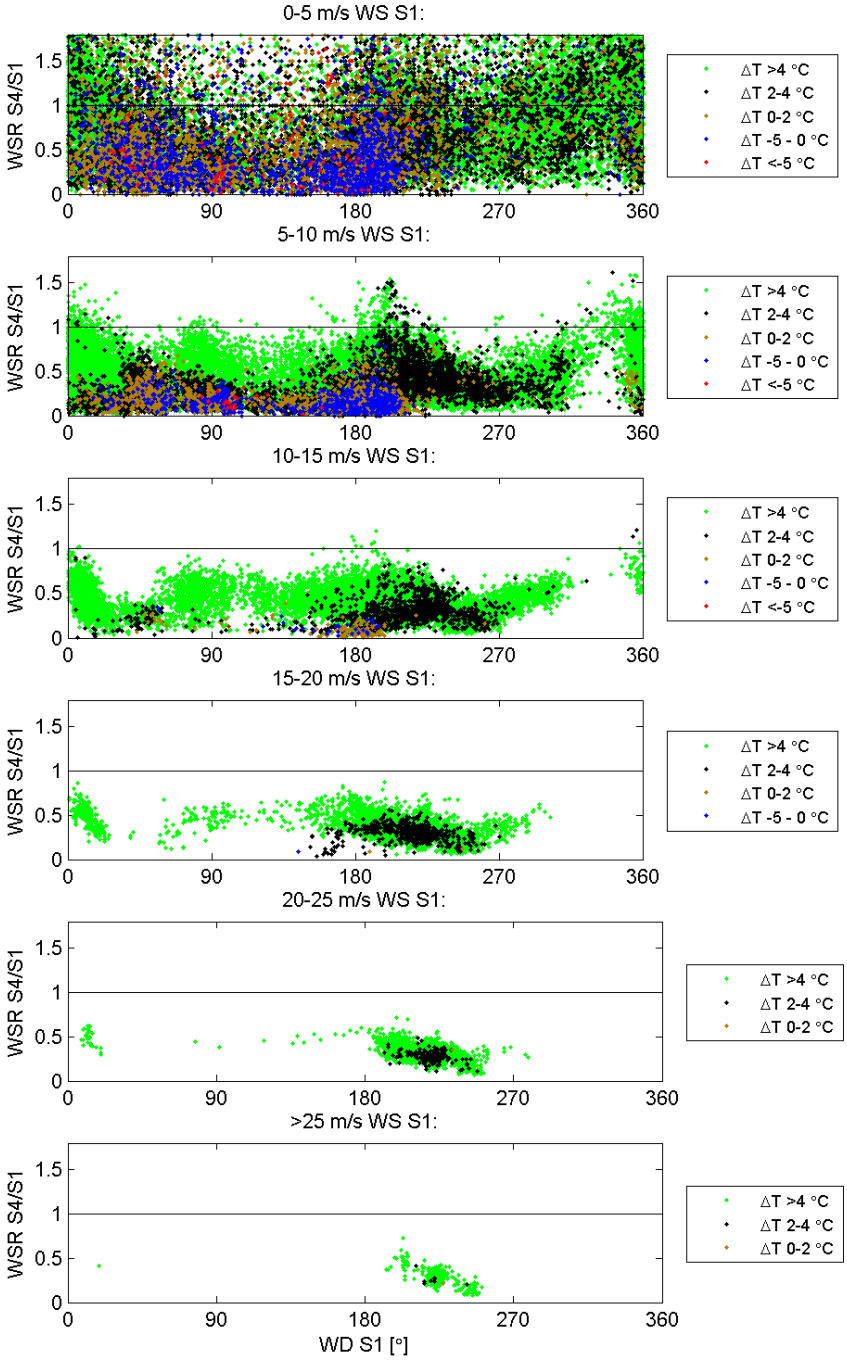

Figure 6.8: *Wind speed ratio for Florida (S4) compared to the temperature difference between Florida and Ulriken for given wind speeds.*

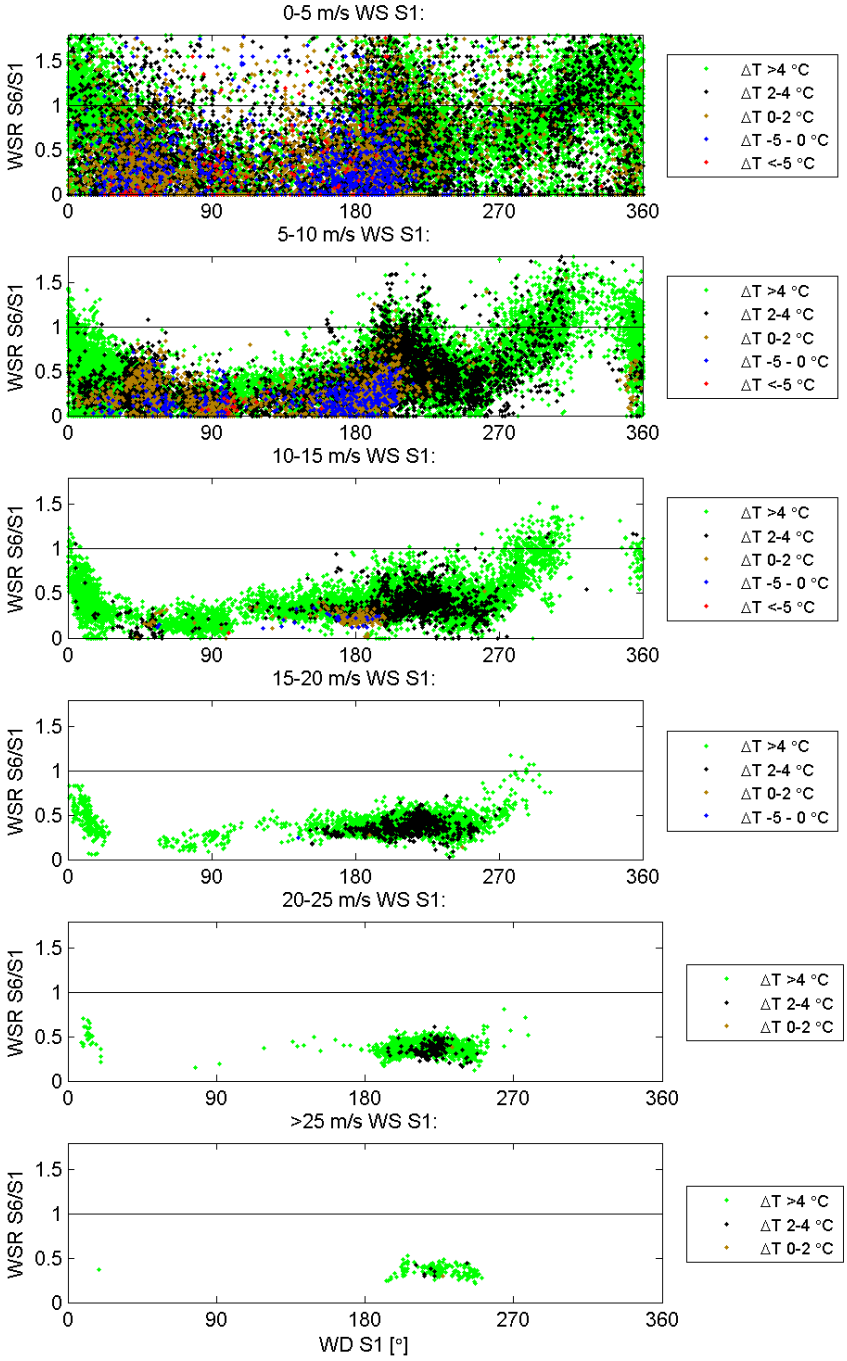

Figure 6.9: *Wind speed ratio for Strandafjellet (S6) compared to the temperature difference between Florida and Ulriken for given wind speeds.*

For increasing wind speed the probability for neutral stratification increases. Inversions rarely occur for wind speeds above 10 m/s at Ulriken, except for very few cases with southerly winds. At very low wind speeds, between 0 and 5 m/s, inversions can occur for wind directions in the sector between 0° and 200°. However, inversions occur most frequently for wind directions around S and NE. The occurrence of the strongest inversions are centered around northeasterly wind direction. At wind speeds between 5 and 10 m/s, inversions are most common if the wind direction is from S, but the strongest inversions occur if the wind comes from E.

The occurrence of WSR>1 is most likely for low wind speeds below 5 m/s at Ulriken, and can happen for any stability. In such situations with weak synoptic flow, small scale processes dominate the local wind field and lead to arbitrary values for the WSR. This is not the main focus for this study, so in the following, mainly the general features occurring for wind speeds above 5 m/s will be discussed.

The probability of WSR>1 increases when the wind at Ulriken turns northerly, southwesterly and in some cases easterly. For most stations, an increase in WSR for these directions is evident. Also evident, is a decrease in WSR as the wind at Ulriken turns westerly or southeasterly. There is one exception in the increase in WSR for northerly directions, and that is at Haukeland, where such an increase is absent. On the other hand, there is a very distinct increase in WSR at Strandafjellet, Løvstakken and Nordnes for northerly directions. At these stations, wind from N at Ulriken gives the highest values of WSR. At Ulriksbakken, Haukeland and Florida, the biggest increase with the highest WSRs are when the wind at Ulriken turns southwesterly.

There is an increase in WSR for all the stations when the wind at Ulriken turns easterly, except at Strandafjellet and Løvstakken. At Ulriksbakken, Haukeland and Nordnes, this peak is evident up to 10-15 m/s at Ulriken, but is also slightly evident at 15-20 m/s. The station where this peak reaches the highest values of WSR, is at Nordnes, where the peak is still very pronounced at wind speeds between 15 and 20 m/s. At Løvstakken, the WSR for easterly directions reaches higher values than at many of the other stations, but there is no tendency to an increase for this direction.

The stations with the lowermost WSRs, is Haukeland. In fact, the WSR exceeds 1 only when there are very low wind speeds between 0 and 5 m/s at Ulriken. When the wind speed at Ulriken exceeds 15 m/s, the WSR is almost 0.

6.2 Discussion

The wind roses

Assuming Ulriken gives the best representation for the large-scale wind above the Bergen valley, the predominant wind direction is from SW. For comparison, Jonassen et al. (2012a) found that the most common wind direction at Ulriken is from southerly directions, with a slightly higher frequency of wind from S-SW than S-SE (see figure 8 in Jonassen et al. (2012a)). This also corresponds to the results by Jonassen et al. (2012a) investigating the large-scale wind field at 850 hPa derived from Era Interim data, showing that wind from SE through the westerly sector to the N, dominates throughout the year. Again the highest frequency of the wind direction is from SW. Seen in figure 6.1, wind from NE is also observed, however, this is absent in the 850 hPa Era Interim data. Here, wind from NW is more common, which does not show up in this study. Jonassen et al. (2012a) found that the wind direction at the surface is shifted anticlockwise compared to the wind at 850 hPa, as expected from Ekman's theory. They found a shift of 30-40° for large-scale wind directions from N-NW, and a 20° shift from W-SW. This can explain that the most common large-scale wind directions are from SW and NW, while the most common wind directions at Ulriken are from SW and NE.

The only station that has wind speeds exceeding 20 m/s, is Ulriken, where the strongest wind comes from SW. Jonassen et al. (2012a) also found that the highest wind speeds in the Bergen area were at the Ulriken station during southwesterly winds. They found that only a small fraction of the wind at Florida exceeds 10 m/s (around 1 % of the wind), while approximately 25 % of the wind at Ulriken are above 10 m/s, and around 2 % above 20 m/s. Seen from figures 6.1 - 6.7, the wind speed at the Florida and Nordnes stations exceeds 10 m/s in just a few cases. One reason for the high wind speeds at Ulriken compared to lower wind speeds in the valley, can be adressed to reduced surface friction in the mountains than further down in the valley, where the stations are surrounded by buildings. In addition, the general increase of wind speed with altitude has to be considered. It might be expected that the wind speeds at Løvstakken would be approximately the same, or at least close to the wind speeds at Ulriken during southwesterly wind, but this is not the case. The wind speeds at Løvstakken do not exceed 20 m/s during this study. Harstveit (2006) did a study of extreme winds in the Bergen area where they suggest an explanation to the high wind speeds at Ulriken. He describes a local speed up for southwesterly winds at Ulriken, due to local terrain features on a small scale.

For the lower elevated stations the synoptic wind conditions are additionally modified by orographic effects. The main wind direction at the four stations, Ulriksbakken

(Fig. 6.2), Florida (Fig. 6.4), Strandafjellet (Fig. 6.6), and Nordnes (Fig. 6.7) is from SE. The second most common wind direction at these stations, is from NW. These directions correspond to the Bergen valley's alignment, indicating a distinct channeling effect. The results are in correspondence with earlier studies. Berge and Hassel (1984) describes that the most common wind directions in the Bergen valley are from SE and NW, since the Bergen valley lies sheltered from southwesterly wind downstream Løvstakken and Damsgårdsfjellet, and from northeasterly wind downstream the Fløyen massif and Sandviksfjellet. Utaaker (1995) also found that the main wind directions were from S-SE and from N-NW, represented by the wind directions at Flesland, the station he found to best represent the Bergen area. Jonassen et al. (2012a) found the most common wind direction in the Bergen area to be from SSE, and secondly from NNW, when looking at observations from different stations at ground level. However, this describes the main wind direction in the Bergen area. A clear channeling effect can also be seen at the individual stations. Utaaker (1995) published wind roses for the Florida station, and a station located at Nordnes, Fredriksberg. He describes a clear channeling effect at these stations, especially at Florida. He further points out that the channeling effect could enhance the wind coming from SE, and that wind coming from Byfjorden toward Nordnes is less affected by the local topography. According to Utaaker, the channeling effect of the wind at least extends as far south as Storetveit and Søfteland, where he also could see indications of the channeling effect. Jonassen et al. (2012a) supports Utaaker (1995)'s findings about a channeling effect of the wind in the Bergen valley. He found that approximately 25 % of the strong wind at the Florida station comes from SSE, indicating a channeling of the wind coming from SE. He also found that large scale flow from S-SE to W-SW is channeled as southwesterly wind at the Florida station, and that large-scale wind coming from N-NE, is channeled as northwesterly wind. In this study, the two higher elevated stations, Strandafjellet and Ulriksbakken, also show indications of a channeling of the wind. This is not unreasonable when large-scale wind is aligned along the topography of the Bergen valley. It is also expected that the indications of a channeled wind at these stations are smaller than at the stations at the bottom of the valley. Thermally induced wind, such as mountain and valley winds, will most likely play a central role in calm large-scale synoptic wind, since the stations are located close to the mountain sides of respectively Løvstakken and Ulriken.

The wind at Haukeland follows a completely different pattern than the rest of the stations. It follows a clear SW-NE wind direction, exactly the same direction as the alignment of Isdalen with the lake, Svartediket. The station at Haukeland is located directly downstream the opening of the Isdalen valley (see figure B.1 in the appendix). The effect of Isdalen is so pronounced, that the flow conditions show two completely different main wind directions compared to Florida, located only 1.7 km apart. The

effect of Isdalen on the flow in the Bergen valley has been documented in earlier studies. Berge and Hassel (1984) set up a weather station at Svartediket during the winter 1983/84, and documented a pronounced flow coming from N-NE during this period. At Storetveit, further S in the Bergen valley, they could not see evidence of this flow, and neither at Marineholmen, which is at approximately the same location as the Florida station. However, they assumed that a 50 m deep layer passing the 300 m wide end of Isdalen would affect the exchange of air in the northwestern part of the Bergen valley, based on calculations and assumptions. Based on the observations made by Berge and Hassel (1984) the winter 1983/84, Utaaker (1995) concluded that the wind at Svartediket will mainly come from NE during wintertime, and that wind originally coming from S-SE will be shifted toward SW. He explained this as a result of the wind aligning with the shape of the valley, as well as katabatic flow during winter. Berge and Hassel (1984) and Utaaker (1995) assumed the flow downstream Isdalen would be deflected northwestwards in the Bergen valley. Dyngeseth (1998) simulated the situation described by Berge and Hassel (1984) and Utaaker (1995), and found that the mountain wind coming from Isdalen was coming from N-NE, and further down the valley, then it shifted toward W, before it continued toward NW in the Bergen valley due to the topography, supporting their theory.

The wind directions in the Bergen valley vary according to seasons. Utaaker (1995) found the station at Flesland to best represent the main wind directions in the Bergen valley. He noted that during wintertime, directions from SSE dominate, while during summertime, directions from NNW dominate but there is also wind coming from SSE. During spring and fall, these directions are more evenly distributed, but slightly closer to the winter distribution than to the summer distribution. He also found that the wind speeds during summertime were low. Jonassen et al. (2012a) also found large-scale wind from NNW to be more frequent during summertime in the Bergen area, than during the other seasons, along with frequent large-scale wind from S. The most frequent large-scale wind direction during winter was from SW. The weakest wind was during summer, and the highest wind speeds were during winter. The results of Utaaker (1995) and Jonassen et al. (2012a) correspond to the results found in this study. During summertime, northwesterly wind directions dominate more than during the other seasons. This is valid for all stations except Ulriken and Haukeland. The northwesterly wind at Ulriksbakken has a more westerly component than at the other stations. Looking at figure B.1 in the appendix, the hillside is directly W of the station. This hillside will presumably be heated during summer, resulting in thermally induced anabatic winds. The northwesterly wind at Florida and Nordnes during summer is more likely caused by sea breeze. Jonassen et al. (2012a) found that large-scale winds below 10 m/s are mostly represented as northwesterly wind at Florida. The sea breeze is possibly the explanation to the northwesterly wind at Strandafjellet and Løvstakken.

This is likely, since the depth of the sea breeze is commonly between 100 and 500 m (Oke, 1987). The wind speed of the sea breeze is most commonly between 2 and 5 m/s (Oke, 1987), so the stronger northwesterly winds are most likely a result of the synoptic wind. The weak winds from SE during summer at these stations are most likely land breezes, while the stronger winds are synoptic winds. During wintertime, southeasterly winds dominate at all stations except at Ulriken and Haukeland, again indicating channeling of the large-scale southwesterly wind found by Jonassen et al. (2012a). The wind distribution during fall is generally quite similar to the winter distribution. This holds for all stations, only that the wind during wintertime at Strandafjellet and Løvstakken has a slightly more southerly wind component than during fall. The wind directions during spring, are generally more evenly distributed between the two main wind directions. The two stations that deviates in the seasonal pattern compared to the other stations are the stations at Ulriken and Haukeland. The reasons for these deviations are that the wind at Ulriken is more similar to the large-scale wind than to the wind at the lower elevated stations, and that the wind at Haukeland is channeled by Isdalen. The wind at Ulriken has a very weak seasonal variation. The main wind direction is from SW, and the second most common wind direction is from NE, as discussed earlier. The seasonal variation in wind at Haukeland is also very weak, but differences between the seasons can still be seen. During wintertime, the main wind direction is from NE, which is expected because of downslope katabatic winds during wintertime (Ch. 2.4). While the main wind direction in the Bergen valley is northeasterly during the summer, the main wind direction is southwesterly at Haukeland. It is possible that the sea breeze traveling up the Bergen valley is deflected toward Isdalen. This may be possible to see in numerical simulations. During fall and spring, the originally SE oriented winds in the Bergen valley are deflected toward Isdalen in a southwesterly direction.

The wind speed ratios

Several of the stations show a clear increase in WSR for southwesterly flow at Ulriken. High WSR in southwesterly flow reveals either high surface wind speeds, or low wind speeds aloft. Seen from the wind roses (Fig. 6.1 - 6.7), the former is the case. The strongest winds observed in the Bergen valley throughout the whole period of the study, comes from SW at Ulriken, which is the station assumed to be most representative for the wind conditions aloft. It can also be seen from the case study of the southwesterly storms in chapter 7, where very high surface wind speeds were observed during these storms. High surface wind speeds in the Bergen area when the flow aloft comes from SW have been documented by Jonassen et al. (2012a) and Barstad and Grønås (2005). Barstad and Grønås (2005) explain the high surface winds in southwesterly flow as the result of a coastal jet, caused by the acceleration and deflection of flow toward the left along the southwestern coast of Norway, due to a weakened Coriolis force as the flow

impignes on the south Norwegian mountain range.

Jonassen et al. (2012a) observed high wind speeds at the Florida station (representing the Bergen valley in their study) during southwesterly winds, even though Florida lies sheltered from SW due to surrounding topography. They suggested that the flow could deflect around the topography, such that the wind speed would be enhanced due to the channeling between the surrounding mountains. Apart from Løvstakken and Haukeland, none of the other stations show strong wind from SW (Fig. 6.1 - 6.7), which can support the findings about channeling of the wind in the Bergen valley. The station at Løvstakken lies unsheltered from southwesterly wind, and the flow at Haukeland will be channeled with respect to Svartediket. Jonassen et al. (2012a) also found that the enhanced wind speed at Florida in southwesterly flow was independent of the stability of the atmosphere.

The stations that react strongest to southwesterly flow in WSR are as mentioned Ulriksbakken, Haukeland and Florida, which are the first stations a southwesterly flow will meet as it is channeled through the Bergen valley. The effect occurs mainly for moderate wind speeds below 15 m/s, i.e. not during southwesterly storms.

High WSRs are also found in flow from northerly directions. According to Jonassen et al. (2012a), both weak and strong surface winds are observed for northwesterly flow, depending on the atmospheric stability. As northwesterly flow hits the mountain range of southern Norway, the Coriolis force weakens, and the flow turns left toward the mountains, consequently the wind speeds at the surface are reduced. If the atmospheric stability increases, so does the magnitude of the blocking, and the surface wind speed is reduced even more. In addition, vertical mixing of momentum is reduced, again reducing the surface wind speed. A low wind speed at the ground and aloft will give a reasonable high WSR, depending on how low the wind speed at the surface is compared to the wind speed at Ulriken. If the atmosphere is unstable, the surface wind speed is higher (Jonassen et al., 2012a). For the northwesterly flow, some of the stations in the Bergen valley are quite unsheltered, such as, Nordnes, Strandafjellet and Løvstakken. The Bergen valley is NW - SE oriented, so wind from NW will be channeled through the valley. Especially the AWS at Nordnes will experience this channeling, as seen from the wind roses (Fig. 6.7). In addition, the wind that hits the Nordnes station will experience less surface friction than the other inland stations, since it is so close to Byfjorden. Utaaker (1995) also observed wind from NW that hit the weather station at Nordnes at that time, Fredriksberg, with full strength from Byfjorden. When this is the case, the WSR will have even greater values than in a stable atmosphere.

Northerly winds are generally strong. Jonassen et al. (2012a) excluded wind speeds

below 10 m/s, and saw that the percentage of northerly winds increased, which they explained was due to a stronger alignment with the topography and coastline in the area for strong winds. When doing the same experiment for northeasterly winds, they found that winds from NE were almost absent. In general, wind from NE in the Bergen valley is blocked by mountains. Jonassen et al. (2012a) found that wind from NE is rare both at the surface and in the mountains, which also can be seen from the wind roses for all stations except Haukeland. The northeasterly wind here is, as explained, due to channeling of the wind through Isdalen.

As for northeasterly flow, flow from E are rare, and is almost absent when wind speeds under 10 m/s are excluded (Jonassen et al., 2012a). Still, there is a pronounced increase in WSR in easterly flow in this study, indicating high surface wind speeds when the wind speed in the mountains remains low. Utaaker (1995) noted that the Bergen valley is sheltered from flow from E, leading easterly flow to channel through the area from north-northeasterly directions instead. He further describes that the wind can be enhanced over mountains, through gaps and constrictions. Jonassen et al. (2012b) also found indications of this, where the wind at Florida could be enhanced as it penetrates through a gap between the mountains E-NE in the area leading to downslope accelerated winds. The WSR increases for easterly wind for all the stations except those at Strandafjellet and Løvstakken. This supports the theory about downslope accelerated winds from the eastside of the Bergen valley, reaching the stations in the middle of the valley, Nordnes and Florida, but not those elevated on the opposite side of the valley. Even if there is no clear peak in increasing WSR for easterly flow at Strandafjellet and Løvstakken, some incidents of WSR>1 is found for Løvstakken, but not Strandafjellet (looking at wind speeds over 5 m/s). This may indicate that easterly flow in some cases does not deflect down the valley, but may flow across it aloft. In the cases where the WSR>1, the wind at Ulriken may have been decelerated due to friction, while the station at Løvstakken is located in a site with less surface friction, leading to higher wind speeds at Løvstakken than at Ulriken. A more detailed study using numerical simulations may give some answers. However, this has not been done in this study.

A decrease in WSR is observed when the flow comes from SE, which is a surprising result since the Bergen valley is SE oriented, and a channeling of the wind is expected. Jonassen et al. (2012a) found low wind speeds in southeasterly wind both aloft and at the surface, and relate this to a theory suggested by Barstad and Grønås (2005) that a large-scale wake is formed in southeasterly wind downstream the mountains in southern Norway. Jonassen et al. (2012a) also noted that southeasterly flow is insensitive to changes in stability. All stations in the Bergen valley have some wind coming from SE, except Haukeland and Ulriken. Southeasterly wind at Ulriken is most likely further dampened due to surface friction, and southeasterly flow at Haukeland is blocked by

Ulriken. The wind roses in figures 6.1 - 6.7 confirm low surface winds in southeasterly flow. The WSR also decreases for westerly flow, a wind direction where the stations in the Bergen valley are sheltered from.

For wind speeds between 5 and 10 m/s, inversions are mainly found for southerly and easterly wind directions, where the strongest inversions occurred when the wind was from E. Berge and Hassel (1984) describe that long inversion periods of more than one day occur in large-scale easterly flow, when the local topography gives a shelter for the wind in the Bergen valley. During southerly winds, the reason for inversion is a bit more unclear. This has been studied in more detail in chapter 9, where an inversion during southeasterly synoptic wind is simulated. Berge and Hassel (1984) defined different groups of inversions, where one of them contains inversions during wintertime with snow-covered ground, where the most intense inversions occurred during southeasterly winds above the Bergen valley. They defined another group which contained inversions with a mixed layer close to the ground, where a high pressure system moved toward NE from SW over southern Norway. For even lower wind speeds at Ulriken, between 0 and 5 m/s, inversions were centered for southerly and northeasterly wind directions. Berge and Hassel (1984) described that short inversion periods between 6 and 24 hours were found when northeasterly flow is blocked by the topography, giving a clear and calm weather, with a stable layer at the ground. For all inversion cases described by Berge and Hassel (1984), there is a high pressure system over southern Norway, with low synoptic wind speeds. However, the cases they studied were very specific, and may not be a general description of typical patterns. To be able to draw certain conclusions, especially for the southerly winds, further investigation will be necessary.

6.3 Conclusions

The Ulriken station may give the best representation of the large-scale wind above the Bergen valley. The most common large-scale wind direction is from SW, and the second most common wind direction is from NW. The main wind direction at Ulriken is from SW and NE. This can be explained by Ekman's theory. Ulriken is also the station with highest wind speeds in the Bergen valley. The high wind speeds are mainly due to a local speed up, but are also presumably due to the high elevation and low surface friction, compared to the lower elevated stations.

The wind at Florida and Nordnes is clearly channeled following the alignment of the Bergen valley, SE-NW. Southeasterly winds experience a speed up as the wind is channeled, while the wind coming from NW toward Nordnes is less affected by topography, so the wind coming from this direction is weaker. The higher elevated stations,

Strandafjellet and Ulriksbakken, are also affected by channeling of large-scale synoptic wind, but are less affected during calm synoptic wind.

The wind distribution at Haukeland deviates clearly from all other stations. The results show that the wind close to Svartediket in Isdalen, will be channeled in a SW-NE direction. Wind coming from Svartediket in a northeasterly direction, will presumably shift and continue toward NW in the Bergen valley, while wind coming from SE close to Svartediket in the Bergen valley will become southwesterly. Thermally driven wind will propagate along the alignment of the Isdalen valley, e.g. katabatic winds during winter and anabatic winds during summer.

The wind directions in the Bergen valley vary according to seasons. For all stations except at Ulriken and Haukeland, the main wind direction during wintertime is from SE, and during summertime, wind from NW dominates, along with southeasterly wind. The main wind direction during fall is similar to the winter distribution, and during spring, the two main wind directions are more evenly distributed between NW and SE. The highest wind speeds are generally found during winter and the weakest wind during summer. During summer, the northwesterly wind at Ulriksbakken has a more westerly component than at the other stations. This can be due to upslope anabatic wind as the hillside is heated by the sun. The weak winds from NW and SE at Florida, Nordnes, Strandafjellet and Løvstakken are most likely caused by land-sea breeze circulation, where the sea breeze coming from NW dominates during daytime, and the land breeze coming from SE during nighttime. Stronger winds are connected to the synoptic wind. The seasonal variation at the Ulriken station is weak, and the main wind direction at this station is closer to the large-scale wind directions than at the surface wind directions. The wind at the Haukeland station follows a completely different seasonal pattern than the rest of the stations, as winds from NNE dominate during winter, and winds from SW dominate during summer. During winter, downslope katabatic flows, and during summer, the sea breeze in the Bergen valley are assumed to be deflected toward Svartediket. During spring and fall, some of the southeasterly winds in the Bergen valley are directed toward Svartediket.

High wind speed ratios (WSRs) are observed for wind coming from southwesterly, northerly and easterly directions at Ulriken. High WSR for southwesterly flow is a result of high wind speeds in southwesterly flow aloft due to a coastal jet, which is deflected around and channeled through the local topography of the Bergen valley, and increasing the surface wind speed. This most commonly happens when the wind speed at Ulriken is between 0 and 10 m/s, and in a few cases, the wind speed can reach up to 15 m/s. For northwesterly flow, both high and low surface wind speeds are observed, depending on the atmospheric stability. Given a high stability, the blocking of the

northwesterly flow due to the mountains in southern Norway is pronounced, and the vertical mixing of momentum is reduced, giving low wind speeds aloft and particular at lower level (Jonassen et al., 2012a). This will give a reasonable high WSR, assuming equally low wind speeds at Ulriken and at the stations located at lower elevations. For the WSR to increase even more, the weather stations unsheltered from northwesterly flow must experience stronger wind speeds, which will most likely happen in an unstable stratification. The Nordnes station will especially experience high wind speeds compared to the other stations, due to less surface friction over Byfjorden. Wind from NE are rare both at the surface and in the mountains (Jonassen et al., 2012a). The WSR also increases for easterly flow at Ulriken for all stations except for those located at Strandafjellet and Løvstakken, which supports a theory about downslope accelerated flow through the mountain gap between the two mountain ranges E in the Bergen valley. The accelerated wind reaches the bottom of the valley, and is most likely channeled through the valley, not reaching the stations at Strandafjellet and Løvstakken. Decreasing WSRs are observed for wind from SE and W at Ulriken. A decrease in WSR for southeasterly wind, is linked to low surface winds both aloft and at the surface due to a wake downstream the mountains in southern Norway (Jonassen et al., 2012a; Barstad and Grønås, 2005). There is also a decrease in WSR for westerly wind at Ulriken, since the low elevated stations in the Bergen valley lies sheltered for westerly wind.

For very low wind speeds between 0 and 5 m/s at Ulriken, the most common wind direction for an inversion to be present is either northeasterly or southerly. For wind speeds between 5 and 10 m/s, southerly wind directions are still common, but the strongest inversions are during easterly wind. Northeasterly and easterly wind is blocked by topography, giving calm weather during high atmospheric stability. For southerly winds, the reason for inversions to develop is a bit more uncertain, but it may be during snow-covered ground with synoptic wind from SE, or as a high pressure system gives synoptic wind from SW. However, further investigation of inversions during southerly winds is necessary to be able to be certain of the circumstances around the development of these types of inversions. General for all inversions, a high pressure system giving low synoptic wind over the Bergen area must be present.

Chapter 7

Case study - Southwesterly storms

The late autumn and winter 2011 were dominated by strong winds and precipitation along the Norwegian west coast. There were two storms that stood out as they caused problems in the form of flooding, property damages, and even casualties along the coast. The storms were given the names Berit and Dagmar by the Norwegian Meteorological Institute (met.no), and hit the coast on respectively on 25 Nov 2011 and on 25 Dec 2011. A description of the synoptic development of the storms is given in sections 7.1.1 and 7.2.1. The local impact of the storms is further presented in sections 7.1.2 and 7.2.2, and discussed in section 7.3 with following conclusions in section 7.4.

7.1 The storm Berit

7.1.1 The synoptic situation

The full sequence of the development of Berit is shown in the appendix, figures C.1(a)-(h), and the two most relevant synoptic charts for Bergen are shown in figures 7.1(a)-(b).

Berit is a rather good example of the development of an extratropical cyclone as described in chapter 2.2. Berit is a slow moving system, propagating northeastward over the North Atlantic Ocean toward Norway. On 24 Nov 2011 06 UTC, the system is located S of Iceland and W of Ireland. The system travels northeastward, and by 24 Nov 18 UTC, the system is located between Iceland and Great Britain. By then, it has developed into an extratropical cyclone with a core pressure of 947 hPa. The warm front is located directly over Bergen at this time. The isobars indicate that the wind over Bergen will be from S, with a slight westerly component. The storm continues to travel northward, and by 25 Nov 00 UTC, the center is located E of Iceland with a core pressure of 944 hPa. Bergen is located in the warm sector, not far from the center of the cyclone. The cold front is about to hit Bergen at this time. The isobars tighten, and the wind direction over Bergen is from SW. Six hours later, on 25 Nov

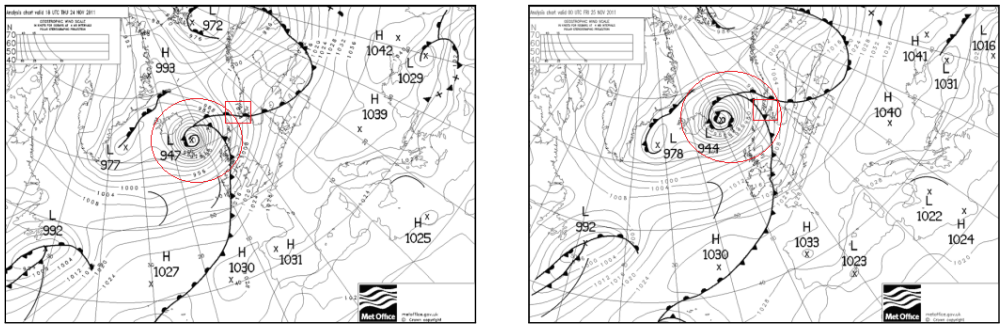

(a) 24 Nov 2011 18 UTC (b) 25 Nov 2011 00 UTC

Figure 7.1: *The synoptic situation of the storm Berit (Source: UK Met Office). Red circles indicate the location of Berit, and the red boxes show the location of the southwest coast of Norway. In (a), the warm front is located directly over Bergen, and in (b), Bergen is located in the warm sector.*

06 UTC, the storm moves northeastward, and the center is located approximately W of Trondheim. The cold front has passed Bergen, and the wind has a more westerly component, but is still coming from SW. By 25 Nov 12 UTC, the core pressure reaches a minimum at 943 hPa, where the center is still located W of Trondheim, and the isobars over Bergen indicate that the wind continues to veer clockwise over Bergen. At 18 UTC the same day, the system moves toward NE, and closer to Norway. The isobars over Bergen remain unchanged, still indicating a southwesterly wind direction. On 26 Nov 00 UTC, the center of the system is located just outside Bodø. The isobars over Bergen decrease in density, and the wind is mainly coming from W. By 26 Nov 18 UTC, Bergen is again located in the warm sector of a new, but weaker system (not shown).

7.1.2 Results - observational study

Three days around the storm Berit, 24 Nov - 26 Nov 2011, are investigated. The wind speed time series for the three day period (Fig. 7.2(a)) show a wave shaped pattern for all the stations, with two distinct peaks and one shorter lasting peak after the first one. The first peak constitutes the storm Berit, which lasts for around 10 hours between 24 Nov 18 UTC and 25 Nov 04 UTC. The wind speeds at Ulriken (S1) by far exceed the wind speeds at Løvstakken (S5), a quite surprising result bearing the small height difference of these two mountain stations in mind. The maximum wind speed at Ulriken is close to 30 m/s, while it is about 17 m/s for Løvstakken. During the largest peak in wind speed, there is almost a 12 hour period with wind speeds over 20 m/s, and a period of around four hours with wind speeds exceeding 25 m/s at Ulriken. At Løvstakken the wind speed has a steady increase from 15 to 17 m/s for around five hours within the same peak, and from 10 to 17 m/s for the whole 12 hour period. The wind speeds at Ulriksbakken (S2) follows the same pattern as at Ulriken, only with

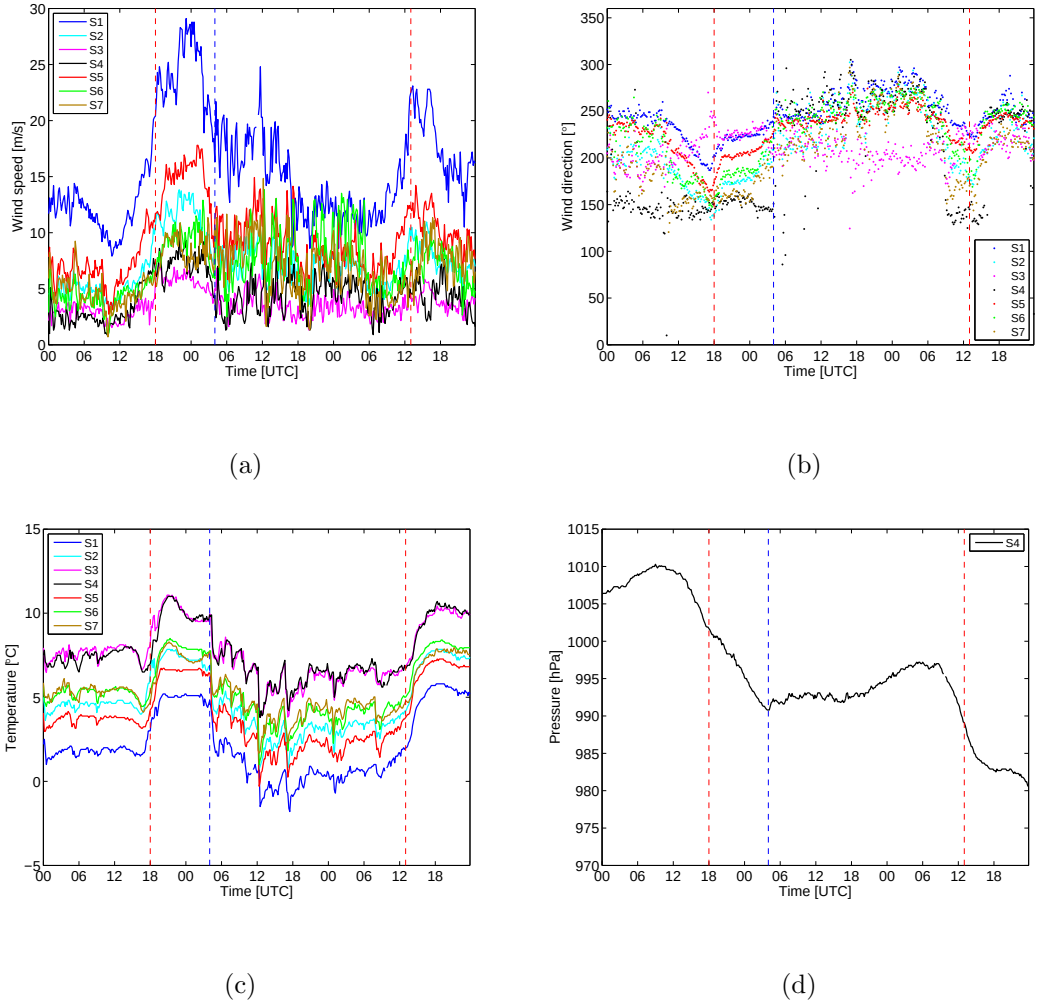

Figure 7.2: *Time series showing the 10 minutes measurements during the three day period around the storm Berit, covering 24 Nov 2011 - 26 Nov 2011 for (a) wind speed, (b) wind direction, (c) temperature, and (d) pressure at S4. The red and blue vertical lines illustrate the times when warm and cold fronts pass Bergen (see the discussion in section 7.3).*

lower winds speeds around 11-13 m/s. The wind speeds at Strandafjellet (S6) has the same steady increase as at Løvstakken, but with lower wind speeds between 7 and 12 m/s within the 12 hour period. The wind speeds at Nordnes (S7) reach the same wind speeds as at Strandafjellet during the first period. After that, the wind speed at Nordnes is somewhat lower than the wind speed at Strandafjellet, with values around 7-10 m/s. The lowest wind speeds during the storm Berit, are observed at Haukeland (S3) and Florida (S4). The wind speeds lie between 5 and 8 m/s at Florida, and around 5 m/s at Haukeland. A shorter lasting peak occurs at 25 Nov around noon. During this period, the wind speed reaches up to almost 25 m/s at Ulriken, 12-15 m/s at Løvstakken, Nordnes and Strandafjellet, around 10 m/s at Ulriksbakken, and 5-7 m/s at Florida and Haukeland. The last distinct maximum in wind speeds is observed in the early afternoon of 26 Nov, and lasts for almost four hours. Then, the wind speed at Ulriken reaches around 23 m/s, 14 m/s at Løvstakken, 10 m/s at Ulriksbakken, Strandafjellet and Nordnes, and between 2 and 6 m/s at Florida and Haukeland.

The prevailing wind direction during this three day period is southwesterly, however, Florida has only wind coming from SE and NW, the same direction as the alignment of the Bergen valley (Fig. 7.2(b)). The wind direction at Haukeland also deviates from the other stations. During the highest peak in wind speed, the wind at Haukeland has a more westerly component than the other stations. As could be expected (for these strong wind situations), the temperature decreases adiabatically with height throughout the whole three day period (Fig. 7.2(c)), indicating a near-neutral and well-mixed atmosphere.

The three day period starts with calm or moderate, steady wind speeds of 10-15 m/s at Ulriken, and 2-8 m/s at the other sites (24 Nov 2011 00 UTC - 12 UTC). After 12 UTC, the wind speeds start to increase, and the wind direction veers anticlockwise from southwesterly to more southerly. The temperature is still constant, and the pressure at Florida increases to a maximum (Fig. 7.2(d)). The pressure decreases rapidly after 12 UTC. At 18 UTC, the wind speed jumps to much higher values, and the wind direction suddenly veers clockwise. All the stations except Ulriksbakken, Florida and Nordnes have wind coming from SW. Florida and Nordnes have wind coming from SE, while the wind at Ulriksbakken has a more southerly direction. The pressure continues to decrease. At around 22 UTC, the wind speed again jumps to higher values, and the wind direction remains steady. The temperature reaches a maximum at this point. On 25 Nov 00 UTC, the wind speed at Ulriken is at its highest during the following three hour period. While the wind speed at Løvstakken has a steady increase before the highest peak, the wind speed at Ulriken seems to have a jump or a speed up. This happens for a period between 24 Nov 18 UTC and 25 Nov 04 UTC. The wind direction is still constant during this period. The temperatures are still high, and the pressure

continues to decrease. At around 04 UTC, the wind speed shows an abrupt decrease, while the gustiness increases. The wind direction starts to veer clockwise, but it also varies more than before, again indicating a gusty tendency. Temperatures fall suddenly by 3-4 °C. The pressure at Florida reaches a minimum of 991 hPa. The coming period is dominated by gusty wind that veers clockwise, temperatures that decrease, and a more or less constant pressure. At 18 UTC, the pressure starts to increase, and so does the temperature. The wind speed on the other hand, decreases, except the wind speed at Strandafjellet, which suddenly increases, and reaches the same wind speeds as at Ulriken. The wind continues to veer clockwise toward north. After 26 Nov 06 UTC, the wind speeds again increase toward a new peak, and the wind turns clockwise after a period with anticlockwise directional change. The temperature increases and the pressure begins to drop. The most rapid increase however, is around 13 UTC. This lasts for a few hours before the wind speed decreases again.

7.2 The storm Dagmar

7.2.1 The synoptic situation

While Berit propagates slowly over the North Atlantic Ocean, Dagmar is a fast moving system, travelling all the way from south of Greenland to Bergen in just 12 hours. The full sequence of the development of Dagmar is shown in the appendix in figures C.2(a)-(h), and the two most relevant synoptic charts for Bergen are shown in figures 7.3(a)-(b).

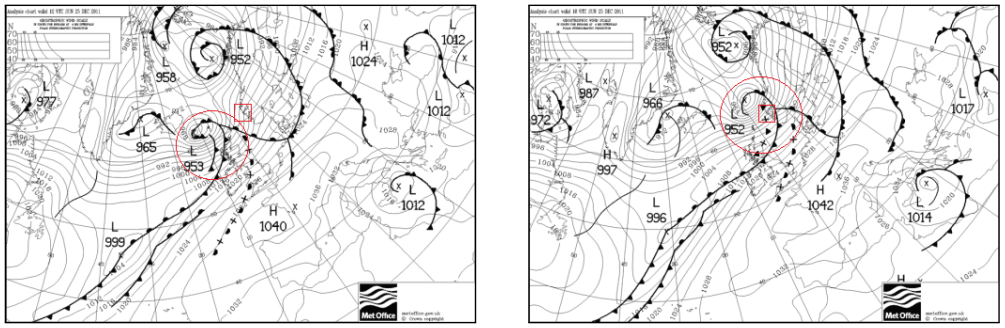

(a) 25 Dec 2011 12 UTC (b) 25 Dec 2011 18 UTC

Figure 7.3: *The synoptic situation of the storm Dagmar (Source: UK Met Office). The red circles indicate the location of Dagmar, and the red boxes show the location of the southwest coast of Norway. In (a), the warm front of the system is moving toward the southwestern part Norway, and in (b), Dagmar's fronts have just passed Bergen, but Møre og Romsdal and Trøndelag are very close to the center of the extratropical cyclone.*

The extratropical cyclone causing the storm Dagmar, starts to develop S of Newfoundland on 24 Dec 2011 00 UTC. By 24 Dec 12 UTC, the system is E of Newfoundland, while the warm front in another extratropical cyclone is moving toward Bergen from SW. Six hours later, the system of Dagmar is in the North Atlantic SE of Greenland and SW of Iceland. The other system over Bergen has moved eastward, and Bergen is located in the warm sector close to the center with a core pressure of 945 hPa. On 25 Dec 06 UTC, an occluded front with a core pressure of 957 hPa has developed in Dagmar's system. The center of this system is now located directly S of Iceland, while Bergen is located behind the fronts of the other system. The warm front of the Dagmar system heading toward Norway is located over Scotland. The system continues northeastward, and the isobars tighten. By 25 Dec 12 UTC, the center of the system is located between Iceland and Scotland with a core perssure of 953 hPa, while the warm front is in the middle between southern Norway and England, moving in a southwesterly direction. Already by 18 UTC, the cold front has passed Bergen. The area in the warm sector closest to the center of the cyclone had its path directly over Bergen. However, the parts of Norway that will experience the highest wind speeds are *Møre og Romsdal* and *Trøndelag*, where the isobars are at its tightest. The center of the system is located directly W of this area, with a minimum in core pressure of 952 hPa. On 26 Dec 00 UTC, the development of the system has slowed down. A new system starts to develop close to Bergen, and by 26 Dec 06 UTC, the warm front is situated directly over Bergen. Seven hours later, Bergen is located in the warm sector just before the next cold front hits Bergen (not shown).

7.2.2 Results - observational study

Time series for the three day period around the storm Berit and Dagmar reveal a similar pattern. The wind speed for the three day period around Dagmar has a wave shaped pattern with three main peaks (Fig. 7.4(a)). The first peak starts around 24 Dec 09 UTC and lasts for around 15 hours. The wind speed at Ulriken reaches much higher values than the wind speed at Løvstakken, with wind speeds around 20-27 m/s, while the wind speeds at Løvstakken are around 10-16 m/s. During this peak, the highest wind speed is approximately 13 m/s at Ulriksbakken, 11 m/s at Strandafjellet, and 10 m/s at Nordnes. The highest wind speed at Florida and Haukeland is respectively around 6 m/s and 5 m/s during this peak. The second peak constitutes the storm Dagmar, which starts around 25 Dec 09 UTC and lasts for almost 12 hours. Within this time period, Ulriken has wind speeds over 25 m/s for approximately 9 hours, reaching a maximum of 33 m/s around 13 UTC. The maximum wind speed at Løvstakken is 18 m/s. The maximum wind speed at Strandafjellet reaches 19 m/s at a time where the wind speed at the other stations decreases. Further, the maximum wind speed at Ulriksbakken is 15 m/s, 14 m/s at Nordnes, 8 m/s at Florida and 6 m/s at Haukeland. The last peak in wind speed starts around 26 Dec 09 UTC, and lasts for another 12

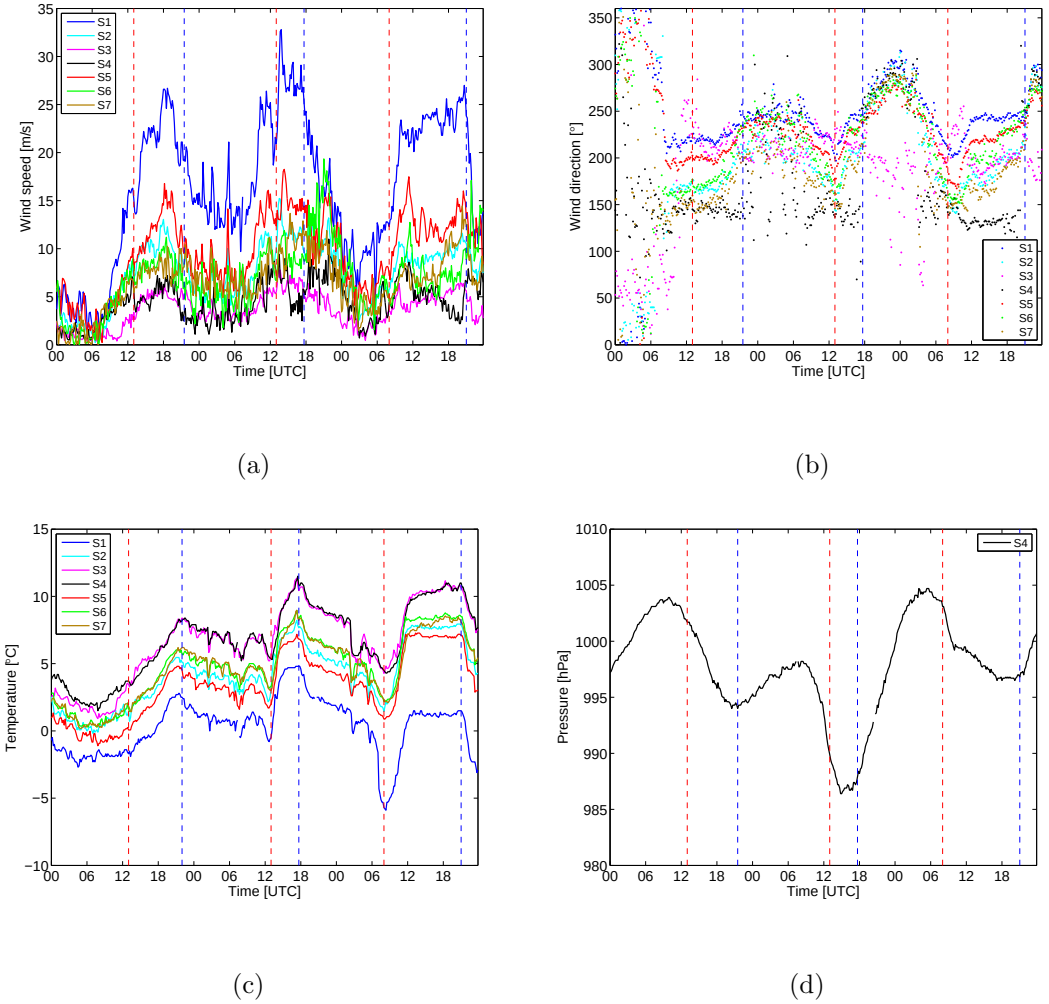

Figure 7.4: *Time series showing the 10 minutes measurements during the three day period around the storm Dagmar, 24 Dec 2011 - 26 Dec 2011 for (a) wind speed, (b) wind direction, (c) temperature, and (d) pressure at S4. The red and blue vertical lines illustrate the times when warm and cold fronts pass Bergen (see the discussion in section 7.3).*

hours. Ulriken has wind speeds exceeding 20 m/s the whole period. Løvstakken has a maximum wind speed around 17 m/s during this peak, and Strandafjellet has 13 m/s. The rest of the stations has maximum wind speeds between 6 and 10 m/s.

As for Berit, the main wind direction during these three days is southwesterly, turning toward W at the end of the storm. The wind at Florida is still only coming from SE and NW, but a small portion of the wind during Dagmar is coming from SW - W. The temperatures are highest at the lowest elevated stations, and decreases with height, as expected.

There is a calm period at the beginning of the investigated time period with low wind speeds coming from varying directions. However, on 24 Dec 09 UTC, there is a rapid increase in wind speed. The wind direction for Ulriken, Haukeland and Løvstakken is steady from SW - W, while the wind direction is from SE - S for the other stations. Both the temperature and the pressure increase. At 12 UTC, the wind speed increases rapidly, but the wind direction stays mainly unchanged. The temperature continues to increase, but the pressure has started to decrease. At 18 UTC, the wind speed hits a maximum in the first peak in the three day period. The wind speeds at Ulriken reaches about 27 m/s, while the wind speed at Løvstakken is about 10 m/s lower. The wind direction starts to veer clockwise, except at Florida, where the wind is still southeasterly, the same direction as the Bergen valley. The temperature continues to increase, and the pressure drops. At around 21:30 UTC the wind speed suddenly drops and becomes gusty. The temperature also drops. The wind direction turns clockwise, and the pressure starts to increase.

On 25 Dec 00 UTC, the wind speed remains gusty, and the wind at all the stations except Florida are veering clockwise. At Florida, the wind still comes from SE. The temperature shows a slight decrease, and the pressure slowly increases. At 06 UTC, the wind speeds are a bit lower, and the wind direction turns anticlockwise. The temperature is still decreasing, and the pressure is still increasing. At 09 UTC, the wind speed starts to increase, while the pressure starts to decrease. The wind direction still turns anticlockwise. At 13 UTC, there is a sudden jump in wind speed, reaching maximum values of almost 35 m/s at Ulriken. These are the maximum values of wind speeds during the whole three day period. The wind direction suddenly veers clockwise, while the temperatures have an abrupt increase by approximately 5 °C. The pressure starts to increase around 15 UTC. Between 16 and 18 UTC, the wind direction remains steady. At around 17:40 UTC however, the wind direction starts to veer clockwise again, while the wind speed and temperature drops. The pressure shifts right before, and at 18 UTC, the pressure is increasing. At around 21 UTC, the wind speed at Strandafjellet reaches, and even exceeds the wind speeds at Ulriken.

The wind direction at this point is turning clockwise toward a more northerly direction.

On 26 Dec 00 UTC the wind speed and temperature is still decreasing, while the pressure increases and the wind direction veers anticlockwise. At 08 UTC, the wind speed starts to increase again, but jumps to even higher values at 12 UTC. The temperature increases rapidly, and the pressure decreases. The wind direction again turns clockwise. At 21 UTC, the pressure shifts to increase, and the wind speed and temperature drops, after a steady, warm period.

7.3 Discussion

With the theory in chapter 2.2 in mind, it is possible to determine when the different fronts pass Bergen. As a warm front passes a location, the temperature and wind speed will increase, the pressure will decrease, and the wind direction will veer clockwise. This is the case for 24 Nov 18 UTC, 26 Nov 13 UTC, 25 Dec 13 UTC and 26 Dec 08 UTC. This also fits with the synoptic charts in figure C.1(c) (see the appendix) for 24 Nov 18 UTC, and figure C.2(f) (see the appendix) for 25 Dec 13 UTC. For 24 Dec, the time series in figure 7.4 indicate a warm front passing Bergen already around 09 UTC. Considering the synoptic chart C.2(b) (see the appendix), it shows that the warm front hits Bergen around 13 UTC. The indications of a warm front hitting Bergen at 09 UTC can rather be explained as a warm front getting close. The synoptic charts of 26 Nov 18 UTC and 26 Dec 12 UTC are not shown, but they respectively reveal Bergen close to the occluded front in the warm sector and Bergen directly under a warm front. The best estimates for the warm fronts passing Bergen are shown in figures 7.2 and 7.4 as red vertical lines.

From the theory, the highest wind speeds are expected to occur in the warm sector, close to the center of the cyclone. This fits well with the observations. The highest wind speeds are found after the warm front has passed, as seen in figures 7.2 and 7.4. The storms Berit and Dagmar give the highest wind speeds during the three day periods, respectively the peaks around 25 Nov 00 UTC and 25 Dec 12 UTC. Comparing these results with the synoptic charts in figure 7.1(b) for Berit, and 7.3(b) for Dagmar, Bergen is located close to the occluded front in the warm sector. This also holds for the other peaks in wind speed, described above. This can be seen in figure C.2(c) (see the appendix) for 24 Dec 18 UTC, and is also valid for the synoptic charts for 26 Nov 18 UTC and 26 Dec 18 UTC (not shown).

When a cold front is passing, the pressure is expected to increase due to advection of cold and dense air, while the temperature will fall. The passage of a cold front is often associated with strong wind gusts before the average wind speed decreases. The

wind direction will veer clockwise. This is the case for 25 Nov 04 UTC, 24 Dec 21:30 UTC, 25 Dec 17:40 UTC, and 26 Dec 21 UTC. Cold fronts are marked in figures 7.2 and 7.4 as blue, vertical lines. The respective times when cold fronts pass Bergen fits well with the synoptic charts.

Regarding the high wind speeds at Strandafjellet exceeding the wind speeds at Ulriken, on 25 Nov after 18 UTC, and on 25 Dec around 21 UTC, the wind speed ratio (WSR) between Strandafjellet and Ulriken has to be considered. As discussed in chapter 6.2, the WSR increases when the wind veers to a more southerly direction, and increases even more if the wind veers to a more northerly direction. The latter is the case for the situations on 25 Nov and on 25 Dec as the wind turns to northwesterly. As discussed in chapter 6.2, the high WSR for northwesterly winds are put in connection with a blockage of NW flow at the mountains in southern Norway during high atmospheric stability, giving low wind speeds aloft and at the ground level, or even higher surface wind speeds in an unstable atmosphere, giving an even higher WSR. The latter is most likely the case for the high WSR at Strandafjellet during the storms, as there will probably be a neutral stratification during these storms. For more details about the discussion of high WSRs, see chapter 6.2.

A clear result in this case study, is the difference in wind speed between Ulriken and Løvstakken. The height difference between these two stations is only 133 meters, while the wind speed difference is about 10 m/s. This is a much bigger difference in wind speed compared to the other stations with the corresponding height difference. The high wind speeds at the Ulriken station compared to Løvstakken is most likely a result of a local speed up effect of the wind at Ulriken (Harstveit, 2006) (see chapter 6.2 for more details). This could explain the large wind speed difference between Ulriken and Løvstakken, and also the sudden speed up at Ulriken on 25 Nov 00 UTC, while the wind at Løvstakken has a steady increase.

Especially Florida shows a clear channeling effect of the wind. The wind at Nordnes also indicates channeling, but not to the same extent as at Florida. On 24 Nov 18 UTC, the wind at Florida and Nordnes has a southeasterly direction, following the direction of the Bergen valley, while the other stations has wind coming from S-SW. A general channeling effect is described at Florida by Utaaker (1995) and Jonassen et al. (2012a), and is also discussed in chapter 6.2. For specifically southwesterly winds, Jonassen et al. (2012b) did a study of the wind in the Bergen area. Two southwesterly windstorms were studied, where one of them was the storm Dagmar. Results showed that the wind direction at Florida deviated from the other stations in southwesterly winds, and that the flow aligned with the valley. However, after 25 Dec 18 UTC, all stations had westerly winds, except Haukeland which had southwesterly wind.

Jonassen et al. (2012b) described the deviation at Haukeland as a result of low wind speeds at Haukeland. However, having the wind rose for Haukeland in mind (Fig. 6.3), a possible explanation can also be an own channeling of the wind at Haukeland following the direction of Isdalen (see the figures 4.7(b) and B.1 (appendix)). This channeling effect is discussed in chapter 6.

As mentioned, the wind speed at the stations closer to sea level is much lower than at the higher located stations. One of the reasons for this can be that there are higher friction at the stations closest to sea level, Haukeland and Florida, than at the higher elevated stations. Harstveit (2006) noted that Florida was located in an area with considerable roughness, compared to stations located at a more open landscape or on top of mountains. However, the wind speed can also be reduced by blocking and wake effects from nearby mountains. Jonassen et al. (2012b) studied the effect of blocking and sheltering of different areas inside the city of Bergen during southwesterly windstorms (including the storm Dagmar). By removing the Løvstakken massif, the Fløyen massif and both massifs from the model topography in numerical simulations, the contribution of each massif to the shelter effect was investigated. The results showed that the sheltering of Bergen seems to be caused by a combination of a downstream wake of the Løvstakken massif, and an upstream blocking of the Fløyen massif. The simulations indicate that the combined effect is close to the sum of them. However, there are spatial differences within the Bergen valley. The effect of each massif is greatest close to the corresponding massif, meaning that the southwestern part of Bergen is mainly affected by the wake of Løvstakken, and the northeastern part of Bergen is mainly affected by the blocking of the Fløyen massif. The northern part of Bergen, including Nordnes, is less affected by surrounding mountains. Florida is affected by both the wake and blocking effect, but the blocking effect of the Fløyen massif is somewhat stronger than the wake effect. If the wind comes from W, such as on 25 Dec after 18 UTC in this study, the location of the area affected by the Fløyen massif shifts farther northward, and the one affected by the Løvstakken massif shifts farther southward (Jonassen et al., 2012b). With these results in mind, the low wind speeds at Haukeland are due to the blocking of the Fløyen massif, and the low wind speeds at Florida are due to both blocking of the Fløyen massif and the wake effect of Løvstakken. According to the results in Jonassen et al. (2012b), the wind at Ulriksbakken can also be reduced due to the blocking effect of the Fløyen massif.

7.4 Conclusions

The highest wind speeds during the storms Berit and Dagmar occur when Bergen is located in the warm sector of the system. The wind speed at Ulriken is much higher than at the other stations, most likely due to a local speed up effect. When the wind

speed at Ulriken and Løvstakken decreases, the wind speed at some of the other stations increases, and even exceeds the values at Ulriken and Løvstakken. This happens when the wind shifts northward, and corresponds to the results in chapter 6. The wind closer to the ground in the Bergen valley is channeled by the shape and geographical orientation of the valley. This is especially clear at Florida, but also at Nordnes in some cases. The results from numerical simulations in a recent study suggest that the topography also causes a wake effect downstream the Løvstakken massif, and a blocking effect of the Fløyen massif. The wind speed at Florida is affected by both, but the strongest effect is the blocking of the Fløyen massif. The wind speed at Haukeland is mainly affected by the blocking of the Fløyen massif. Ulriksbakken is also located within this same area. The wind speed at Nordnes however, is less affected by the topography.

Chapter 8

Case study - Sea breeze

In this chapter a period of two days, with one day showing a clear land-sea breeze circulation and the other characterized by stronger synoptic winds, is investigated. Therm-ally driven circulations typically occur under rather calm fair weather conditions with weak synoptic winds, and are a major influencing factor on air and pollution transport. This period has been simulated using the WRF model, for a comparison with the observations. The aim is to investigate the flow conditions in the Bergen valley during the land-sea breeze circulation. The WRF model is also tested, to see if it manages to separate the land-sea breeze circulation from the synoptic flow the second day. The period of interest is 23 August 2011 00 UTC to 25 Aug 2011 00 UTC, where the land-sea breeze circulation occurs on 23 Aug and the stronger synoptic flow on 24 Aug.

Time series of the seven AWSs are evaluated to describe the real situation in the Bergen valley. Time series of the numerical simulations for the same seven locations as the AWSs are then compared to the observational time series. Finally, horizontal cross sections of the sea breeze from the simulations are presented to visualize the strength and extension of the phenomenon.

8.1 Synoptic situation

The complete synoptic development of the period 23 Aug 2011 00 UTC to 25 Aug 2011 00 UTC is shown in figures D.1(a)-(e) in the appendix. The maps for 23 Aug 00 UTC and 24 Aug 12 UTC are shown in figure 8.1.

On 23 Aug 2011, an extended high pressure system is located over Norway and the North Sea, with a core of around 1020 hPa (Fig. 8.1(a) and D.1(a) in the appendix). Weak low pressure systems are located in the northern part of Norway, S of Iceland, and S of Great Britain. The pressure gradient is small, the wind is weak and a synoptic wind direction can therefore not easily be defined. At 12 UTC, the high pressure sys-

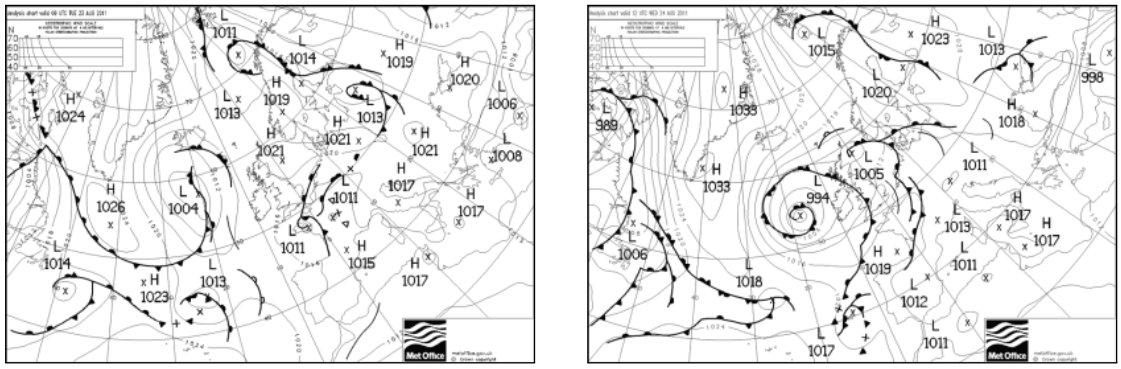

(a) 23 Aug 2011 00 UTC (b) 24 Aug 2011 12 UTC

Figure 8.1: *The synoptic situation during the sea breeze 23 Aug 2011 and during the stronger synoptic wind 24 Aug 2011 (Source: UK Met Office).*

tem is moving eastward, while the low pressure system south of Iceland is deepening from a core pressure of 1004 hPa to 999 hPa (Fig. D.1(b) in the appendix). Some low pressure systems are slowly moving toward Norway from SE. There is still no clear wind direction over southern Norway, and the synoptic wind speed is still expected to be low. At 24 Aug 00 UTC, the high pressure system, now with a core pressure of 1024 hPa, is located in the middle of Norway (Fig. D.1(c)). The low pressure system moving in from SE is closer to Norway, with its front directly south of Norway. The synoptic wind direction in the Bergen area is expected to be from S-E, and an increase in wind speed is expected. At 12 UTC, the high pressure over Norway has been replaced with a low pressure, and the low pressure south of Norway continues to move in from S (Fig. 8.1(b) and D.1(d) in the appendix). The wind speed in the Bergen area is expected to increase even more. At 25 Aug 00 UTC, the occluded front of the low pressure system is located directly over the Bergen area (Fig D.1(e) in the appendix). The wind direction is expected to veer from E-SE direction to a more southerly component as the front is approaching the Bergen area.

8.2 Results

Observational time series

The observational results are shown in figure 8.2 in form of time series. The figure shows the development of wind speed, wind direction and temperature for the seven AWSs together with the radiation balance measured at Florida. For the longwave (LW) radiation, the balance is measured directly, for shortwave (SW) radiation, it has to be estimated as only the incoming SW radiation is measured. The outgoing SW is calculated by multiplying the incoming SW radiation by the albedo, here assumed to

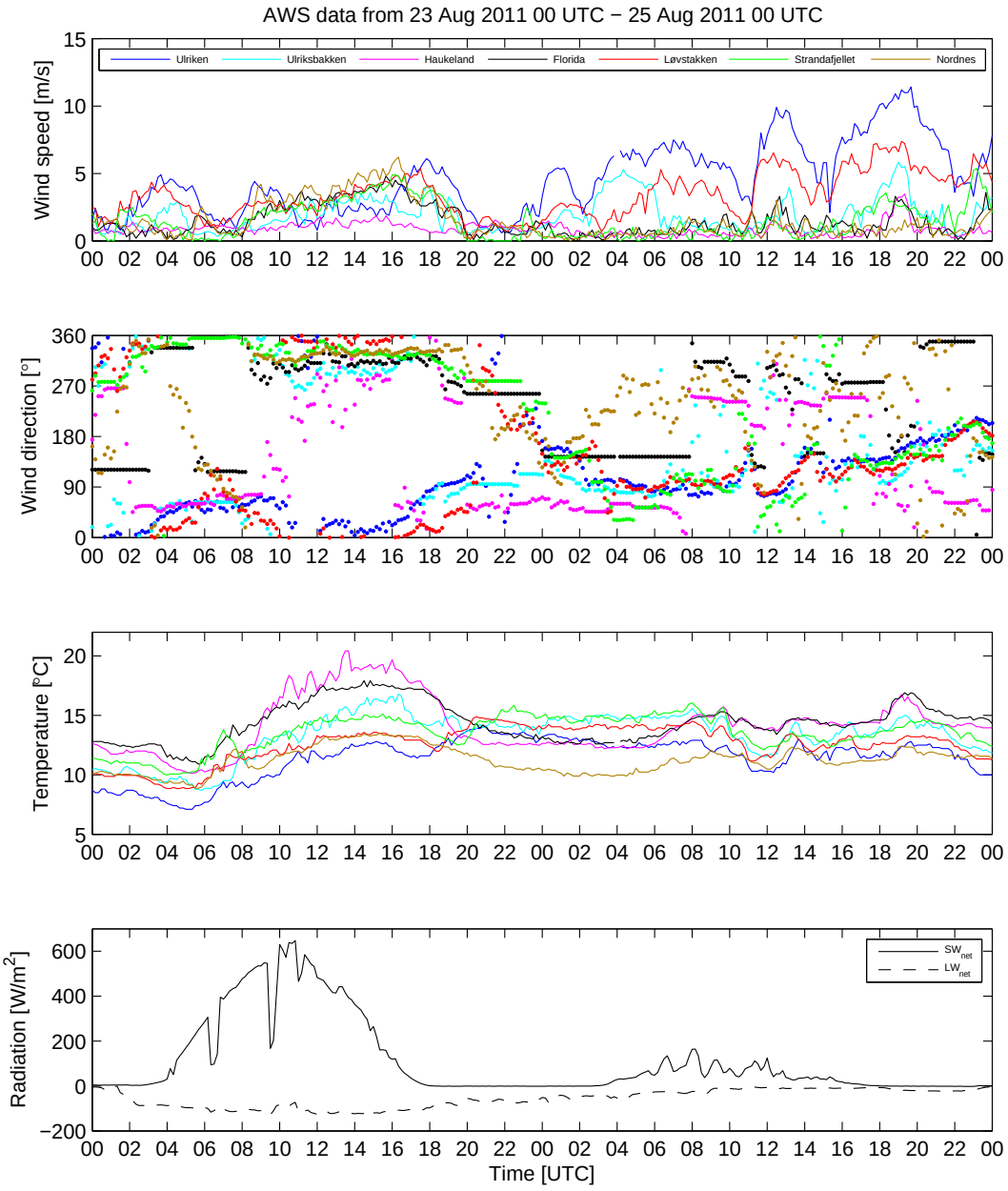

Figure 8.2: *AWS time series for 23 Aug 2011 00 UTC to 25 Aug 2011 00 UTC.*

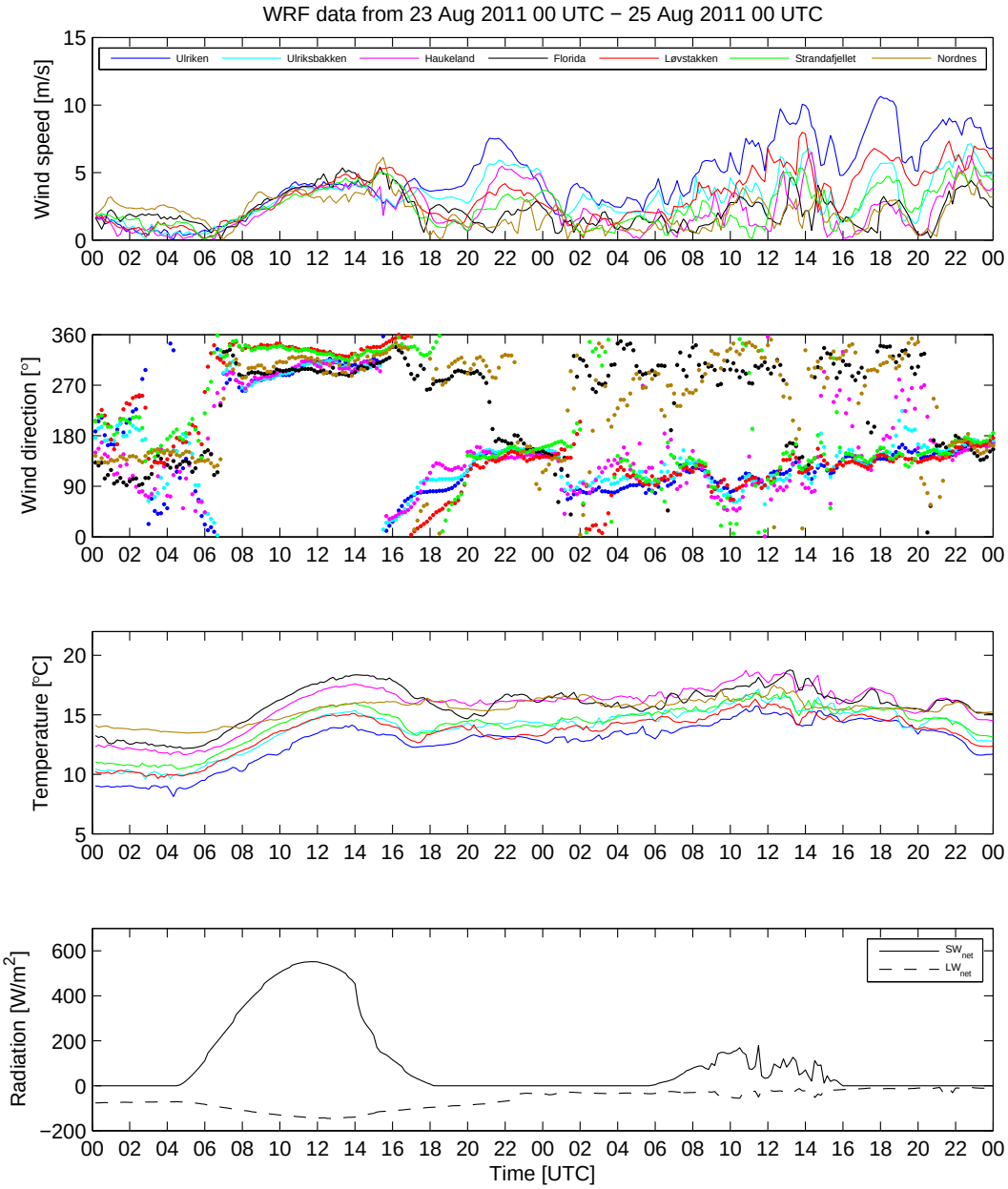

Figure 8.3: *Simulated time series for 23 Aug 2011 00 UTC to 25 Aug 2011 00 UTC for the same location as the seven AWSs.*

be 0.15 [1]. The net radiation is determined by subtracting the outgoing SW radiation from the incoming SW radiation. The sum of net LW and SW radiation shows when the surface is cooled or heated, where downward radiation is defined as positive. The surface is heated when the net SW radiation is higher than the net LW radiation.

This case study consists of two days with different flow conditions. The land-sea breeze circulation dominates during 23 Aug, while synoptic wind dominates on 24 Aug. This is also quite evident in figure 8.2 where all observed parameters reveal different regimes for the two days. For 23 Aug, the wind speeds vary between 0 and 6 m/s for all stations, increasing throughout the day, before they calm down around sunset. In contrast, for 24 Aug, the wind speed at the highest elevated stations (Ulriken, Løvstakken and Ulriksbakken) is higher, varying between 3 and 11 m/s, while the wind speed at the lower elevated stations is very low. The wind speeds at these stations are in fact lower than during 23 Aug. The main wind direction between the two days is also quite different. For 23 Aug, the main wind direction is from NNE for Ulriken and Løvstakken, while it is from NNW for the other stations. For 24 Aug, the main wind direction is from E. The temperatures also have completely different patterns for the two days. They show a steady increase from 06 UTC to 16 UTC on 23 Aug, before they decreases to around 20 UTC and remain steady until 24 Aug 08 UTC, where they start to fluctuate a bit more, without a clear pattern. The temperature distribution on 23 Aug follows the tendency of the solar radiation throughout the day. From around 23 Aug 22 UTC, there is a steady cooling of the surface for the same period as the temperatures remain steady. After 24 Aug 08 UTC, there is only little incoming SW radiation. The pattern of surface heating is absent on 24 Aug.

Looking at figure 8.2 in more detail, there are some local differences. At the beginning of the period, the wind speed at all stations except Ulriken, Løvstakken and Ulriksbakken is very low. The wind speed at Ulriken and Løvstakken reaches almost 5 m/s. Between 06 UTC and 08 UTC, the wind speeds however, calm down. At 08 UTC, there is a sudden jump in wind speed at all stations except Haukeland. The jumps at Nordnes and Ulriken are especially pronounced. After that, there is a steady increase in wind speed throughout the day, where the highest wind speeds are found at Nordnes. The lowest wind speeds are registered at the Haukeland station, and the variation in wind speed at this station is much less compared the other stations. At around 16 UTC, the wind speed reaches a maximum of 6 m/s at Nordnes, and approximately between 2 and 5 m/s for the other stations. After that, the wind speeds at all

[1] Arya (2001)[p.23] states that built-up urban surfaces (like roofs, streets and highways) have low surface albedos between 0.1 and 0.2. In addition, Hartmann (1994)[p.88] states that short green vegetation have albedos ranging between 0.1 and 0.2, and concrete and pavement have albedos between 0.15 and 0.35. Considering these albedos, 0.15 give a reasonable value for the Bergen valley, as it consists of a combination between the aforementioned surface types.

stations decrease, and remains steady at low wind speeds for a few hours. On 24 Aug 00 UTC, the wind speed at Ulriken, Løvstakken and Ulriksbakken increases, while it remains below 1 m/s at the other stations. After that, several periods with increasing wind speeds followed by drops in wind speeds a few hours later at these three stations occur. The wind speeds at the other stations remain calm the entire period, except for a few incidents at 12 UTC, 19 UTC and finally 22 UTC on 24 Aug. For the last incident, the wind speed at Strandafjellet just exceeds the wind speed at Ulriken. The maximum wind speed during the entire period is at Ulriken on 24 Aug 19 UTC with wind speeds of 11 m/s.

The only stations with a clearly defined wind direction in the beginning of the period, are Ulriken and Løvstakken, where the wind comes from NNE. At Haukeland, the wind is coming from NE, but the wind speeds are very low. Wind at the other stations is very low before 08 UTC. After 08 UTC, the wind directions are more pronounced. The wind at Ulriken still comes from NNE, while the wind at the other stations comes from NNW. The wind direction at Haukeland varies more than at the other stations. After approximately 18 UTC, the wind starts to veer toward a more easterly wind direction, and after around 24 Aug 00 UTC, all stations except Haukeland, Florida and Nordnes have wind coming from E. The wind at Florida and Nordnes is coming from NNW, while the wind at Haukeland comes from NE. The synoptic wind after this remains easterly (seen from Ulriken and Løvstakken, and some at Ulriksbakken), while the wind direction at the other stations are more fluctuating due to very low wind speeds. After around 20 UTC at the end of the entire period, the wind veers to a more southerly direction.

Both before and during the sea breeze, the temperatures are mainly decreasing with height, except that the temperature at Nordnes has lower values than usually, with values approximately the same as at Løvstakken. The highest temperatures are registered at Haukeland, reaching approximately 20 °C at the most, and the lowest at Ulriken, where the maximum temperature reaches around 12 °C. The temperature at Nordnes does not exceed 13 °C. From around 23 Aug 19 UTC, after the temperatures have decreased, the temperature at Ulriken, Løvstakken and Strandafjellet increases, while the temperature at Haukeland, Florida and Nordnes decreases. The temperature at Ulriksbakken mainly remains unchanged. As the temperatures remain steady from around 22 UTC, the lowest temperature is at Nordnes (10 °C), then Haukeland, Florida and Ulriken (12 °C), followed by Løvstakken (13 °C) and Ulriksbakken and Strandafjellet (14 °C). After 24 Aug 10 UTC, the temperatures decrease with height, except that the temperature at Nordnes shares the lowest temperatures with Ulriken.

The solar radiation shows a clear day with only a few clouds on 23 Aug, while the

24 Aug is characterized by heavy clouds. The radiation balance is negative during the night, resulting in a cooling of the surface.

Simulated time series

The simulated time series for the same seven locations as the AWSs for the period from 23 Aug 2011 00 UTC to 25 Aug 2011 00 UTC are shown in figure 8.3. The WRF model output has been interpolated to fit the 10 minute intervals of the observations. The quality of the simulations compared to the observations for each station can be seen in detail in figures D.2 - D.8 in the appendix. The last subplot containing radiation has a different approach. The net SW radiation balance and the incoming LW radiation was directly calculated in the WRF model, however the LW radiation balance had to be calculated manually using the Stefan-Boltzmann's law, where the outgoing LW radiation was calculated by multiplying the Stefan-Boltzmann constant with the fourth power of the skin temperature of the surface (Hartmann, 1994), calculated by the WRF model.

The trends in the simulated time series look generally very similar to the observations, except that the time series are more smoothed out in the simulations (Fig. 8.3). The wind speed over the two days show one day with a steady increase in wind speed, before a decrease in the evening, followed by a day with stronger synoptic wind speeds. The main wind direction for these two days is from NNW for 23 Aug and from E for 24 Aug, as for the observations. The temperatures increase steadily during the day on 23 Aug, and decrease toward the night. During the night, the temperatures remain steady, and start to vary more the following day, the 24 Aug, as for the observations. The incoming solar radiation on 23 Aug shows a clear sky, with a following day with less incoming solar radiation, also similar to the observations.

The local differences in figure 8.3 are, as mentioned less than for the observations. A spin-up time of 6 hours in the WRF model is considered, so the time series are evaluated from 23 Aug 06 UTC. The decrease in wind speed around 06 UTC is also found for the simulations, and the wind speeds start to increase around 07 UTC (in the observations the increase starts at 08 UTC). A sudden jump in wind speed at 08 UTC for the Nordnes station is also evident in the simulations, as for the observations. The wind speeds ranges between 3 and 6 m/s during the sea breeze. In the beginning of the increase, the highest wind speeds are at the Nordnes station, which is the same as for the observations. However, later in the increase, the lowest wind speed is at the Nordnes station, when it is observed to be the highest. The wind speed at especially the Haukeland station is overestimated compared to the observations. Otherwise, the details that separate the different stations from each other are very small. The decrease in wind speed starts around 16 UTC for the simulations, while it starts around 18 UTC for the observations. The model fails in simulating the following calm period

for a few hours before an increase in the wind speed. After that, the wind speed in the simulations is highly overestimated, especially for the lower elevated stations. However, the simulations show lower wind speeds for the lower elevated stations between approximately 24 Nov 02 UTC and 08 UTC, and for the last part of the period. The maximum wind speed during the entire period is at Ulriken on 24 Aug between 19 and 20 UTC, reaching approximately 10-11 m/s. In comparison, the maximum wind speed for the observations is also at Ulriken with values around 11 m/s on 24 Aug 19 UTC.

After the sea breeze has started, the wind direction at all stations are from NNW, which is mostly the same as in the observations, except that the wind at Ulriken and Løvstakken has a slightly more easterly component. After this, the wind direction in the simulations is very similar to the observations, except that the model does not pick up the local NE channeling of the wind at Haukeland. The model show a veering from a northerly to easterly wind direction, which veers to more southerly directions toward the end of the period, as for the observations. The local channeling of Nordnes and Florida with wind coming from NNW is also evident, as for the observations.

The temperature distribution for the entire period shows the same results as for the observations, with two exceptions. While the temperature at Nordnes was generally very low and directly comparable to the temperature at Løvstakken in the observations, the temperatures at Nordnes in the simulations seem to be overestimated through the entire period. As the heating occurs throughout the day, the warmest temperatures in the simulations are found at Florida, Haukeland and then Nordnes, and then with a decreasing order with height accordingly. This temperature distribution remains the same for the rest of the entire period, although followed by a steady period during the night, and a bit more varied period the next day, as for the observations. The second main difference between the temperature distribution for the observations and the simulations, is the temperature during the night. In the observations, the temperatures show an inversion by an increase with height between approximately 23 Aug 22 UTC and 24 Aug 09 UTC. This is not found in the simulations.

The simulated radiation is very similar to the observations, with a clear sky the first day, and less incoming solar radiation the second day. The radiation balance shows slightly less cooling during the night than in the observations.

Simulated cross sections

Horizontal cross sections of the model simulations of two different levels, 850 hPa (Fig. 8.4(a)-(b)) and 10 m over the terrain (Fig. 8.4(c)-(d)), allow for a detailed study of the development and extension of the sea breeze circulation on 23 Aug.

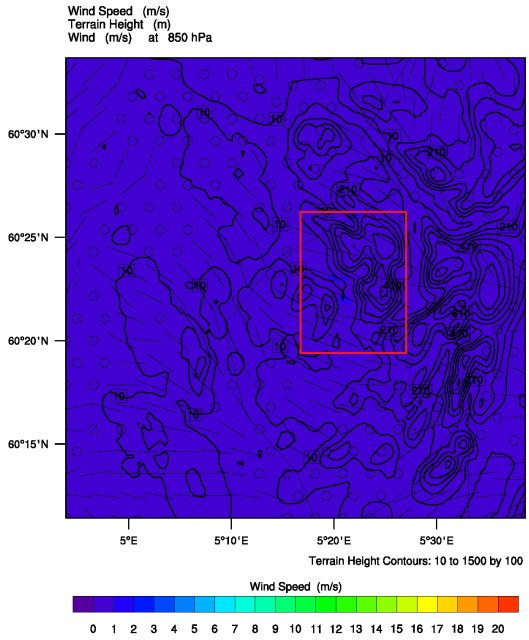

(a) WS 850 hPa - 23 Aug 2011 07 UTC

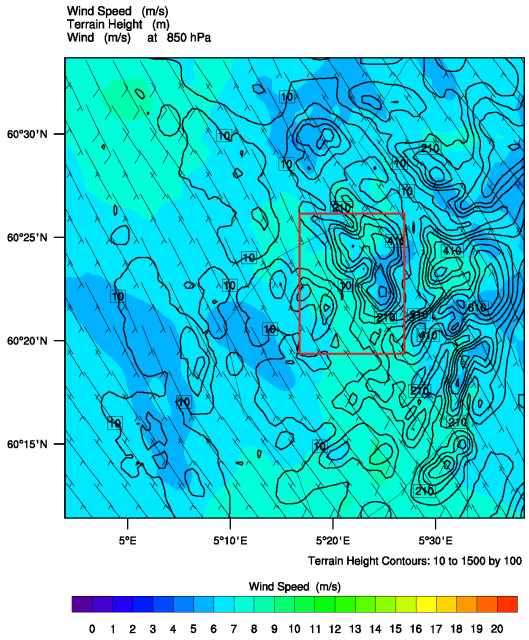

(b) WS 850 hPa - 23 Aug 2011 14 UTC

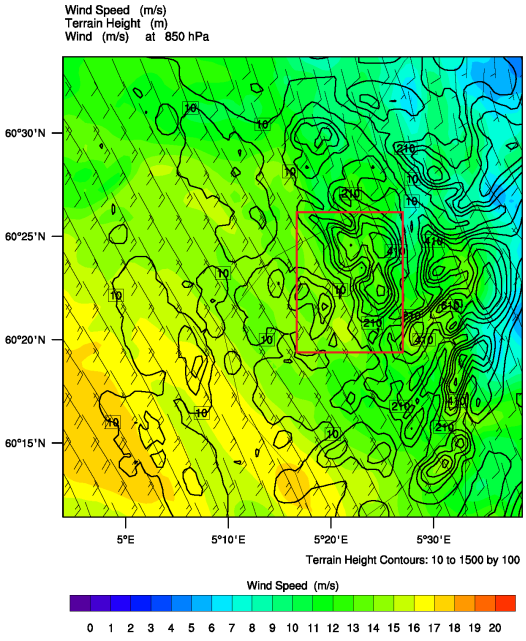

(c) WS 10 m - 24 Aug 2011 12 UTC

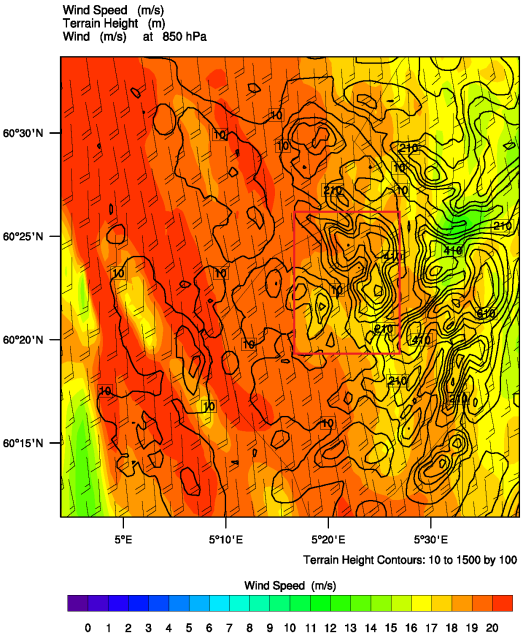

(d) WS 10 m - 24 Aug 2011 20 UTC

Figure 8.4: *The simulated synoptic wind speed at 850 hPa shown before the sea breeze has developed (a), at maximum sea breeze (b), after the stronger synoptic wind has started (c), and at the end of the period (d). The location of the Bergen valley is framed by the red box, with Løvstakken to the left and Ulriken to the right.*

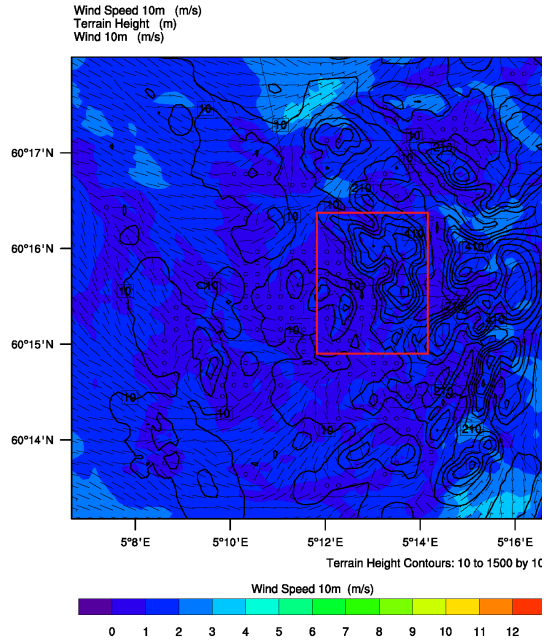

(a) 23 Aug 2011 07 UTC

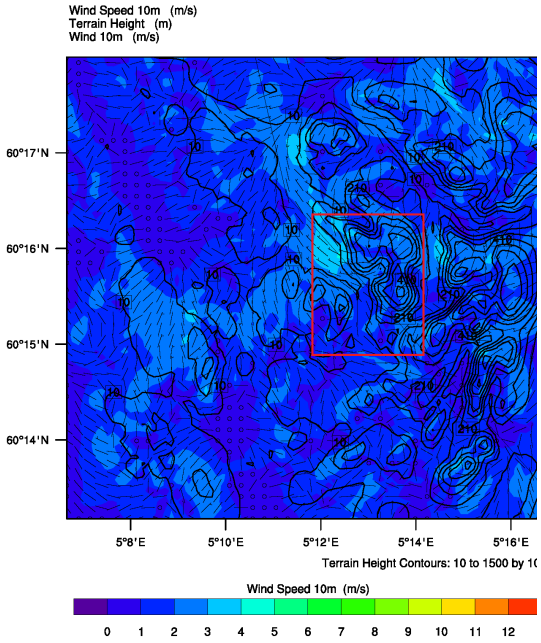

(b) 23 Aug 2011 09 UTC

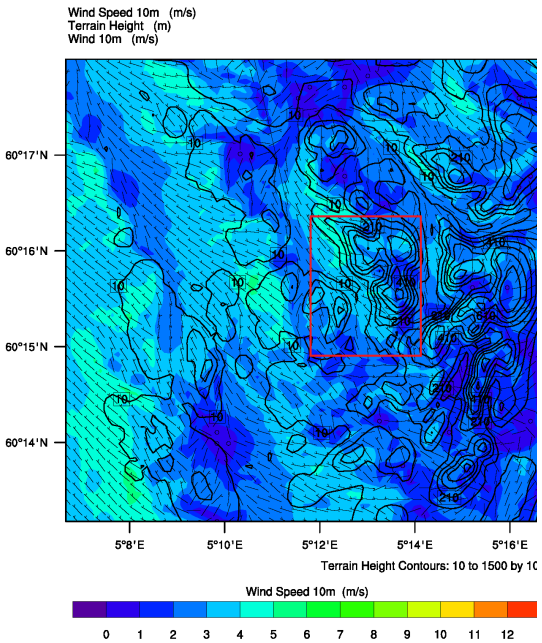

(c) 23 Aug 2011 11 UTC

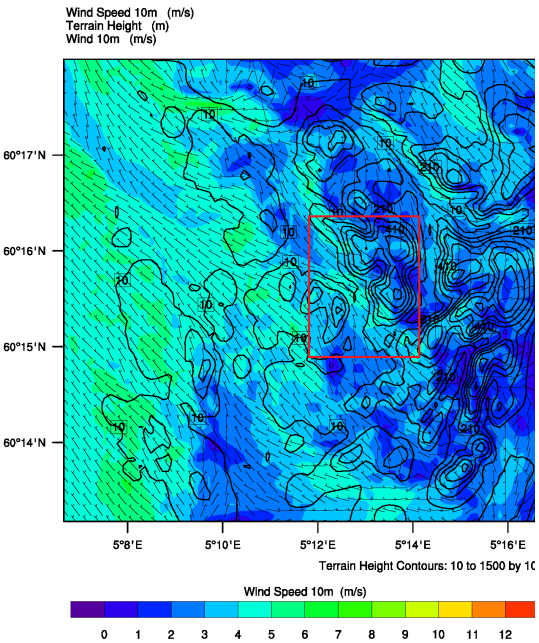

(d) 23 Aug 2011 12 UTC

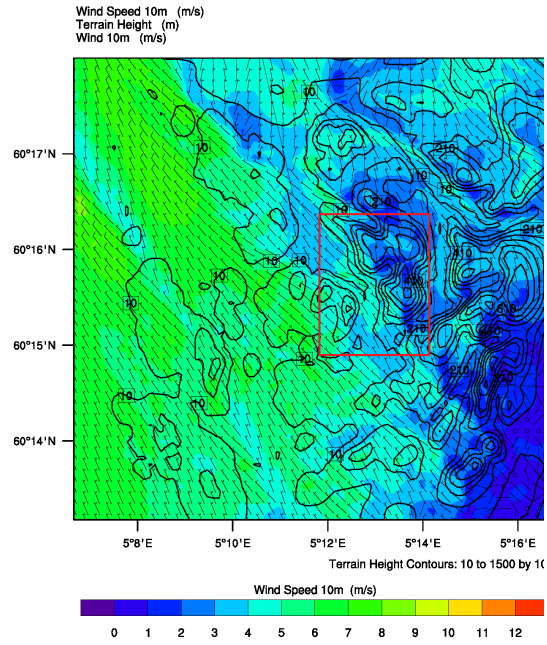

(e) 23 Aug 2011 14 UTC

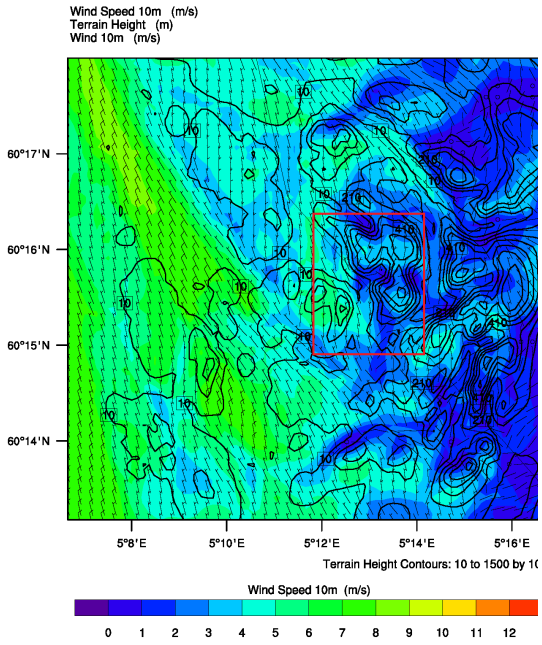

(f) 23 Aug 2011 16 UTC

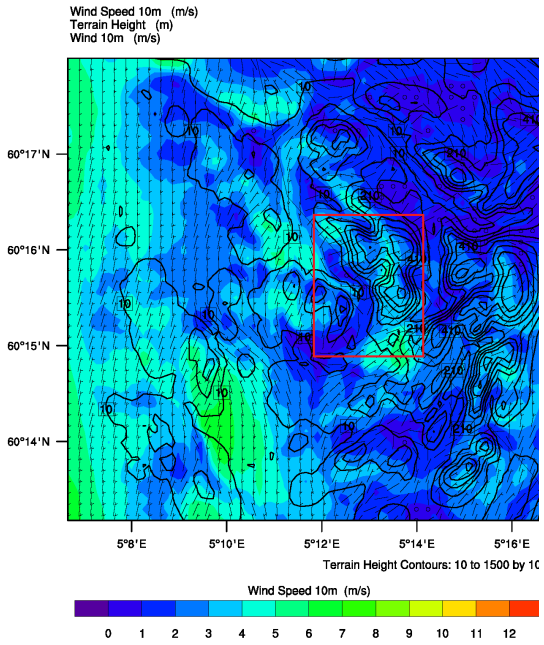

(g) 23 Aug 2011 18 UTC

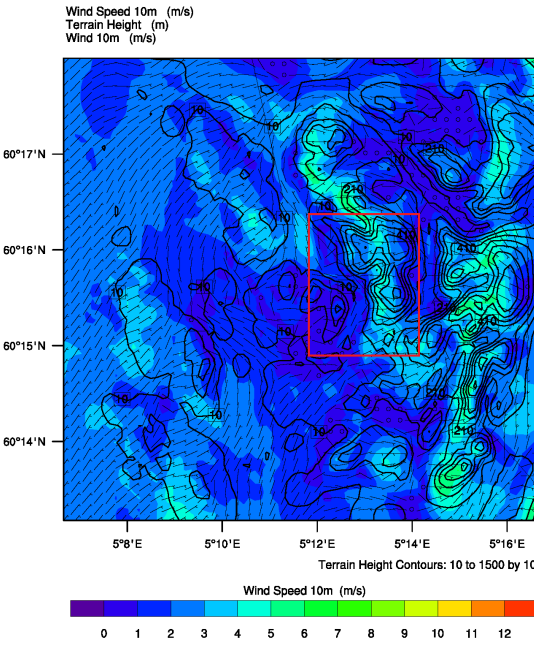

(h) 23 Aug 2011 20 UTC

Figure 8.5: *The development of the simulated sea breeze on 23 Aug 2011. The wind speed [m/s] is shaded and shown in wind barbs. The location of the Bergen valley is framed by the red box.*

The low synoptic wind before the sea breeze starts is shown in figure 8.4(a) for 23 Aug 07 UTC. The surface situation is shown in figure 8.5(a), with calm conditions in the Bergen valley, and weak easterly wind over Ulriken. At 09 UTC the sea breeze has started to develop (Fig. 8.5(b)). 4 m/s wind coming from Eidsvågneset to the north channels toward the Bergen valley. At this point, the sea breeze has approximately reached the Nordnes station. The sea breeze travels further inland, and by 11 UTC it has filled most of the Bergen valley, even reaching Strandafjellet, Løvstakken and Ulriksbakken (Fig. 8.5(c)). The sea breeze has a wind speed of 4 m/s in the Begen valley, but starts to reach 5 m/s just outside Nordnes. The sea breeze is also starting to show west of Bergen, as it comes in from the sea from NW. By 12 UTC, the sea breeze coming in from NW has intensified, now reaching 4 to 6 m/s (Fig. 8.5(d)). These winds seem blocked by the topography of Askøy and west of Løvstakken. The sea breeze in the Bergen valley has also increased in strength up to 5 m/s in areas close to Nordnes and Florida. The sea breeze is still evident over Strandafjellet and Løvstakken, but is not reaching the top of Ulriken. The sea breeze reaches its maximum extent at 14 UTC (Fig. 8.5(e)). The wind speed in the Bergen valley is now 6 m/s, even at the top of Løvstakken, but decreases up along the slope of Ulriken. The wind coming in from NW has also increased in strength, reaching 7-8 m/s. A wake SE of Askøy and SE of Løvstakken is evident, with wind speeds of 4 m/s. The sea breeze affecting the Bergen valley still comes from outside Eidsvågneset, and channels through the Bergen valley from NW. The wake downstream Askøy and Løvstakken is still present. The synoptic wind at 850 hPa at 14 UTC is around 7 m/s coming from SSE (Fig. 8.4(b)). At 16 UTC, the sea breeze has started to decrease, and Haukeland is out of the area affected by the sea breeze (Fig. 8.5(f)). The wind speed at Nordnes, Strandafjellet and Løvstakken lies between 5 and 6 m/s, while the wind speed at Florida is below 4 m/s. The wind coming from NW in the west is still strong, but reaches less inland than at 14 UTC. A small region over the ocean has wind speed reaching 10 m/s. By 18 UTC the sea breeze has withdrawn from the Bergen valley, but is still evident over the ocean (Fig. 8.5(g)). Wind from NE and E starts to develop in some areas, for example over Ulriken. At 20 UTC, the wind in the Bergen valley is absent or very low (Fig. 8.5(h)). Offshore wind ranging between 1 and 6 m/s is present in some coastal areas such as Sotra, Askøy and Eidsvågneset. Winds from E are starting to develop.

8.3 Discussion

According to the theory described in chapter 2.5, ideal conditions for sea breeze are low synoptic wind speeds and clear skies during anticyclonic weather in the summer. Looking at the synoptic chart in figure 8.1(a), this seems to be the case for 23 Aug 2011. Jonassen et al. (2012a) found that the large-scale wind speed should not exceed 10 m/s to develop sea breeze in the Bergen valley. This requirement is fulfilled for

the simulated wind speeds at 850 hPa before and during the sea breeze. On 24 Aug 2011, the synoptic wind direction is expected to be from S-E, and veers toward a more southerly direction at the end of the period. The synoptic wind speed has increased. This is also the case for the simulations where the wind is from SE with 10-15 m/s on 24 Aug 12 UTC (Fig. 8.4(c), turning toward S and increasing to 19 m/s at 20 UTC (Fig. 8.4(d)).

The sea breeze starts with a jump in wind speed, especially at Nordnes, on 23 Aug 08 UTC in both the observations and the simulated time series. The time for the maximum wind speed during the sea breeze occur at 16 UTC for the simulated time series and the observations, while in the cross sections, the sea breeze reaches a maximum extension at 14 UTC. The sea breeze lasts until 20 UTC in the observations, and 18 UTC in the simulated time series. The incoming solar radiation lasts respectively until 20 UTC and 18 UTC for the observations and the simulations.

The wind speed during the sea breeze in the observations varies between 0 and 6 m/s, and the maximum wind speed during the sea breeze is found at Nordnes with 6 m/s at 16 UTC. The wind at Ulriken reaches the same maximum two hours later. The wind speeds during the simulated time series vary between 3 and 6 m/s, and here also, the maximum is at Nordnes at 16 UTC with wind speeds reaching 6 m/s. The wind speeds during the sea breeze are mainly below 5 m/s in the Bergen valley, with a maximum wind speed of 6 m/s at 14 UTC. At some locations, the wind speed is up to 6 m/s at 16 UTC, for instance at Nordnes, Strandafjellet and Løvstakken. According to the theory in chapter 2.5, typical wind speeds for sea breeze vary between 2 and 5 m/s, while the sea breeze front propagates with 5 to 7 m/s (Oke, 1987). Both values correspond well with the results of this study. It is also possible that the sea breeze in the Bergen valley is enhanced by valley wind (Ch. 2.4). The wind speed of the sea breeze coming in from NW will be discussed later.

The vertical extension of the sea breeze can be seen best from the horizontal cross sections in figure 8.5, but also for a more statistical point of view in the wind roses in chapter 6. Jonassen et al. (2012a) and Utaaker (1995) found that NW wind dominates locally during summer, which is also seen in the wind roses in this study. The northwesterly sea breeze is evident in the wind roses for Nordnes, Florida, Strandafjellet, Løvstakken and Ulriksbakken. At Haukeland, the sea breeze is channeled up Isdalen, giving the wind a southwesterly direction. Low wind speeds coming from W are also evident at Ulriken, which may indicate that the sea breeze enhances the anabatic flow. The wind at Ulriksbakken also has this westerly component. This indicates that in general, the sea breeze will at least reach the height of Strandafjellet and Løvstakken in the Bergen valley, and propagate up the slope of Ulriken. The amount of wind

coming from this sector at Ulriken is smaller than at Ulriksbakken, indicating that the sea breeze that most likely enhances the anabatic wind, will reach Ulriksbakken and in some cases the AWS at Ulriken. The simulated sea breeze shown in figure 8.5 shows that the sea breeze travels in and over Strandafjellet and Løvstakken with a speed up to 6 m/s. The sea breeze also reaches the location of the AWS at Ulriksbakken, and may reach the AWS at Ulriken, which is seen in the simulated time series (Fig. 8.3). The height of Løvstakken and Ulriken is respectively 472 m and 605 m in reality, and 335 m and 475 m for the simulations (Tab. 9.1). According to theory, a normal vertical extension of the sea breeze is between 100 and 500 m without the return flow (Oke, 1987). This corresponds well with the results in this study. Dyngeseth (1998) also simulated a sea breeze case during the summer in 1997 and found that the height was around 250 m, which is somewhat lower than the sea breeze in this study.

Dyngeseth (1998) found that the sea breeze in 1997 did not propagate further inland than Storetveit. Comparing with the results in this study, this also applies for the 6 m/s sea breeze at 14 UTC, which is only coming from outside Eidsvågneset, but the 4 m/s sea breeze reaches up to Fana. However, Dyngeseth (1998) did not capture the sea breeze coming in from NW, which probably enhances the sea breeze channeled through the Bergen valley, resulting in a sea breeze reaching farther south than Storetveit. However, the sea breeze does not reach the mountainous part SE of Fana, probably due to blocking of topography. Dyngeseth (1998) also found that the sea breeze coming in from Grimstadfjorden would cancel out the sea breeze in the Bergen valley at Storetveit. However, Dyngeseth (1998) did not account for the islands outside of Bergen, and thereby could not capture the strong sea breeze coming in from NW found in this study. The sea breeze over Grimstadfjorden in this study is a part of the sea breeze coming in from NW, which enhances the sea breeze in the Bergen valley, and not cancelling it out.

The strong sea breeze coming in from NW is stronger than normal propagation speed of sea breeze, with wind speeds of 7-8 m/s, and even up to 10 m/s in a small region over the ocean. This wind is not enhanced by the synoptic wind, since the synoptic wind is coming from SE (Fig. 8.4(b)). The scale of this sea breeze is larger than the sea breeze observed in the Bergen valley.

The two main differences in temperatures between the simulations and the observations are an overestimation of the temperature at Nordnes, and the lack of inversion during the night. The high temperatures at Nordnes may be due to higher sea surface temperature (SST) in the simulations compared to the reality. The SST is not measured in the observations, but the SST in the simulations shows a value of 14.7 °C, which is not unreasonable, but may be a bit high. Regarding the inversion during the night, figures

D.8 and D.5 in the appendix show that the temperature at both Nordnes and Florida are overestimated during the night. The WRF model's performance during inversions is tested and further discussed in chapter 9.

Regarding the surface wind direction, the simulations are generally quite similar to the observations. The model picks up the channeling of Florida and Nordnes, but not the local channeling of Isdalen. Dyngeseth (1998) did simulations with the MEMO model with 500 m resolution, which managed to pick up on this local channeling. Even though the MEMO model picked up the local channeling, it has its restrictions, for example not to consider the synoptic wind.

Dyngeseth (1998) found clear results of land breeze circulation. The land breeze is much weaker than the sea breeze, with typical wind speeds of 1-2 m/s (Oke, 1987). In this case study of 23 Aug 2011, the day with sea breeze was directly followed by a day with stronger synoptic wind. The night after the sea breeze situation was therefore not ideal for investigation of the land breeze. The simulations should rather be started at an earlier time, resulting in an earlier spin-up time, such that the land breeze could be investigated the night before the sea breeze. Another aspect not investigated in this study is the strength and height of the return flow.

8.4 Conclusions

23 Aug 2011 had ideal conditions for a development of sea breeze, with low synoptic wind during a clear day in the summer. The sea breeze reaches wind speeds up to 6 m/s, which corresponds well with the theory. The vertical extension of the sea breeze exceeds the height of Løvstakken, and barely reaches the Ulriken station, giving it a height of approximately 500-600 m. The numerical simulation of the sea breeze is quite accurate, which also reveals a strong sea breeze on either a larger scale or a sea breeze front hitting the west coast of Bergen with strength of around 7-8 m/s. Due to this front coming in from NW, the sea breeze propagates far inland. This front is not enhanced by synoptic wind, since the synoptic wind comes from SE.

The WRF model overestimates the temperature at Nordnes during the whole period, which may be put in connection to the SST. The model also overestimates the temperature at Florida, which may be the reason for the failure of simulating the inversion which followed the night after the sea breeze. Nevertheless, the WRF model shows good quality in the case study. The chosen simulation period has resulted in restrictions of the investigation of the land breeze. Details about the return flow also remain open for future investigation.

Chapter 9

Case study - Inversion

Inversions in the Bergen valley are frequently associated with high pollutant concentrations. An example of such a situation is investigated in the following case study by a detailed analysis of the observations at the seven AWSs and WRF model simulations.

The selected period for this case study is 10 Nov 2011 18 UTC to 12 Nov 2011 06 UTC, a period with a strong inversion in the Bergen valley. The temperatures above the boundary layer were relatively high (>10 °C), and no ice or snow was present during these days.

9.1 Synoptic situation

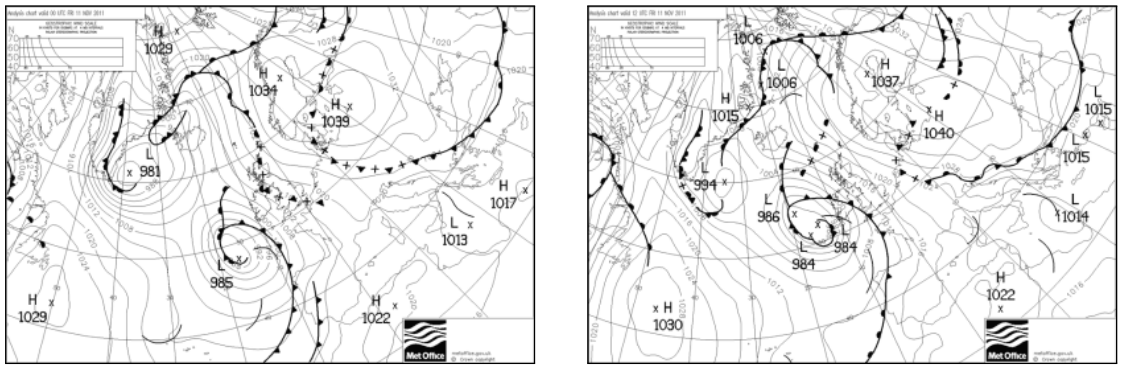

(a) 11 Nov 2011 00 UTC

(b) 11 Nov 2011 12 UTC

Figure 9.1: *The synoptic situation during the inversion 11 Nov 2011 (Source: UK Met Office).*

The full synoptic development during the inversion period between 10 Nov 2011 and 12 Nov 2011 is shown in figures E.1(a) - E.1(f) in the appendix, while the main day with inversion, 11 Nov 2011, is also presented in figure 9.1. The synoptic situation

during the overall period is dominated by an extended high pressure system, with its center located over Finland and the Baltics. The core pressure has a steady increase from 1034 hPa on 10 Nov 00 UTC to 1041 hPa on 12 Nov 12 UTC. On 10 Nov 00 UTC, the center of the high pressure is located over western Finland, and by 11 Nov 00 UTC, a second high pressure core with 1034 hPa develops over the middle of Norway. On 12 Nov 00 UTC, these two pressure systems joines into one system with a core pressure of 1040 hPa. The whole system propagates slowly eastward during the entire period. In addition, an occluded front propagates slowly toward the southwest coast of Norway, which is located over Great Britain on 12 Nov 00 UTC, and between Great Britain and the southwest coast of Norway on 12 Nov 12 UTC. Calm synoptic wind is expected from 10 Nov to 11 Nov, but an increase in wind speed can be expected due to densification of the isobars on 12 Nov. The main wind direction during the three day period is from SSE. The wind has a slightly more southerly component on 10 Nov than on 11 Nov, and a small shift toward a more westerly component in wind direction is expected as the occluded front gets close on 12 Nov.

9.2 Results

Observational time series

Figure 9.2 shows the observations from the seven AWSs from 11 Nov 2011 18 UTC to 12 Nov 06 UTC. The three first subplots show the wind speed, wind direction and temperature at the seven AWSs. The fourth subplot shows the temperature difference between Florida and Ulriken, which can give an indication of the occurrence and strength of the inversion. The more negative the value is, the stronger the inversion. The last subplot shows the shortwave (SW) and the longwave (LW) radiation balance at Florida. The procedure of calculating these radiation balances is described in chapter 8.2. The net LW and SW radiation show when the surface is cooled or heated, where downward radiation is defined as positive. The surface is heated when the net SW radiation is higher than the net LW radiation.

Figure 9.2 shows that the inversion in the Bergen valley starts to build up around 11 Nov 00 UTC, and lasts for approximately 29 hours until 12 Nov 05 UTC. The inversion top is generally somewhere between Strandafjellet and Ulriksbakken, at 300-400 m height. At some occasions, the inversion top reaches the height of Løvstakken, at approximately 470 m altitude. The wind speeds for all stations, except the mountain stations Ulriken and Løvstakken, are very low, and typically varying between 0 and 2 m/s. This also includes the stations at Strandafjellet and Ulriksbakken, indicating that they are also located within the inversion, where the weak wind inhibits downward mixing of momentum. The wind speed observations for Nordnes are missing for most of the period. At the low elevated stations with low wind speeds, the wind is

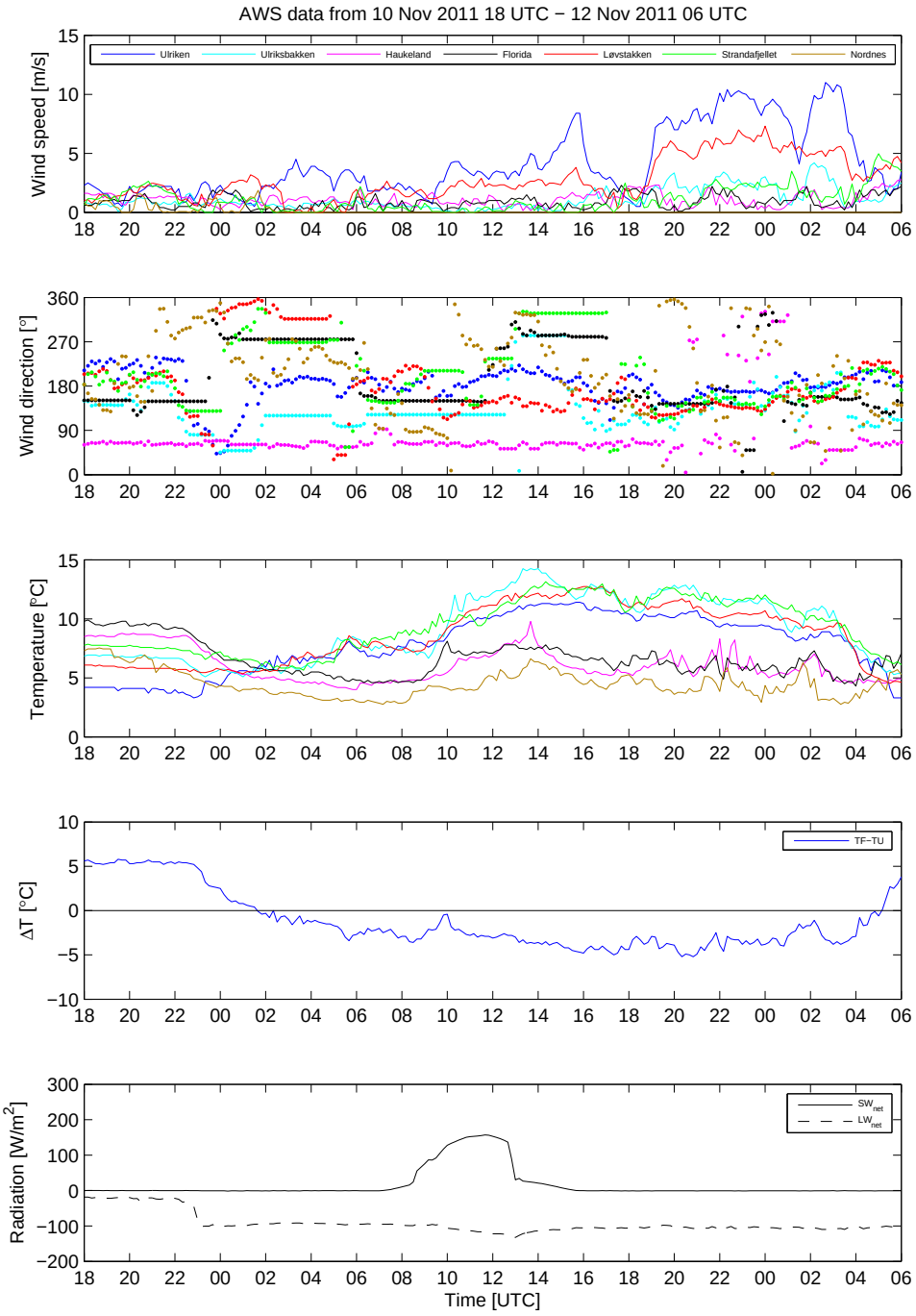

Figure 9.2: *AWS time series for 10 Nov 2011 18 UTC to 12 Nov 2011 06 UTC. The steep decline in SW radiation around 13 UTC is when the sun, seen from Florida, is disappearing behind the Løvstakken massif.*

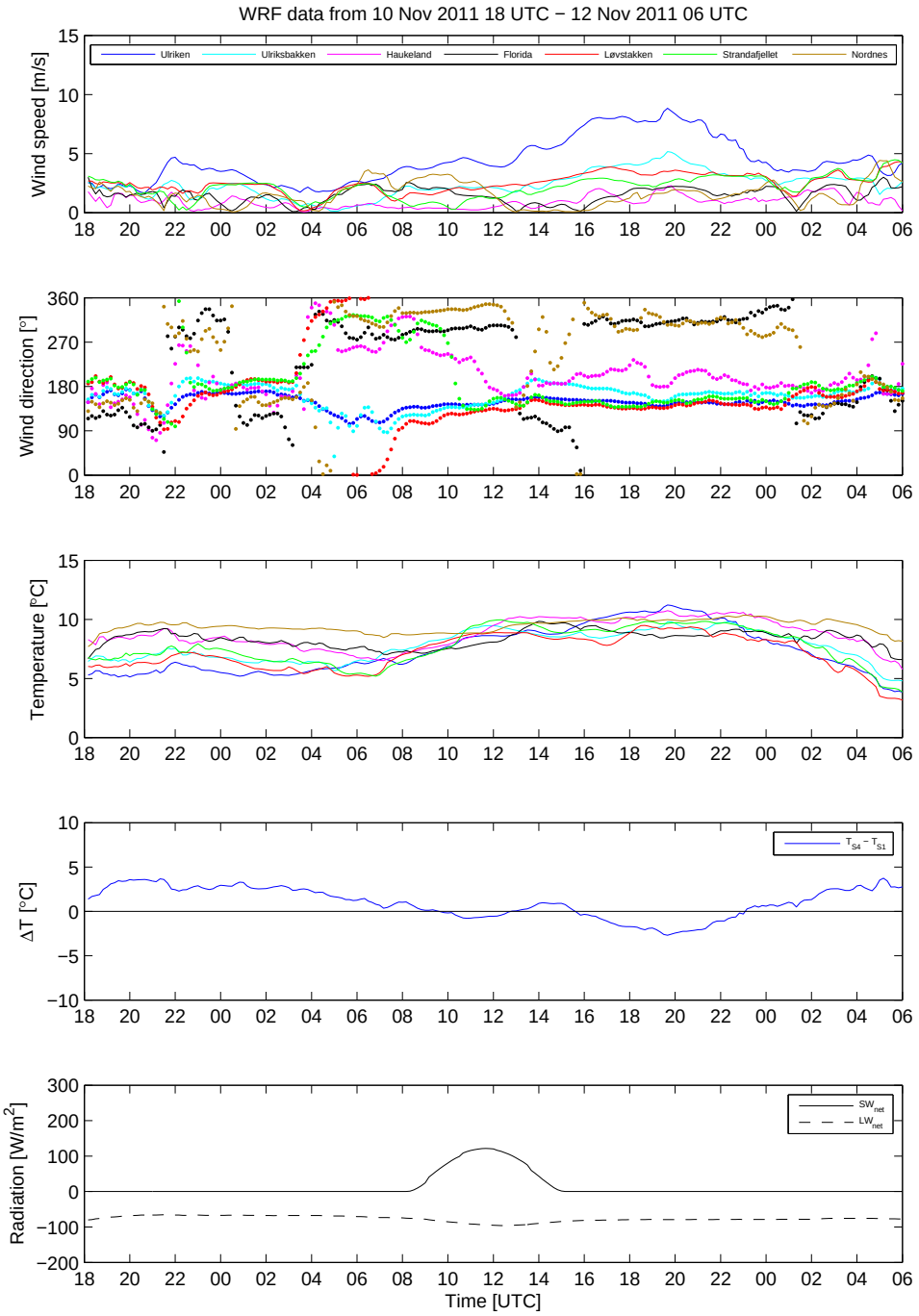

Figure 9.3: *Simulated time series for 10 Nov 2011 18 UTC to 12 Nov 2011 06 UTC for the same location as the seven AWSs.*

highly variable and strongly influenced by local features. A clear example is the wind at Haukeland, which only comes from NE, following the alignment of Isdalen. The other low elevated stations mostly follow the alignment of the Bergen valley. When the wind direction follows a straight line, it indicates that the wind is too weak to move the wind vane. This is the case for many of the stations during the inversion period. When the wind speeds at Løvstakken and Ulriken are at their highest, the wind direction is from SSE, which is the same wind direction as the synoptic wind (Fig. 9.1). The temperatures decrease with height before the inversion starts to build up, with the lowest temperatures at Ulriken and Løvstakken, and the highest temperatures at Florida and Haukeland. During the inversion, the stations are separated into two groups, one with low temperatures and one with high temperatures. Nordnes, Haukeland and Florida have the lowest temperatures, in an increasing order, and Ulriksbakken, Strandafjellet, Løvstakken and Ulriken have the highest temperatures, in a decreasing order. Seen from the radiation balance (difference between net LW and net SW radiation at the Florida station), there is a sudden cooling of the surface just before 11 Nov 00 UTC when the inversion starts to build up. Also seen from the radiation balance, is a heating of the surface between 11 Nov 08 and 13 UTC. A sudden increase in temperature follows somewhere after 08 UTC, and a decrease somewhere after 13 UTC, followed by a period with a strong inversion (ΔT in figure 9.1). When the inversion breaks down around 12 Nov 05 UTC, the wind speeds at all stations calm down, before they slowly increase again. The wind direction veers from SSE to SSW, while the temperatures at Florida, Haukeland and Nordnes start to increase, and the temperatures at Strandafjellet, Ulriksbakken, Løvstakken and Ulriken decrease.

Simulated time series

Like in chapter 8, the WRF time series have been interpolated to 10 minutes intervals. The comparison between simulations and observations for each station can be seen in figures E.2 - E.8 in the appendix. For the comparison it has to be considered that there is a difference in altitude above sea level between the actual location of the AWS and their representation in the model. The corresponding values are summarized in table 9.1. For the stations situated on a building, the height of the building is subtracted before the difference is calculated. The model topography consequently underestimates the height of the stations, except at Haukeland, where the model topography overestimates the height. The largest differences are found at the two mountain stations, which are located more than 100 m lower than in reality. The smallest differences are found at Nordnes and Florida, between approximately 10 to 20 m. However, in reality, the difference is higher due to the height of the buildings. The station at Strandafjellet and Ulriksbakken are located approximately 80 m too low, and Haukeland around 60 m too high. In general, the model topography represents the heights fairly well, in particular the separation into the low-, middle- and high elevated stations.

Table 9.1: *Actual and model height of the stations. Both m a.s.l. and m a.g.l. are given for the actual height. The model height is from the third and innermost domain, which is the domain used in the time series. The height of the buildings is subtracted before the difference between actual and model height is calculated, since the model does not take account for the height of buildings.*

Station	Actual height [m a.s.l.]/[m a.g.l.]	Model height [m a.s.l.] (D03)	Difference [m]
Ulriken (S1)	605 / 4	474.8	130
Ulriksbakken (S2)	408 / 2.1	325.1	83
Haukeland (S3)	64 / 10	112.4	-58
Florida (S4)	48 / 30	6.7	11
Løvstakken (S5)	472 / 2.1	334.9	137
Strandafjellet (S6)	303 / 2	237.5	66
Nordnes (S7)	48 / 30	1.4	17

When evaluating the simulated time series in figure 9.3, it can be seen that the wind speeds are smoothed out compared to the observations, but the model manages to capture the increase in wind speed at Ulriken at approximately the same time and with similar wind speed as the observations. The maximum wind speeds at the end of the period are clearly underestimated by the model. In contrast, the lower elevated sites show a slight overestimation. The main wind direction is clearly from SE, however, the wind at Florida and Nordnes have a completely different wind direction for most of the period, with wind mostly coming from NW, except at the end where they join the SE wind direction on 12 Nov 02 UTC. For the Haukeland station, the model does not pick up the local channeling of Isdalen. For the temperature distribution, the model does not capture the lowermost or the highest temperatures, resulting in a narrow temperature distribution. The temperature at Nordnes also seems to be highly overestimated (Fig. E.8 in the appendix). However, the model picks up the temperature increase due to incoming solar radiation from around 11 Nov 08 UTC. The model also indicates an inversion between 11 Nov 10 UTC to 13 UTC, and from 11 Nov 16 UTC to 23 UTC, however much weaker than in the observations. The top of the inversion in the beginning does not exceed the height of Strandafjellet. Afterward, it even seems to exceed the height of Ulriken. For the radiation balance, there are some important results from the model run. There is generally a cooling of the surface, a condition supporting the possibility to get an inversion. However, the sudden LW radiation loss in the beginning of the inversion period observed for the AWS at Florida is missing in the model run. The sudden drop in SW radiation around 12 UTC in the observations is due to the blocking of direct radiation at Florida by the Løvstakken massif, and is not captured by the model.

Simulated cross sections

In addition to the time series, the output for the innermost domain from the numerical simulations was used to produce horizontal and vertical cross sections, for a more detailed three-dimensional analysis of the inversion. Plots showing vertical cross sections for temperatures up to 1.2 km are shown in figures 9.4(b)-(k), while the location of the cross section is shown in figure 9.4(a). The black arrow in figures 9.4(a)-(b)) shows the location of the Bergen valley, with Løvstakken to the left and Ulriken to the right. The valley to the right of Ulriken is the Haukeland / Espeland area, with the Gullfjellet massif to the far right. This valley will hereafter be referred to as the Espeland valley to avoid confusion with the Haukeland station, even though Espeland is located a bit farther north. In figure 9.4(a) the cross section goes approximately over the Florida station, and in 9.4(b), Florida is located approximately in the middle of the valley. Plots showing the wind speeds for the same vertical cross section and times are shown in figure E.9 in the appendix. Horizontal cross sections showing the synoptic wind speed at 850 hPa for two chosen times, are shown in figures 9.5(a) and (b), while the 10 m wind speed for the same times are shown in figures 9.5(c) and (d).

Figure 9.4(b) shows the situation on 11 Nov 2011 03 UTC before the inversion starts to build up. At this time, the temperature in the Bergen valley is 9 °C and decreases with height in a statically stable atmosphere. The wind aloft at 850 hPa is approximately 10 m/s and coming from the S (Fig. 9.5(a)), while the surface wind is calm or absent (Fig. 9.5(c) and E.9(b) in the appendix). At 06 UTC the air above Ulriken and the Espeland valley starts to heat up, creating a weak inversion over the Espeland valley, while the temperature in the Bergen valley decreases to 8 °C (Fig. 9.4(c)). However, the temperature at the slope of Løvstakken starts to increase. The wind speed increases to 4 m/s at the same locations as the temperatures increases (Fig. E.9(c) in the appendix). At 09 UTC, an inversion over the Bergen valley has built up (Fig. 9.4(d)). The temperature in the Bergen valley is back to 9 °C, while the layer aloft is 10 °C, with the inversion top at approximately 700-800 m. The wind speed in the Bergen valley decreases, while it increases at the mountain tops, and continues to increase with height (Fig. E.9(d) in the appendix). The temperature continues to increase, and by 12 UTC it increases with 1 °C both in the Bergen valley, and aloft (Fig. 9.4(e)). The top of the inversion decreases to around 500 m. However, the inversion is still weak, with only 1 °C in difference between the Bergen valley and the air above it. The wind speed in the valley decreases, and is now only 1 m/s (Fig E.9(e) in the appendix). The temperature at the Espeland valley increases even more, but here, the temperature decreases with height. The increasing temperature (Fig. 9.4(f)) and decreasing wind speed (Fig. E.9(f) in the appendix) tendencies continue at 15 UTC. The top of the inversion increases to around 700 m. The inversion moves away from the top of Ulriken toward W, but it is still present above the Bergen valley.

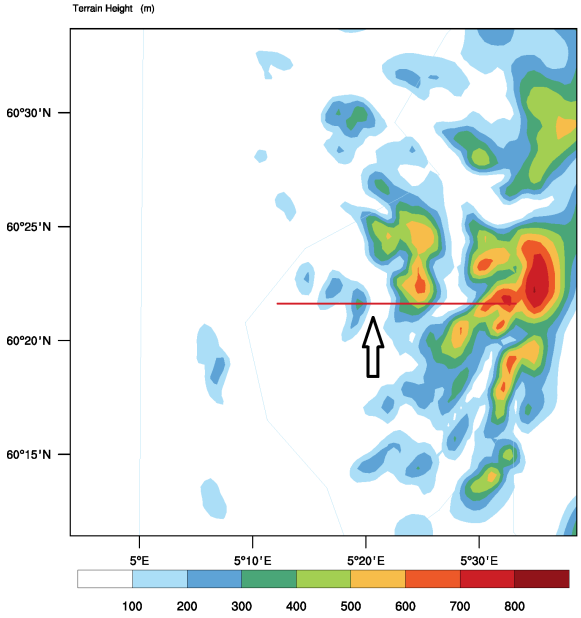

(a) The cross section

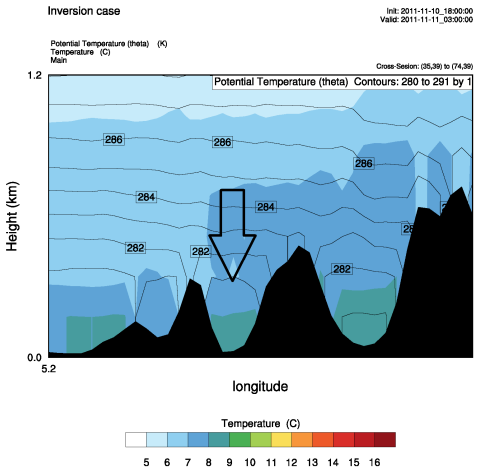

(b) 11 Nov 2011 03 UTC

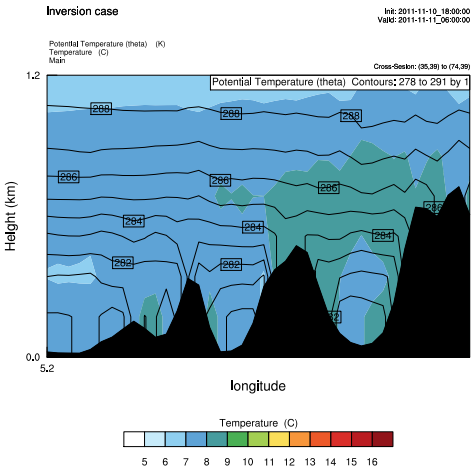

(c) 11 Nov 2011 06 UTC

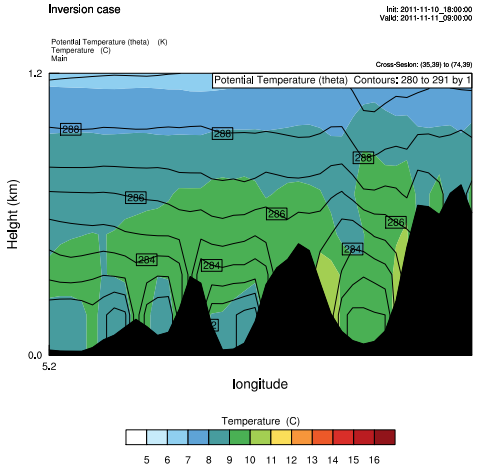

(d) 11 Nov 2011 09 UTC

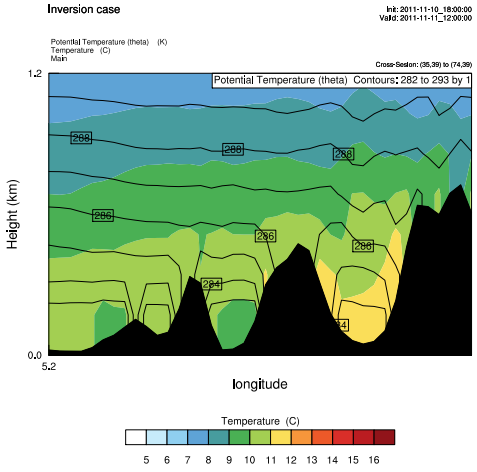

(e) 11 Nov 2011 12 UTC

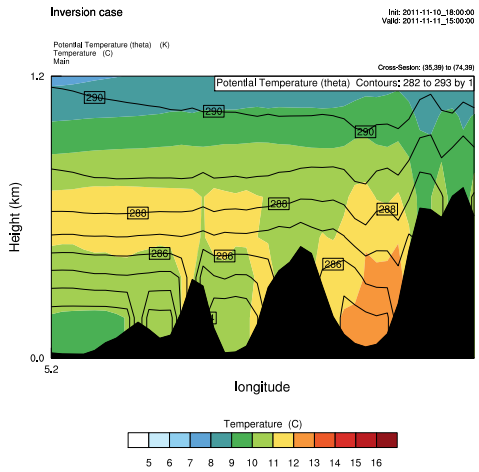

(f) 11 Nov 2011 15 UTC

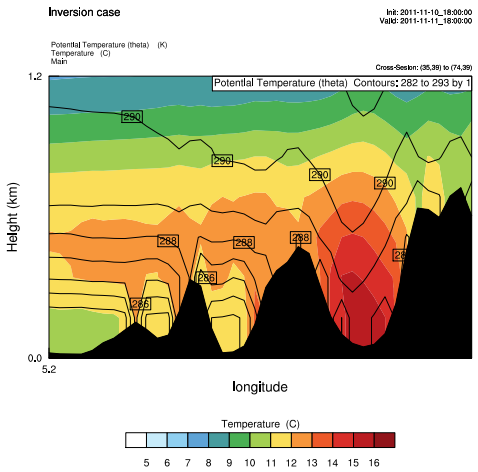

(g) 11 Nov 2011 18 UTC

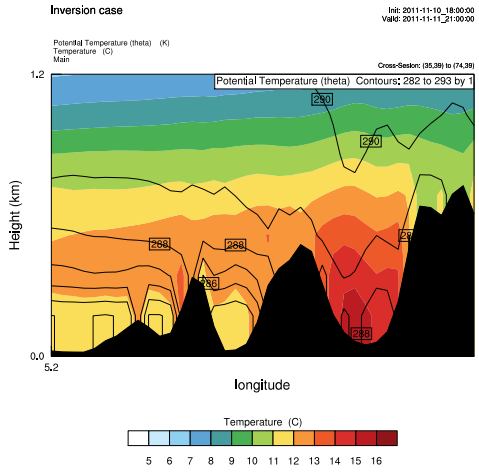

(h) 11 Nov 2011 21 UTC

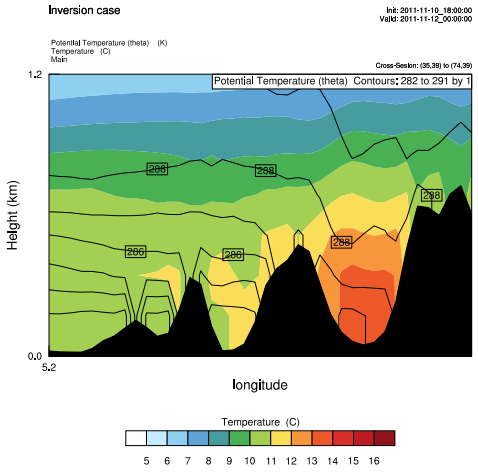

(i) 12 Nov 2011 00 UTC

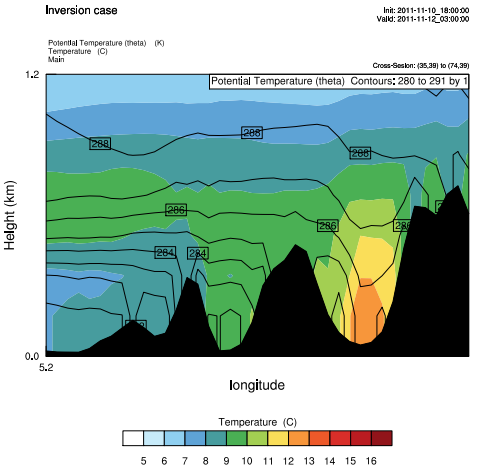

(j) 12 Nov 2011 03 UTC

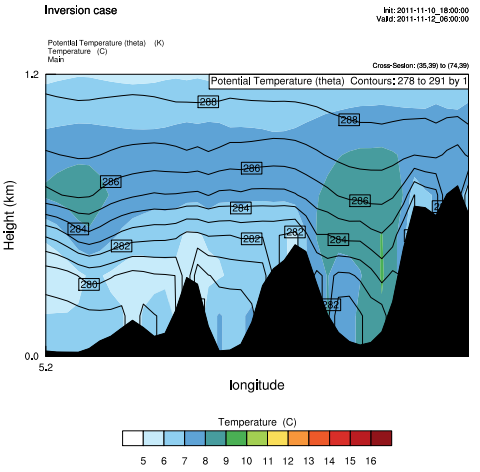

(k) 12 Nov 2011 06 UTC

Figure 9.4: *The development of the simulated inversion every third hour from 11 Nov 2011 03 UTC to 12 Nov 2011 06 UTC. The temperature [°C] is shaded, and the potential temperature [K] is shown in the contours. The cross section is shown in (a), and the location of the Bergen valley is shown with a black arrow in (a) and (b), with Løvstakken to the left, and Ulriken to the right.*

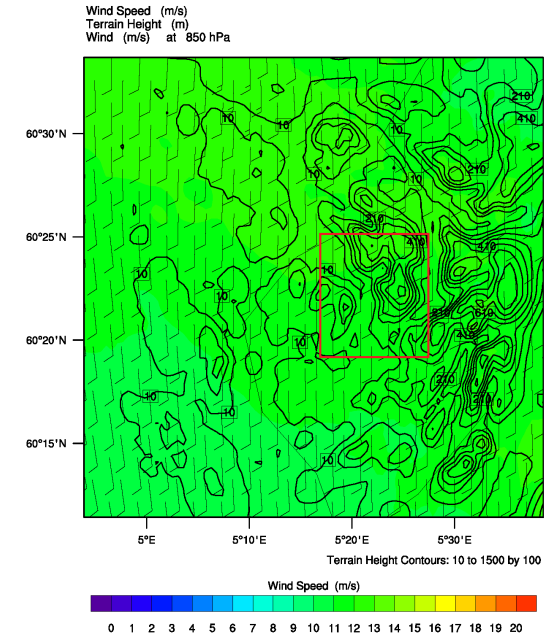

(a) WS 850 hPa - 11 Nov 2011 03 UTC

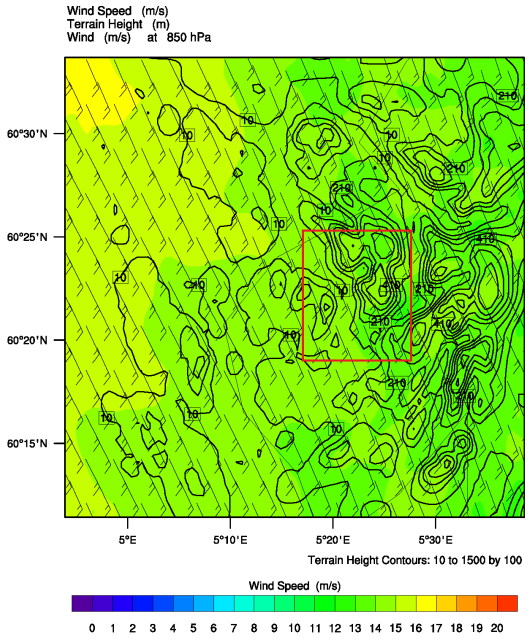

(b) WS 850 hPa - 11 Nov 2011 18 UTC

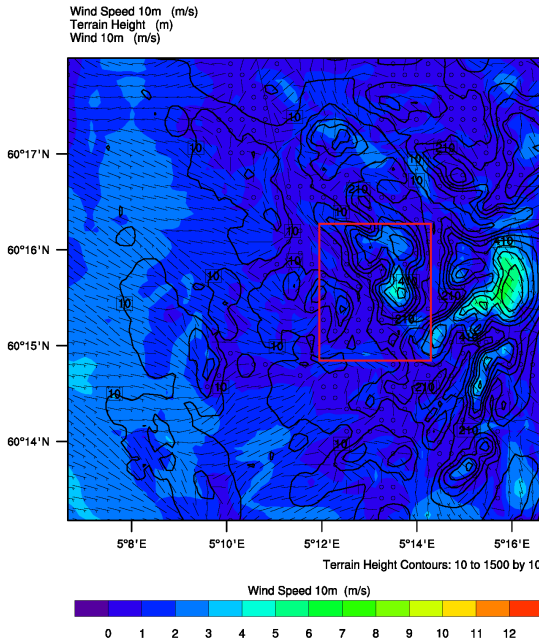

(c) WS 10 m - 11 Nov 2011 03 UTC

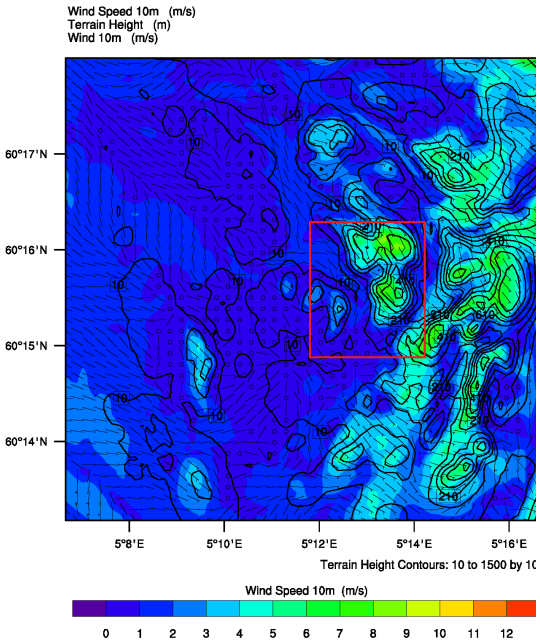

(d) WS 10 m - 11 Nov 2011 18 UTC

Figure 9.5: *The simulated synoptic wind speed at 850 hPa shown before (a) and during (b) the inversion, as well as the simulated surface wind speed at 10 m for the same times, on 11 Nov 03 UTC (c) and on 11 Nov 18 UTC (d). The location of the Bergen valley is framed by the red box, with Løvstakken to the left and Ulriken to the right.*

By 18 UTC, the inversion over the Bergen valley has grown, now covering the valley, Ulriken and Løvstakken. The temperature in the Bergen valley reaches its highest temperature at 12 °C, and 13 °C aloft. The top of the inversion is at approximately 600 m height. A strong heating is observed in the Espeland valley, reaching 16 °C all the way down to the ground. The temperature is still decreasing with height in this valley. The wind speed in the Bergen valley is 1 m/s, while the wind speed at the Espeland valley has increased to 6 m/s in some places (Fig. E.9(g) in the appendix). It seems like the strong heating is somehow connected to the wind coming into the Espeland valley. Figure 9.5(d) shows that the 10 m wind in the Espeland valley comes from SE at this moment, while the wind in the Bergen valley is either absent or channeled. Either way, the wind is weak. The synoptic wind at 850 hPa is from SE with an approximate wind speed of 12 m/s (Fig. 9.5(b)). The situation at 21 UTC is very similar, only that the top of the inversion decreases to around 500 m height (Fig. 9.4(h)). On 12 Nov 00 UTC, the inversion starts to break down, leaving only a small area with inversion close to Løvstakken (Fig. 9.4(i)). The temperatuere in the Bergen valley is now 11 and 12 °C. The low wind speed in the Bergen valley remains approximately the same. At 03 UTC, the only area left with inversion is directly above Løvstakken and west of Løvstakken (Fig. 9.4(j)). The temperature at Løvstakken is 9 °C, and the temperature above is 1 °C higher. The air in the Bergen valley is isotherm, with a temperature of 10 °C. At the last time step (06 UTC), the temperatures are lower, and decreasing with height in the Bergen valley (Fig. 9.4(k)). However, from around 500 m height and above, a new inversion builds up, with its top at approximately 1 km height. The temperature in the Bergen valley is 7 °C and 6 °C at Løvstakken, before it reaches 8 °C all the way up to 1 km. The wind speed at this height is around 15 m/s (Fig. E.9(k) in the appendix), indicating that warm air follows the wind that is coming in aloft over the Bergen valley.

9.3 Discussion

The two main driving mechanisms for an inversion to build up are low wind speeds and a negative radiation balance (Ch. 2.6). For the inversion period from 11 Nov 18 UTC to 12 Nov 06 UTC, both mechanisms are present in the observations and in the simulations. The wind speeds are low, at least for the stations that are not located at the mountain tops, and there is a negative radiation balance for most of the period.

The main wind direction for the observations (Fig. 9.2) seems to be in agreement with the synoptic wind direction (Fig. 9.1), both indicating wind coming from SE during the inversion period. This is also the main wind direction in the simulations. The synoptic charts for 10 Nov (Fig. E.1 in the appendix) and the time series for the observations (Fig. 9.2) also show a slightly more southerly wind component for 10

Nov than for 11 Nov. Weak synoptic and surface winds are expected in SE flow, as discussed in chapter 6.2.

The observed inversion in the Bergen valley is relatively strong and shallow, typically ranging between 5 °C at the ground and 13 °C at the top of the inversion, which is at around 300-400 m height. The simulated inversion however, is much weaker, varying with only 1 °C from the bottom to the top of the inversion. The height of the simulated inversion is typically around 700 m, and reaches even around 1 km on 12 Nov 06 UTC. If this inversion aloft really occurred, remains unanswered since the AWSs observations are located at lower altitudes. In general, the model seems to underestimate the strength of the inversion, and is not able to pick up the strong local differences in temperatures. The model also seems to overestimate the height of the inversion. This can also be an effect of less local temperature variation in the simulations. The simulated time series in figure 9.3 show that the wind speeds and the temperatures are smoothed out compared to the observations (Fig. 9.2). The wind speeds are slightly overestimated. The simulated temperature distribution is much narrower than the observational distribution, revealing that the model does not capture the local differences in temperature as well as the reality, which is expected. This may well be the main reason for the weak simulated inversion. The reason for the low local differences in temperature may to some extent be put in connection with the model topography. As seen in table 9.1, the topography is somewhat smoothed out, giving lower height differences within the Bergen valley, which is also expected. However, the height differences are not large enough to be the whole reason for the low local differences in temperature. It is expected that the model is not able to capture all the local differences in such a complex terrain as the Bergen valley. One of the clear local effects that the simulations did not capture, is the strong channeling effect of the wind at Haukeland due to the valley Isdalen. On the other hand, what the model manages to reproduce in a precise manner is the increase in wind speed at the Ulriken station at the end of the inversion period (Fig. 9.2 and 9.3). This shows that the model is very good on situations closer to the synoptic scale.

Others have also studied inversions in the Bergen valley. Berge and Hassel (1984) observed inversions in SE flow, but with snow or ice cover on the ground, as described in chapter 6.2. Dyngeseth (1998) simulated such an inversion in SE flow using the MEMO model based on the observations by Berge and Hassel (1984) during the winter 1983/84. Dyngeseth (1998) found that the height of the simulated inversion was lower than the observed inversion, which they ment was due to turbulence restrictions in the model. The observed inversion was between 100-120 m high (Dyngeseth, 1998; Berge and Hassel, 1984) at the most, which is much lower than the height of the inversion in this study. Berge and Hassel (1984) explained this low inversion due to SE wind

through the Bergen valley, hindering the inversion to grow higher. Utaaker (1995) also studied temperatures in the Bergen area, and found that the height of typical inversions was different for different areas. He found that the height of inversions in the area around Florida was typical between 90-130 m high, and up to 200 m during clear conditions, while the strongest inversions were found when Store Lundgårdsvann was covered in snow. The height of inversions further south in the Bergen valley for the Minde area were typically between 110 and 150 m, and 220 m. Dyngeseth (1998) explains that areas further away from the ocean are expected to have deeper inversions than closer to the sea, due to temperature differences at ground level.

The reason for inversions to develop in SE flow remained an unanswered question in the study of the general flow conditions in the Bergen valley in chapter 6. The results in this case study however, may indicate that under the right conditions (low wind speeds in a stable atmosphere with a negative radiation balance) warm air from SE is transported toward the Bergen area, giving higher temperatures aloft than at the ground. A strong heating in the Espeland valley is observed (Fig. 9.4) as the wind speed increases in this area (Fig. E.9 in the appendix). The reason for the strong heating in the Espeland valley compared to the Bergen valley remains unanswered without further investigation. However, this warm air seems to propagate over Ulriken and toward the Bergen valley. In addition, heating in areas in the Bergen valley that experienced a slight increase in wind speed at the same locations, is also observed. This may indicate that some sort of Föhn effect not reaching the ground may lead to inversions in the Bergen valley under the aforementioned conditions during SE flow.

9.4 Conclusions

One purpose of this case study is to test the quality of the WRF model in an inversion case in the period from 10 Nov 2011 18 UTC to 12 Nov 2011 06 UTC. The simulations are compared to the observations for the same time period. The wind speeds turns out to be slightly overestimated in the simulations, and the temperatures follows a much narrower distribution than the observations with less local temperature differences than the observations. One of the reasons for this narrow distribution could be the less detailed topography in the WRF model compared to reality. The simulated wind speeds on the other hand, are a bit overestimated. These two aspects result in a weaker inversion in the simulations compared to the observed strong inversion. In addition, the model seems to overestimate the height of the inversion.

A local feature that the model does not capture is the strong channeling effect of Isdalen at the Haukeland station. However, the model simulates the wind at Ulriken with great detail, and it also has the right synoptic wind direction. This shows that

the model is very good on situations that are close to the synoptic situation.

This particular inversion case is for southeasterly flow. Generally low wind speeds in a stable atmosphere with a negative radiation loss give good conditions for development of inversions in the Bergen valley. Results from this case study indicate that a Föhn effect brings warm air coming from SE toward the Bergen valley, warming the air above the valley, resulting in an inversion that lasts as long as the conditions remains unchanged.

Chapter 10

Summary and outlook

A network of seven automatic weather stations (AWSs) has gathered observations for more than 17 months to be used in the study of the characterization of the local flow conditions in the Bergen valley. Measurements at some of the locations of the AWS have never been done in earlier studies. The new observational sites combined with the use of a fine scale numerical model, have led to new results and improved understanding of the flow conditions in the Bergen valley.

Of the seven AWSs, the wind at Ulriken is the best representative for the large-scale synoptic wind. Here, the main wind direction is from SW, and the second most common wind direction from NW. Wind speeds at Ulriken are markedly higher than at Løvstakken, which is presumably a result of a local speed up at Ulriken. The wind in the Bergen valley is strongly channeled, resulting in a main wind direction from SE and secondly from NW, the same direction as the alignment of the Bergen valley. There are also large local differences in the distribution of wind directions in the Bergen valley. At Haukeland, located only 1.7 km apart from Florida, the wind follows a completely different directional distribution due to the strong channeling effect caused by the Isdalen valley. During winter, katabatic flow from NE dominates at Haukeland, and during summer, anabatic wind along with a channeling of wind results in wind from SW. The wind distribution in the rest of the Bergen valley is also highly seasonal dependent. During summer, sea breeze coming from NW dominates, and during winter, wind from SE dominates. The results indicate that the sea breeze commonly exceeds the height of Løvstakken, but also affects the wind at Ulriksbakken and to some extent at Ulriken. At Ulriksbakken and Ulriken, anabatic wind is presumably enhanced by the sea breeze, resulting in a more westerly wind direction at these stations.

The wind speeds at all stations are compared to the wind speed at Ulriken in form of wind speed ratios (WSR), to better understand the conditions for when the wind speed at the lower elevated stations gets close to or exceeds the wind speed at Ulriken. High WSRs are observed when the wind at Ulriken turns southwesterly, northerly and

easterly. High WSR for southwesterly flow at Ulriken is linked to high wind speeds aloft and at the surface due to a coastal jet. The wind speed at Ulriken is generally below 10 m/s when this happens. Northerly flow is generally strong, and northeasterly flow weak. For northwesterly flow, both high and low surface wind speeds are observed, depending on the atmospheric stability. During high atmospheric stability, northwesterly flow is blocked by the mountains in southern Norway, giving low wind speeds aloft and at lower levels. This will give a reasonably high WSR when assuming equally low wind speed at Ulriken and at the lower elevated stations. For the WSR to increase even more, the AWS unsheltered from northwesterly flow must experience higher wind speeds, which will most likely happen in an unstable stratification. The Nordnes station will in particular experience high wind speeds compared to the other stations, due to less surface friction over Byfjorden. The increase in WSR when the wind at Ulriken turns easterly supports a theory about downslope accelerated flow through the mountain gap between the two mountain ranges on the eastside of the Bergen valley. The accelerated wind reaches the bottom of the valley, and is most likely channeled through the valley, not reaching the stations at Strandafjellet and Løvstakken.

Decreasing WSRs were observed for wind from SE and W at Ulriken. A decrease in WSR for southeasterly wind at Ulriken is linked to low surface winds both aloft and at the surface due to a wake downstream the mountains in southern Norway, as found in previous studies. There is also a decrease in WSR for westerly wind at Ulriken, since the low elevated stations in the Bergen valley lie sheltered from wind coming from this direction.

For inversions to develop in the Bergen area, a high pressure synoptic system giving low synoptic wind and a stable atmosphere must be present. This typically happens when the wind at Ulriken is from NE or around S for low wind speeds between 0 and 5 m/s. For wind speeds between 5 and 10 m/s, this happens for southerly wind directions or wind from E. The latter gives the strongest inversions. Wind from E and NE are blocked by topography, giving calm conditions in the Bergen valley, while southerly wind brings in warm air aloft, as indicated by numerical simulations.

The theory about the local effect of fronts passing a location is confirmed when strong synoptic wind in the Bergen valley is investigated. The strongest wind speeds occur in the warm sector. Evidence of a local speed up at Ulriken is also present. The Bergen valley lies sheltered from strong southwesterly wind and the wind closer to the ground is channeled through the Bergen valley.

The 23 Aug 2011 had ideal conditions for a development of sea breeze, with low synoptic wind during a clear day in the summer. The sea breeze had wind speeds ranging

up to 6 m/s at the most, which corresponds to the theory. The height of the sea breeze exceeded the height of Løvstakken, and barely reached the Ulriken station, giving it a height of approximately 500-600 m. The numerical simulation of the sea breeze was quite accurate, which also revealed a strong sea breeze on either a larger scale or a sea breeze front hitting the west coast of Bergen with strength of around 7-8 m/s. Due to this strong sea breeze coming in from NW, the sea breeze propagated far inland. The front was not enhanced by synoptic wind, since the synoptic wind came from SE.

The inversion between 10 Nov 2011 18 UTC and 12 Nov 2011 06 UTC occurred during southeasterly flow. Results from this case study indicate that a Föhn effect brings warm air coming from SE toward the Bergen valley. For a valley further E, the warm air reaches all the way down to the ground, while only the air above the Bergen valley is heated. The observed inversion in the Bergen valley was relatively strong and shallow, typically ranging between 5 °C at the ground and 13 °C at the top of the inversion, which was at around 300-400 m height. The simulated inversion however, was much weaker, varying with only 1 °C from the bottom to the top of the inversion. The height of the simulated inversion was at around 700 m. The performance of the WRF model in the inversion case was less accurate than for the sea breeze scenario.

There are several aspects of the flow conditions that have not been investigated in this study. Future investigations may answer questions that are still remaining, which are described in the following.

One result that appears when investigating the wind speed ratios is the increase as the wind at Ulriken turns easterly. The explanation to this given in this study, is an acceleration and a channeling of the wind through a gap in the mountains on the east-side of the Bergen valley. The WSRs indicates that this increase in wind speed would stop before it reaches Strandafjellet and Løvstakken. Although easterly wind in the Bergen area is rare, this is a theory that has yet to be investigated in detail. Numerical simulations may give further information about this theory.

The dates for the sea breeze scenario were chosen to test the WRF model in a day with sea breeze versus a day with synoptic wind. However, due to the increase in wind speed the night after the sea breeze, and the spin-up time of the model in the hours before the sea breeze started, the phenomenon of land breeze remains unanswered in this study. It would be interesting to compare the results of land breeze effects with newer numerical simulations compared to the one performed by Dyngeseth (1998), to see if new results for example show the extension of the land breeze out toward the sea. This study did not focus on the return flow of the land-sea breeze either. Vertical cross sections from simulations may give more results about this.

The WRF model's performance during inversions was moderate. More detailed testing of the WRF model for inversions scenarios in the Bergen valley could lead to more accurate simulations, for example by testing different planetary boundary layer (PBL) schemes.

This study has only used ground based observations from AWSs. For future investigation, observations for the air aloft could enhance the understanding of the interaction between synoptic and local flow conditions. There are several remote sensing instruments on the market that can provide profiles of wind and temperature. Wind lidar, sodar or radar can be used for wind measurements, while Sodar-RASS (Radio-Acoustic Sounding System) or microwave radiometer can be used for temperature profiling. A microwave radiometer and a wind lidar have recently been installed at the roof of the GFI, and can give new information about the conditions of the temperature and flow above the Bergen valley, such as the height of inversions.

Future investigations based on temperature and wind profiles of the atmosphere above the Bergen valley, along with an improved performance of the WRF model for inversion scenarios, may be a step toward better prediction of pullution related problems in the Bergen valley.

Appendix A

WRF landuse and topography

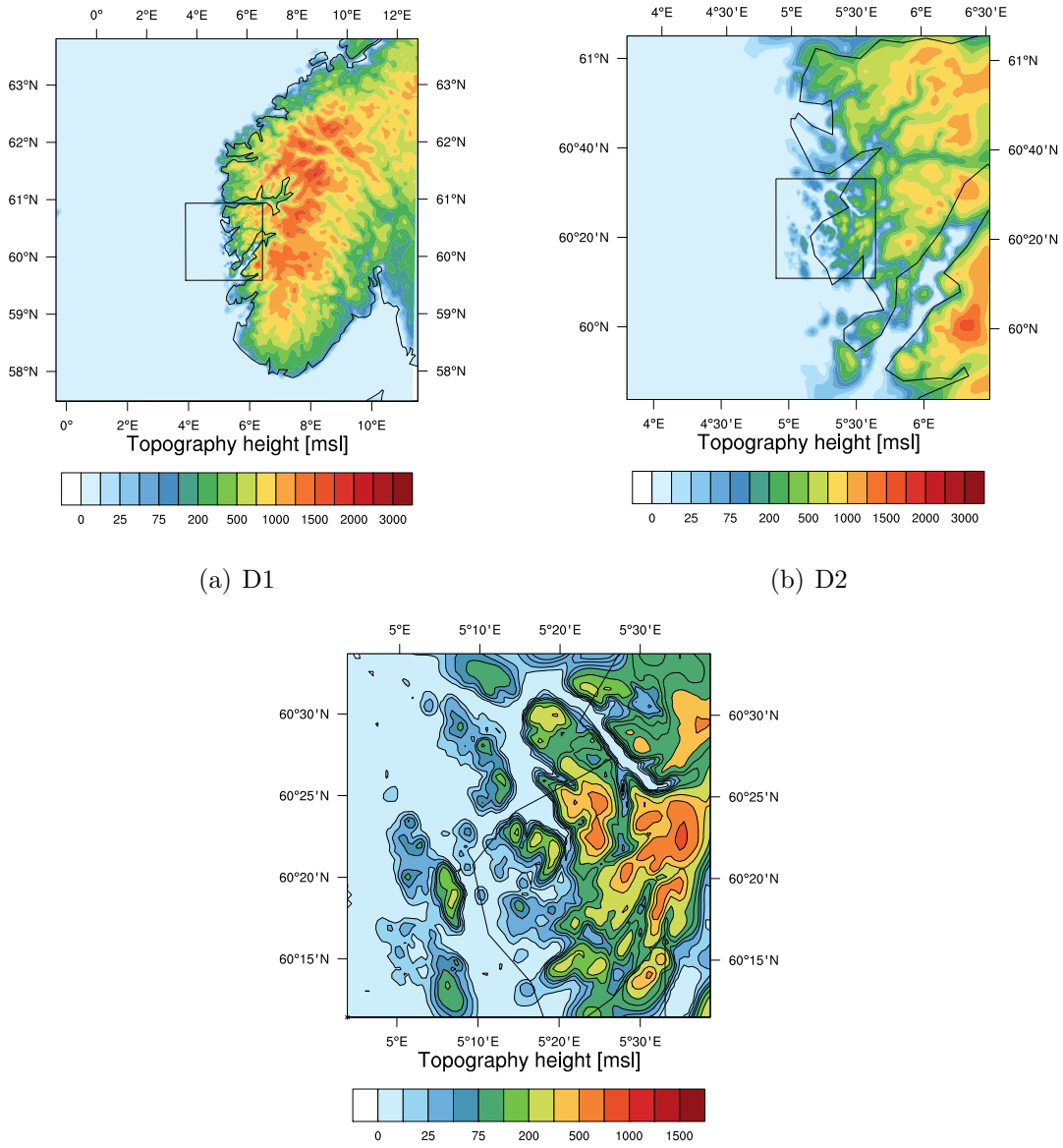

(a) D1

(b) D2

(c) D3

Figure A.1: *Plotted topography for Domain 1 and the location of Domain 2 in (a), topography for Domain 2 and the location of Domain 3 in (b), and the topography for Domain 3 in (c).*

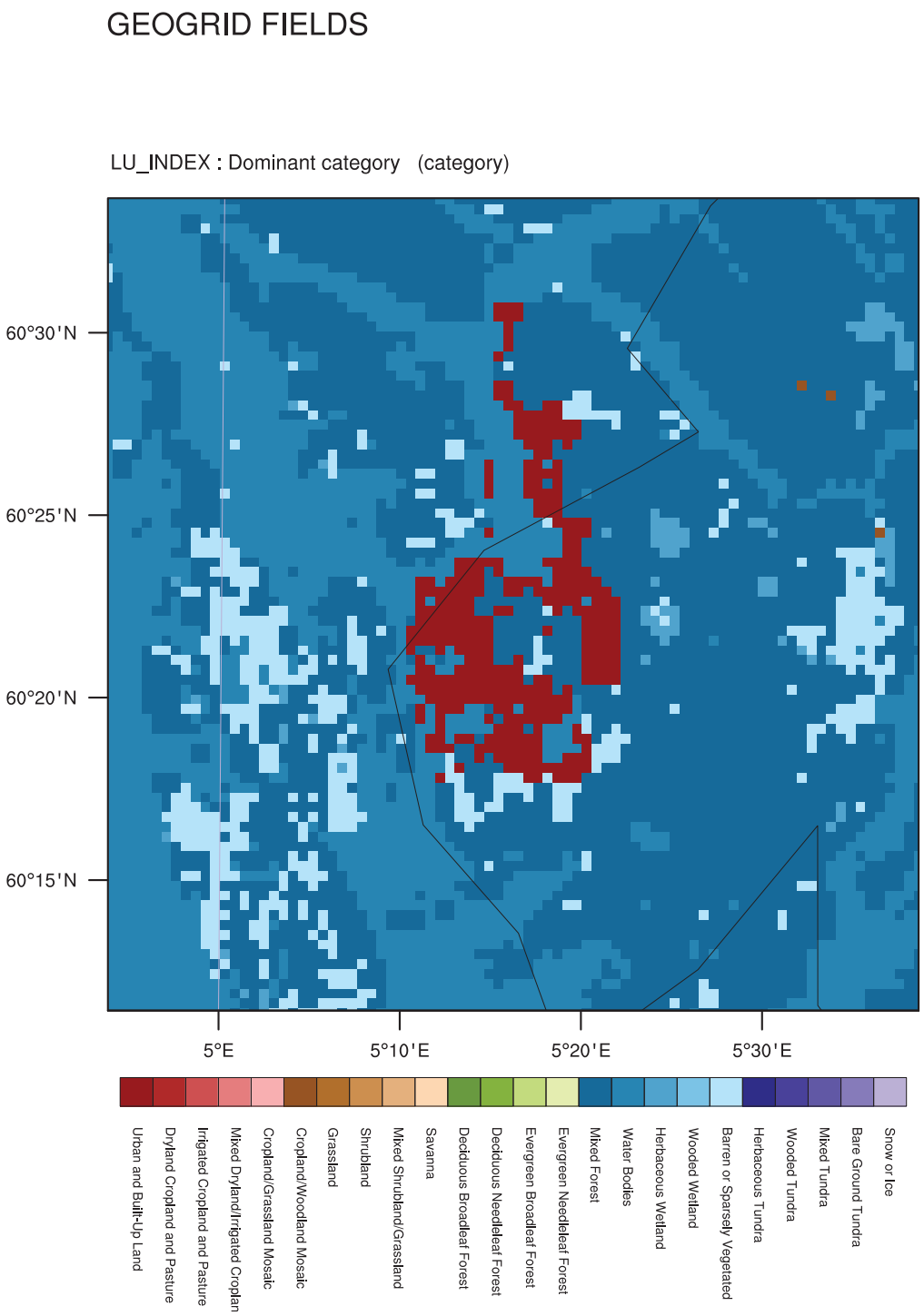

Figure A.2: *Landuse for the innermost domain. The red indicates urban and built up land.*

Appendix B

General flow conditions

Figure B.1: *The location of Haukeland Elementary School with respect to Svartediket, both marked in red. The AWS at Haukeland is located directly downstream the water, Svartediket, located in the Isdalen valley which is SW-NE oriented. The location of the AWSs at Ulriken, Ulriksbakken and Florida are marked in blue.*

B.1 Wind speed ratios for all the seven AWSs

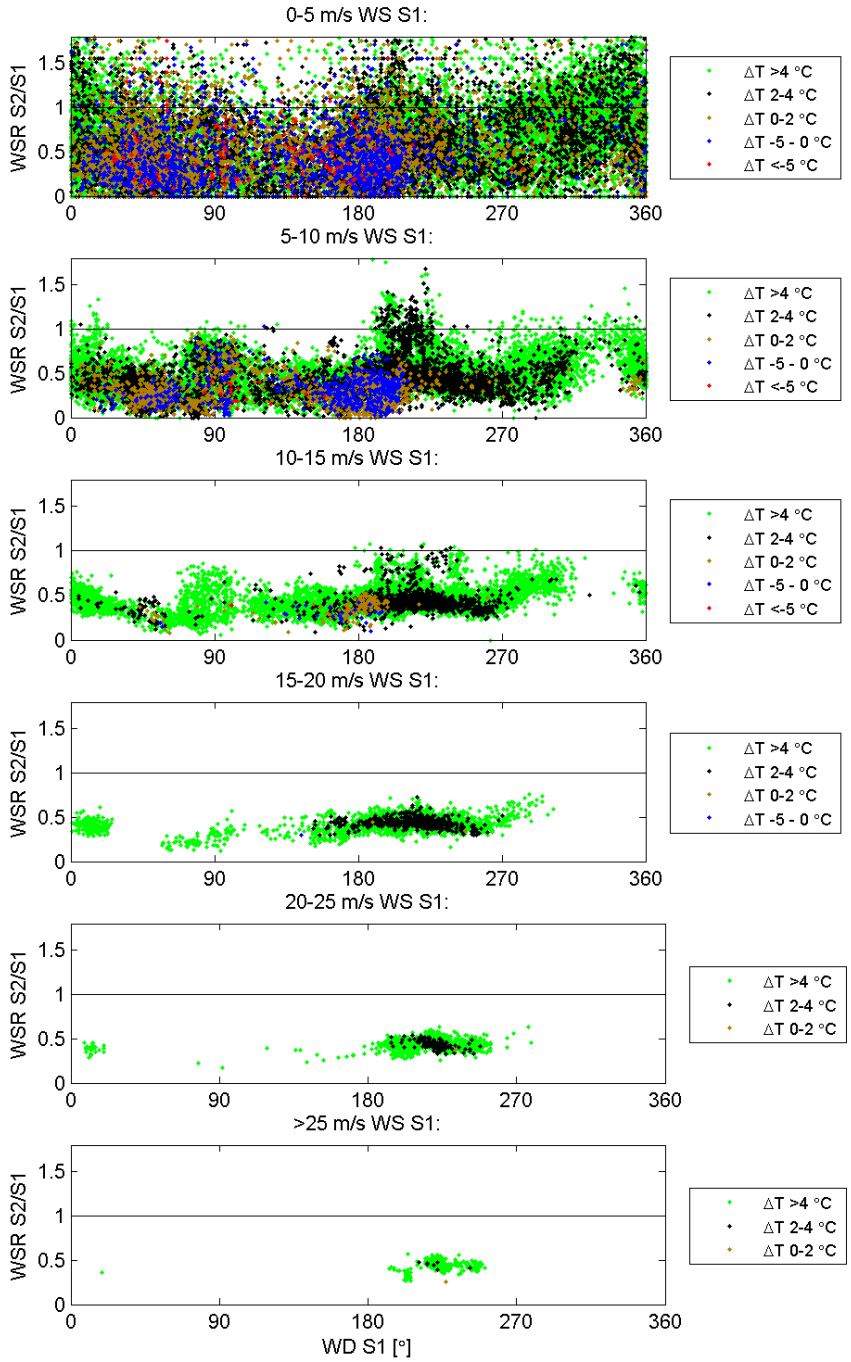

Figure B.2: *Wind speed ratio for Ulriksbakken (S2) compared to the temperature difference between Florida and Ulriken for given wind speeds.*

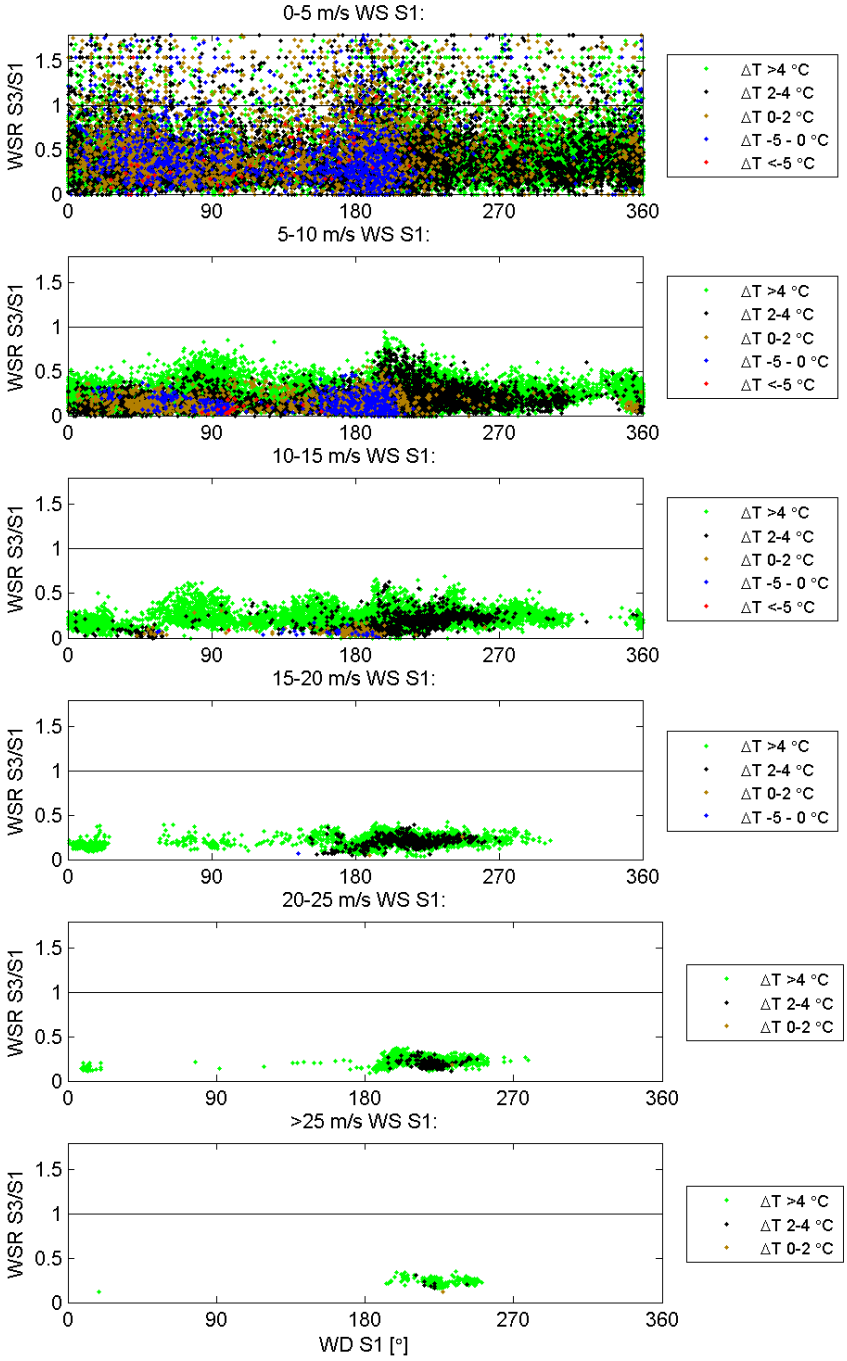

Figure B.3: *Wind speed ratio for Haukeland (S3) compared to the temperature difference between Florida and Ulriken for given wind speeds.*

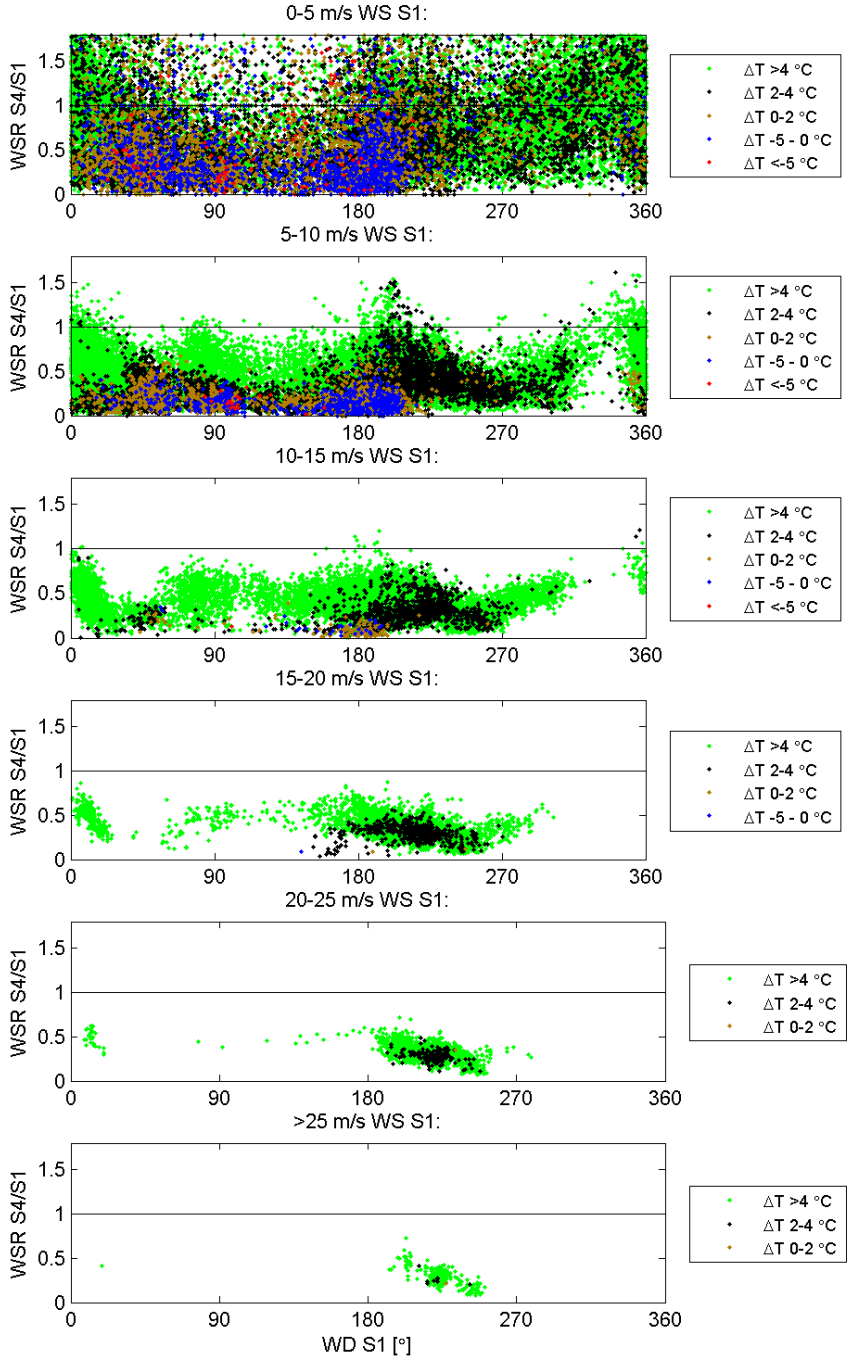

Figure B.4: *Wind speed ratio for Florida (S4) compared to the temperature difference between Florida and Ulriken for given wind speeds.*

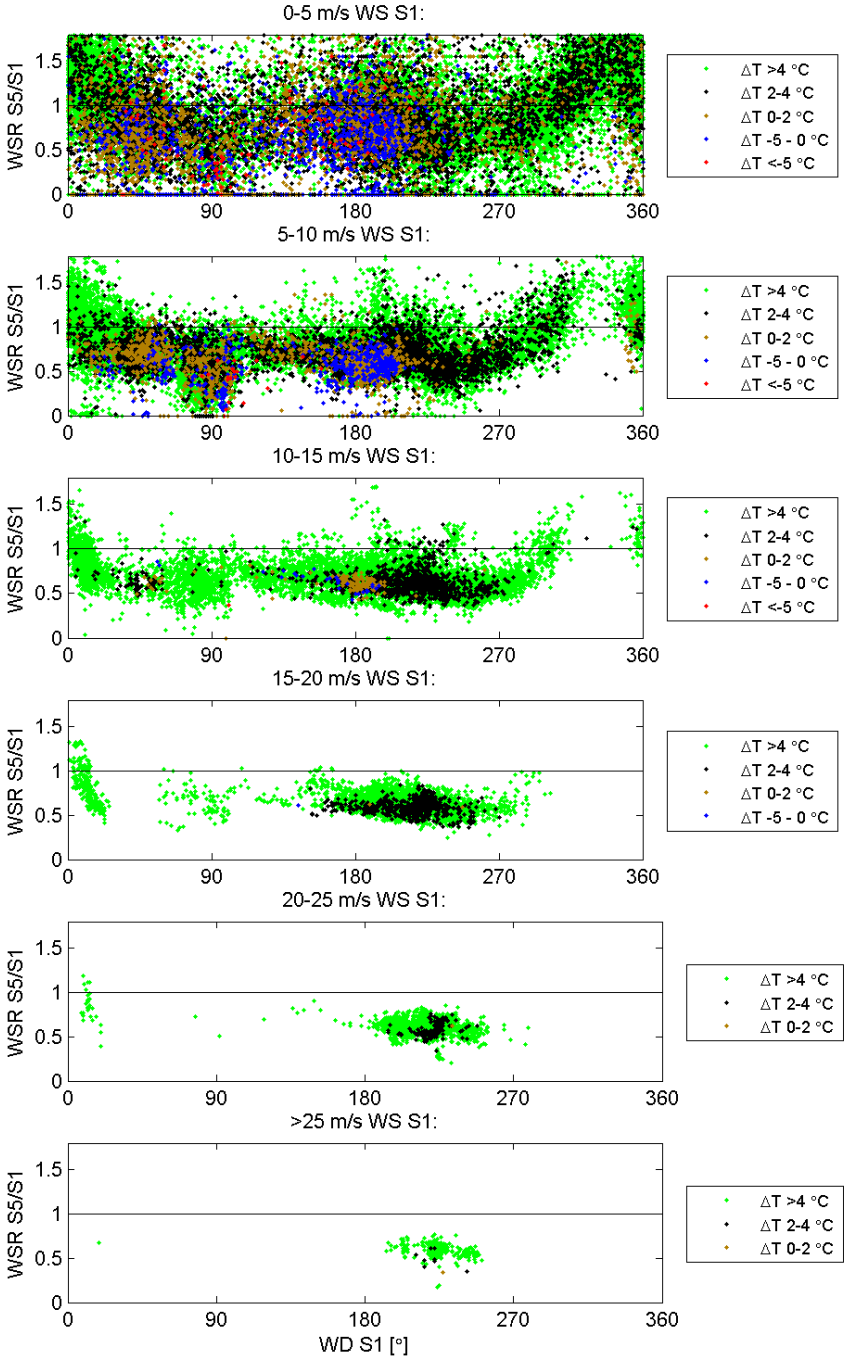

Figure B.5: *Wind speed ratio for Løvstakken (S5) compared to the temperature difference between Florida and Ulriken for given wind speeds.*

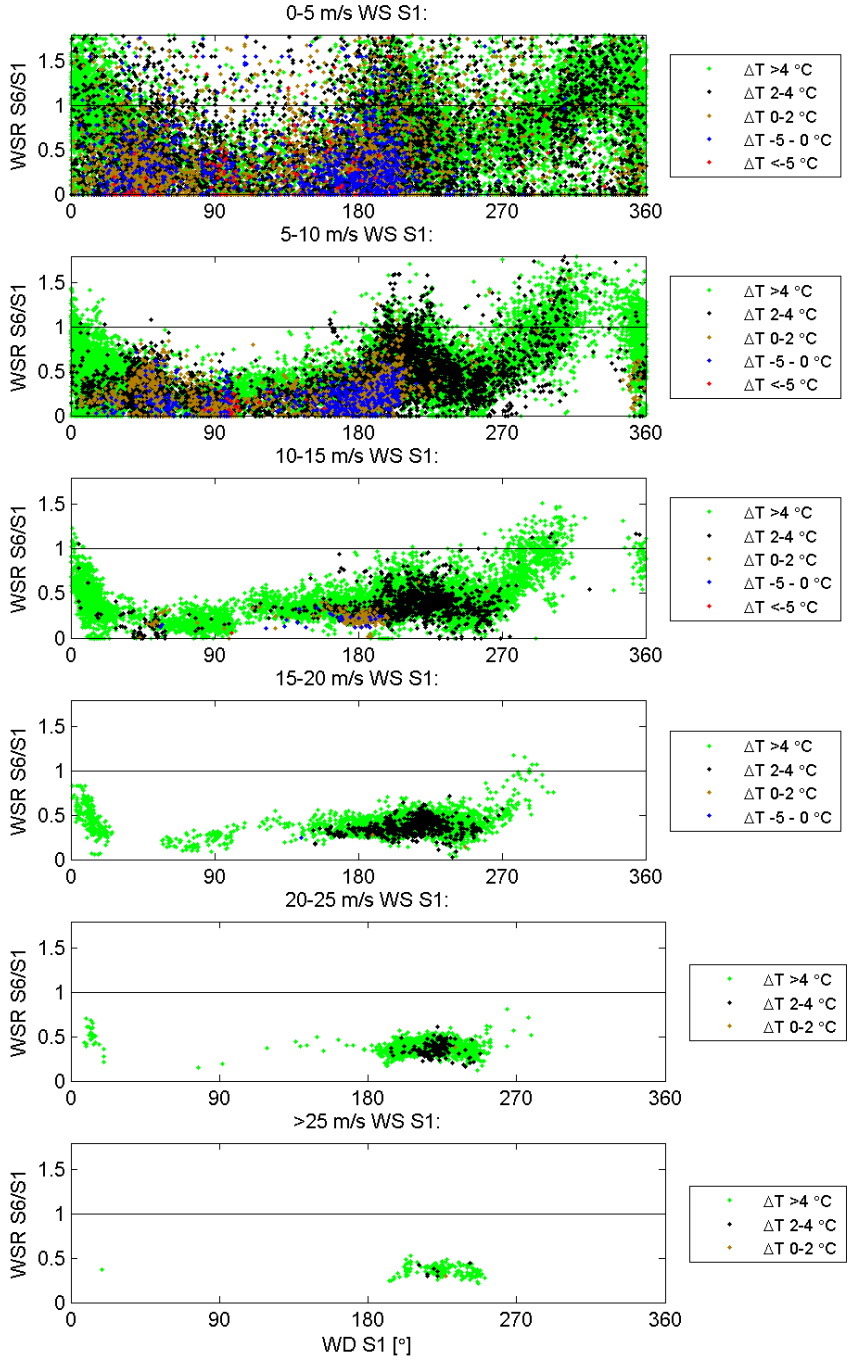

Figure B.6: *Wind speed ratio for Strandafjellet (S6) compared to the temperature difference between Florida and Ulriken for given wind speeds.*

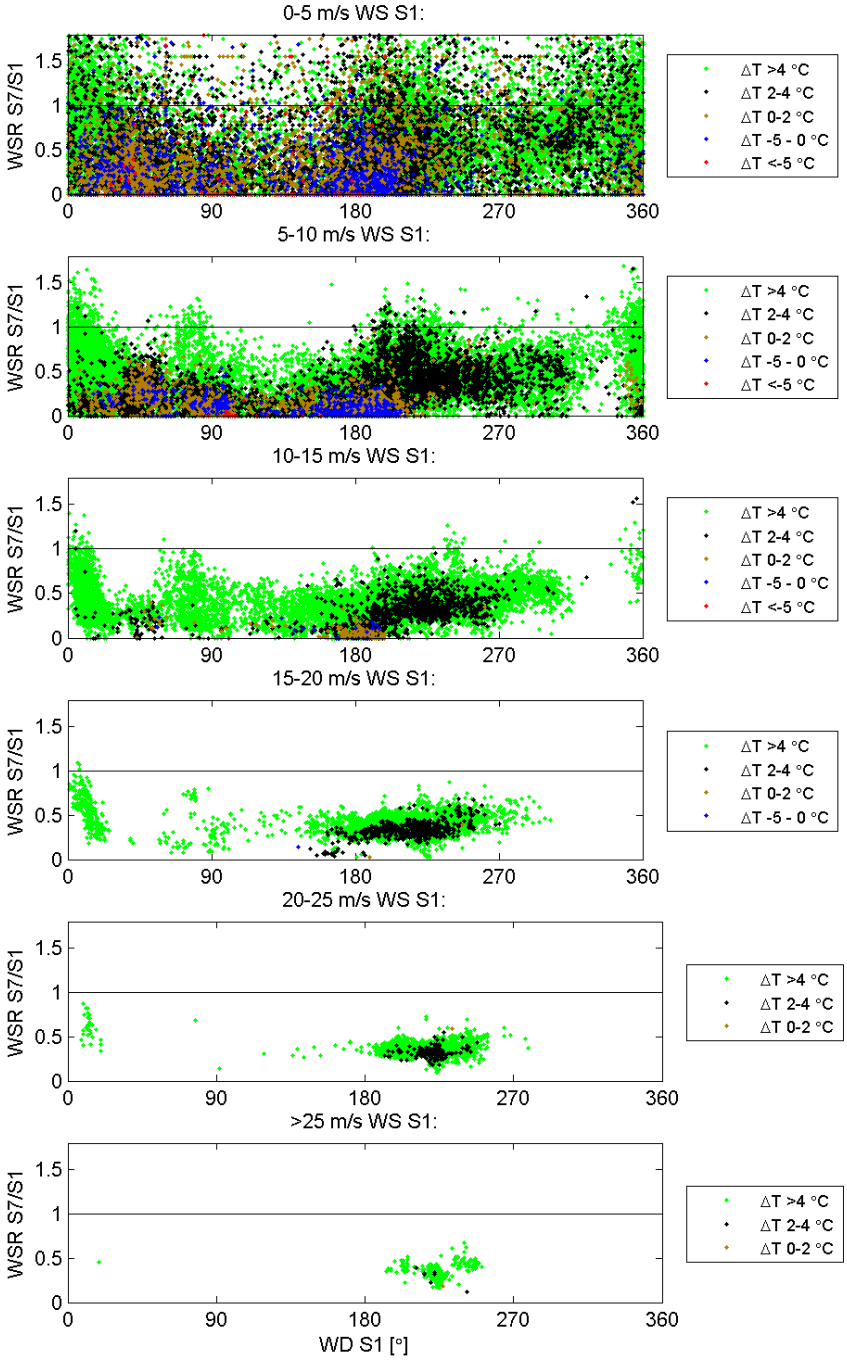

Figure B.7: *Wind speed ratio for Nordnes (S7) compared to the temperature difference between Florida and Ulriken for given wind speeds.*

Appendix C

Southwesterly storms - the full synoptic developments

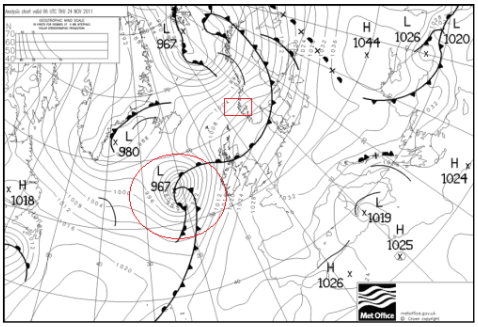

(a) 24 Nov 2011 06 UTC

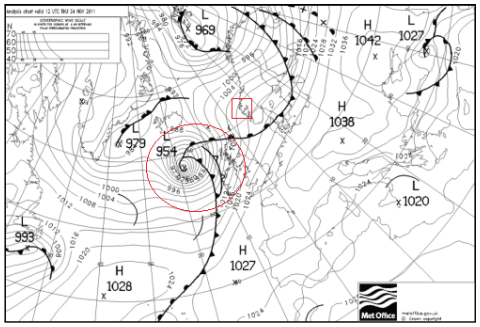

(b) 24 Nov 2011 12 UTC

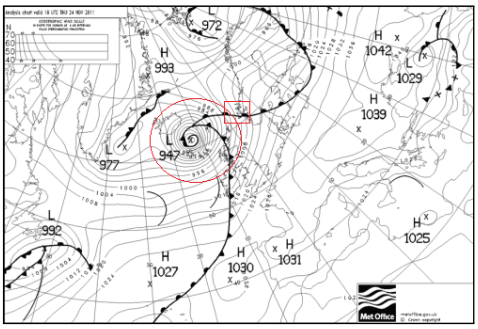

(c) 24 Nov 2011 18 UTC

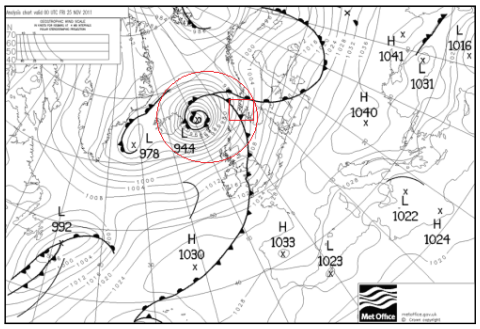

(d) 25 Nov 2011 00 UTC

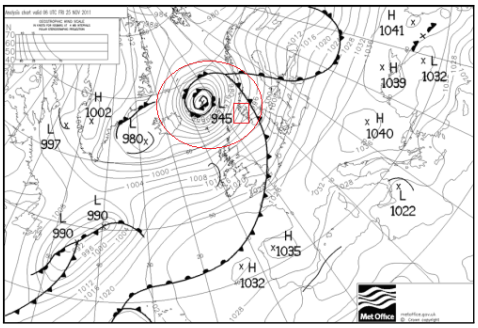

(e) 25 Nov 2011 06 UTC

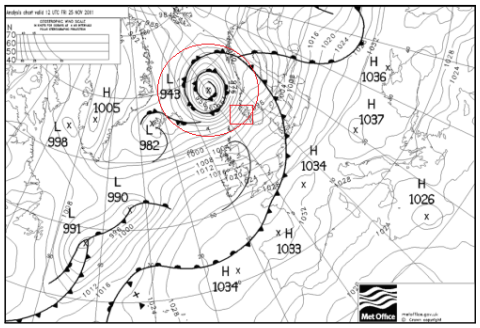

(f) 25 Nov 2011 12 UTC

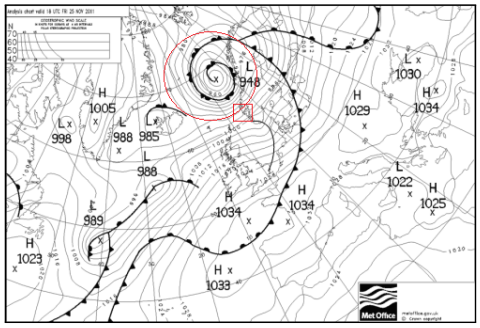

(g) 25 Nov 2011 18 UTC

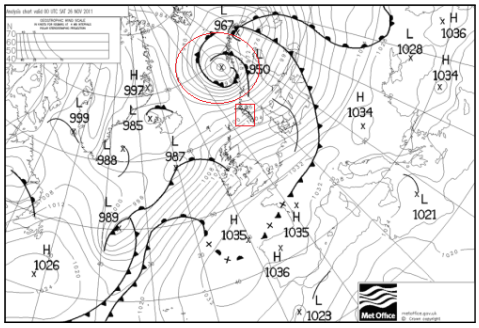

(h) 26 Nov 2011 00 UTC

Figure C.1: *The synoptic development of the storm Berit. Red circles indicate the location of Berit, and the red boxes show the location of the southwest coast of Norway (Source: UK Met Office).*

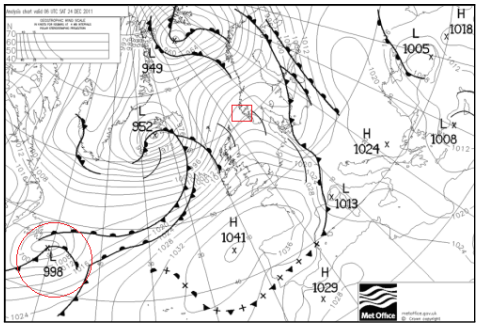

(a) 24 Dec 2011 06 UTC

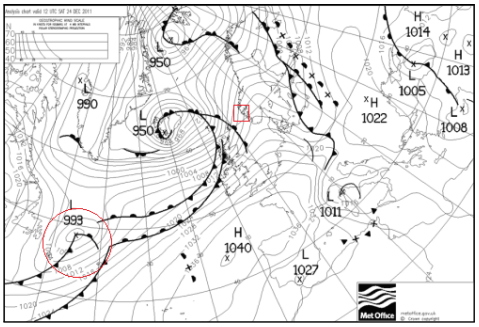

(b) 24 Dec 2011 12 UTC

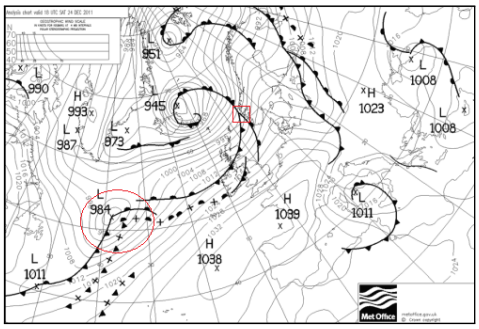

(c) 24 Dec 2011 18 UTC

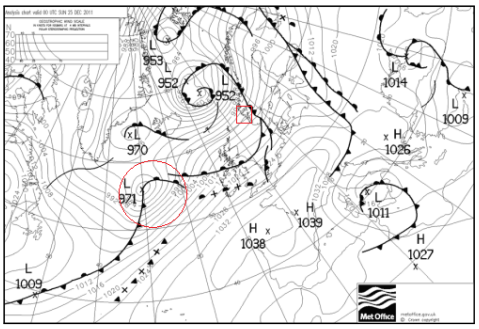

(d) 25 Dec 2011 00 UTC

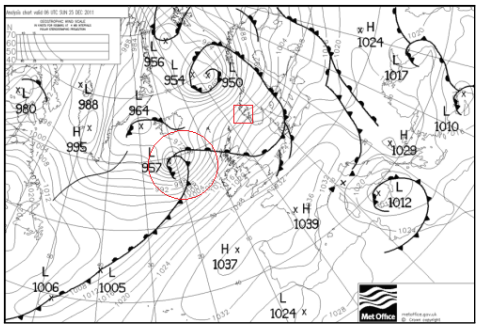

(e) 25 Dec 2011 06 UTC

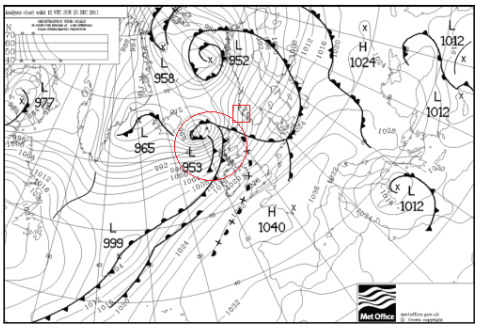

(f) 25 Dec 2011 12 UTC

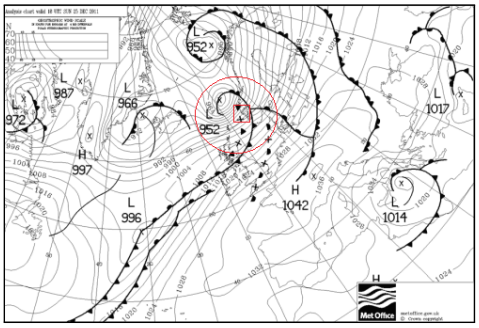

(g) 25 Dec 2011 18 UTC

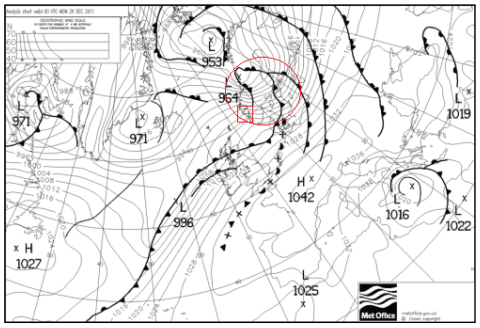

(h) 26 Dec 2011 00 UTC

Figure C.2: *The synoptic development of the storm Dagmar. Red circles indicate the location of Dagmar, and the red boxes show the location of the southwest coast of Norway (Source: UK Met Office).*

Appendix D

Sea breeze

D.1 The full synoptic development

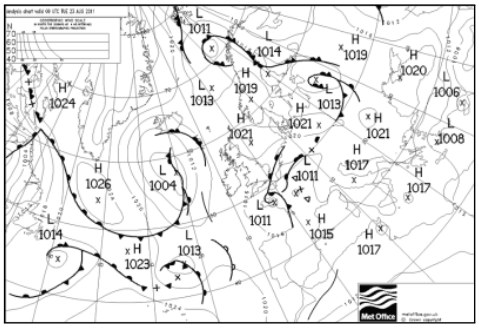

(a) 23 Aug 2011 00 UTC

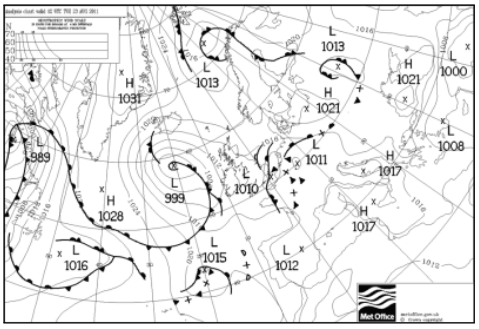

(b) 23 Aug 2011 12 UTC

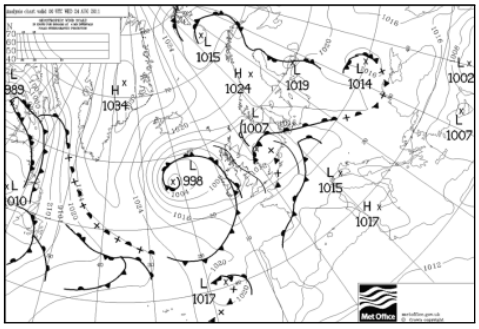

(c) 24 Aug 2011 00 UTC

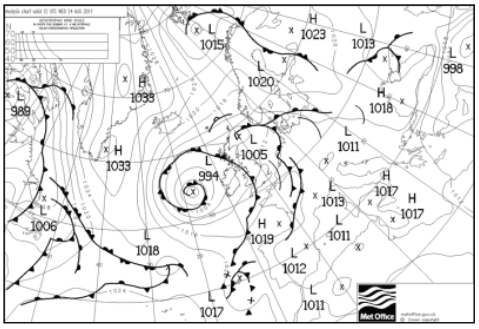

(d) 24 Aug 2011 12 UTC

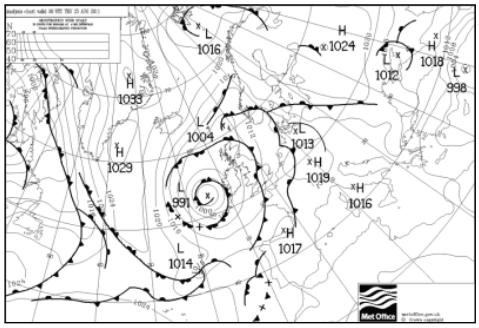

(e) 25 Aug 2011 00 UTC

Figure D.1: *The synoptic development of the sea breeze case 23 August 2011 with a following day with stronger synoptic wind 24 Aug 2011 (Source: UK Met Office).*

D.2 Measured and modeled time series for all the seven AWSs

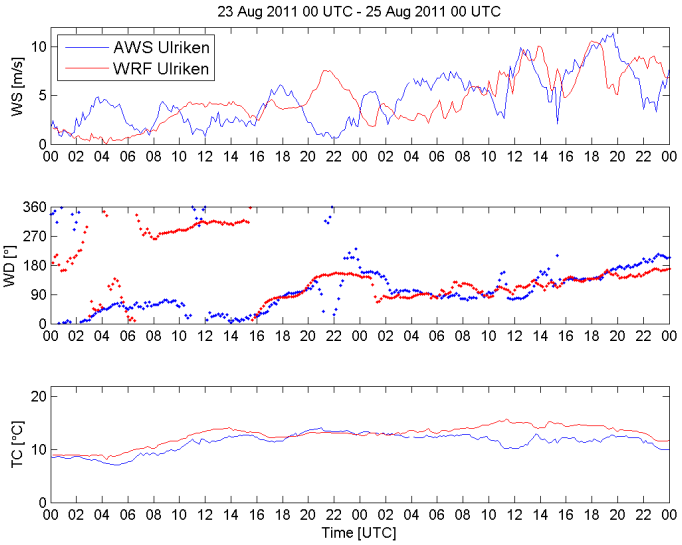

Figure D.2: *Model results (red) compared to the observations (blue) at Ulriken for the period 23 Aug 2011 00 UTC - 25 Aug 2011 00 UTC.*

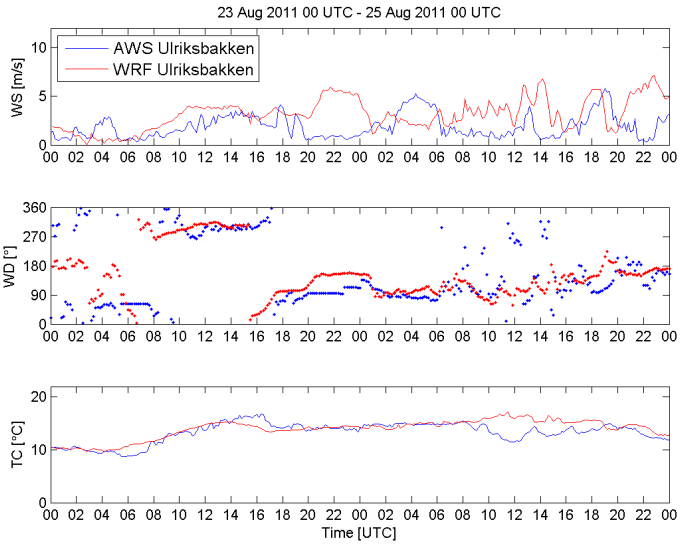

Figure D.3: *Model results (red) compared to the observations (blue) at Ulriksbakken for the period 23 Aug 2011 00 UTC - 25 Aug 2011 00 UTC.*

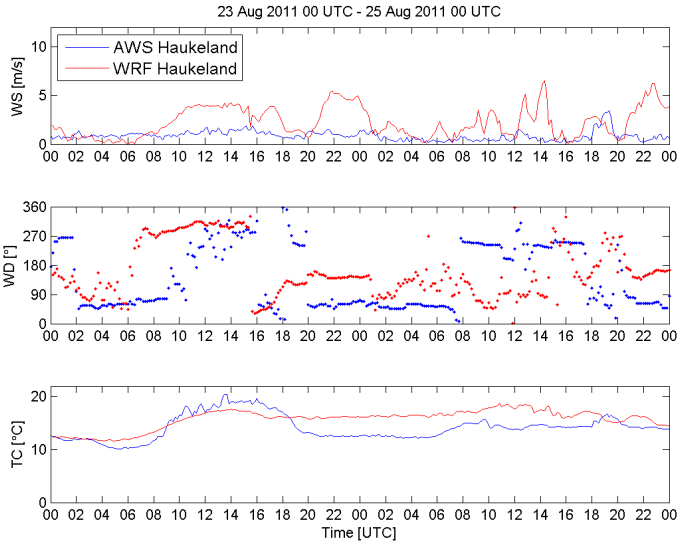

Figure D.4: *Model results (red) compared to the observations (blue) at Haukeland for the period 23 Aug 2011 00 UTC - 25 Aug 2011 00 UTC.*

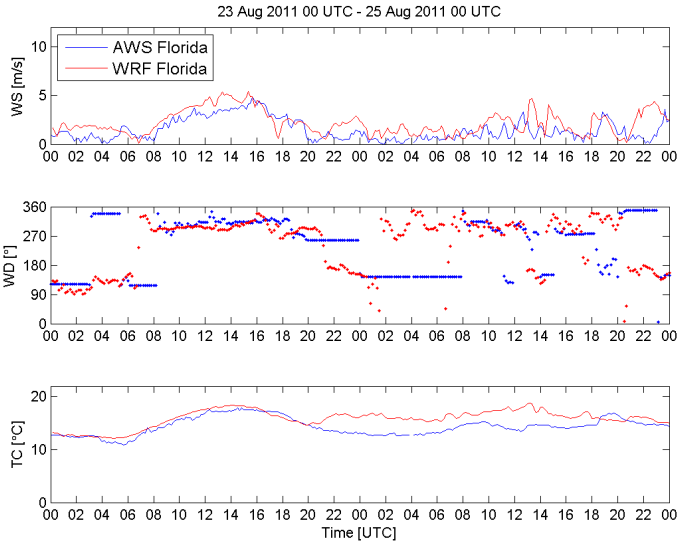

Figure D.5: *Model results (red) compared to the observations (blue) at Florida for the period 23 Aug 2011 00 UTC - 25 Aug 2011 00 UTC.*

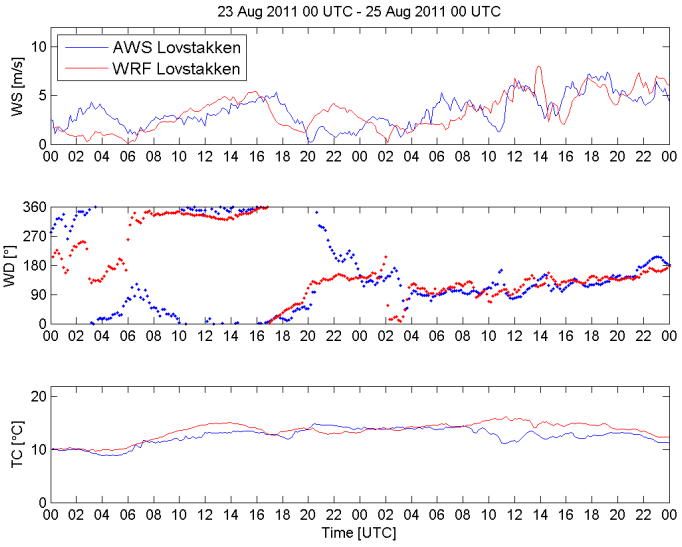

Figure D.6: *Model results (red) compared to the observations (blue) at Løvstakken for the period 23 Aug 2011 00 UTC - 25 Aug 2011 00 UTC.*

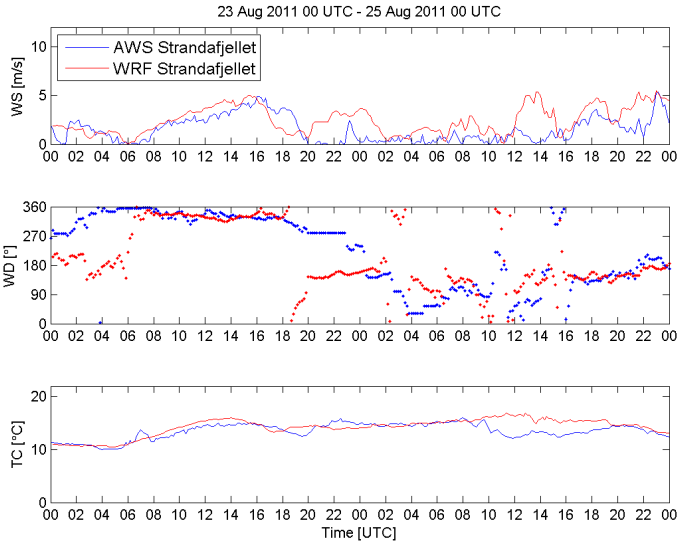

Figure D.7: *Model results (red) compared to the observations (blue) at Strandafjellet for the period 23 Aug 2011 00 UTC - 25 Aug 2011 00 UTC.*

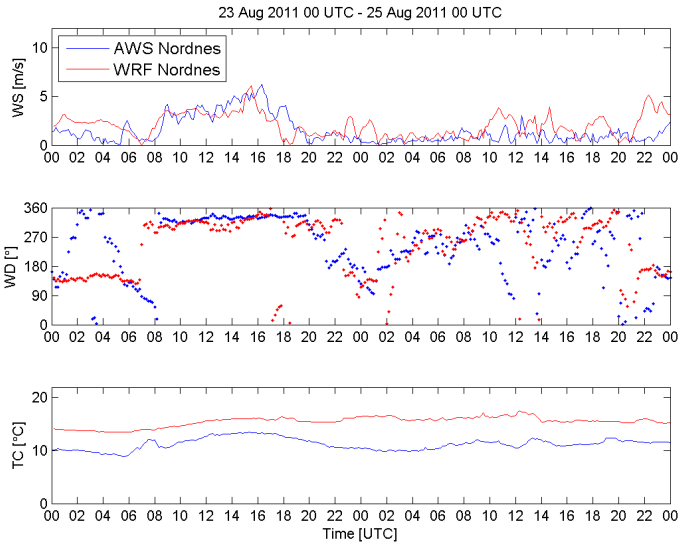

Figure D.8: *Model results (red) compared to the observations (blue) at Nordnes for the period 23 Aug 2011 00 UTC - 25 Aug 2011 00 UTC.*

Appendix E

Inversion

E.1 The full synoptic development

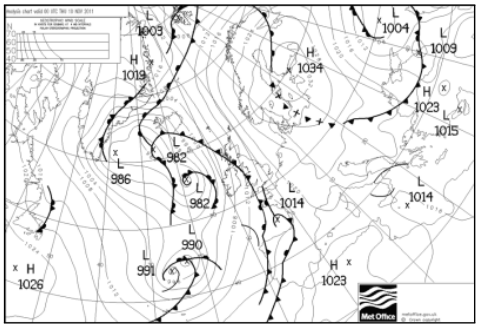

(a) 10 Nov 2011 00 UTC

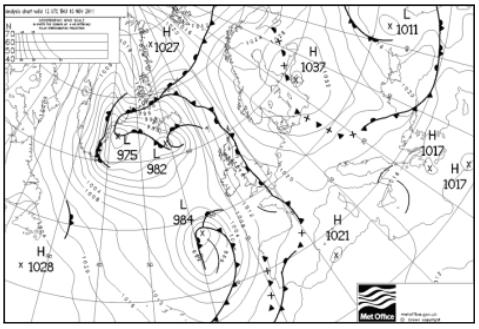

(b) 10 Nov 2011 12 UTC

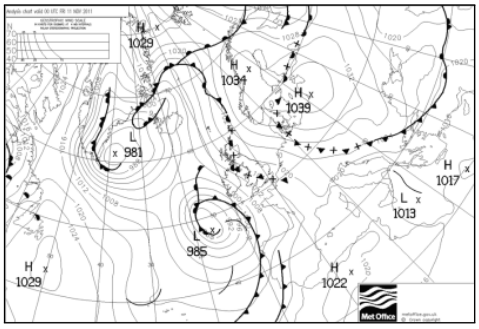

(c) 11 Nov 2011 00 UTC

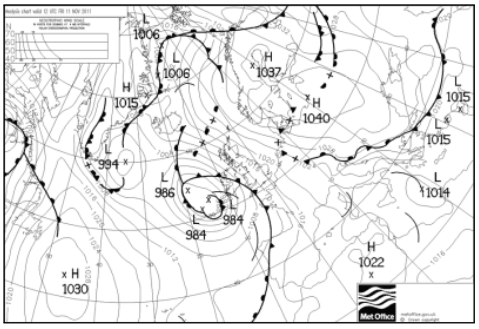

(d) 11 Nov 2011 12 UTC

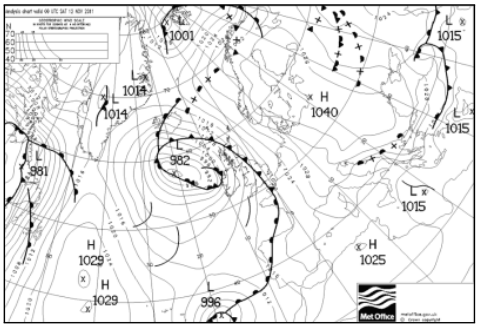

(e) 12 Nov 2011 00 UTC

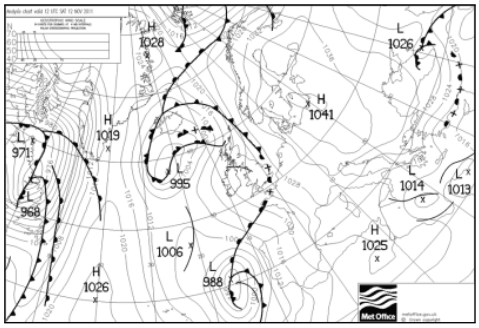

(f) 12 Nov 2011 12 UTC

Figure E.1: *The synoptic development of the inversion case during November 2011 (Source: UK Met Office).*

E.2 Measured and modeled time series for all the seven AWSs

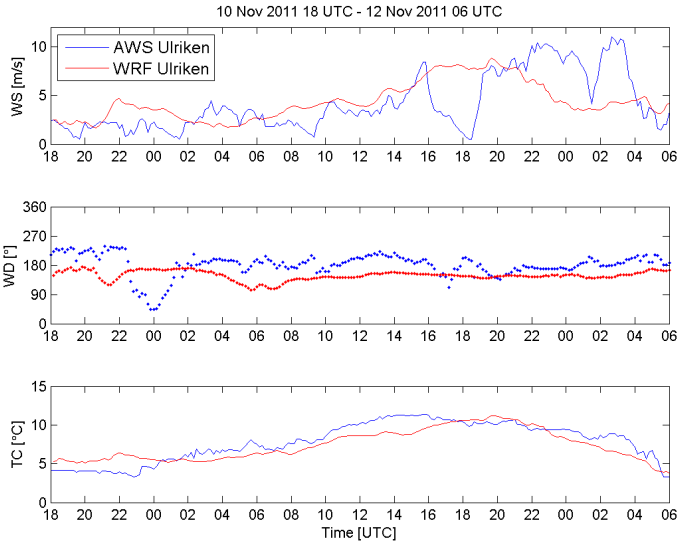

Figure E.2: *Model results (red) compared to the observations (blue) at Ulriken for the period 10 Nov 2011 18 UTC - 12 Nov 2011 06 UTC.*

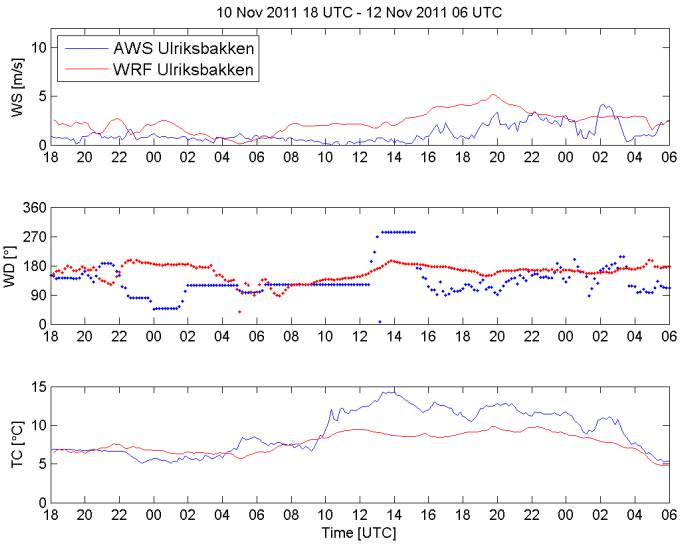

Figure E.3: *Model results (red) compared to the observations (blue) at Ulriksbakken for the period 10 Nov 2011 18 UTC - 12 Nov 2011 06 UTC.*

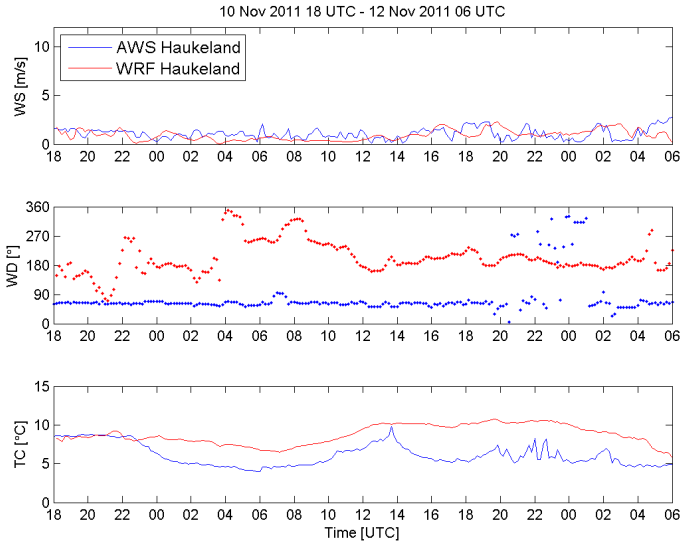

Figure E.4: *Model results (red) compared to the observations (blue) at Haukeland for the period 10 Nov 2011 18 UTC - 12 Nov 2011 06 UTC.*

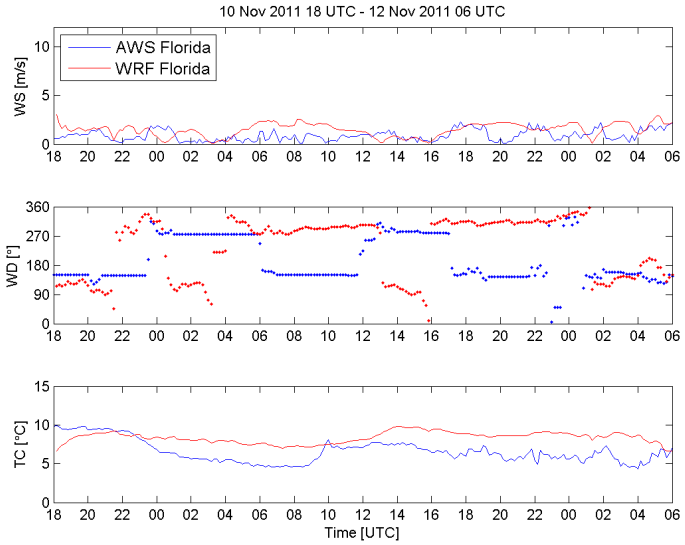

Figure E.5: *Model results (red) compared to the observations (blue) at Florida for the period 10 Nov 2011 18 UTC - 12 Nov 2011 06 UTC.*

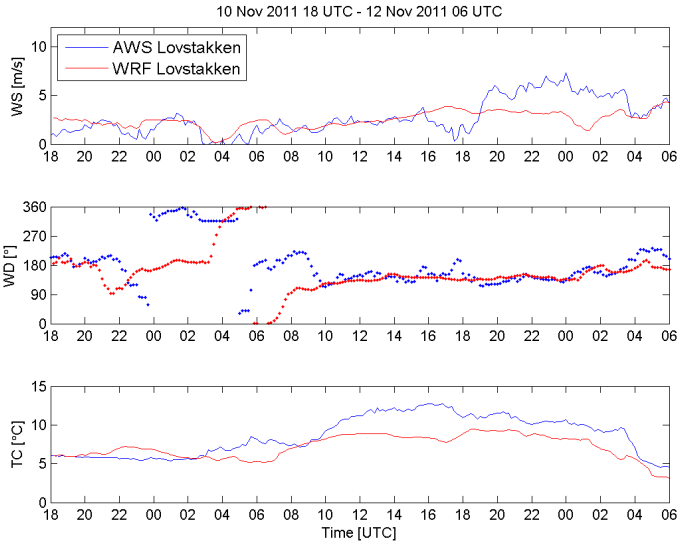

Figure E.6: *Model results (red) compared to the observations (blue) at Løvstakken for the period 10 Nov 2011 18 UTC - 12 Nov 2011 06 UTC.*

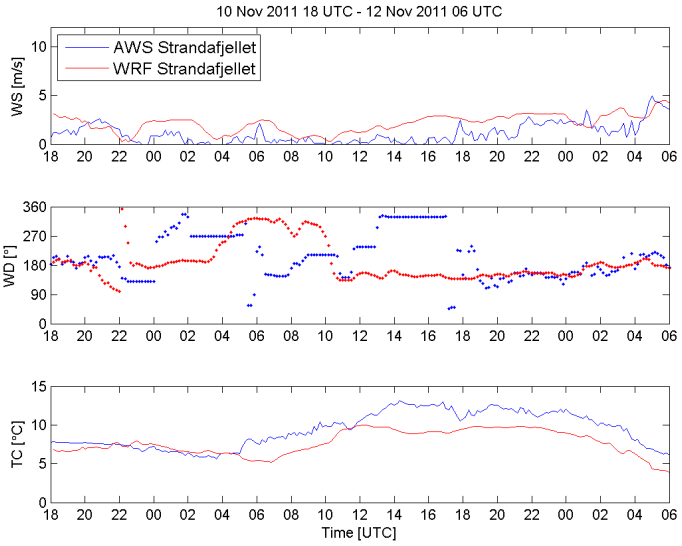

Figure E.7: *Model results (red) compared to the observations (blue) at Strandafjellet for the period 10 Nov 2011 18 UTC - 12 Nov 2011 06 UTC.*

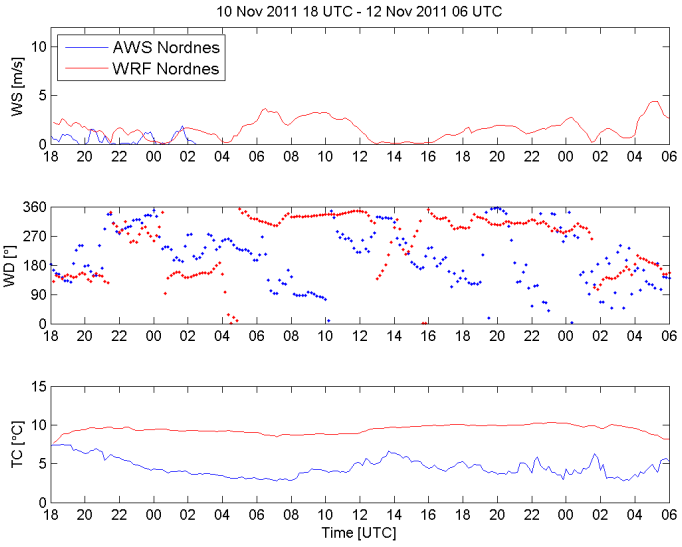

Figure E.8: *Model results (red) compared to the observations (blue) at Nordnes for the period 10 Nov 2011 18 UTC - 12 Nov 2011 06 UTC.*

E.3 Vertical cross sections of wind speed

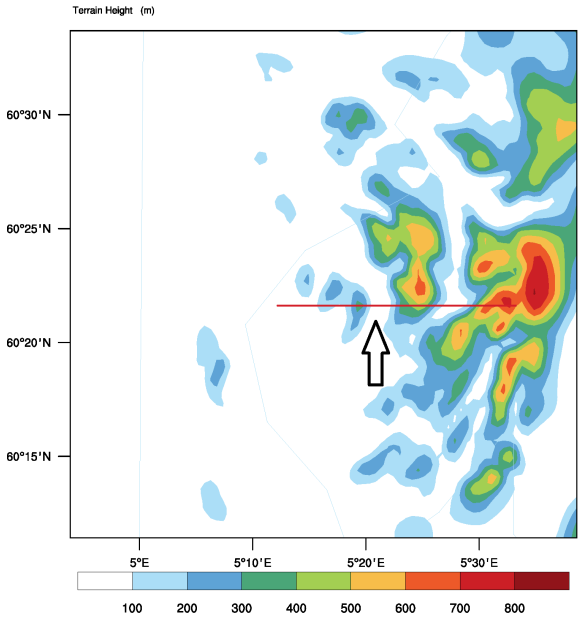

(a) The cross section

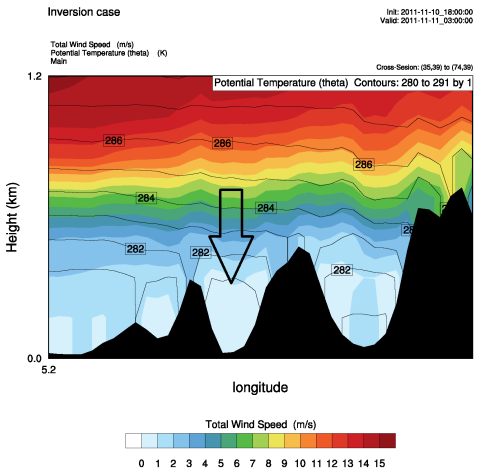

(b) 11 Nov 2011 03 UTC

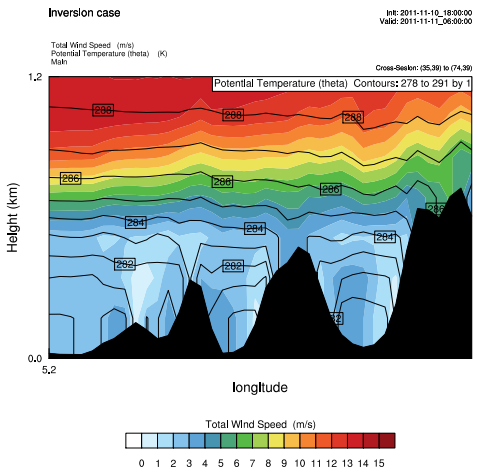

(c) 11 Nov 2011 06 UTC

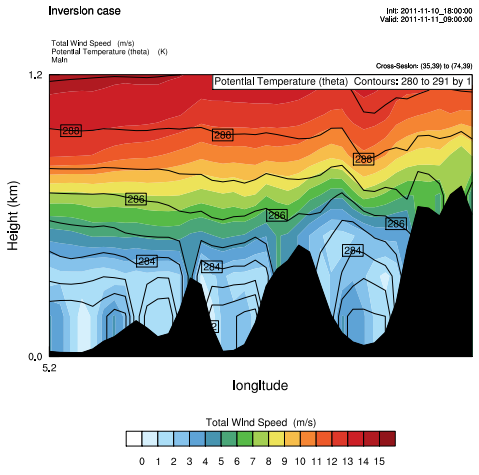

(d) 11 Nov 2011 09 UTC

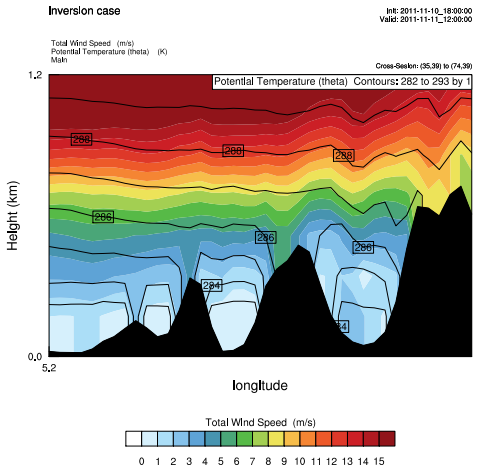

(e) 11 Nov 2011 12 UTC

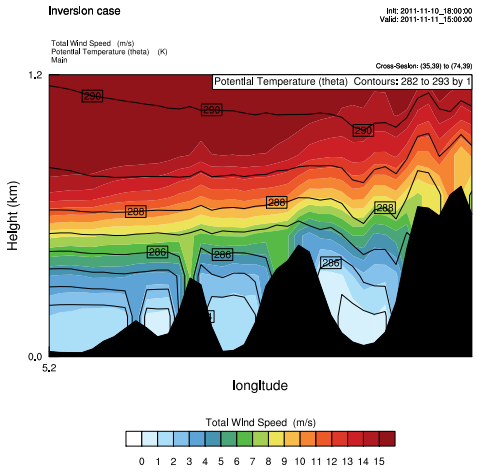

(f) 11 Nov 2011 15 UTC

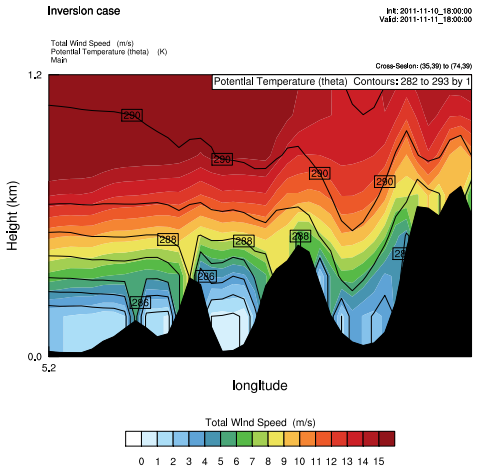

(g) 11 Nov 2011 18 UTC

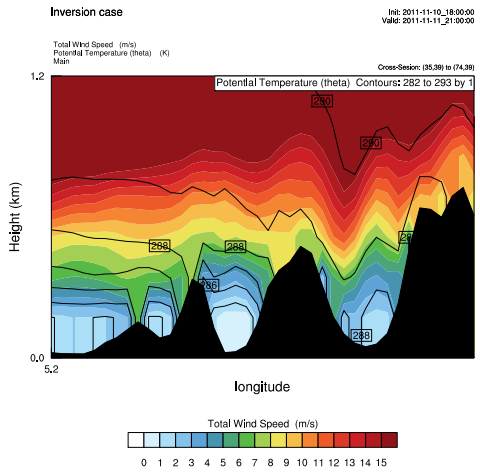

(h) 11 Nov 2011 21 UTC

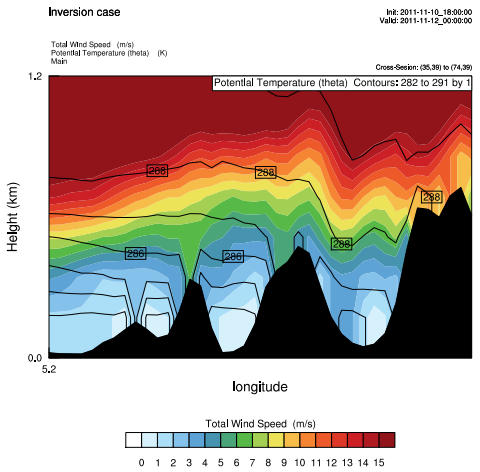

(i) 12 Nov 2011 00 UTC

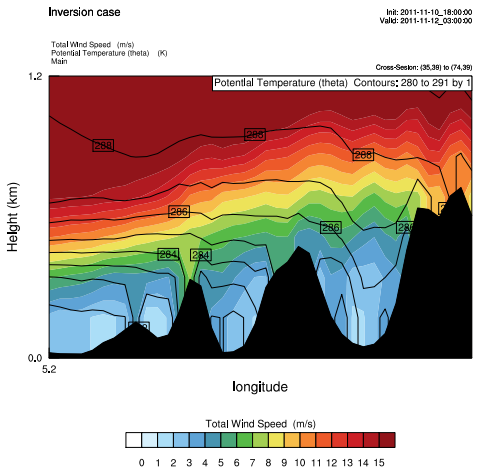

(j) 12 Nov 2011 03 UTC

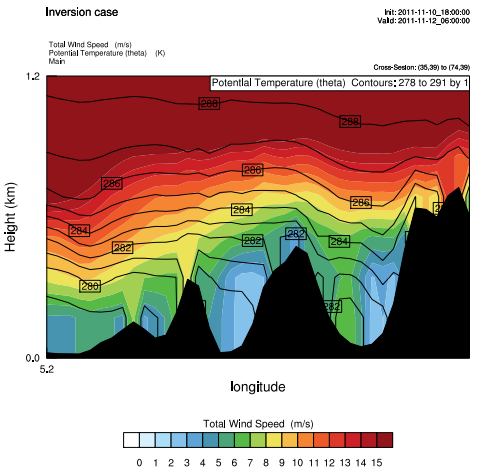

(k) 12 Nov 2011 06 UTC

Figure E.9: *The development of the simulated wind speed during the inversion case every third hour from 11 Nov 2011 03 UTC - 12 Nov 2011 06 UTC. The wind speed [m/s] is shaded, and the potential temperature [K] is shown in the contours. The cross section is shown in (a), and the location of the Bergen valley is shown with a black arrow in (a) and (b), with Løvstakken to the left, and Ulriken to the right.*

Bibliography

Aanderaa Data Instruments AS (AADI). Aanderaa Instruments - Data Collecting Instruments for Land Sea and Air. Technical Data Sheet, October 2000. URL `http://www.hymetco.com.vn/images/images_pro/f_128.pdf`. Accessed: 23/05/2012.

Aanderaa Data Instruments AS (AADI). Sensor Scanning Unit 3010. Product Data Sheet, D175, November 2001.

Aanderaa Data Instruments AS (AADI). Data Storage Unit 2990. Product Data Sheet, D174, April 2010.

P.S. Arya. *Introduction to Micrometeorology*, volume 79 of *International Geophysics Series*. Academic Press, 2001.

I. Barstad and S. Grønås. Southwesterly flows over southern Norway – mesoscale sensitivity to large-scale wind direction and speed. *Tellus A*, 57(2):136–152, 2005.

E. Berge and F. Hassel. *En undersøkelse av temperaturinversjoner og lokale drenasjestrømmer i Bergen*, volume 2-1984 of *Meteorological Report Series*. Universitetet i Bergen, 1984.

F. Chen and J. Dudhia. Coupling an advanced land surface-hydrology model with the Penn State-NCAR MM5 modeling system. Part 1: Model implementation and sensitivity. *Monthly Weather Review*, 129(4):569–585, 2001.

J. Dudhia. Numerical study of convection observed during the winter monsoon experiment using a mesoscale two-dimensional model. *Journal of the Atmospheric Sciences*, 46(20):3077–3107, 1989.

H.V. Dyngeseth. Simuleringar av lokale sirkulasjonar og inversjon i Bergensområdet med ein mesoskala modell. Master's thesis, Universitetet i Bergen, 1998.

Fischer. Aspirations-Psychrometer Assman. Product Data Sheet, March 2005. URL `http://fischer-barometer.de/meteoclima/datenblaetter/E430101.pdf`. Accessed: 23/05/2012.

K. Harstveit. Kartlegging av ekstreme vindforhold i Bergen kommune. *met.no Report*, 3, 2006.

D.L. Hartmann. *Global physical climatology*, volume 56 of *International Geophysics Series*. Academic Press, 1994.

S.Y. Hong, J. Dudhia, and S.H. Chen. A revised approach to ice microphysical processes for the bulk parameterization of clouds and precipitation. *Monthly Weather Review*, 132(1):103–120, 2004.

Z.I. Janjic. Physical package for the step-mountain, eta coordinate model. *Monthly Weather Review*, 118:1429–1443, 1990.

Z.I. Janjic. The surface layer in the NCEP eta model. *11th conference on numerical weather prediction, American Meteorological Society*, pages 354–355, 1996.

Z.I. Janjic. Nonsingular implementation of the Mellor–Yamada level 2.5 scheme in the NCEP Meso model. *NCEP Office Note*, 437:61, 2002.

M.O. Jonassen, H. Ólafsson, J. Reuder, and J.A. Olseth. Multi-scale variability of winds in the complex topography of southwestern Norway. *Tellus A*, 64(0), 2012a.

M.O. Jonassen, H. Ólafsson, A.S. Valved, J. Reuder, and J.A. Olseth. Simulations of the Bergen orographic wind shelter. Submitted to Tellus A in 2012, 2012b.

R. Laprise. The euler equation of motion with hydrostatic pressure as an independent variable. *Monthly Weather Review*, 120(1):197–207, 1992.

E.J. Mlawer, S.J. Taubman, P.D. Brown, M.J. Iacono, and S.A. Clough. Radiative transfer for inhomogeneous atmospheres: RRTM, a validated correlated-k model for the longwave. *Journal of Geophysical Research*, 102(D14):16663–16682, 1997.

T.R. Oke. *Boundary Layer Climates*. Routledge, London, 1987.

H. Ólafsson and P. Bougeault. Nonlinear Flow Past an Elliptic Mountain Ridge. *Journal of the Atmospheric Sciences*, 53:2465–2489, 1996.

Onset Computer Corporation. RG2 & RG2-M Mounting Template - Data Logging Rain Gauge Manual, 2001. URL `http://www.onsetcomp.com/files/manual_pdfs/5470-B-MAN-RG2.pdf`. Accessed: 23/05/2012.

G. Rampanelli, D. Zardi, and R. Rotunno. Mechanisms of up-valley winds. *Journal of the Atmospheric Sciences*, 61(24):3097–3111, 2004.

W.C. Skamarock, J.B. Klemp, J. Dudhia, D.O. Gill, D.M. Barker, M.G. Duda, X.Y. Huang, W. Wang, and J.G. Powers. A Description of the Advanced Research WRF Version 3. NCAR Technical Note, NCAR/TN-475+STR. June 2008.

R.B. Stull. *An Introduction to Boundary Layer Meteorology*. Springer, 1988.

K. Utaaker. *Mikro- og lokalmeteorologi: det atmosfæriske miljø¸ på liten skala*. Alma Mater, Bergen, 1991.

K. Utaaker. *Energi i arealplanleggingen: lokalklima i Bergen*, volume nr 1-1995 of *Meteorological Report Series*. Geofysisk Institutt, Universitetet i Bergen, 1995.

Vaisala. PTB220TS Barometer Case and Battery. Technical Data Sheet, November 2001. URL `http://www.gbm.co.kr/data/pro_dwn/pdf/pro12_01_02_01_01.pdf`. Accessed: 23/05/2012.

J.M. Wallace and P.V. Hobbs. *Atmospheric science: an introductory survey*, volume 92 of *International Geophysics Series*. Academic Press, 2006.

C.D. Whiteman and J.C. Doran. The relationship between overlying synoptic-scale flows and winds within a valley. *Journal of Applied Meteorology*, 32:1669–1682, 1993.

L.J. Wicker and W.C. Skamarock. Time-splitting methods for elastic models using forward time schemes. *Monthly Weather Review*, 130(8):2088–2097, 2002.

D. Zardi and C.D. Whiteman. *Mountain weather research and forecasting, Ch.2: Diurnal Mountain Wind Systems*. Springer, Berlin, 2012.

During this master's thesis I have contributed
to the manuscript of the following article
which has been submitted to
Tellus A in 2012.

Tellus **000**, 000–000 (0000) Printed July 25, 2012 (Tellus LaTeX style file v2.2)

Simulations of the Bergen orographic wind shelter

By Marius O. Jonassen[1]*, Haraldur Ólafsson[1,2], Aslaug S. Valved[1], Joachim Reuder[1], Jan A. Olseth[1],

[1] *Bergen School of Meteorology, Geophysical Institute, University of Bergen, Allégaten 70, Bergen, Norway;* [2] *Dpt. of Physics, University of Iceland. Icelandic Meteorological Office, Bústaðavegi 9, IS-150 Reykjavík Iceland*

July 25, 2012

ABSTRACT

Even though the coast of Western Norway is very windy, the centre of Bergen is rather calm. To gain further understanding of this wind shelter, we study the flow in the complex topography of Bergen during two southwesterly windstorms, using surface observations and high resolution numerical simulations. The results reveal large spatial variability in the local wind field. In some areas, there are periods of sustained winds of more than 25 m s^{-1}, while at nearby locations the winds are typically less than 5 m s^{-1}. The centre of Bergen is among the calmest areas. To investigate the effect of the individual mountains upstream (Løvstakken) and downstream (Fløyen) of the Bergen city centre, they have stepwise been removed from the model topography. Areas with relatively large wind speed reductions are found immediately downstream of Løvstakken and immediately upstream of Fløyen. At Florida, situated close to the city centre, both a wake effect of Løvstakken and a blocking effect of Fløyen are evident, but the latter is most prominent. The total impact of both mountains on the winds in the city is close to the sum of each of them. A spillover effect of Løvstakken acts to substantially increase the local precipitation in the centre of Bergen.

1 Introduction

The centre of Bergen, as represented by the weather station "Florida", appears to be remarkably sheltered during strong southwesterly flow (Harstveit, 2006; Jonassen et al., 2012). It is, however, unclear if this sheltering effect (hereby referred to as the "Bergen

* Corresponding author.

e-mail: marius.jonassen@gfi.uib.no

shelter") is caused by a wake of the upstream mountain massif of Løvstakken, a blocking by the downstream mountain massif of Fløyen or a combination of both. It is also unclear whether the wind observations at Florida are representative for the city centre of Bergen as a whole. These are the main questions to be answered in this study. The results may serve as guidance for studies of local dispersion of pollutants and weather forecasting in the area.

There are numerous studies on how larger scale flow is affected by the south Norwegian mountain range. Such investigations were initiated already during the early days of the Bergen School of Meteorology (Bjerknes and Solberg, 1921; 1922). Their studies were continued by Spinnangr (1943) and Andersen (1975). More recently, Barstad and Grønås (2005; 2006) identified and explained several meso-scale flow structures frequently forming over and around the topography of Southern Norway for flow within the sector south to west. Studies on local scale flow in the Bergen area, on the other hand, are few and focus mainly on thermally driven winds (Utaaker, 1995) and temperature inversions (Berge and Hassel, 1984).

Many of the flow patterns forming in connection to topography can be diagnosed using the non-dimensional mountain height $\hat{h}{=}Nh/U$ (e.g. Pierrehumbert and Wyman, 1985), where N is the Brunt-Väisälä frequency, describing the buoyancy on a vertically displaced air parcel, h is the mountain height and U is the flow speed of the airmass impinging on the mountain (e.g. Lin and Wang, 1996; Trüb and Davies, 1995; Ólafsson and Bougeault, 1996; Peng et al., 1995). High values of $\hat{h}$ facilitate for blocked flow leading to more of the flow going around than over the mountain. For low values of $\hat{h}$, the flow typically passes over the mountain and weak gravity waves may form. In the complex topography of southwestern Norway, these flow patterns frequently form at the larger scale as documented in the aforementioned literature. The same flow patterns should be expected to form at the lesser documented smaller scale, which we focus on in this study.

Topographically modified flow also affects precipitation (e.g. Jiang, 2003; Smith, 2006). Orographic precipitation, i.e. precipitation that is formed as moist air is forced to ascend over mountains, is an integral part of the climate of Western Norway, both in terms of mean values (e.g. Reuder et al., 2007), as well as extremes (Steensen et al., 2011). The phenomenon is of essential importance to a range of environmental factors of both direct and indirect influence on people, such as the local hydrology, long-term trends in terrain evolution, development of glaciers etc. Mountains enhance precipitation on their upwind side, but this enhancement may extend downstream of the mountains' crest as the precipitation elements are transported

downwind while forming and falling to the ground (the 'spillover effect') (e.g. Sinclair et al., 1996). The mean annual precipitation in the city of Bergen is 2250 mm, which is almost twice the value of precipitation at locations along the Norwegian southwest coast that are far away from mountains, such as Stavanger (1250 mm). It is well recognized that the larger scale topography of southern Norway has a central role in creating the high precipitation amounts along the southwest coast of Norway where Bergen is situated (e.g. Teigen, 2005). It is, however, not clear how large the contribution from the local topography is, e.g. through the above described spillover effect.

The primary purpose of this paper is to investigate the above introduced Bergen shelter effect. As a bi-product of this investigation, some results on precipitation will be presented. We study the local flow field in Bergen during two southwesterly windstorms that hit the southwest coast of Norway on 10 January, 2009 (Case 1) and 25 December, 2012 (Case 2). Data from a dense network of automatic weather stations (AWS) along with high resolution numerical simulations with the Weather Research and Forecasting model (WRF) (Skamarock et al., 2008) are used. The latter storm, named Dagmar by the Norwegian Meteorological Institute (met.no), caused floodings, property damage and even casualties along the coast in the areas most severely affected. The former windstorm is believed to be a more typical storm for the winter season in the region.

2 Atmospheric data

2.1 Case studies: Two southwesterly windstorms

On 10 January, 2009, a low pressure system to the south of Iceland and a high pressure system over central Europe induced a strong southwesterly flow along the coast of Southwestern Norway (Figure 1). This low pressure system moved slowly towards the northeast, and the associated flow over the Bergen area remained fairly stationary throughout the day. The system of 25 December, 2011, on the other hand, moved rather quickly eastwards. The general flow direction over Southwestern Norway thus shifted from southwesterly in the beginning of the day to westerly towards the evening.

2.2 Observations

There is a fairly dense network of AWSs in the Bergen area. The main AWS in Bergen is situated in the city centre and called "Florida". At Florida, the observations are made on

the top of the building of the Geophysical institute (GFI), University of Bergen, around 30 m above the surrounding ground. There is also a station on the top of the highest nearby mountain, Mount Ulriken. In addition, there is an AWS at the airport of Flesland, some 10 km to the south of Florida, and at Mount Sotra, situated to the west of the latter. Another station is situated at the Sotra bridge. All these stations were in service during the windstorm on 10 January, 2009. From the windstorm on 25 December, 2011, data from a network of 5 additional stations in Bergen are available from a research project at GFI.

An overview over the AWSs is given in Table 2 and their geographical locations are indicated in Figure 2.

The observed wind speed presented in the following, is from the unprocessed raw data. In the later comparison with the simulated wind speed, however, we have converted the observed wind speed (u_z) to the height of the lowermost half sigma level in the WRF model setup (z=19.5 m.a.g.l.) using the following following formula:

$$u_z = \frac{u_*}{\kappa}\left[\ln\left(\frac{z-d}{z_0}\right) + \psi(z, z_0, L)\right]$$

Here, u_* is the friction velocity (m s^{-1}) and z_0 is the roughness length in metres. The value of z_0 used for each AWS is indicated in Figure 5. d is the zero displacement length (m), i.e. the height adjacent to the obstacle (here building) at which the wind speed is zero. d is set to 2/3 of z_0, where z is 30 m for Florida and Nordnes. In the calculations, we have assumed neutral atmospheric stability, and hence $\psi(z, z_0, L)$, in which the Monin-Obukhov stability parameter, L, is set to zero. Setting L to zero is presumably a close approximation to reality because the investigated weather situations contain relatively high wind speeds, thus providing significant turbulent mixing of momentum.

During the two studied windstorms, the AWS observations reveal a large spatial variability in the wind field in the area (Figure 3). While the wind speed at the top of Mount Ulriken reaches more than 25 m s^{-1} in both cases, the wind speed at Florida, situated in the middle of the Bergen valley, barely exceeds 12 m s^{-1} in any of the cases.

The results from Case 2 allow for a more detailed investigation of the wind in the centre of Bergen because they include more AWS observations from the area. The wind speed observed in the northern part of the city centre (Nordnes) is stronger than at Florida. It is in fact more similar to the wind speed observed at Flesland, which is situated some 10 kilometres to the south of Florida and is more exposed to the strong winds.

While the wind speed at most AWSs decreases as the flow turns westerly in Case 2 (after 1800 UTC), it remains the same or is even slightly higher at Florida (the same is seen at the mountain stations of Strandafjellet and Løvstakken). When compared to the wind direction at Ulriken, which is on average found to be in reasonable agreement with the larger scale flow direction (Jonassen et al., 2012), the wind direction observed at the other AWSs show large deviations towards a more south and southeasterly direction for the southwesterly flow of Case 1. In the southwesterly flow of Case 2 (before 1800 UTC), the deviations are even larger and it is particularly large at Florida. This deviation is undoubtedly caused by the strong alignment of the flow to the Bergen valley at this location. In the westerly flow of Case 2 (after 1800 UTC), there is, on the other hand, a clear agreement in the wind direction for all stations. An exception is the AWS at Haukeland, where the wind speed is very low at this time.

2.3 Numerical simulations

In order to further investigate the local wind in the Bergen area during the two studied windstorms, and how it is modified by the surrounding topography, we have numerically reproduced the flow during both case studies with high horizontal resolution using the WRF model. The modeling system is fully compressible and is in this study run in non-hydrostatic mode using three one-way nested domains with horizontal resolutions of respectively 4.5, 1.5 km and 500 m. The outermost and coarsest domain (720 x 270 km^2) covers approximately the extent of Southern Norway and the innermost domain (42.5 x 42.5 km^2) covers a limited area centred around the city of Bergen. There are 61 vertical terrain following sigma levels with an increased density towards the ground and the lowest level is at approximately 36 m above the ground. The prognostic variables for temperature, humidity and wind are vertically staggered implying that they are calculated at each model half-level with the lowermost at an altitude of approximately 19.5 m above the ground. The two simulations cover respectively the 24 hour periods of 10-11.01.2009 and 25-26.12.2011 which of the first 6 hours are considered as spin-up. The RRTM scheme (Mlawer et al., 1997) is used for long wave radiation, the Dudhia scheme (Dudhia, 1989) for short wave radiation, and the Unified NCEP/NCAR/AFWA Noah land-surface model (Chen and Dudhia, 2001) with soil temperature and moisture in four layers for surface physics. Furthermore, the Mellor Yamada Janjic scheme (Janjic, 1990; 1996; 2002) is used for the parameterisation of the boundary

layer. The WSM 3-class simple ice scheme (Dudhia, 1989; Hong et al., 2004) is chosen for the parameterisation of microphysics with cloud water/ice, and rain/snow as prognostic variables. Operational analysis from the European Centre for Medium-Range Weather Forecasts (ECMWF) with a horizontal resolution of 0.125 degrees is used to initialise and force the model at its boundaries every 6 hour.

2.4 The simulation results

2.4.1 Sensitivity to model topography and landuse data We have carried out a number of sensitivity experiments in this study. The first set of experiments concerns the landuse and topography datasets. These are the datasets describing the physiographical model surface in terms of land coverage of e.g. sea, forest, agricultural landscape and cities, and topography height. The landuse determines to a large extent the local surface energy and momentum budget. Of probably the greatest importance to this study, which is focused on strong wind speeds, are accurate descriptions of the surface roughness length for momentum (z_0). In WRF, z_0 is along with the albedo, the emissivity and other parameters prescribed for each landuse type using a lookup table.

The most frequently used landuse dataset in WRF originates from the United States Geological Survey (USGS), and has a horizontal resolution of approximately 1 km (30 arc seconds). For high resolution simulations, the resolution and accuracy of this dataset is previously found to be insufficient (e.g. Cheng and Byun, 2008; Arnold et al., 2012). To further investigate the validity of this finding to the present study, a new dataset from GlobCorine is used in an additional set of sensitivity experiments. This dataset is based on data from 2009 and is thus of newer date than the USGS dataset (1992-1993). GlobCorine has a horizontal resolution of approximately 300 m and it has fewer landuse categories than the USGS set (13 vs. 24). In this study, we use the same look-up table for albedo, roughness etc. for the GlobCorine data as for the USGS dataset. Each landuse category in the GlobCorine dataset has been manually adopted to its closest approximate in the USGS dataset, meaning that for example the GlobCorine "forest" has been set to "mixed forest" and so on. A complete list of these conversions is given in table 3.

The roughness length for both the landuse datasets as well as the true roughness length at each of the AWSs are indicated in Figure 5. The true roughness length is estimated

Table 1. WRF sensitivity experiments with different landuse and topography datasets. See text for further explanations.

name	landuse	topography
USUS	USGS	USGS
USAS	USGS	Aster
GLUS	GlobCorine	USGS
GLAS	GlobCorine	Aster

by using the values from the WRF lookup table that correspond to the realistic landuse category at the location of each AWS.

Figure 4 shows the landuse over a zoom-in of the finest model domain (500 m horizontal resolution) for the USGS and GlobCorine datasets. It can be seen that, even though GlobCorine has fewer categories, it displays significantly more fine scale spatial details in the land use field. Also, the GlobCorine coastline matches the high resolution coastline from the Global Self-consistent, Hierarchical, High-resolution Shoreline Database, (GSHHS) significantly better than does the USGS coastline.

In addition to the USGS topography dataset, we employ a topography dataset from the Advanced Spaceborne Thermal Emission and Reflection Radiometer (ASTER). The dataset is made in a joint effort between the Ministry of Economy, Trade, and Industry (METI) of Japan and the United States National Aeronautics and Space Administration (NASA). The horizontal resolution is 1 arc second (30 m) as opposed to the 30 arc seconds of the USGS topography dataset. We have made a couple of adjustments to the USGS topography and GlobCorine landuse datasets. The USGS topography dataset features in its standard WRF setup an apparent westwards shift of approximately 500 m when compared to reality (AWS station heights) and the ASTER dataset. We therefore corrected it accordingly in the preprocessing of the model data input. Also, a smaller area (approximately 1x1 km) surrounding Nordnes does not have an urban landuse category in the GlobCorine dataset. Since this area is a part of the centre of Bergen, which is of central interest to this study, the error was corrected accordingly.

The main results from the landuse and topography sensitivity experiments are presented in Figure 6. The figure shows the average root mean squared error (RMSE) and mean error (bias) between the available AWS wind speed observations and the corresponding model point estimations.

The error statistics reveals only a marginal sensitivity to the applied model landuse and topography datasets. In Case 1, using the GLAS setup gives both the lowest average RMSE

(2.4 m s^{-1}) and the lowest average bias (1.3 m s^{-1}). In Case 2, there is no such consistent improvement for any of the experiments. Relatively large wind speed biases are found at Mount Ulriken, with the largest ones being around 6 m s^{-1} in the USUS setup for Case 2. Using the high resolution terrain dataset from ASTER has a clear advantage over using the USGS dataset for Ulriken. At this location, there is a reduction in the wind speed RMSE and bias of around 1 m s^{-1} in both cases. In the further analysis of the model results, the GLAS setup is used, which combines the two highest resolution datasets (GlobCorine and ASTER).

2.5 The Bergen shelter

The simulated larger scale flow (Figure 7) compares reasonably well with surface stations situated along the South Norwegian coast. The synoptic flow pattern in southwestern Norway did not change much during the course of the day in Case 1. The flow during Case 2, on the other hand, started out as southwesterly and ended as westerly. The simulation results show that both cases are associated with strong wind with more than 30 m s^{-1} off the northwestern corner (west cape) and over the central mountain range of Southern Norway (Langfjella). These flow patterns are typical for southwesterly storms in the region (Barstad and Grønås, 2005).

In the Bergen area, the model matches in general the near surface observed wind speed and wind direction well (Figures 8 and 9). As commented on in the above error statistics analysis, the largest average deviations are found at mount Ulriken. Also the simulated wind direction at Ulriken is off by some 20° towards the south in both cases. The model times quite accurately the shift towards westerly winds around 1500 UTC in Case 2 at all stations. An exception is Florida, where this shift is delayed by a couple of hours. The wind speed at Florida is, however, less than 5 m s^{-1} at this time.

A main goal of this article is to investigate how the mountains surrounding the centre of Bergen impact the local flow field in the southwesterly storms. We have done this through three different sensitivity experiments, in which the following modifcations to the model topography have been applied (see Figure 2): 1) the Løvstakken massif is removed (NOL), 2) the Fløyen massif is removed (NOF) and 3) both of them are removed (NOFL). The results from these experiments are presented in the following.

From Figure 10, showing the near surface wind speed at 0000 UTC on 11 January, 2009,

in the CTRL run and the difference between this and the three topography sensitivity experiments, several deducations can be drawn. Firstly, the simulated local flow field evidently features a considerable spatial variability (Figure 10 a), ranging from 2-20 m s^{-1} thus supporting the impression given from the above analysis of the AWSs observations. The highest wind speeds are found along the coast and at the mountain tops. The lowest wind speeds are found immediately up- and downstream of the local mountains and hills. The centre of Bergen appears to be one of the calmer areas. Removing the mountain massif of Løvstakken (Figure 10 b) gives a wind speed increase in most parts of the centre of Bergen of 2-6 m s^{-1}. The highest increase is found closest to the massif itself. Removing Fløyen (Figure 10 c) causes a wind speed increase of up to 6 m s^{-1} in an area immediately upstream of the massif. When removing both massifs (Figure 10 d), the effect on the wind field in the Bergen valley is the largest and wind speed increases of up to 8 m s^{-1} are seen over larger parts of the city centre. The wind field in the northernmost part of the city centre (around the AWS at Nordnes) is least affected by the model topography modifications.

The above findings allow for the definition of four areas with characteristic flow patterns during the large-scale southwesterly flow, as indicated in Figure 11: The 'Wake area' is the area immediately downstream of Løvstakken, which is mainly affected by this massif. The 'Less calm area' experiences the smallest effect of the surrounding mountains. The 'Block area' is mainly affected by 'Fløyen' and 'Florida area', which is the area representative for the main AWSs in the centre of Bergen, is affected by both the presence of Løvstakken and Fløyen. The temporal development of changes in wind speed within each of the areas, as caused by the topography modifications, is shown in Figure 12. The situation is fairly stationary in most of Case 1, with a slight tendency towards an increased shelter effect and a more westerly synoptic flow towards the end of the day. In Case 2, there is a complete change in wind speed within the four areas at around 1600 UTC, as the synoptic wind turns from southwest to west. The area categorisation made above for the southwesterly wind does no longer hold for the westerlies. The location of the area affected by Løvstakken shifts further to the south (Figure 13). Fløyen, on the other hand, affects an area further to the north and the effect of removing both mountain massifs resembles a superposition of the two former effects. Otherwise, for the southwesterly part of Case 2, the spatial flow patterns seen for the topography modifications resembles closely that of Case 1 (not shown).

2.6 The vertical flow structure

As in the above described horizontal near surface wind field, the wind speed reduction in the vertical is largest immediately down- and up-stream of respectively Løvstakken and Fløyen (Figure 14). The vertical extent of the effect from removing Løvstakken is relatively low when compared to the effect from removing Fløyen, which extends to levels roughly twice that of the nearby mountain tops. Upstream of Løvstakken, there is a sign of a small blocking effect (equal to or less than 2 m s^{-1}), which extends to elevations between 1.5 (NOL) and 2 times the height of this mountain (NOFL).

The combined effect of removing both mountain massifs (NOFL, Figure 14 d) is close to the effect of the blocking alone and it is strongest at around 50 m.a.g.l., where it reduces the wind speed by up to 8 m s^{-1}. Above all mountain crests, there are signs of speedup when comparing the runs with and without the original model topography.

2.7 Impact of the local topography on the precipitation field

It is evident that the local topography surrounding Bergen should have an impact on the precipitation in the area. Although precipitation is not the main focus of this article, a short analysis of this parameter is presented. Figure 15, shows the simulated precipitation accumulated between 0600 and 2400 UTC on 10 January 2009. The largest precipitation amounts are found downstream of the local mountain and hill tops. In most of the centre of Bergen, the simulated 18 hour accumulated precipitation is between 15 and 20 mm, which compares quite well with the observed amount at Florida of 18 mm. In the flat area immediately upstream of Løvstakken, the model predicts only roughly half of this amount. Removing Løvstakken from the model topography (Figure 15 b), brings the amount of precipitation down by 10-12 mm in most parts of the city centre. Removing Fløyen, on the other hand, has barely any impact at all (Figure 15 c). The results for Case 2 are similar to those of Case 1, with no effect on the precipitation in Bergen from removing Fløyen and a slightly smaller effect than in Case 1 from removing Løvstakken (not shown).

3 Discussion

Numerical sensitivity experiments, where the atmospheric flow during two southwesterly windstorms that hit southwestern Norway on 10 Januar, 2009 and 25 November 2011, has been reproduced. The results show that the sheltering of the northwestern part of the city

centre of Bergen is caused by the decelerating effect upstream of the the Fløyen massif, while the sheltering in the southwestern part of Bergen is largely a wake effect of the Løvstakken massif. These findings seem reasonable, as these areas lie both close to the foothills of the mountains with the largest impact on the wind. A more interesting result is that the total sheltering effect of both mountains is close to the sum of the blocking effect of Fløyen and the wake effect of Løvstakken. This is roughly valid in all central parts of the city as well as aloft, above the Bergen valley. No existing theory supports this fact. There are indeed several studies that reveal that stratified flow in the vicinity of two mountains can be very sensitive to both horizontal and vertical scales of the topography. Through the modification of gravity waves, a mountain downstream of a valley can thus both contribute to acceleration and deceleration of the flow inside the valley. Such effects have been studied by e.g. Hunt and Richards (1984), Grubiŝić and Stiperski (2009) and Stiperski and Grubiŝić (2011) for idealised flows and Ágústsson and Ólafsson (2007) for real flows. Seen from an energetic point of view, a reduction of the speed or the kinetic energy by the wake of the first mountain moves the flow deeper into a regime of orographic blocking as it meets the second mountain and the non-dimensional mountain height is increased. A wake may also be enhanced or sustained by a downstream mountain, blocking the low-level flow.

The simulated near surface wind speed compares relatively well with the observations from a local AWS network. A sensitivity analysis using two different model topography datasets (USGS and ASTER) and two different landuse datasets (USGS and GlobCorine) shows only a marginal sensitivity in the wind speed error statistics to the choice of these datasets. Previous studies have found larger differences when comparing lower and higher resolution datasets (e.g. Cheng and Byun, 2008; Arnold et al., 2012). One consistent improvement, however, is seen in the wind speed at Ulriken when applying the ASTER topography dataset instead of the USGS dataset. This improvement is most likely caused by a more accurate description of the topography in the ASTER dataset. In reality, Ulriken AWS is situated at 605 m.a.g.l., whereas in the simulations using the USGS dataset it is at 459 m.a.g.l. and in those using the ASTER dataset it is at 470 m.a.g.l. In a study of extreme winds in the Bergen region, Harstveit (2006) asserted that Ulriken experiences a local speed up of winds from the sector south to west. He attributed this speed up to small scale features in the local terrain. It is evident that a simulation, even at a high horizontal resolution of 500 m, will not accurately capture all such features. Larger improvements from using higher resolution topography model datasets can probably be expected when going to even higher

horizontal grid resolutions. Then, however, one approaches scales at which the normal ABL model schemes are no longer suited and Large-Eddy Simulation (LES) schemes should rather be applied. Such simulations are beyound the scope of the present study.

Although the studied windstorms are quite typical in terms of wind pattern (see climatology by Jonassen et al. (2012)), there do exist cases where strong and gusty winds in southwesterly flow reach down to parts of the centre of Bergen (e.g. Harstveit, 2006). Such cases are, however, not common and they are presumably related to rare details in the vertical profile of the flow and are left for future studies.

A significant downstream shift of the precipitation maximum around the mountain massif of Løvstakken, largely affecting the city centre of Bergen, is found in the simulation of the southwesterly windstorm of 10 January, 2009. This 'spillover effect' is typical for strong wind events as described by e.g. Sinclair et al. (1996) and during the Reykjanes experiment described in Rögnvaldsson et al. (2007). The removal of Løvstakken from the model topography confirms that this mountain is the source of the described precipitation pattern. Removing the Fløyen mountain massif, which is downstream of the city centre, has hardly any effect on the precipitation in the city. Previous simulations of orographic precipitation with a clear spillover, as e.g. Rögnvaldsson et al. (2007), have revealed a limited sensitivity of the precipitation pattern to the choice of microphysics parameterisation scheme. The topographic and atmospheric conditions in Rögnvaldsson et al. (2007) were quite similar to those in the present study, but in order to establish a conclusive and quantitative result on the impact of individual mountains of the precipitation climatology, many more simulations would be needed.

4 Summary and conclusions

In this study, our main goal has been to investigate why the centre of Bergen is sheltered during southwesterly windstorms. A series of numerical sensitivity experiments, in which we have stepwise removed larger parts of the topography surrounding the city centre from the model topography during two southwesterly windstorms, give some answers. The sheltering of Bergen appears to be caused by a combination of a downstream wake of the Løvstakken mountain massif and an upstream blocking from the Fløyen massif. The combined effect is close to the sum of each of them.

Regarding the initially posed question whether the AWS at Florida is representative of

the Bergen centre as a whole, this is only partly true. The effect from each of the mountains is strongest closest to their foothills. Hence, downstream of Løvstakken a wake dominates and upstream of Fløyen, there is a zone of blocking. At Florida, the blocking effect from Fløyen is most prominent.

Through spillover, the Løvstakken massif acts to increase the precipitation in the centre of Bergen during both of the investigated windstorms. The Fløyen massif turns out to have a minimum impact on the precipitation upstream of it. The strength of the spillover effect is known to increase with increasing wind speeds. Thus, the effect is likely less pronounced on the average than in the present strong wind cases.

A series of numerical sensitivity experiments using high resolution landuse and topography datasets have been carried out. The wind speed error statistics reveal only a marginal sensitivity to the choice of these datasets. This result may, however, be sensitive to the horizontal grid resolution.

5 Acknowledgment

The present study is partly the result of a long-lasting collaboration between AADI and GFI on weather observations at Mount Ulriken. We also owe our gratitude to Avinor and met.no for giving access to data from Sotra.

REFERENCES

Ágústsson, H. and Ólafsson, H. 2007. Simulating a severe windstorm in complex terrain. *Meteorologische Zeitschrift* **16**(1), 111–122.

Andersen, F. 1975. Surface winds in southern Norway in relation to prevailing H. Johansen weather types. *Meteor. Ann.* **6**(14), 377–399.

Arnold, D., Schicker, I. and Seibert, P. 2012. Towards high-resolution environmental modelling in the alpine region. *NATO Science for Peace and Security Series C: Environmental Security* **14**, 269–273.

Barstad, I. and Grønås, S. 2005. Southwesterly flows over southern Norway-Mesoscale sensitivity to large-scale wind direction and speed. *Tellus 57A* pp. 136–152.

Barstad, I. and Grønås, S. 2006. Dynamical structures for southwesterly airflow over southern Norway: the role of dissipation. *Tellus 58A* pp. 2–18.

Berge, E. and Hassel, F. 1984. An investigation of temperature inversions and local drainage flow in Bergen, Norway (in Norwegian). *Meteorological report series, University of Bergen* .

Bjerknes, J. and Solberg, H. 1921. Meteorological conditions for the formation of rain. *Geofys. Publ* .

Bjerknes, J. and Solberg, H. 1922. Life cycles of cyclones and polar front theory of the atmospheric circulation. *Geofys. Publ* **3**(1), 1–18.

Chen, F. and Dudhia, J. 2001. Coupling an Advanced Land Surface-Hydrology Model with the Penn State-NCAR MM5 Modeling System. Part 1. Model Implementation and Sensitivity. *Mon. Wea. Rev.* **129**, 569–585.

Cheng, F.-Y. and Byun, D. W. 2008. Application of high resolution landuse and land cover data for atmospheric modeling in the HoustonâĂŞGalveston metropolitan area, Part I: Meteorological simulation results. *Atmospheric Environment* **42**, 7795âĂŞ7811.

Dudhia, J. 1989. Numerical study of convection observed during the winter monsoon experiment using a mesoscale two-dimensional model. *J. Atmos. Sci* **46**, 3077–3107.

Grubiŝić, V. and Stiperski, I. 2009. Lee-Wave Resonances over Double Bell-Shaped Obstacles. *J. Atmos. Sci* **66**, 1205–1228.

Harstveit, K. 2006. Mapping of extreme wind conditions in Bergen kommune (in Norwegian). *met.no report* **3**, 55pp.

Hong, S., Dudhia, J. and Chen, S. 2004. A revised approach to ice microphysical processes for the bulk parameterization of clouds and precipitation. *Mon. Weather. Rev* **132**, 103–120.

Hunt, J. C. R. and Richards, K. J. 1984. Stratified airflow over one or two hills. *Bound.-Lay. Meteorol.* **30**, 223–229.

Janjic, Z. 1990. The step-mountain coordinate: physical package. *Mon. Weather Rev.* **118**, 1429–1443.

Janjic, Z. 1996. The surface layer in the NCEP eta model. *11th conference on numerical weather prediction, American Meteorological Society* pp. 354–355.

Janjic, Z. 2002. Nonsingular implementation of the Mellor-Yamada Level 2.5 Scheme in the NCEP meso models. *NCEP Office Note* p. 61p.

Jiang, Q. 2003. Moist dynamics and orographic precipitation. *Tellus 55A* pp. 301–316.

Jonassen, M. O., Ólafsson, H., Reuder, J. and Olseth, J. A. 2012. Multi-scale variability of winds in the complex topography of southwestern Norway. *Tellus 64A* pp. 1–17.

Lin, Y.-L. and Wang, T.-A. 1996. Flow regimes and transient dynamics of two-dimensional flow over an isolated mountain ridge. *J. Atmos. Sci.* **53**, 139–158.

Mlawer, E. J., Taubman, S. J., Brown, P. D., Iacono, M. J. and Clough, S. A. 1997. Radiative transfer for inhomogeneous atmospheres: RRTM, a validated correlated-k model for the longwave. *J. Geophys. Res.* **102**, 16663 – 16682.

Ólafsson, H. and Bougeault, P. 1996. Nonlinear Flow Past an Elliptic Mountain Ridge. *J. Atmos. Sci.* **53**, 2465–2489.

Peng, M. S., Li, S.-W., Chang, S. W. and Williams, R. T. 1995. Flow over mountains: Coriolis force, transient troughs and three dimensionality. *Q. J. R. Meteorol. Soc.* **121**, 593–613.

Pierrehumbert, R. and Wyman, B. 1985. Upstream effects of mesoscale mountains. *J. Atmos. Sci.* **42**, 977–1003.

Reuder, J., Fagerlid, G. O., Barstad, I. and Sandvik, A. 2007. Stord Orographic Precipitation Experiment (STOPEX): an overview of phase I. *Advances in Geosciences* **1o**, 17–23.

Rögnvaldsson, O., Bao, J.-W. and Ólafsson, H. 2007. Sensitivity simulations of orographic precipitation with MM5 and comparison with observations in Iceland during the Reykjanes Experiment. *Meteorol. Z.* **16**, 87–98.

Sinclair, M. R., Wratt, D. S., Henderson, R. D. and Gray, W. R. 1996. Factors Affecting the Distribution and Spillover of Precipitation in the Southern Alps of New Zealand - A Case Study. *J. Appl. Meteor.* **36**, 428–442.

Skamarock, W. C., Klemp, J. B., Dudhia, J., Gill, D. O., Barker, D. M., Duda, M. G., Huang, X.-Y., Wang, W. and Powers, J. G. 2008. A description of the Advanced Research WRF Version 3. *NCAR Tech. Note* **TN-475+STR**, 125.

Smith, R. B. 2006. Progress on the theory of orographic precipitation. *Geological Society of America, Special paper 398* pp. 1 – 16.

Spinnangr, F. 1943. Synoptic studies on precipitation in southern norway. ii front precipitation. *Meteor. Ann.* **1**(17), 433–468.

Steensen, B. M., Ólafsson, H. and Jonassen, M. 2011. An extreme precipitation event in Central Norway. *Tellus 63A* pp. 675–686.

Stiperski, I. and Grubišić, V. 2011. Trapped Lee Wave Interference in the Presence of Surface Friction. *J. Atmos. Sci* **68**, 918–936.

Teigen, R. 2005. Numerical simulation of orographic precipitation in West Norway (in Norwegian). *Master's thesis. Geophysical institute, University of Bergen. http://www.ub.uib.no/elpub/2005/h/406004/Hovedoppgave.pdf* .

Trüb, J. and Davies, H. C. 1995. Flow over a mesoscale ridge: Pathways to reg transition. *Tellus 47A* pp. 502–524.

Utaaker, K. 1995. Energy in the planning of area - local climate in Bergen (in Norwegian). *Meteorological report series,*

447 *University of Bergen* (1).

6 Figure captions

Figure 1: Mean sea level pressure at 1200 and 1800 UTC on 10 January 2009 (a and b) and 25 December 2011 (c and d). Based on analysis from the European Centre for Medium-Range Weather Forecasts. The location of Bergen is indicated with a black diamond.

Figure 2: The topography of the area of main interest, the locations and names of the AWSs (S1-S10), and indications of the geographical extent of the two dominating mountain massifs in the area: Løvstakken (1) and Fløyen (2). The dashed, red line indicates the approximate extent of the centre of Bergen. The dashed, black line between the points "A" and "B" indicates the position of the cross section in Figure 14.

Figure 3: Observed wind speed and wind direction during the investigated windstorms on 10 Januar, 2009 and on 25 December, 2011 in the Bergen area

Figure 4: A zoom-in of the landuse of domain 3 (500 m horizontal resolution) using the datasets of a) USGS and b) GlobCorine. See Table 3 for a list over landuse categories and respective numbers indicated on the colorbar. The coastline from GSHHS is indicated with a solid, black line.

Figure 5: Roughness length for momentum at the different AWSs for the simulations using the USGS and GlobCorine landuse datasets. The real roughness length is indicated as well.

Figure 6: Root mean square error (RMSE) and mean error (bias) for wind speed (observed minus simulated) using four different combinations of model landuse and topography datasets. Table 1 lists and explains the different experiments. Case 1 is 10 January, 2009 and Case 2 is 25 December, 2011

Figure 7: Simulated near surface (19.5 m.a.g.l.) horizontal wind speed at a) 1200 UTC on 11 Januar 2009 and at b) 2100 UTC on 25 December 2011. The results are from the outermost domain (4.5 km horizontal resolution). Observations from selected AWSs along the coast are indicated with red wind barbs. Each barb is 2.5 m s^{-1}. The location of Bergen is indicated with a "B".

Figure 8: Observed and simulated wind speed at selected AWSs on 10 Januar 2009 (Case 1) and 25 December 2011 (Case 2). The simulation results are from the innermost domain (500 m horizontal resolution)

Figure 9: As in Figure 8, but for wind direction.

Figure 10: a) near surface wind speed at 0000 UTC on 11 January in the CTRL sim-

ulation, b) wind speed in CTRL minus NOL, c) wind speed in CTRL minus NOF, and d) wind speed in CTRL minus NOFL. The dashed, red line indicates the approximate extent of the centre of Bergen.

Figure 11: Areas of characteristic location and flow patterns. The terrain height is given with contours every 100 m.

Figure 12: Difference in simulated near surface wind speed between the CTRL and the sensitivity simulations with topography modifications averaged within the areas indicated in Figure 11. The wind barbs at the top of the panels denote the simulated wind speed and direction at 900 hPa averaged within a box centred at 4.3°E and 61°N. Each half barb is 2.5 m s^{-1}.

Figure 13: Same as in Figure 10, but for 2100 UTC on 25 December, 2011.

Figure 14: a) cross section of horizontal wind speed at 0000 UTC on 11 January in the CTRL simulation, b) wind speed in CTRL minus NOL, c) wind speed in CTRL minus NOF, and d) wind speed in CTRL minus NOFL. The geographical location of the cross section is indicated in Figure 2.

Figure 15: a) 18 hour accumulated precipitation at 0000 UTC on 11 January, 2009, in the CTRL simulation, b) precipitation in CTRL minus NOL, c) precipitation in CTRL minus NOF, and d) precipitation in CTRL minus NOFL.

Table 2. Automatic weather stations. The height for Ulriken is set to 15 m.a.g.l., representing an average elevation above its immediate surroundings.

Station	Timeres. (min)	Source	m.a.s.l.	m.a.g.l.
Florida	10	GFI	48	30
Ulriken	10	AADI/GFI	605	15
Flesland	60	met.no	48	10
Sotra bridge	10	NPRA	50	50
Sotra	60	Avinor	341	10
Ulriksbakken	10	GFI	408	2.5
Haukeland	10	GFI	64	10
Løvstakken	10	GFI	472	2.5
Strandafjellet	10	GFI	303	2.5
Nordnes	10	GFI	48	30

Table 3. Table used in this study to convert GlobCorine landuse categories to USGS landuse categories.

	GlobCorine categories	USGS categories
1	urban and associated areas	urban and built-up land
2	rainfed cropland	dryland and cropland pasture
3	irrigated cropland	Irrigated cropland and pasture
3	complex cropland	irrigated cropland and pasture
4	not converted	mixed dryland / irrigated cropland and pasture
5	mosaic cropland / natural vegatation	cropland / grassland mosaic
6	mosaic of natural vegetation	cropland/woodland mosaic
7	grassland	grassland
8	heathland and sclerophyllus vegetation	shrubland
9	not converted	mixed shrubland/grassland
10	not converted	savanna
11	not converted	deciduous needleleaf forest
12	not converted	deciduous broadleaf forest
13	not converted	evergreen broadleaf forest
14	not converted	evergreen needleleaf forest
15	forest	mixed forest
16	water bodies	water bodies
17	vegetated low lying areas on regularly flooded soil	herbaceous wetland
18	not converted	wooded wetland
19	sparsely vegetated area	barren or sparsely vegetated
20	not converted	herbaceous tundra
21	not converted	wooded tundra
22	not converted	mixed tundra
23	not converted	bare ground tundra
24	permanent snow and ice	snow or Ice

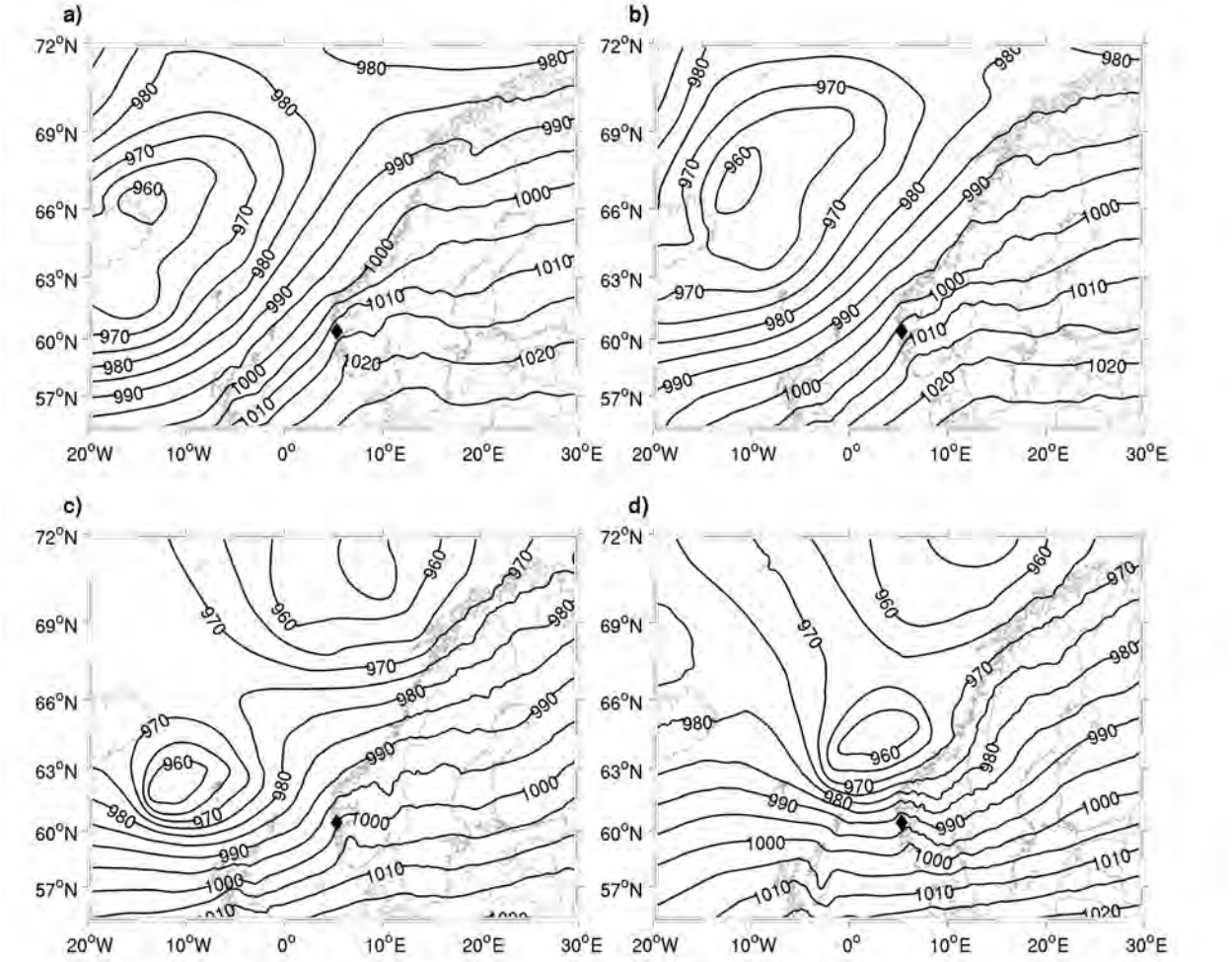

Figure 1. Mean sea level pressure at 1200 and 1800 UTC on 10 January 2009 (a and b) and 25 December 2011 (c and d). Based on analysis from the European Centre for Medium-Range Weather Forecasts. The location of Bergen is indicated with a black diamond.

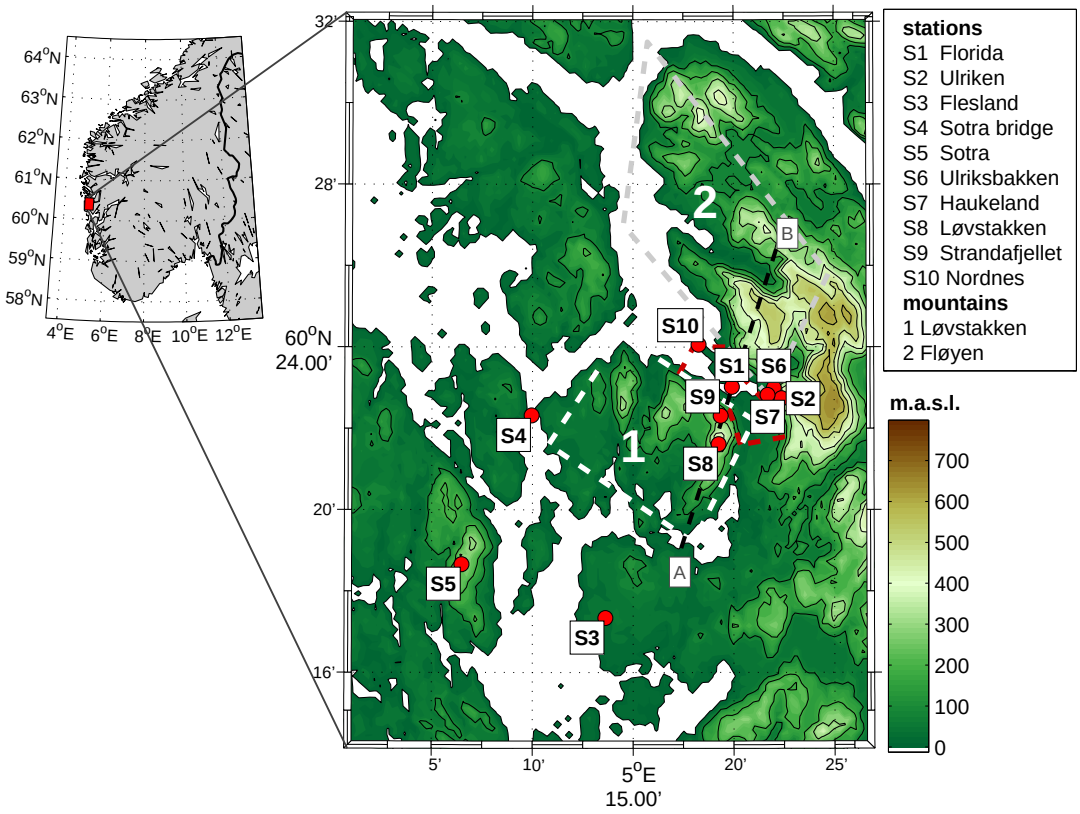

Figure 2. The topography of the area of main interest, the locations and names of the AWSs (S1-S10), and indications of the geographical extent of the two dominating mountain massifs in the area: Løvstakken (1) and Fløyen (2). The dashed, red line indicates the approximate extent of the centre of Bergen. The dashed, black line between the points "A" and "B" indicates the position of the cross section in Figure 14.

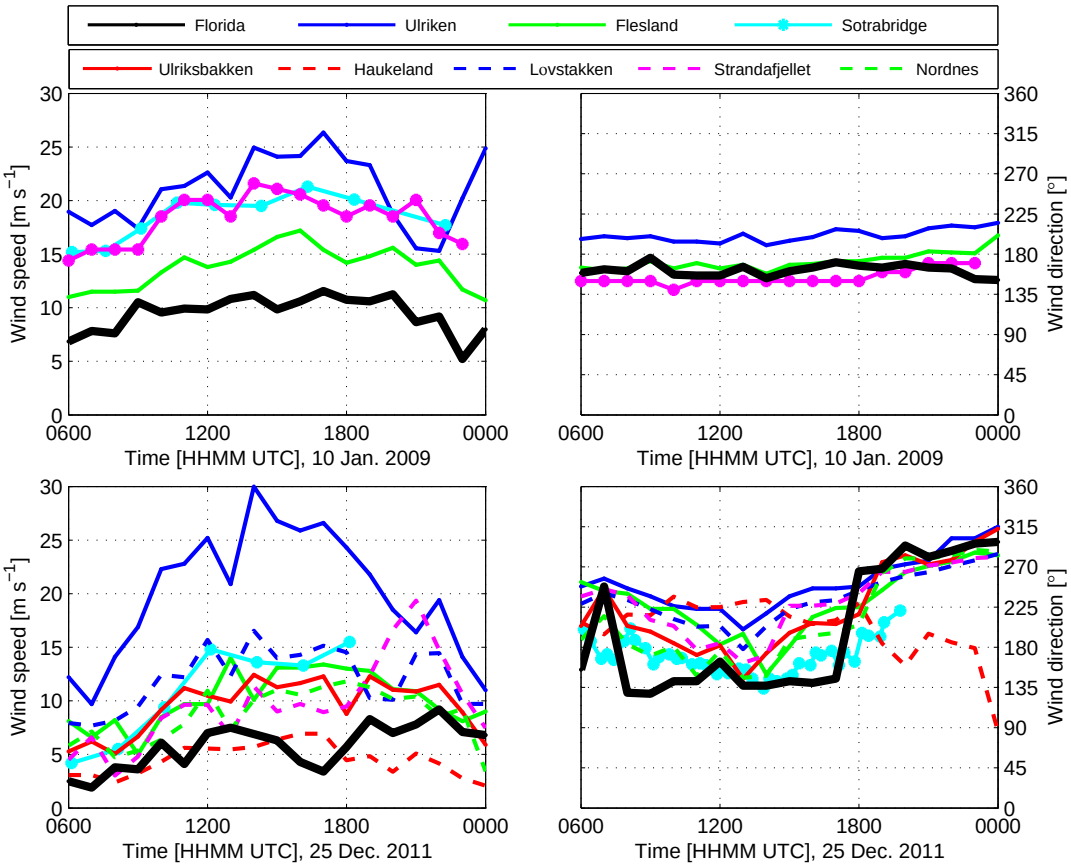

Figure 3. Observed wind speed and wind direction during the investigated windstorms on 10 Januar, 2009 and on 25 December, 2011 in the Bergen area.

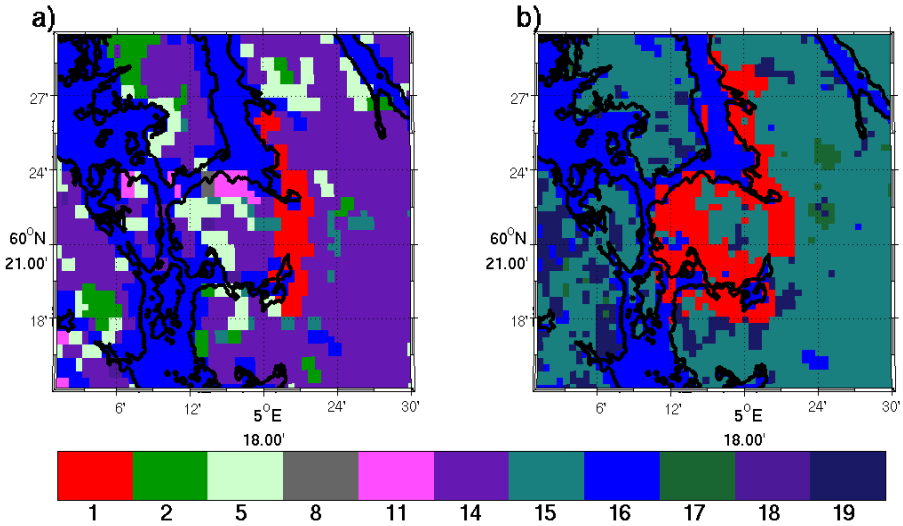

Figure 4. A zoom-in of the landuse of domain 3 (500 m horizontal resolution) using the datasets of a) USGS and b) GlobCorine. See Table 3 for a list over landuse categories and respective numbers indicated on the colorbar. The coastline from GSHHS is indicated with a solid, black line.

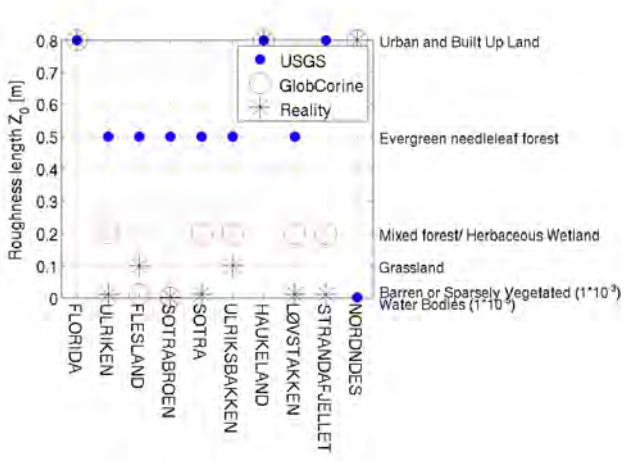

Figure 5. Roughness length for momentum at the different AWSs for the simulations using the USGS and GlobCorine landuse datasets. The real roughness length is indicated as well.

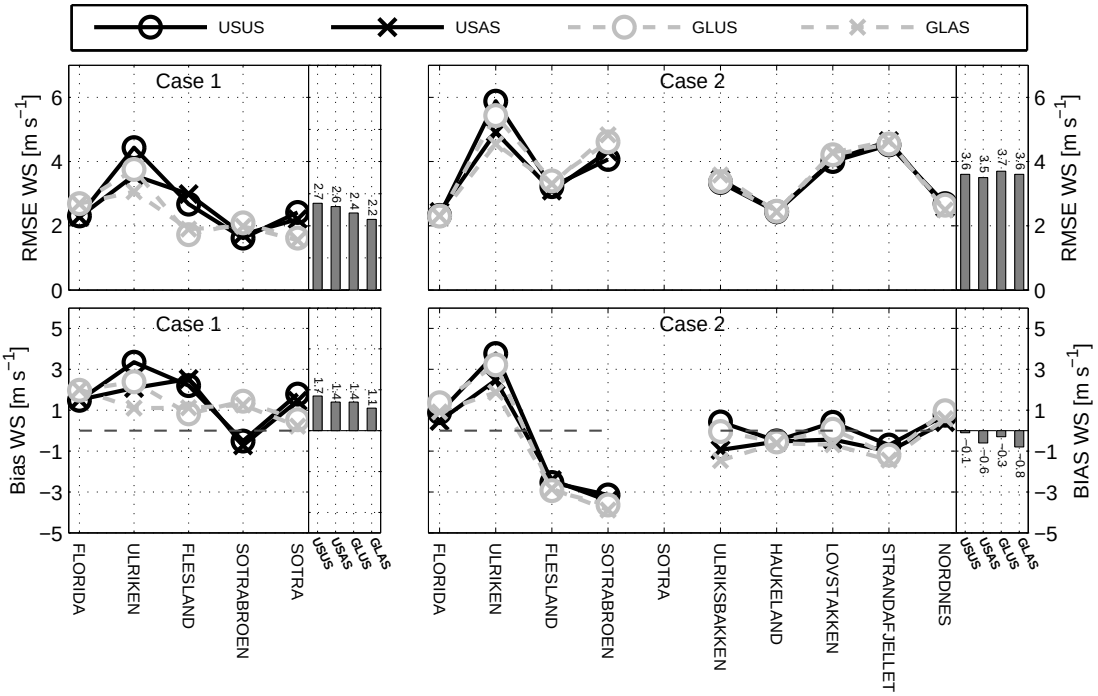

Figure 6. Root mean square error (RMSE) and mean error (bias) for wind speed (observed minus simulated) using four different combinations of model landuse and topography datasets. Table 1 lists and explains the different experiments. Case 1 is 10 January, 2009 and Case 2 is 25 December, 2011.

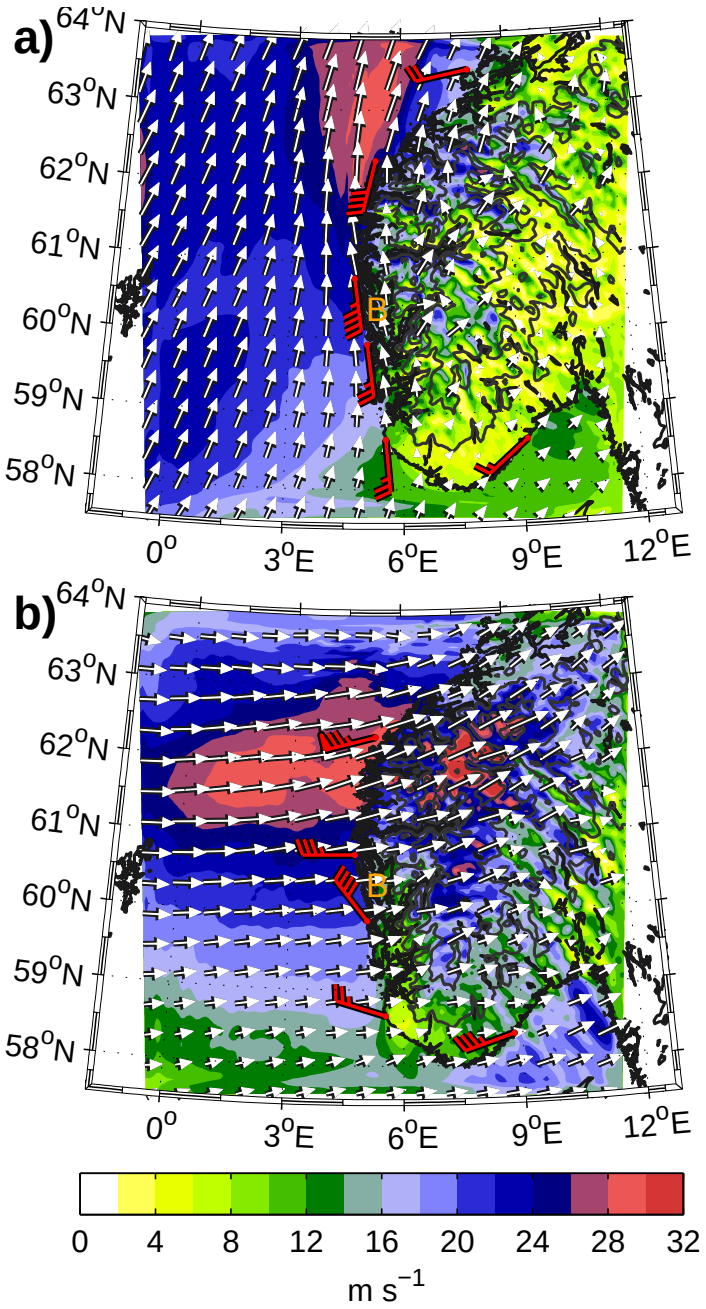

Figure 7. Simulated near surface (19.5 m.a.g.l.) horizontal wind speed at a) 1200 UTC on 11 Januar 2009 and at b) 2100 UTC on 25 December 2011. The results are from the outermost domain (4.5 km horizontal resolution). Observations from selected AWSs along the coast are indicated with red wind barbs. Each barb is 2.5 m s^{-1}. The location of Bergen is indicated with a "B".

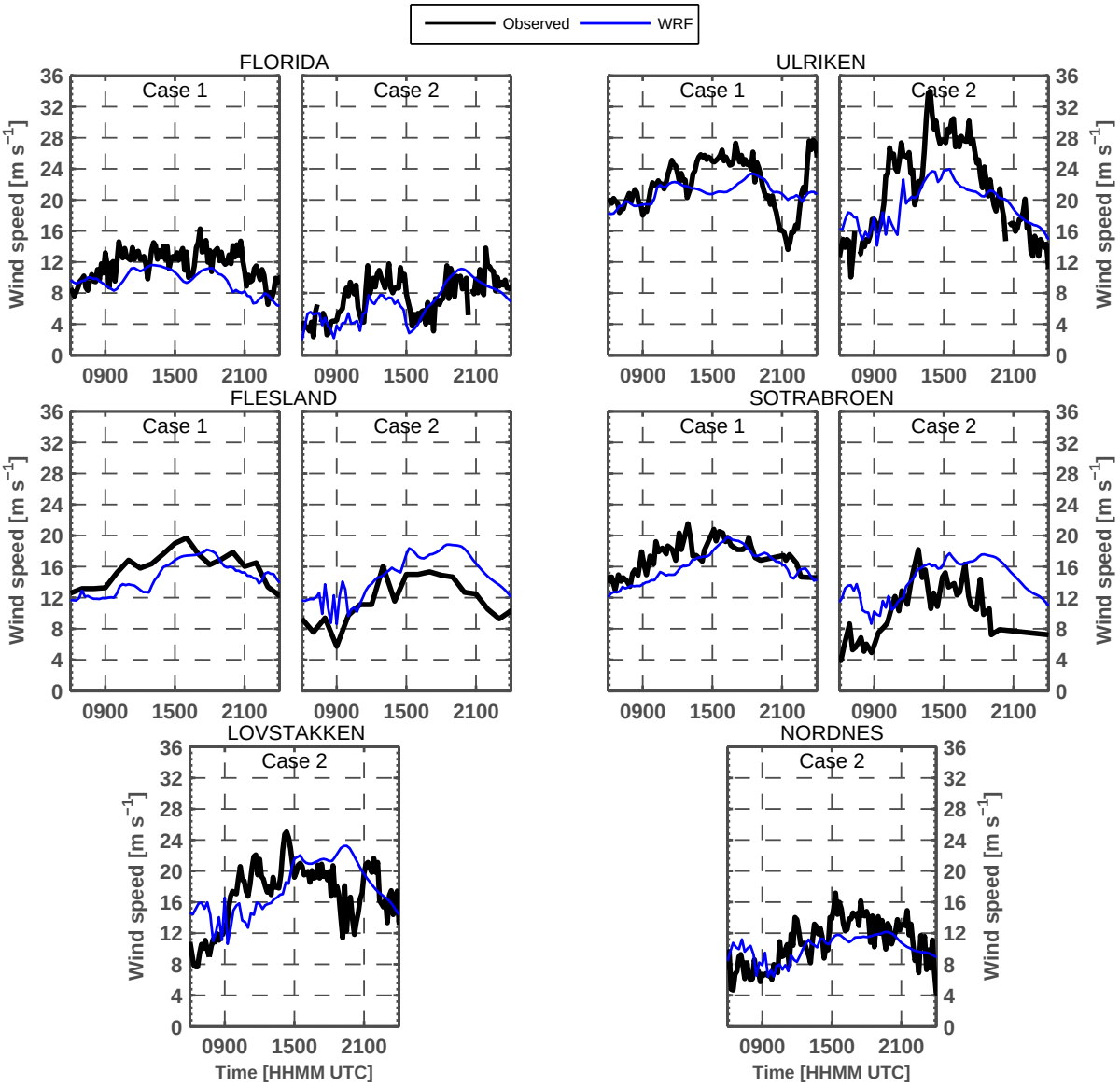

Figure 8. Observed and simulated wind speed at selected AWSs on 10 Januar 2009 (Case 1) and 25 December 2011 (Case 2). The simulation results are from the innermost domain (500 m horizontal resolution).

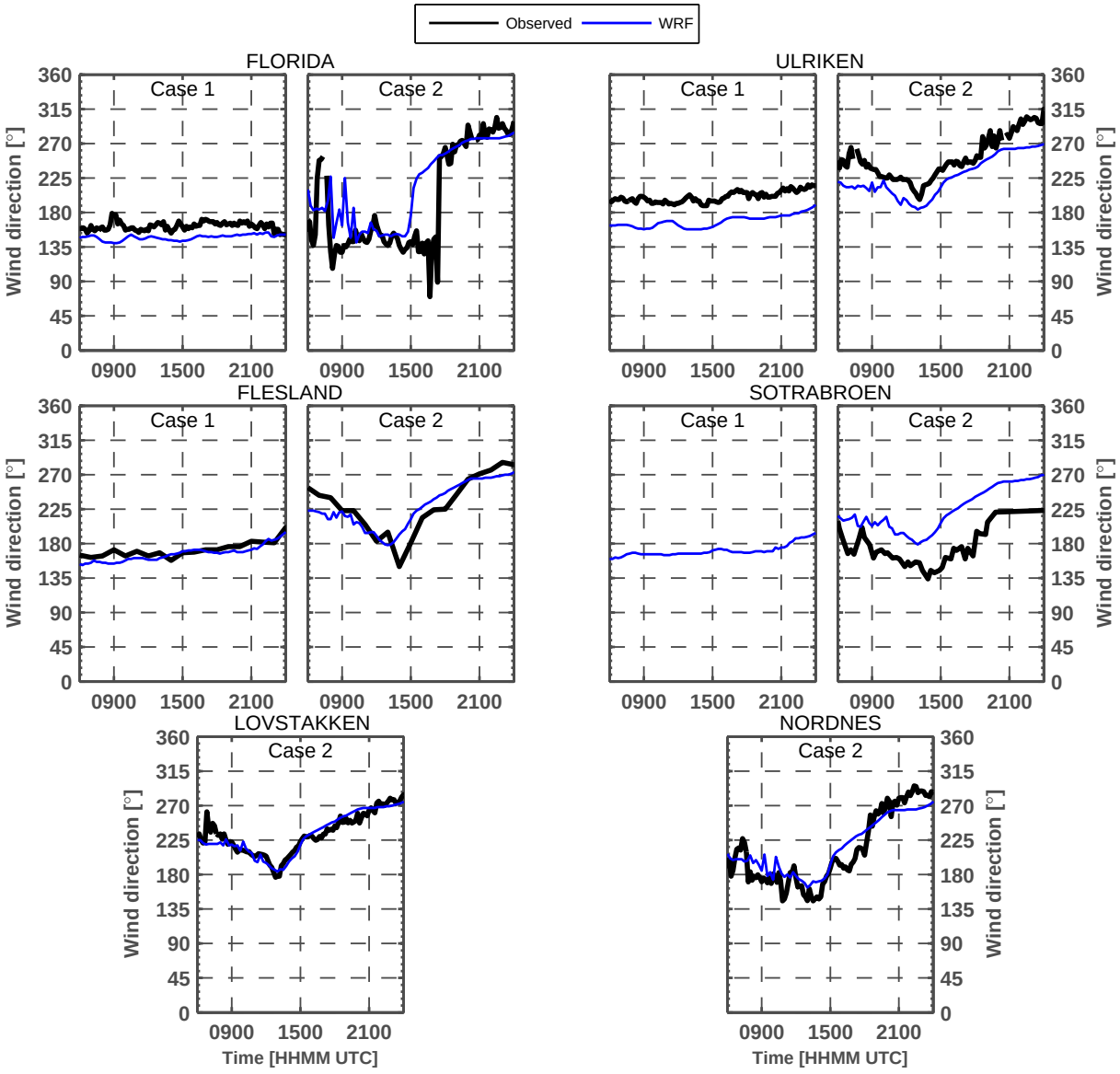

Figure 9. As in Figure 8, but for wind direction.

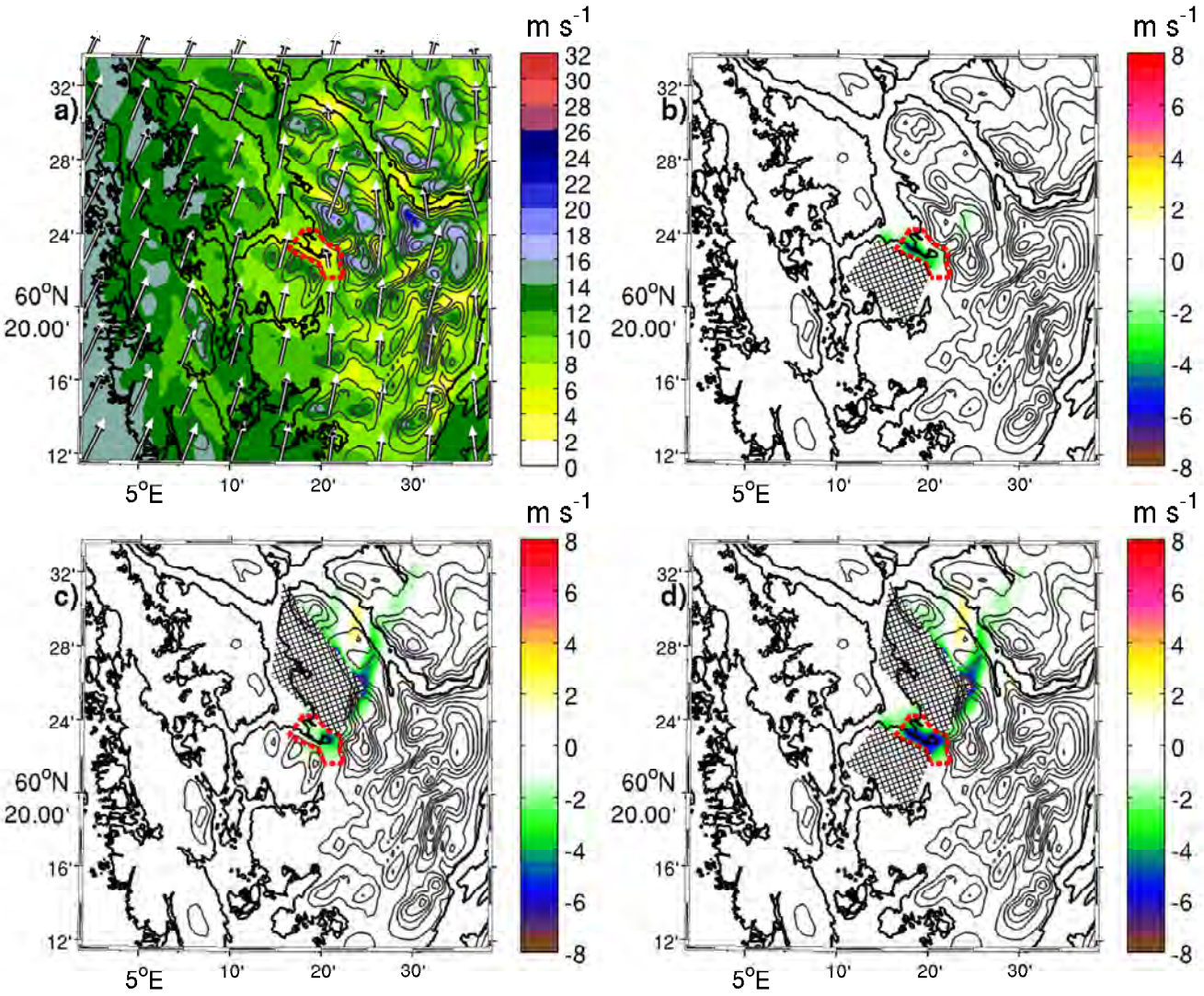

Figure 10. a) near surface wind speed at 0000 UTC on 11 January in the CTRL simulation, b) wind speed in CTRL minus NOL, c) wind speed in CTRL minus NOF, and d) wind speed in CTRL minus NOFL. The dashed, red line indicates the approximate extent of the centre of Bergen.

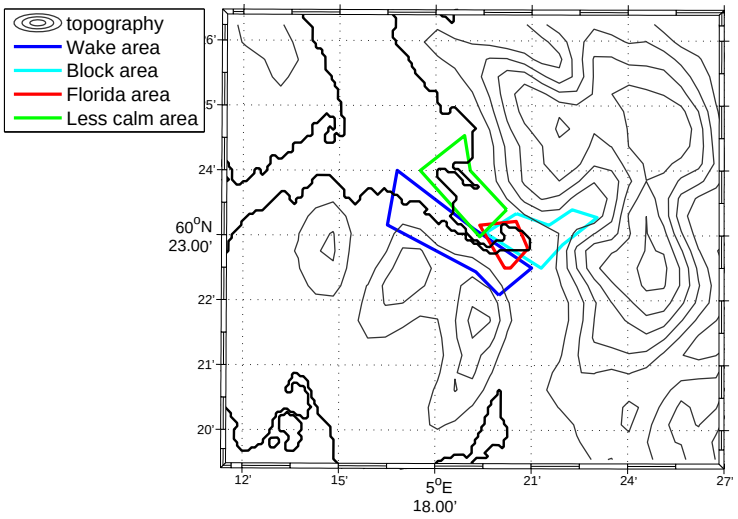

Figure 11. Areas of characteristic location and flow patterns. The terrain height is given with contours every 100 m.

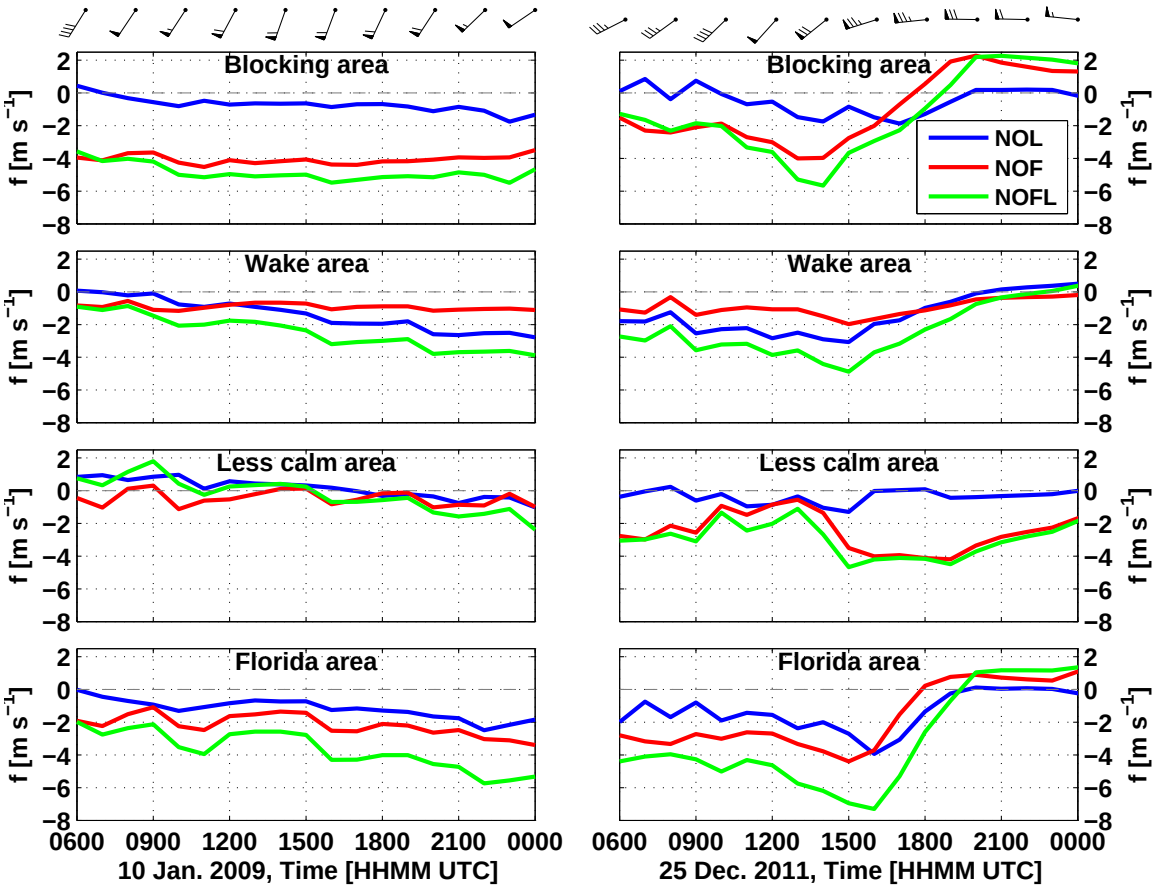

Figure 12. Difference in simulated near surface wind speed between the CTRL and the sensitivity simulations with topography modifications averaged within the areas indicated in Figure 11. The wind barbs at the top of the panels denote the simulated wind speed and direction at 900 hPa averaged within a box centred at 4.3°E and 61°N. Each half barb is 2.5 m s^{-1}.

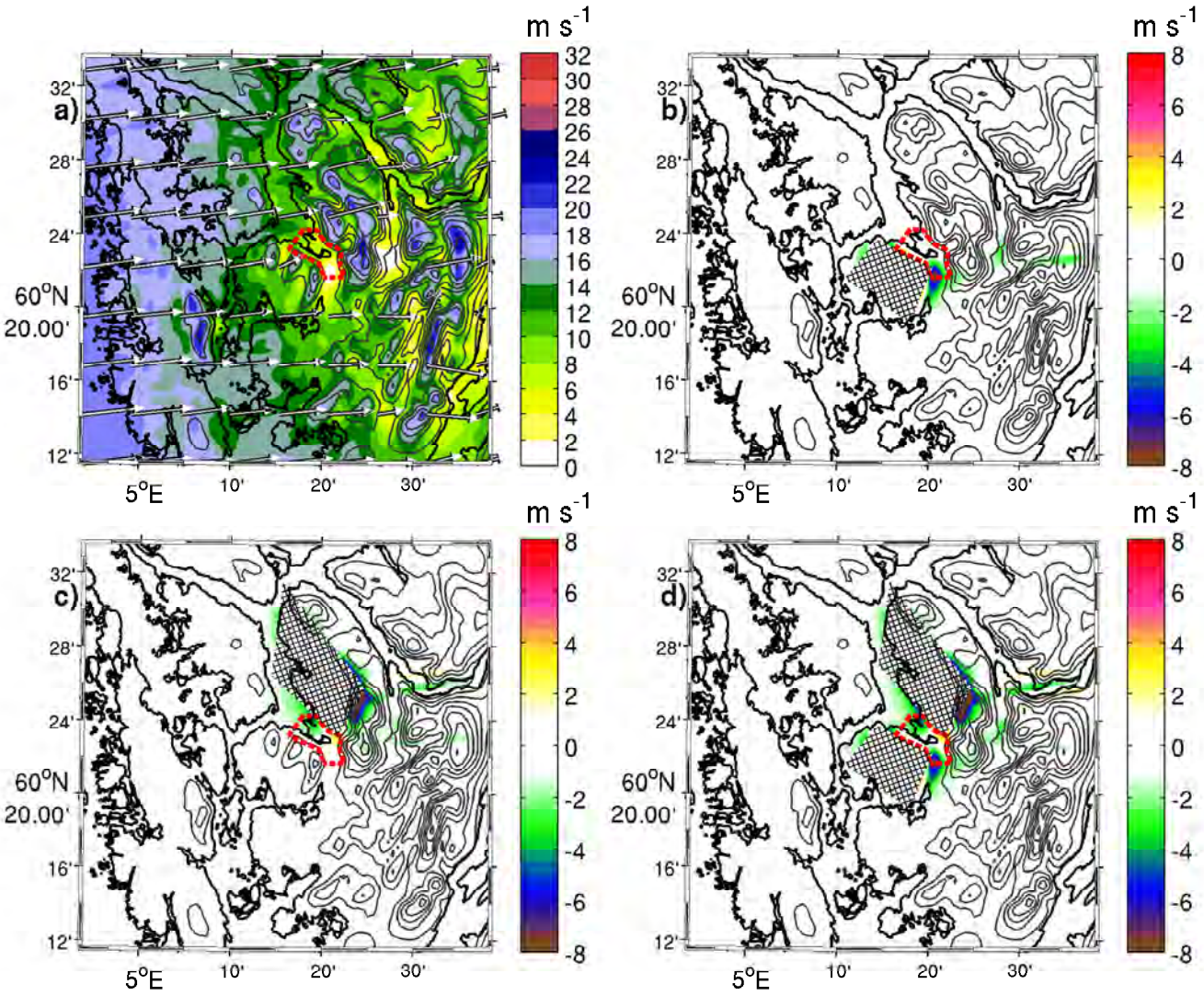

Figure 13. Same as in Figure 10, but for 2100 UTC on 25 December, 2011.

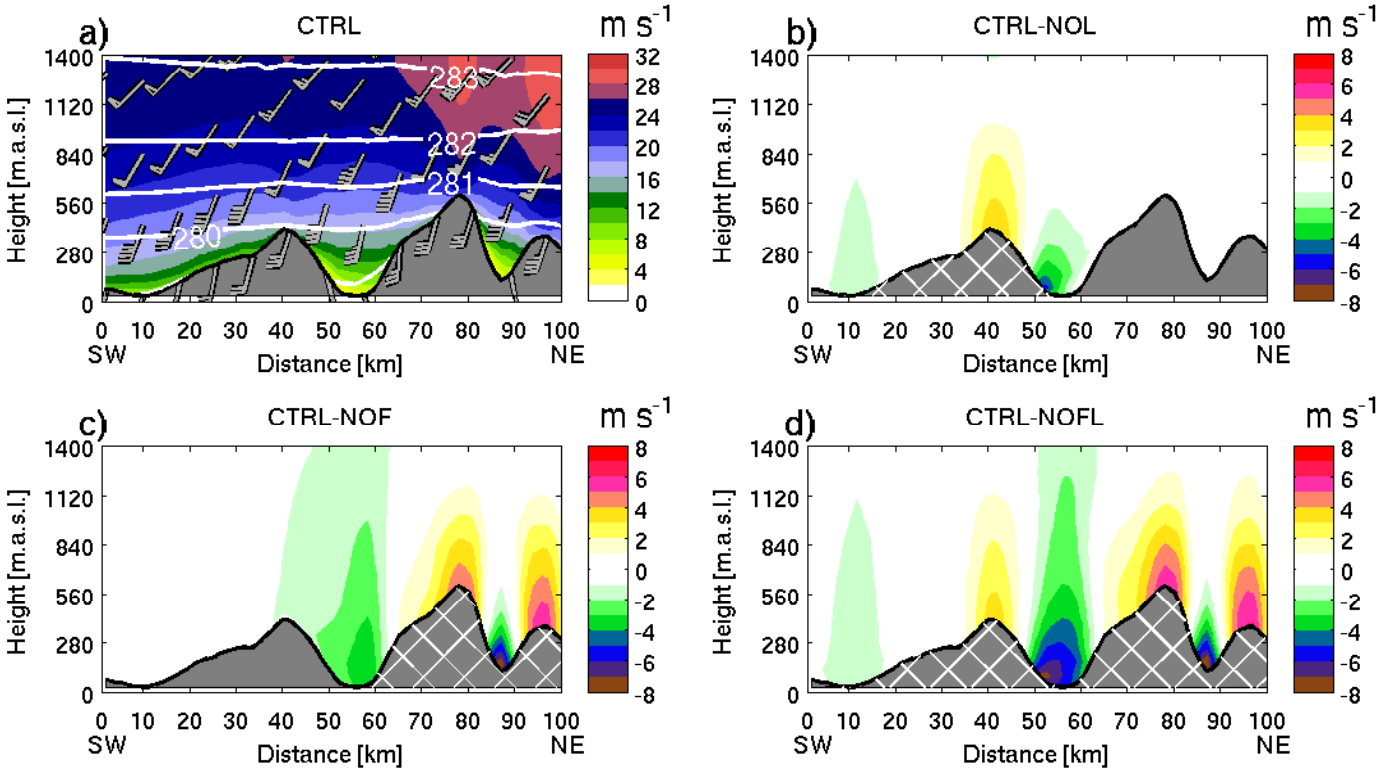

Figure 14. a) cross section of horizontal wind speed at 0000 UTC on 11 January in the CTRL simulation, b) wind speed in CTRL minus NOL, c) wind speed in CTRL minus NOF, and d) wind speed in CTRL minus NOFL. The geographical location of the cross section is indicated in Figure 2.

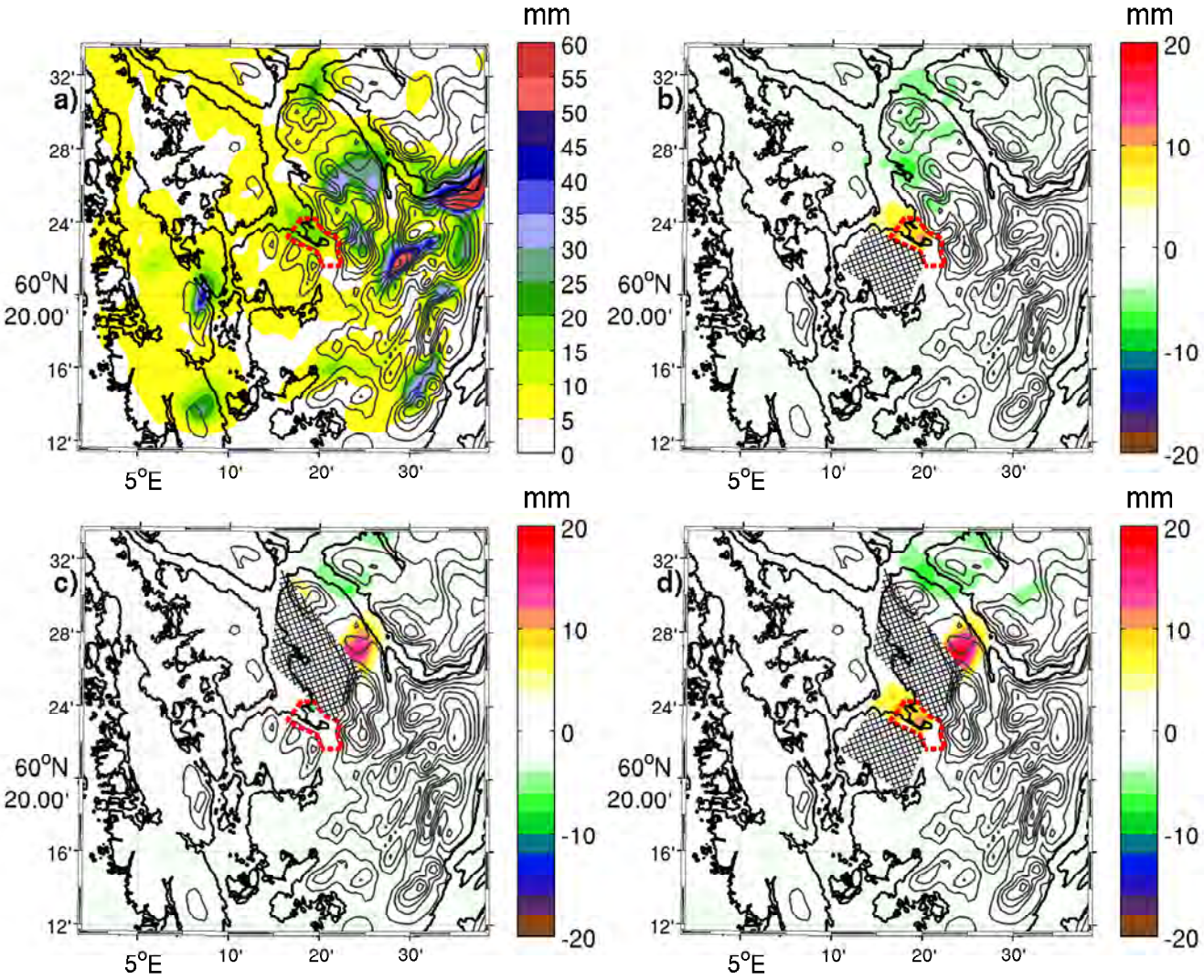

Figure 15. a) 18 hour accumulated precipitation at 0000 UTC on 11 January, 2009, in the CTRL simulation, b) precipitation in CTRL minus NOL, c) precipitation in CTRL minus NOF, and d) precipitation in CTRL minus NOFL.